Additively Manufactured Polymers and Polymer Composites for Minerals Processing Technology

A thesis in fulfilment of the requirements for the degree of Doctor of Philosophy

By

Ashlee Espinoza

Department of Mechanical and Aerospace Engineering

University of Strathclyde

Glasgow

UK

Dedicated to the memory of Mrs. Eleanor Schmid
and her everlasting support of my education.

Declaration of Authenticity and Author's Rights

This thesis is the result of the author's original research. It has been composed by the author and has not been previously submitted for examination which has led to the award of a degree.

Signed: Ashlee Espinoza

Date: 30-September-2023

Acknowledgements

I would like to thank Dr. Liu Yang, my PhD supervisor, for his continued support, motivation, and knowledge throughout this degree. His guidance was invaluable, and the research would not have been possible without this.

Thank you to the Weir Group for their sponsorship of the project. Lauren Youd (WARC Programme Manager), thank you for guiding this project to success and for your constant encouragement. To Steven Hunter (Technology group leader: Separation) and Eduardo Cepeda (Chief engineer) for championing this project and industrial advice. Thank you to Alan Stewart (Head of Innovation and Research) and the entire Additive Manufacturing team for their support and enthusiasm for this work.

I would like to thank Mr. James Kelly, Mr. Drew Irvine, Mr. James Gillepsie, Prof. David Nash, Dr. Alice Macente, Dr. Maider Olasolo, and Dr. Tiziana Marrocco for their technical support of this project. Completing an experimental PhD would be impossible without your advice, time, and knowledge.

Thank you to the members of the WARC Erosion Corrosion Lab, Dr. Frazer Brownlie and Dr. Trevor Hodgkiess, for educating me on slurry erosion and providing company during long hours of testing in the lab.

Lastly, to my family and friends who have continued to support me in this process through all the highs and lows.

Publications

Conference oral presentations:

"Investigation of composites wear under slurry flow conditions".

5th International Conference on Mechanics of Composites

July 2019

Planned publications:

1. Experimental investigation of solid particle erosion of additively manufactured polyetherimide.
2. Performance of an additively manufactured pressure vessel.
3. A review of wear of additively manufactured polymers and polymer composites.

Abstract

Hydrocyclones are particle separation equipment used in the minerals processing industry. They are exposed to aggressive environments and thus are normally comprised of structural steel casings with rubber liners for erosion resistance. The use of additively manufactured polymers and polymer composites for hydrocyclones was investigated. This was necessary as limited knowledge was available to determine the merit of the materials for the application. Two work packages were undertaken that highlight the novelty of the field.

The first case study explored the use of fused deposition modelling (FDM) for a hydrocyclone casing. Analysis was performed for hydraulic loading relevant to the application and for 3 bar pressure certification using ANSYS. Locations of stress concentrations were identified; however, the majority of the structure exhibited low stress. From this initial analysis, acrylonitrile butadiene styrene (ABS) was chosen for an experimental study of a cylindrical pressure vessel manufactured by FDM. The vessel was tested to a pressure of 3 bar and strain was recorded. The vessel withstood the pressurisation, but did exhibit creep behaviour. After 6 days with only hydrostatic force applied, there were further creep events, however, the material did not fail or show significant signs of elongation or dilation. Subsequently, the vessel was pressurised to failure which occurred at 11 bar. Catastrophic failure can be anticipated to occur at locations where deposited material rasters meet.

A novel fundamental study of erosion of polymers and polymer composites manufactured using FDM was completed. To date, published studies for the erosion of FDM materials were very limited. A recirculating slurry impingement rig was used to test Ultem 1010 and Nylon 12CF specimens and the epoxy sealed counterparts in a slurry of water and angular silica sand. The effects of the manufacturing method, presence of epoxy, and testing conditions were analysed. The Ultem 1010 specimens were compared to a traditionally manufactured counterpart, Ultem 1000. Overall, Ultem 1000 performed better than all additively manufactured materials. The sealed and unsealed Ultem 1010 specimens performed second best, with Nylon 12CF (sealed and unsealed) having the worst erosion performance. Ultem 1010 exhibits semi-ductile

behaviour with the peak of erosion observed at the 45° impingement angle and highest material loss when the flow is 0° to the raster orientation. Ultem 1010 sealed with epoxy results in peak erosion at 90° to the raster orientation at 45° and 20° impingement angles. Overall, sealing the specimens provided protection at all angles except 20° impingement. Nylon 12CF experiences the most material loss at 90° impingement angle. The epoxy sealed Nylon 12CF exhibited different behaviour than the as deposited Nylon 12CF. The peak of material loss is at 45° impingement and 90° to the raster orientation. The epoxy provided protection at the 90° imingement angle with a significant reduction in material loss. 45° impingement with 90° to the raster orientation and 20° with 0° to the raster orientation had worse wear than the unsealed specimens for the same angle and orientation. The wear mechanisms observed for all materials were cracking, micro-cutting, micro-ploughing, and plastic deformation. Abrasive wear outside the direct impingement zone cannot be considered negligible in a number of cases.

Contents

List of acronyms and symbols

ABS	Acrylonitrile butadiene styrene
AM	Additive manufacturing
Al_2O_3	Aluminium oxide
ANOVA	Analysis of variance
U	Average exit velocity
BSP	British Standard Pipe
CF	Carbon fibre
τ_p	Characteristic time of the particle
CFD	Computational fluid dynamics
°	Degree(s)
°C	Degrees Celsius
ρ	Density
P09	DMC used by industrial sponsor
DMC	Dough moulding compound
η	Erosion efficiency
FEA	Finite element analysis
FEM	Finite element modelling
μ_f	Fluid viscosity
FDM	Fused deposition modelling
FFF	Fused filament fabrication
GPa	Giga-pascal
GF	Glass filled
g/L	Grams per litre
kN	Kilo-newton
kPa	Kilopascal
L	Litre
MPa	Megapascal
m	Metre
m/s	Metres per second
μm	Micro-metre

mg	Milligram
mm	Millimetre
mm/s	Millimetres per second
N	Newton
D	Nozzle diameter
ρ_p	Particle Density
d_p	Particle diameter
Pa	Pascal
PA	Polyamide
PCL	Polycaprolactone
PC-ABS	Polycarbonate blend of ABS
PEEK	Polyether ether ketone
PEI	Polyetherimide
PLA	Polylactic acid
PMMA	Polymethylmethacrylate
PTFE	Polytetrafluorethylene or Teflon
PVC	Polyvinyl chloride
RPM	Rotations per minute
SEM	Scanning electron microscope
s	Second
SLS	Selective laser sintering
SiC	Silicon carbide
SiO_2	Silicon dioxide
SLA	Stereolithography
St	Stokes number
TPE	Thermoplastic elastomer
TiO_2	Titanium dioxide
vol%	Volume percentage
wt%	Weight percentage
w.r.t.	With respect to
XCT	X-ray computed tomography

List of figures

List of tables

1. Introduction to thesis

1.1 Mining processes and environment

The mining industry is one of the cornerstones of modern industrialisation. The extraction of precious materials, such as copper, has uses that are inextricable from our lives. The process of separating valuable minerals from ore is an energy intensive process [1]. The environments within a mining circuit can be harsh and the processing equipment used is exposed to slurries of various mediums [2]. The three main stages of mining are extraction, transportation and processing [3]. Part of the processing phase is the crushing of ore into smaller fragments known as comminution [4]. Within a mining circuit there is a need to be able to distinguish and separate particles based on size. One of the widely used technologies for separation is the hydrocyclone, which utilises inertial and gravitational forces to classify the particles by size.

A field visit to the El Soldado copper mine in Chile provided understanding of the environment and practical application of a hydrocyclone within a milling circuit before conducting the research described in this thesis. In this circuit, the extracted ore is taken to a crusher and then transported by conveyor to the semi-autogenous grinding (SAG) mill shown in Figure 1. The SAG mill operates by rotating and utilising metal balls to further reduce the average size of the minerals. Figure 2 shows this process of size reduction and classification.

Figure 1. Minerals leaving a conveyor after a series of crushing (left) and the SAG mill (right).

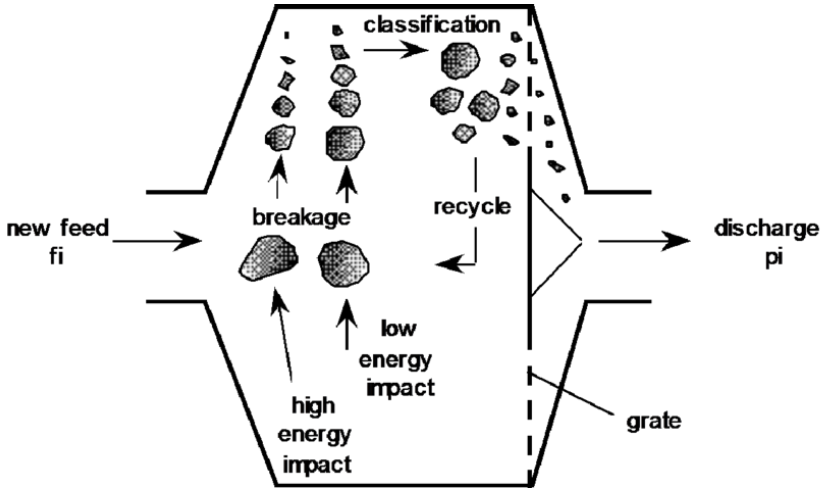

Figure 2. Diagram of the internal mechanisms of a SAG mill [4].

After going through the SAG mill, the minerals are then fed onto a screen which provides further classification. Those that are small enough pass through the screen to be combined with water to become a slurry. The slurry is carried to a hydrocyclone cluster by a centrifugal pump. The minerals that were not small enough to pass through the screens are sent back to the crusher and repeat the process. The grinding environment has a significant effect on the extraction of the ore via processes such as flotation, thus accurate particle separation and performance of the hydrocyclone is crucial [5].

Hydrocyclones are also capable of separating clean water from different density liquids and sand. Geographic locations that are rich in minerals, such as the Norte Grande region of Chile, which covers a large portion of the Atacama Desert, are not as abundant in the resources necessary for mining activity such as water. Proper management and usage of water is necessary to adhere to environmental regulations and economical means [6]. There is also a need for processes such as de-watering so that the environmental effect of potential pollutants can be mitigated [6].

1.2 Hydrocyclones at The Weir Group

The Weir Group is a multinational engineering company providing advanced engineering solutions for the mining and minerals industry. Among their products is the Cavex® range of hydrocyclones varying in size from 40 to 800 mm in diameter and capable of a large range of particle and fluid separation. The primary focuses for the design of the Cavex® hydrocyclones are improved performance and capacity, increased separation efficiency, sustainability, cost savings, and improved safety.

Figure 3. Hydrocyclones in a cluster formation (rendering provided by the Weir Group).

The main operating concerns for hydrocyclones in mining circuits are erosion and corrosion. Corrosion is an electro-chemical reaction that is due to the charge of the ions in the medium and the metal. The metal will release electrons resulting in a more stable state, such as an oxide. In slurry conditions, the water carrying the minerals will create this oxide layer on the metal. The oxide layer is more ductile than the original metal and is prone to flaking away the substrate [7]. This is exacerbated by the mechanical damage of erosion taking place by the minerals in the slurry. The Weir Group has made great investments into the investigation of corrosion and how to

protect metals from this damage. Polymers do not undergo corrosion and have historically been used as to protect metals from corrosion in the form of films or coatings [7]. As the capability of Weir's additive manufacturing team grows, a range of additively manufactured polymers and polymer composites have become available in house using the Stratasys F900 printer. Additive manufacturing processes, specifically material extrusion, will be discussed in Chapter 2.

A hydrocyclone of 150 mm in diameter was chosen by the Weir Group to be the subject of this study. This is denoted as the '150 CVD'. The 150 CVD is a perfect candidate for exploration of additive manufacturing method due to size and structural requirements. At the time of this research, this particular model had only been designed and tested using structural steel. Within the company, there is also the option to fabricate them from a glass fibre reinforced polyester. This research was proposed in order to create a lightweight casing that utilised additive manufacturing for the 150 CVD.

Mining is an industry with a strong emphasis on prohibiting occupational hazards and ensuring the safety of those working in the milling circuit [8]. Light-weighting is one way to help increase the safety of those that install hydrocyclones on site. While mining is an industry that is extractive, but nonetheless essential, reducing the carbon footprint where possible is important to the industrial sponsor. There is a global supply chain that involves transit of raw material and finished products around the world. There is a possibility to reduce fuel consumption per hydrocyclone by creating lighter components.

In some applications, the structural loading is such that using a metallic component is the only option. However, for the 150 CVD, it has already been proven that the previous generation of designs could successfully be made by the glass reinforce polyester resin. Traditionally, the casing is protected by a thick inner layer of natural or synthetic rubber which takes on the erosive wear. Therefore, the casing is only subjected to corrosion from the external environment (i.e., humidity or moisture) and leakage. For the applications of the 150 CVD, the Weir group is interested in the option to create a future design in which the polymer casing is used without a rubber liner.

1.3 Research Objectives

This research explores the possibility of using additively manufactured (AM) polymers and polymer composites in two distinct studies.

The first is a study of the hydrocyclone itself and the 3-bar pressurisation test that is used to certify the design by the industrial sponsor. The 150 CVD is currently manufactured in fabricated steel and glass fibre reinforced polyester resin dough moulding compound (DMC) denoted as P09. Using Ansys software the structural requirements of the hydrocyclone are understood for the P09 (as this has lower mechanical properties than the steel) for hydraulic and 3 bar pressurisation scenarios. This informed the selection of additive materials for component testing. A cylindrical component manufactured using fused deposition modelling was used for pressure testing to understand the behaviour of the material and therefore the feasibility of its use for the 150 CVD.

The second study is a fundamental investigation of the wear resistance of AM materials under slurry conditions. Specimens were placed in a slurry impingement rig and examined to understand their behaviour during erosion. This information supports further exploration of 150 CVD designs and protective measures. In addition, it provides an important contribution to the understanding of the behaviour of these novel materials for any erosive environment.

As presented in Chapter 2 and Chapter 4, the study of additively manufactured polymer vessels subjected to internal pressure and the erosive wear of such materials are novel topics. Few prior studies had been completed at the time of this research. While this study is focused on meeting the requirements of an existing application, the investigations provide great value to the larger body of work on the capability of additively manufactured polymers and polymer composites.

1.3.1 Research Statement and Questions

The main focus of the research was to investigate the application of additively manufactured polymers and polymer composites in processing equipment through a case study on hydrocyclones and a fundamental investigation of wear of materials under slurry conditions.

1. How can additively manufactured polymers and polymer composites be utilised to meet the structural and wear requirements of the 150 CVD hydrocyclone?
2. How will additively manufactured polymers and polymer composites wear in a slurry?

1.4 Thesis Outline

Chapter 2 contains background information on hydrocyclones and their uses, an overview of the manufacturing process (specifically fused deposition modelling (FDM)), and the physical and mechanical properties of polymers manufactured via FDM. Additionally, the state of the art of additively manufactured polymers for pressure vessels is discussed.

Chapter 3 covers the 150 CVD hydrocyclone case study undertaken. An initial analysis of the structural requirements of the 150 CVD is performed using finite element analysis. This informed the material selection for the testing of an additively manufactured pressure vessel in order to understand the material response. The vessel was tested up to a pressure of 3 bar (as designated by the industrial sponsor) and then to failure.

The erosion study spans Chapter 4-6. Chapter 4 provides a literature review of the solid particle erosion of polymers and polymer composites and the current status of wear studies for additively manufactured polymers.

Chapter 5 is the methodology for the erosion testing performed. The materials, apparatus, testing conditions, testing protocol and post-test procedures are described.

Chapter 6 covers the findings of the erosion testing. This includes quantitative results of material loss as well as qualitative results determining the wear mechanisms present.

The thesis conclusions and future work are found in Chapter 7.

1.5 Current status of work

At the time this thesis was authored, the industrial partner had recognised the value of the work and moved forward with the process of incorporating additively manufactured hydrocyclones. Printing of full scale prototypes has begun for the 150 CVD and for smaller sized hydrocyclones. Additionally, further research work on the investigation of erosion of additively manufactured thermoplastics for a broader range of materials and redesign of the 150 CVD for AM was proposed and funded by the industrial partner. This work will be performed by the author and is commencing in July of 2023 at the University of Strathclyde.

2. Additive manufacturing and its application to hydrocyclones

2.1 Introduction

Additive manufacturing has gone from being a research focused topic to commercially available for thermoplastics and fibre reinforced thermoplastics, including continuous and discontinuous fibres [9]. 3D printing enables rapid prototyping and reduction of tooling for manufacturing without the geometry limitation of traditional manufacturing. Of these manufacturing methods, those of the most significance are selective laser sintering (SLS) and fused deposition modelling (FDM). SLS converts digital CAD models to 3D objects via sintering of powder layer by layer while FDM lays molten thermoplastic down layer by layer [10]. Additive manufacturing has gained popularity in a number of sectors including military equipment, aerospace, energy and power, biomedicine, marine engineering, and transportation [11].

The industrial sponsor put forward a hydrocyclone as a case study in replacing traditional materials with AM polymers. The need for the separation of solids from liquids, or particles of varying size, is prevalent across industries. Hydrocyclones can be found in processes ranging from pharmaceuticals, biotechnology, water purifying and more [12-14]. The first hydrocyclone is dated back to a US patent filed in 1891 by Bretnai, however their use in industry is dated back to the 1940s [15]. In mining hydrocyclones can be used for closed circuit grinding, desliming, liquid clarifying, degritting and more [16-20]. Hydrocyclones took up less floor space than traditional separation technology of the time and therefore gained popularity.

In the modern day, hydrocyclones come in a range of sizes that correlate to different applications and separation capabilities. One such capability is known as classification in which particles that are larger than what is desired can be separated from smaller particles [21]. In a mining circuit, series of crushers and grinders break down minerals so that the ore can be more easily extracted. This will occur in stages; between each stage it is necessary to remove anything that need to be re-crushed. This is where the

hydrocyclone fits in. Hydrocyclones come in two basic set-ups: conical and flat bottom as seen in Figure 4.

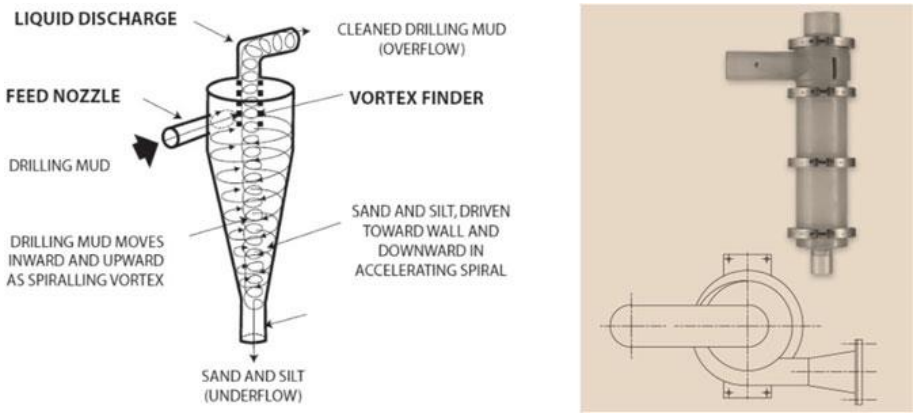

Figure 4. Conical (left) and flat-bottom (right) hydrocyclone [21].

The basic principles of a hydrocyclone are the creation of a vortex and counter-vortex which uses inertial and gravitational force for separation. The larger particles will travel towards the bottom of the cyclone (also known as the spigot) and lighter particles or pure liquid will travel upwards [21]. The main challenge in designing hydrocyclones is the need to control and quantify the separation. This is dominated by the fluid dynamics within [22]. The vortices do not lead to great structural loading, which will be discussed in Chapter 3, Section 3.1. The focus of this research is on the performance of materials not hydraulic performance; thus, this review and the subsequent chapters will cover topics pertaining to this. The fluid dynamics will only be used as a means to describe induced loading on the material.

The industrial sponsor of this research certifies the hydrocyclone by testing the 'worst case' condition in which all entry and exit points of the hydrocyclone blocked. In this scenario the hydrocyclone will effectively become a pressure vessel.

Commercially available hydrocyclones come in a range of materials, however the majority are made from metallic casings with rubber or other abrasion resistant lining such as ceramic or a corrosion resistant alloy [23, 24]. However, research is emerging using AM for small hydrocyclones in the biotechnology industry [22, 25].

This review will cover the basics of AM (specifically fused deposition modelling), background on how the strength of these materials is classified and differs from isotropic materials, and applications for pressure vessels.

2.2 Review of 3D printing process

ASTM 52900 defines additive manufacturing as the 'process of joining materials to make parts from 3D model data, usually layer upon layer, as opposed to subtractive manufacturing and formative manufacturing methodologies' [26]. Material printing technology was developed in 1986 by Charles Hull and was performed via a process known stereolithography (SLA)[27].

According to Ngo et al. [28], there are four main methods for additive manufacturing of polymers: fused deposition modelling, inkjet printing, stereolithography and powder bed infusion as seen in the schematic below (from Wang et al. [29]). This review will focus on fused deposition modelling (FDM) as the research conducted was solely using this manufacturing method. However, other methods will be discussed for the purpose of perspective and comparison.

2.2.1 Fused deposition modelling.

Fused deposition modelling (FDM) is a method that was invented by Stratasys Inc. in 1988 (with patents filed in the early 1990's) as a way for manufacturing to match the speed and accuracy of computer aided design that built on their previous experience with thermos-fusion control mechanisms and thermoplastics [30-35]. In some literature it is also referred to as fused filament fabrication (FFF) [36] as the name 'FDM' is a trademark of the Stratasys company.

Thermoplastic polymers in the form of a filament are wound onto a spool so that the material can be fed through a heated nozzle and extruded onto the printing bed as seen in Figure 5 and Figure 6.

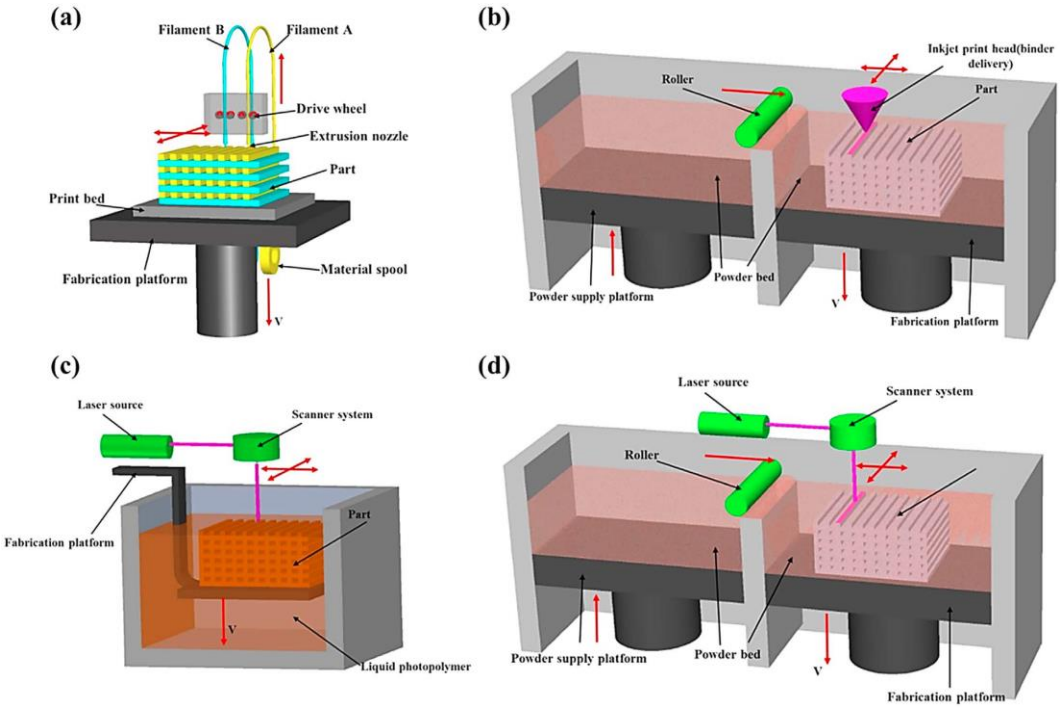

Figure 5. Four main types of additive manufacturing of polymers according to Wang et al. [29]; a) fused deposition modelling, b) inkjet printing, c) stereolithography and d) powder bed infusion.

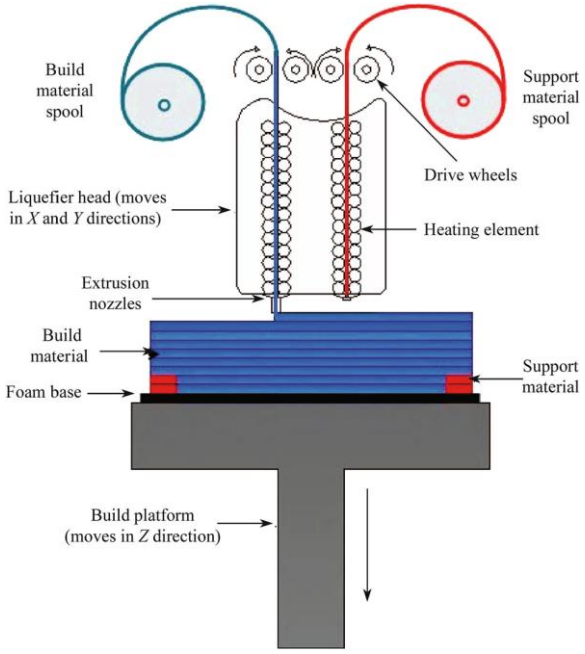

Figure 6. Principle of FDM process [37].

In 2015, Mohamed et al. [37] studied the optimisation of FDM modelling process parameters. These parameters associated with FDM according to the authors are:

1. Build orientation- how the part is oriented on the build platform with respect to X, Y, Z axes where Z is the height.
2. Layer thickness- thickness of material deposited by the nozzle. It is dependent on the nozzle diameter and material characteristics.
3. Air gap- the gap between rasters (the material deposited, also referred to as a bead) within a layer.
4. Raster angle- angle of the raster pattern with respect to the X axis on the bottom layer. The raster angle varies from 0° to 90° and is particularly important for parts with small curves.
5. Raster width- width of the material bead, with larger values associated with a stronger interior structure. However, smaller values result in less material use and production time. The raster width is dependent on the nozzle tip size.
6. Contour width- width of the tool path surrounding the part curves.
7. Number of contours- number of contours surrounding the part curves.
8. Contour to contour air gap- the gap between contours if multiple contours are used.
9. Perimeter to raster air gap- the gap between the inner contour and the raster fill.

These parameters are represented in Figure 7 and Figure 8. They play a key role in the quality and mechanical performance of the final product [38, 39].

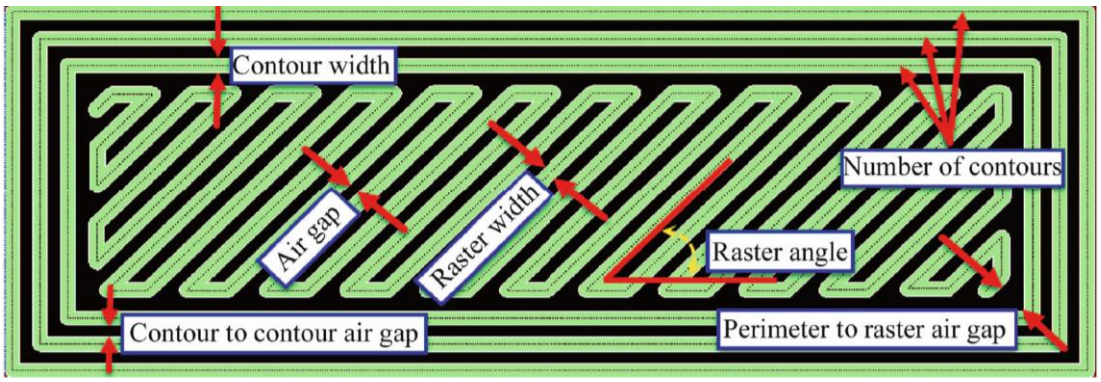

Figure 7. Parameters of FDM printing [37].

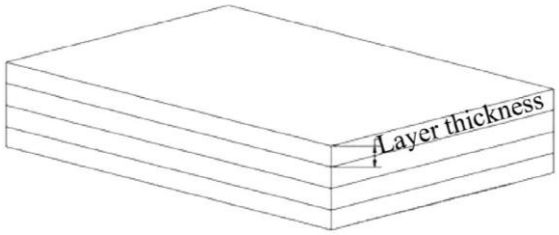

Figure 8. Representation of layer thickness of FDM printed parts [37].

In addition to the printing parameters, there are different build styles that will affect the quality of the part [37]. These are also known as infill density and describes the number of gaps within the material volume. 100% infill density would refer to the maximum amount of material the printer is capable of depositing within the volume, usually utilising a crosshatch raster pattern.

One of the main physical characteristics of FDM parts is surface roughness [40-43]. Due to the nature of the manufacturing method, there will be texture on the surface of parts made by FDM. An example of this surface roughness can be seen in Figure 9. In order to reduce the time needed to build a geometry, thicker layers can be utilised, however, this will result in more surface roughness [43]. As this is not suitable for all applications, especially those where roughness may affect the efficiency of a process, methods have been developed for surface finishing of FDM parts [42]. According to Oropallo and Piegl, there are post-processing options to improve the surface quality such as sanding by hand, melting, bead blasting, traditional manufacturing and acetone finishing [44]. For biomedical applications, vapour smoothing has been explored to improve the surface quality as well [45].

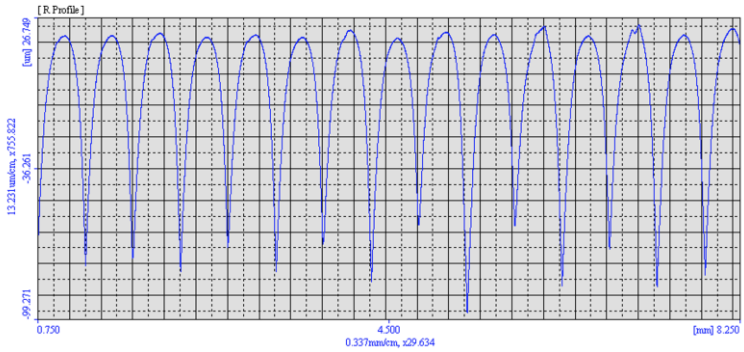

Figure 9. Example of a surface profile of FDM part with layer thickness of 0.254mm measured on the Mitutoyo SurfTest.

FDM filaments are commercially and industrially available for a range of thermoplastic polymers. The materials that can be used is dependent on the capability of the printing system, specifically the temperature range of the nozzle and printing bed as extrusion is dependent on the melt flow characteristics of the polymer [46]. For this research, all samples were printed on the Stratasys F900. The materials available have three ranges: standard, engineering grade, and FDM high performance materials. From the range, those explored for this research were acrylonitrile butadiene styrene (ABS), polyetherimide (PEI or Ultem 1010 as it is known commercially) and Nylon 12CF (a polyamide reinforced with chopped carbon fibre). Ultem 1010 and Nylon 12CF were used for the erosion case study and will be discussed further in Chapters 4-6. For the structural strength case study in Chapter 3, ABS was explored.

2.2.2 Other polymer printing methods

As discussed in the introduction to Section 2.2, the first type of additive manufacturing was SLA and was developed in the late 1980's. It is a type of solid free form fabrication with many applications [47]. A resin or monomer solution is exposed to UV light which initiates the reaction and formation of the polymer chains. The UV laser is used to create a solid pattern within the resin reservoir. The layer formed by this process then hold subsequent layers. SLA is known to create parts with very good resolution as low as 10 μm [28]. This is dependent on the intensity of the laser, scan speed and duration of exposure [48]. The main advantage of this process is the high resolution

and the elimination of a nozzle which can be prone to clogging, however the cost of the printing system keeps it from being widely used in industry [29].

Powder bed infusion was developed at the Massachusetts Institute of Technology in 1993 [49]. Polymer in a powder form is spread onto a build platform and a layer is formed by depositing liquid binder via an inkjet head. This process is also known as inkjet printing. Similarly, to SLA, subsequent layers are built, and any unused powder is removed. There are many advantages to this system such as operation at room temperature (where as FDM required elevated temperatures), however there is not a wide range of printing resolutions available. The quality is dependent on powder size, viscosity of the liquid binder, the chemical reaction between binder and polymer powder and the speed of deposition [50].

Selective laser sintering (SLS) utilises a similar approach to powder bed infusion, however a laser is used to generate heat that binds the polymer via molecular diffusion [29]. The laser follows a desired path, as the light beam in SLA does, in order to create layers. Any powder that was not reacted is removed to create the final product. Resolution of these parts is dependent on powder particle size, power of the laser, scan spacing and speed [51]. Polycaprolactone (PCL) and polyamide (PA or Nylon) are commonly used for SLS, however material choice is limited due to the molecular diffusion process [52].

2.2.3 Polymer matrix composite printing methods

In addition to printing neat polymers, there are currently a number of options for printing fibre reinforced polymer composites. Fibre reinforced polymer composites come in many different forms, however in the context of additive manufacturing there are two main types: discontinuous and continuous. According to Goh et al. [53], continuous fibre reinforced composites describe fibres that are as long as the composite material and discontinuous fibre reinforced composites describe fibres that are short with respect to the size of the composite material. Most composite printing is based on the FDM method and is available for both types of fibre reinforcement. For the purposes of this research, only chopped carbon fibre reinforced nylon was studied, therefore this is the only process described below.

For discontinuous fibre reinforced composites, the additive manufacturing method is similar to that of non-reinforced polymers [54]. The fibres are embedded in the filament before the material is printed. Commercially, the main option for chopped fibre reinforcement is carbon fibre which is usually embedded in a thermoplastic matrix. Plastic pellets and chopped fibres are blended together and passed through and extruder in order to create the filament used for the FDM printers as seen in Figure 10. Nylon 12CF was introduced to the Stratasys range of materials for FDM printing in 2017. It was cited to contain 35 wt% chopped carbon fibre [55]. In 2015 Ning et al. found that adding chopped carbon fibres to an ABS matrix increased tensile strength and Young's modulus [56].

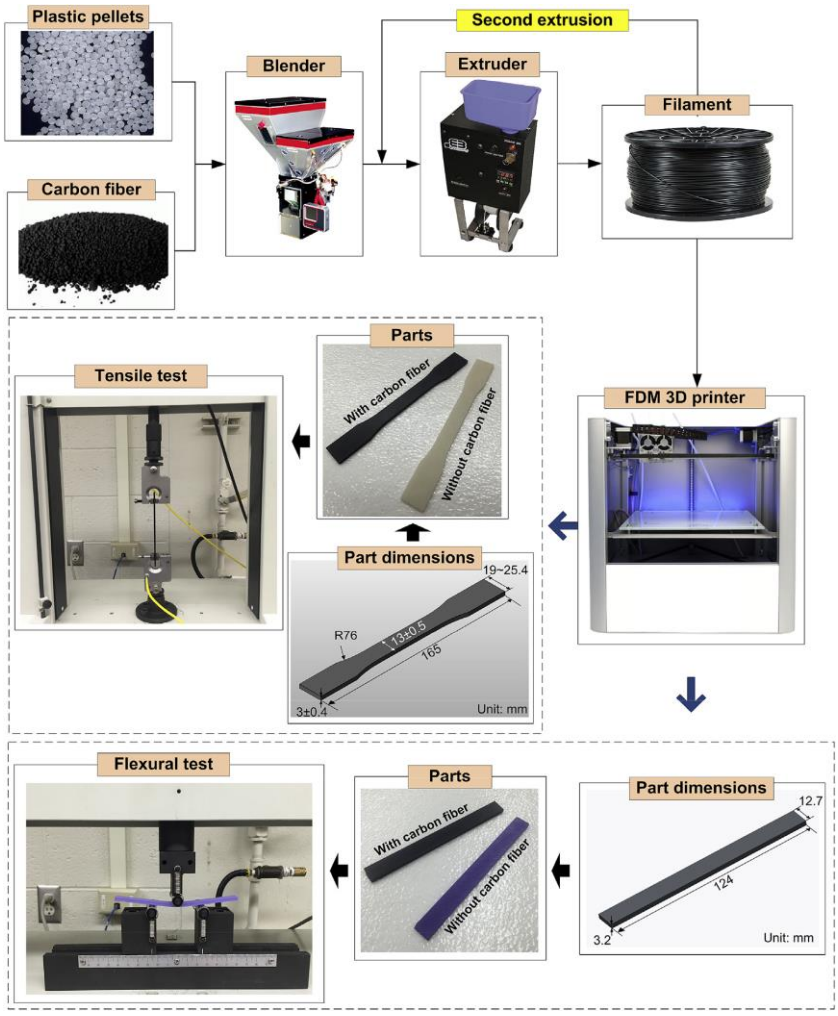

Figure 10. Fabrication and testing process for study of chopped carbon fibre reinforced ABS printed using FDM [56].

2.3 Mechanical properties and behaviour of ABS manufactured using FDM

In 2002, Ahn et al. [57] studied the anisotropic material properties of ABS manufactured using FDM using a design of experiment approach. The process parameters that were explored were: raster orientation, air gap, bead width, colour, and temperature. The testing coupons were printed using the FDM 1650. A view of the variation of specimens is shown in Figure 11.

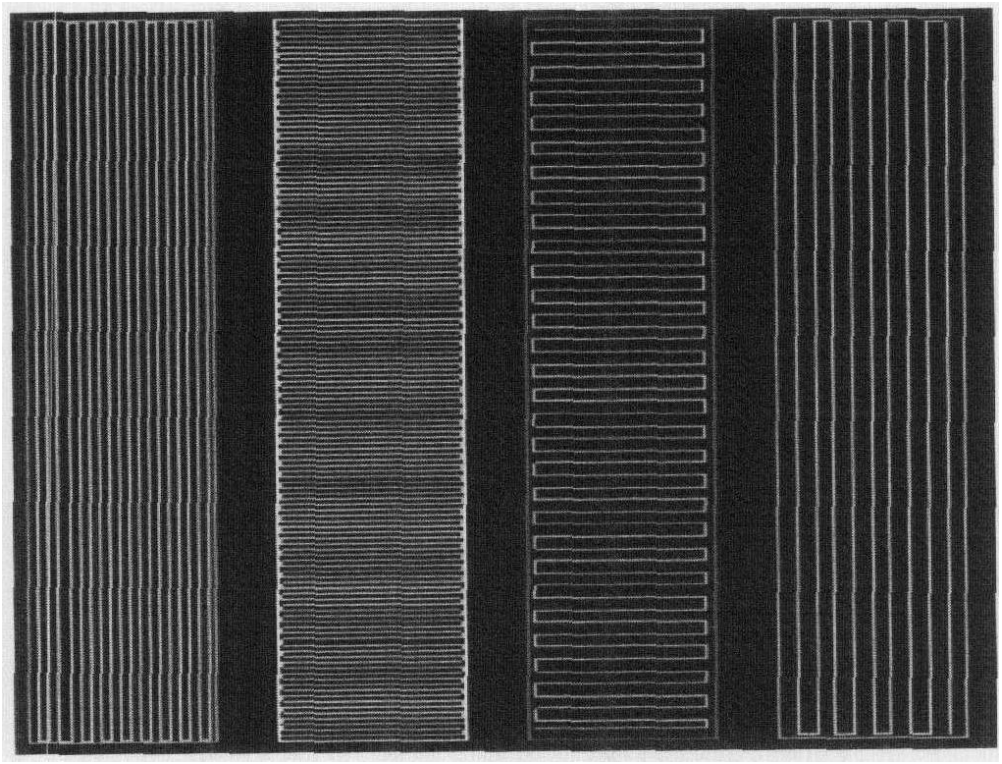

Figure 11. Quickslice SML file showing samples with variation in bead width, air gap and raster orientation [57].

The samples were loaded in tension, per ASTM D638 [58], on an Instron 8872 load frame with a load of 25 kN. Initial samples failed prematurely at the radius of the dog-bone specimen due to shear stress. The specimens were re-printed with an adapted geometry from ASTM D3039 [59] to prohibit this from occurring. ASTM D638 [58] is the standard test method for tensile properties of plastics.

This study, by Ahn et al. [57], is an early example of the ways in which the mechanical behaviour of additively manufactured polymers deviates from the expected and proven behaviour of polymers manufactured by traditional methods. In order to measure the reference strength, ABS manufactured by injection moulding was also tested. The results concluded that air gap and raster angle greatly affected the tensile strength, and the behaviour was anisotropic. From the results, the authors made 6 recommendations for printing of parts.

1. Tensile loads should be carried axially along the fibres (what the authors refer to the printed filament as).
2. Stress concentrations occur at radius corners due to discontinuities in printing at transitions.
3. Negative air gap, achieved by overlapping the rasters, increases strength and stiffness, however this should not be used because of material build up. A gap of 0.003 inches was found to be the minimum.
4. Small bead width (raster width) improves surface quality but increases build time. The wall thickness of the part should be an integer multiple of the bead width to avoid gaps.
5. Build orientation effects the part accuracy.
6. Tensile loaded areas fail easier than compression loaded areas.

Building upon initial studies of the strength of FDM printed parts, such as the Ahn et al. [57] study above, further investigations were published reflecting the increasing popularity and availability of 3D printing systems. Sun et al. [60] investigated the effect of processing conditions on the bond quality of FDM polymer filaments. The formation of bonds between layers in FDM parts is dependent on the thermal energy of the material as it is printed and the temperature history of the interfaces. Neck growth, as seen in Figure 12, and molecular diffusion of polymer chains drive the interfacial strength.

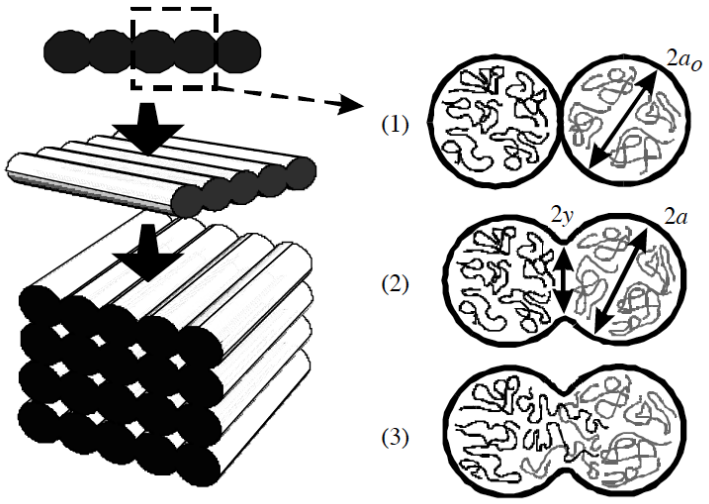

Figure 12. Bond formation between two filaments: (1) surface contacting, (2) neck growth, (3) molecular diffusion and randomisation [60].

In this study [60], ABS specimens were printed on a Stratasys FDM 2000 and the micro- and meso-structure were assessed in order to determine the bond quality. The specimens were then subjected to flexural testing. A main finding was that the thermal history has a large influence on the quality of the bond, with most material experiencing temperatures above glass transition but below critical sintering temperatures. This led to creep deformation which must be considered when predicting the bond strength. It was also found that existing heat transfer models were not sufficient to describe the FDM process.

Sood et al. [61] also studied the flexural, tensile and impact properties of FDM printed ABS and how the printing parameters effected these qualities. The parameters studied were layer thickness, orientation, raster angle, raster width and air gap. Specimens were printed using the FDM Vantage SE machine. Tensile testing was performed per ISO R527:1966 [62], flexural testing per ISO R178:1975 (3-point bending) [63] and Charpy impact testing per ISO 179:1982 [64].

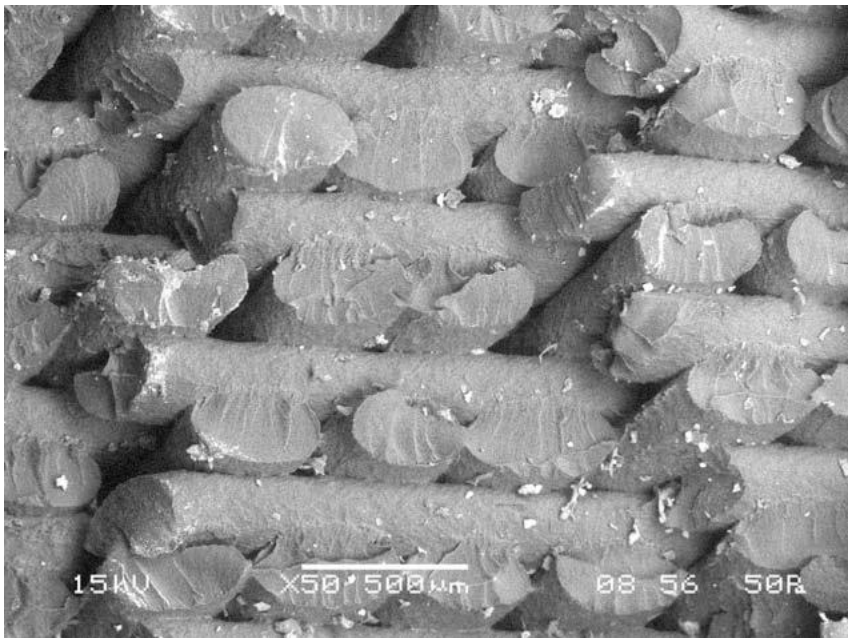

Figure 13. SEM image of tensile failure [61].

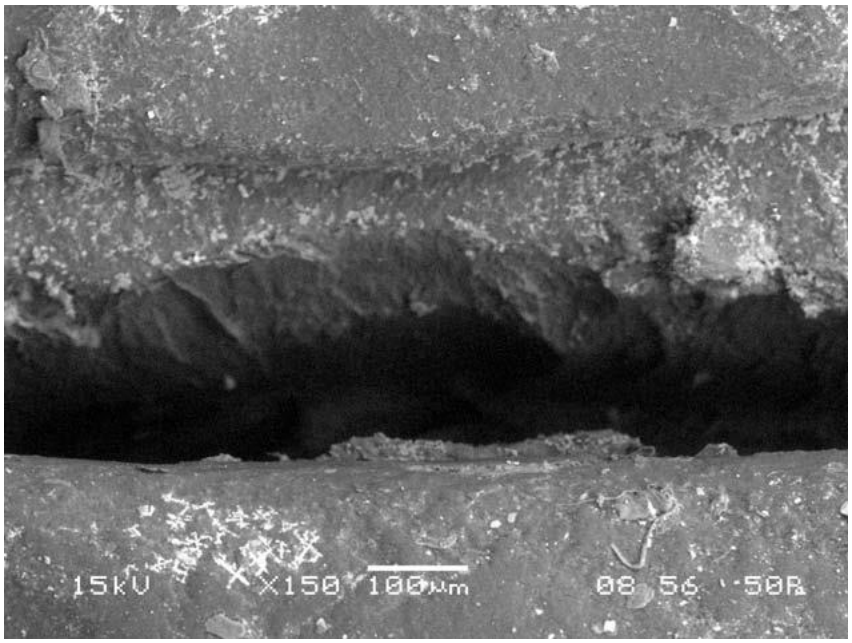

Figure 14. Crack surface of flexural specimen [61].

Figure 13 and Figure 14 show examples of the failure of the specimens. Sood et al. concluded that the number of layers has an impact on the temperature gradient and therefore diffusion of layers on the bottom of the part. This will improve strength, but the higher temperatures can also cause distortion. The smaller the layer thickness, the

greater the number of layers. More layers can lead to more cycles of heating and cooling, which results in an accumulation of residual stresses in the part. This will reduce strength via distortion, interlayer cracking and delamination. Smaller raster angles improve performance by allowing the raster to be in line with the loading direction, however this can also lead to long rasters with more distortion and therefore weaker bonding. Along the width of the part, thicker rasters also lead to stress accumulation, but the higher temperature associated with this also improved bonding. To improve the diffusion between layers, it is recommended to have zero air gap [61]. Overall, it was deemed to be a complex phenomenon and the authors found it difficult to assign exact reasoning to the results. Reduction of distortion seems key to achieving strong printed parts.

Torrado Perez et al. [65] studied the surface of 3D printed ABS specimens at the site of fracture and compared neat ABS to composite alternatives. The composites studied were ABS with 5 wt% jute fibre and 5 wt% TiO_2. Additionally, ABS with 5 wt% of thermoplastic elastomer (TPE). Tensile tests were performed on an Instron 5866 machine with a 10kN load cell. The tests were performed at a speed of 10 mm/min and a temperature of 23 °C. The additives led to brittle characteristics of the fracture surfaces. The titanium reinforced ABS had a higher ultimate tensile strength than neat ABS and the other composites, but with brittle fracture. The materials were tested in two different orientations, with the filaments in line with the loading and transverse to. For the parts with transverse orientation, the presence of cavities and the dependence on interfacial strength of filaments led to lower mechanical strength and different morphology on the surface of the fracture. The TPE composite, however, exhibited reduced anisotropy comparatively. The fracture surfaces are shown in Figure 15 and Figure 16. Cole et al. [66] studied the interfacial mechanical behaviour of 3D printed ABS and found that at the interface there is a lack of the rubbery butadiene phase which could be the cause of the lower mechanical properties when testing in this direction.

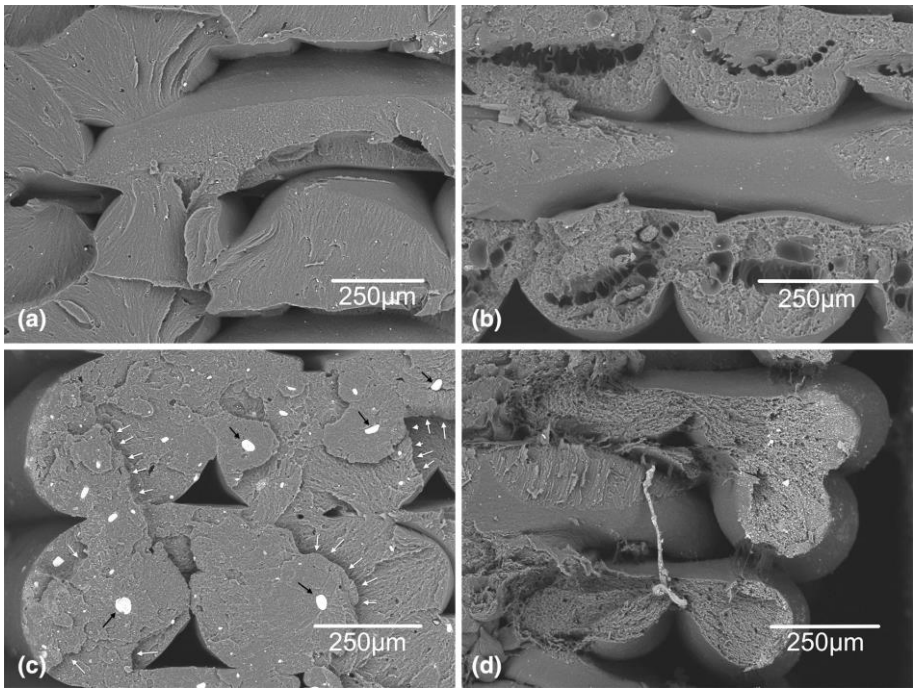

Figure 15. SEM images of fracture of longitudinally loaded (a) ABS, (b) ABS and jute fibre, (c) ABS and TiO2, (d) ABS and TPE [65].

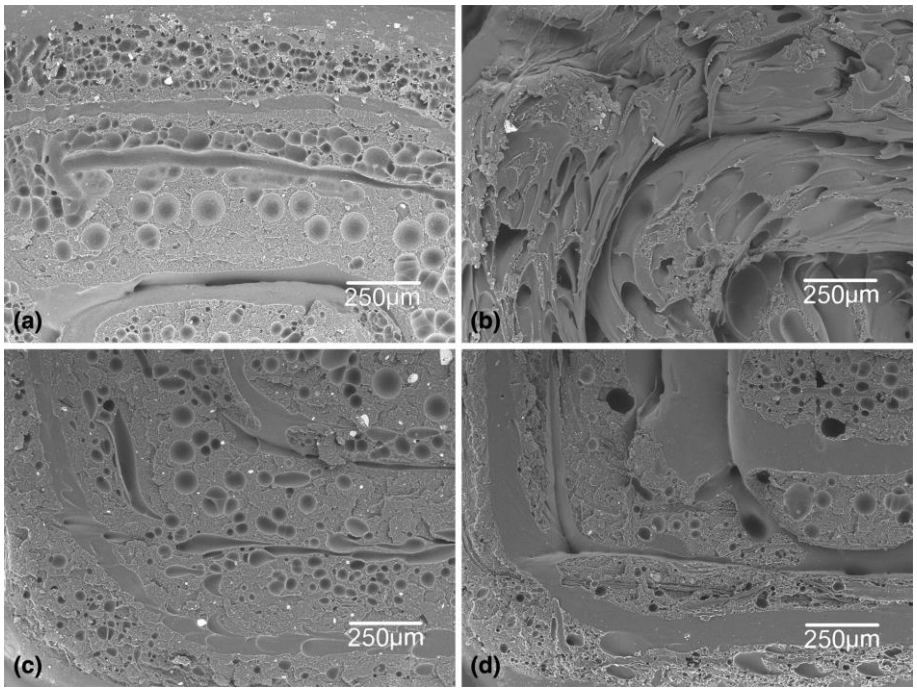

Figure 16. SEM images of fracture of transversely loaded (a)ABS, (b) ABS and jute fibre, (c) ABS and TiO2, (d) ABS and TPE [65].

Goh et al. [67] created a database of FDM mechanical properties which outlined the difficulties in determining the strength and correlation between different printing parameters with respect to mechanical performance. Torrado and Roberson [68] stated the need for specific mechanical testing standards for 3D printed materials following on from Roberson's earlier work [69]. This theme persists throughout the literature with the need for further research on modelling and optimisation being highlighted as well [70].

2.4 Additive manufacturing for pressure vessels

For decades, pressure vessels have been made from polymers and fibre reinforced polymer composites [71, 72]. These have been manufactured by traditional and application specific techniques such as filament winding for fibre reinforced polymers [73-75]. Design standards for pressure vessels have historically be geared towards metallic structures taking into account corrosion and welded joints, however the principles of stress are applicable regardless of material choice [76]. For thin walled vessels the theoretical hoop stress is two times larger than the axial stress experienced for a cylindrical vessel (this will be explained in depth in Chapter 3) [77].

The use of additive manufacturing for pressure vessels is an emerging area of research that shows promise for shape optimisation and rapid prototyping [78, 79]. Some studies have been focused on metallic additive manufacturing and how the effects of the printing method can be optimised for internal pressure loading [79, 80]. However, the challenges associated with polymer printing processes will be different. The studies in this review provide an insight to the current state of this research area and context for the research performed.

Šafka et al. studied rapid prototyping for special pressure vessels using FDM, and SLS [78]. The specific application was an expansion vessel for engine cooling. The vessel requirements were the capability to store coolant without deformation, compensation for changes in volume and temperature (up to 100 °C) while staying within the parameters for overpressure tolerances. Additionally, the vessel design was required to be built without internal support structures and to be able to withstand shock and vibration. The three AM technologies chosen were: FDM using Ultem 1010 material,

SLA with a ‘high temperature, durable material’, and SLS with PA 2200 and PA 3200 GF (glass filled) materials. The FDM part was printed on the Fortus 450mc by Stratasys with a layer thickness of 0.254 mm and a printing time of 17 hours. The SLA part was created with a Formlabs printer from ‘durable and high temperature’ material resins similar to polypropylene. The printing of the ‘durable’ material with a layer thickness of 0.05 mm took 53 hours to print, while the ‘High temp’ material took 33 hours. The SLS parts were made from PA 2200 with a layer thickness of 0.1 mm and a printing time of 6 hours and the PA 3200GF material which took 8 hours for the same thickness. The parts are shown in Figure 17 and Figure 18.

Figure 17. Printed model from ULTEM 1010 material on Stratasys Fortus 450mc [78].

Figure 18. Prepared models from Šafka et al [78].

The vessels were tested based on the Czech Institute for Standards 1986 ČSN 69 0012 standard for operation of stationary pressure vessels. The vessel was hydraulically pressurised to 4.5 bar, which is 1.5 times the operational pressure. The first pressurisation was performed at 20°C with the purpose of ensuring that the parts were sealed then again at 100°C to observe if a rapid loss of pressure was observed. The initial test revealed that Ultem 1010 had a porous structure due to the FDM process and leaking began from 1 bar. The other parts did not exhibit leaks. The FDM part was redesigned with a new internal structure which resulted in no leaking; however, the authors do not provide an example or discuss this structure. The second pressure test at elevated temperature did not result in any leaking or damage to the FDM and SLS parts. The SLA 'Durable' vessel showed visible deformation but was not destroyed. Upon cooling the geometry returned to its original dimensions. The 'High temp' SLA part survived the pressurisation but experienced brittle behaviour and cracked upon cooling.

Gordeev et al. [81] conducted a study to improve the quality of 3D printed objects by eliminating microscopic structural defects for FDM parts. The parts were submerged in water and pressurised with compressed air in order to observe leaking in the form of air bubbles. It was found that the permeability is reduced slightly based on shape in the following series: cylinder > cube > pyramid > sphere > cone. The parameters with the greatest impact on quality were filament feed rate, wall geometry and G-code-defined wall structure. This provides some insight to how printing parameters and design can be employed to mitigate the leaking.

As seen in the previous study, one of the main disadvantages of utilising FDM printed parts for pressurised vessels is the internal voids [82]. A study by Al-Hasni and Santori [83] examined 3D printing for pressure tight polymer vessels used in thermally driven chillers and heat pumps. These parts must be able to function in a vacuum or high-pressure environments dependent on the refrigerant medium. These parts are also rarely made from lightweight materials and have labour intensive manufacturing processes, thus the appeal of 3D printed polymers. Using the methodology seen in Figure 19 (which was developed from the Gordeev et al. study [81]) the authors attempted to print a FDM part that was pressure tight.

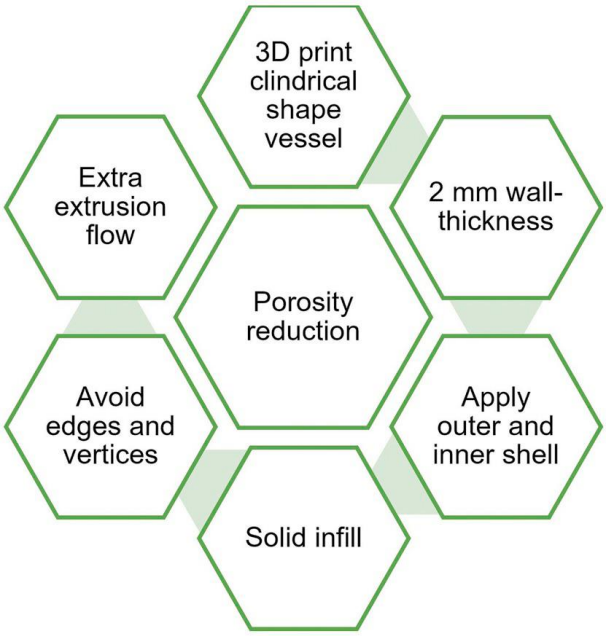

Figure 19. Summary of variable that could assist in the reduction of the porosity of a 3D printed part by FDM [83].

For FDM parts, the enclosed Desktop FDM Zortrax M200 printer was used and for the SLA parts the Formlabs 1 printer. The FDM parts were printed with 275°C extrusion, 100% infill, with a 0.4mm diameter nozzle and 36 mm/s retraction speed. The chosen materials were ABS and polylactic acid (PLA). The SLA parts were printed with 0.1mm layer thickness and the 'Grey Resin' material from the manufacturer. The FDM vessels were cylindrically shaped with an external diameter of 30 mm, thickness of 6 mm, and height of 30 mm. The SLA samples were cylindrical with one flat end and a domed end. Two samples were printed, denoted as Sample A and Sample B. Sample A had an external diameter of 40 mm, wall thickness of 4 mm and a height of 40 mm. Sample B had an external diameter of 60 mm, thickness of 4 mm and a height of 70 mm.

Under scanning electron microscope (SEM), it was found that [83] ABS showed better bonding than PLA samples for FDM. Additionally, lowering the printing speed to 30 mm/s resulted in a smoother surface. Despite the better layer bonding, ABS still displayed porosity. In order to assess the printing parameter's influence on leak rate the layer height and extrusion flow were varied. These were then tested for a pressure

of 412 kPa and 8.2 kPa (vacuum). The SLA samples were tested at 434 kPa and varying vacuum tightness tests.

In order to approach the issue of porosity in FDM parts, resin infusion was used by Al-Hasni and Santori. Belter and Dollar [84] have also studied the effects of filling the voids with resin via the fill compositing technique in order to increase the strength of 3D printed FDM parts. For this study, voids were purposefully created within the printed structure that would then be filled with epoxy. This strengthened the structure overall with a 19% increase in failure load. Al-Hasni and Santori used a liquid epoxy resin for self-infusion of voids. This allowed the vessel to be compliant with a bubble test.

Al-Hasni and Santori concluded that SLA produces less porosity than the FDM process. For FDM parts, porosity cannot be completely eliminated. Resin sealed FDM parts resulted in a leak rate 12 times lower than that of the unsealed components (which was 1.16e-5 Pa m^3/s for 412 kPa pressurisation). However, even with the resin infusion the part was not acceptable for the application's needs. SLA parts produced leak rates compliant with the necessary standard and it was found that SLA polymerisation can result in void free parts.

There is a need for more research into industrial applications involving pressurisation of 3D printed parts. From the studies produced thus far, not all 3D printing methods will result in the same capabilities with porosity being the primary challenge. Additionally, existing designs that suited the capability of metallic structures as well as the limitations of traditional manufacturing may not be optimal for printing [85]. The studies above also do not explore the failure of the material from internal pressure once the leaking has been mitigated.

3. Hydrocyclone case study

The 150 CVD hydrocyclone has a height of approximately 1 metre and is classified by the diameter of the upper cone of the hydrocyclone body (in this case 150 mm). This particular model is currently manufactured with the option of fabricated steel or DMC as the material of the casing. The lining is available in solid poly, monolithic ceramic, urethane, and rubber according to the industrial sponsor. This is separate from the casing and installed to fit depending on the conditions. It is a smaller cyclone within the Weir Group's range and can be fitted at any point in a milling circuit or at the tailings of a mine. Additionally, their versatility lends them to be used in almost any type of industrial applications dependent on the needs of the end user. For this reason, it is hard to necessarily test for the worst case scenario seen in the field. It is therefore assumed that in the event of a total blockage of all inlets and outlets the pressure inside the cyclone will reach 3 bar which is the maximum operating pressure as designated by the industrial sponsor.

This chapter is comprised of 3 main sections:

1. A study of the structural requirements of the hydrocyclone and a material down-selection.
2. An experimental study of the behaviour of an ABS cylinder manufactured via FDM subjected to internal pressures up to 3 bar (300 kPa).
3. Pressurisation to failure of the ABS cylinder to identify the pressure at which failure occurs and the mechanism of failure.

3.1 Understanding structural requirements of the 150 CVD

The first step to determining if AM is a viable option for the application is to understand the structural requirements of the hydrocyclone. This was completed using finite element modelling (FEM) in ANSYS. The 3D model of the 150 CVD was provided by the industrial sponsor. The first is normal operating conditions based on the in house computational fluid dynamics (CFD) data. This will translate to loads induced by the velocity and pressure of the system. Because this is a dynamic loading,

the load will not be equivalent at all locations on the hydrocyclone. The second condition is that in which all inlets and outlets have become obstructed, and the 150 CVD operates as a pressurised vessel.

3.1.1 Materials

At the time of the research, the 150 CVD had only been manufactured and tested using fabricated steel Grade 250 per the Australian Standard AS3678 [86]. The predecessor to the 150 CVD, the 150 CVX, had the option of a DMC casing. The difference between the 150 CVX and the 150 CVD is an improvement of the particle separation efficiency, thus it was advised by the Weir Group that the driving factor in the design of the 150 CVD was not the structural loading. The mechanical properties of the AS3678 Grade 250 structural steel, the DMC and the corresponding rubber liner are shown in Table 1, Table 2 and Table 3. A comparison of the two casing materials demonstrates that the structural steel has a tensile strength nearly four times that of the DMC. The function of the rubber liner is to provide wear resistance, thus is not considered to be a load bearing component. For the purpose of this research, DMC was the baseline with which to compare the available AM materials.

Table 1. Mechanical properties of AS3678 Grade 250 structural steel [86].

AS3678 Grade 250 Structural Steel Mechanical and Physical Properties	
Density (g/cm^3)	7.85
Hardness	N/A
Tensile Strength (MPa)	410
Elongation at Break (%)	22
Young's Modulus (MPa)	206
Poisson's Ratio	0.3

Table 2. Mechanical and physical properties of glass reinforced polyester resin DMC.

DMC Mechanical and Physical Properties	
Density (g/cm^3)	1.69
Hardness (Barcol)	43
Tensile Strength (MPa)	40
Elongation at Break (%)	0.5
Compressive Strength (MPa)	137
Poisson's Ratio	0.23

Table 3. Mechanical and physical properties of natural rubber.

Natural Rubber Mechanical and Physical Properties	
Density (g/cm^3)	1.06
Hardness (Shore A)	50
Tensile Strength (MPa)	22
Elongation at Break (%)	600
100% Strain Modulus (MPa)	1.0
300% Strain Modulus (MPa)	5.0

The industrial sponsor uses a Stratasys F900 commercial printer. This is capable of printing higher temperature polymers such as polyether ether ketone (PEEK) and PEI. Their PEI material is known under the trade name Ultem 1010 (properties shown in Table 4). PEI is known to have good wear resistance when used as a coating for metals [87] and is less expensive than the related PEEK. The industrial sponsor proposed two materials as options for the 150 CVD: ABS and Ultem 1010. The material properties of each are shown in Table 4 and Table 5 with an explanation of the orientation provided in Figure 20. The mechanical properties of the XZ and ZX orientation are provided by Stratasys.

Table 4. Mechanical and thermal properties of Ultem 1010 provided by Stratasys.

Ultem 1010 Mechanical Properties	**XZ Axis**	**ZX Axis**
Ultimate Tensile Strength (MPa)	79.2	28.2
Tensile Modulus (MPa)	3040	3000
Elongation at Break (%)	4	1.1
Yield Compressive Strength (MPa)	245	438
Glass transition temperature (°C)	209.37	

Table 5. Mechanical properties of ABS provided by Stratasys

ABS Mechanical Properties	**XZ Axis**	**ZX Axis**
Ultimate Tensile Strength (MPa)	28.1	26.8
Tensile Modulus (MPa)	2400	2300
Elongation at Break (%)	8.1	1.8
Yield Compressive Strength (MPa)	88.3	208
Glass transition temperature (°C)	105.2	

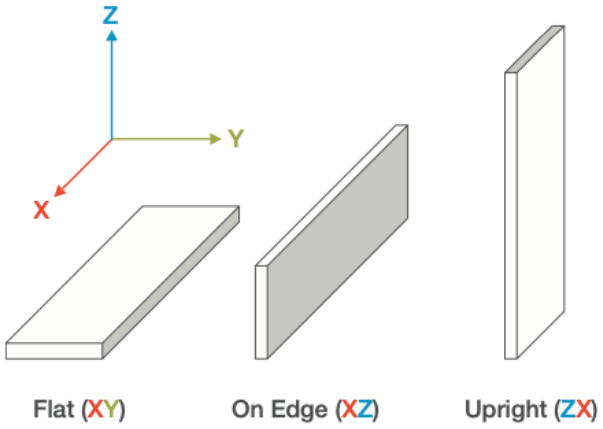

Figure 20. Printing orientations (image provided by Stratasys).

As shown in the review of literature, the mechanical properties of 3D printed thermoplastic components is driven by not only the isotropic properties of the polymer, but also the strength of the fused layers resulting in orthotropic properties. This will not be of the same strength as the polymer itself because the bonding cannot be assumed to be perfect [60, 66]. As layers are deposited, they will start to cool to the temperature of the chamber. The chamber is heated to an elevated temperature in order to enable bonding of the thermoplastic between layers, but not as high as melt temperature so that the structure being printed can retain the rigidity to support subsequent layers. For Ultem 1010, the extrusion temperature is 410 °C with an oven temperature of 225 °C, for ABS the temperatures are 320 °C and 95 °C respectively per the Stratasys F900 user guide. The properties shown in Table 4 have two directions, the ‘XZ’ and ‘ZX’. The ‘XZ’ direction denotes a printing set up in which the layers run in the direction of loading. Similarly to unidirectional composites, the greatest strength will be when the tensile force is applied along the direction of the fibres (or in this case the rasters). The ‘ZX’ then denotes a printing set up in which the force will be applied perpendicular to the raster orientation. For the testing specimens, each layer has rasters with the same orientation.

In order to rule out materials, ABS was chosen to be compared to DMC first as it had the lower strength and modulus of the two chosen AM materials. If this material's performance is not satisfactory, then it can be ruled out and Ultem 1010 can be explored.

3.1.2 Hydraulic loading: Set-up

The model for analysis was provided by the Weir Group. The geometry was very comprehensive and had all parts, including bolts, modelled explicitly. The parts were designed with the intention of being used to create fabricated steel components. The model used for this analysis has been refined and only the load bearing components have been retained.

3.1.2.1 Computational fluid dynamics

The CFD analysis was received from the industrial sponsor and reviewed. The analysis was completed in Fluent within the ANSYS workbench. The pressure contour in Figure 21 shows that the highest pressure experienced is at the initial inlet to the hydrocyclone, the highest pressure experienced by the structure will be approximately 25 kPa. The inlet pipe is considered to be ancillary structure attached to cyclone and therefore is not considered for analysis. This pressure is more than order of magnitude lower than the 300 kPa pressure testing requirement.

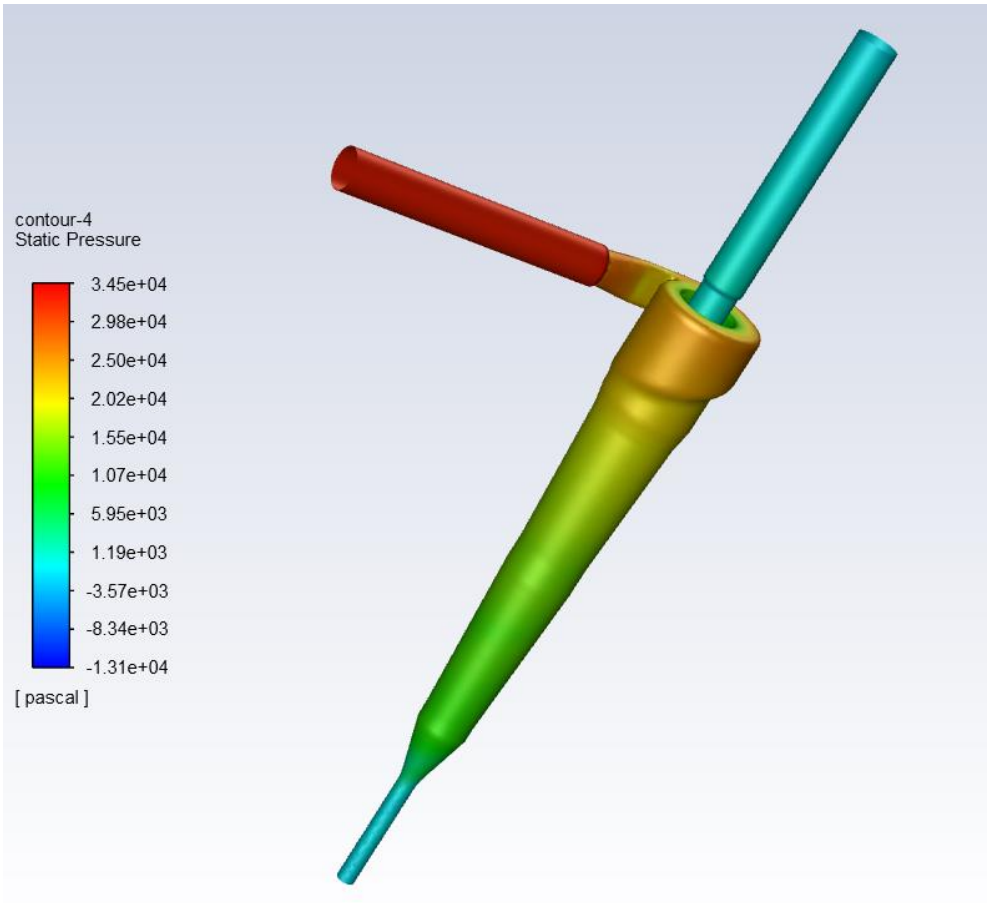

Figure 21. Static pressure contour from ANSYS Fluent analysis showing maximum pressure on the body of the hydrocyclone at approximately 25 KPa.

3.1.2.2 Finite element modelling boundary conditions, mesh, and loading

In order to verify the geometry and begin meshing, the geometry for the casing and the rubber liner were inputted into ANSYS. A default mesh with a resolution of 5, 99261 elements and 24796 nodes was used and is shown in Figure 22.

Figure 22. Mesh of 150 CVD in 'ANSYS Static Structural'.

The CFD pressure profile from Fluent was inputted as the loading condition. DMC was assigned as the material for the casing and a natural rubber from the engineering database on ANSYS ,that was comparable to the Weir Group's proprietary rubber, was assigned to the liner. The material data provided by the industrial sponsor did not provide information on the non-linear response of the material, thus the decision to use a standard neoprene rubber was made. This considered some of the actual properties of the material, such as low tensile strength, that would affect the bearing capability of the cyclone.

The elasticity was determined by Poisson's ratio and Young's modulus. The modulus input was 1 MPa per the data in Table 3 for 100% strain. At higher strains, the modulus will increase (i.e., as the rubber is stretched it will become more rigid). The lowest modulus provided by the supplier was used for modelling the material as a conservative approach, however this assumes that the material response to stress will be linear. In reality, the relationship of stress to strain is non-linear meaning that at strains less than 100% the modulus will be less than 1 MPa. Therefore, the values for deformation will not be comparable to reality. A Poisson's ratio of 0.49 was assigned to the neoprene rubber per experimental data [88].

The model was constrained as shown in Figure 23 at the four bolt holes shown on the flange of the cones to represent rigging to the cluster. The cyclone was kept at 0-degrees inclination, so gravity is acting in the -Z axis. At all bolt locations, a beam was placed to represent the bolt and create an elastic response between joined parts. All bolts were modelled as circular connections between bodies. These had a radius of 5mm with varying beam length depending on the distance between mating holes. The material used for these beam elements is structural steel.

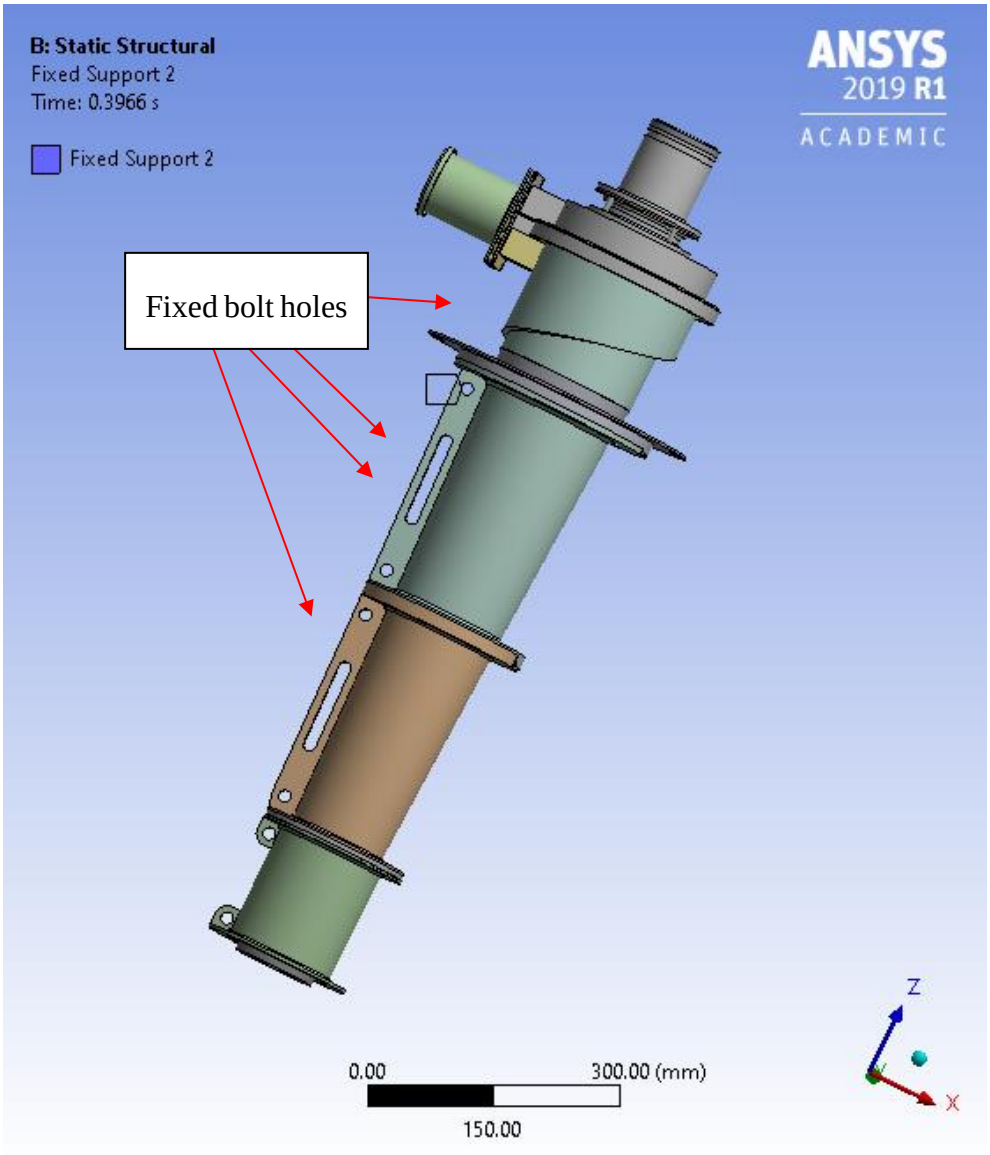

Figure 23. Location of fixed constraints for the model.

3.1.3 Hydraulic Loading: Results and discussion

Figure 24 represents the contour for the maximum principal stress of the casing. For most of the body of the cyclone, this falls below 2 MPa, which is well within the strength of most composite materials and polymers without reinforcement. The stress concentration shown in Figure 25 is at the corner of the inlet and the first turn that will help create the vortex. This is still only 6.8 MPa and well within the strength

limitations. In Figure 26 the contour for the von-Mises equivalent stress is shown and is quite similar to that of the maximum principal stress. However, the maximum stress concentration is shown at a bolt hole in Figure 27.

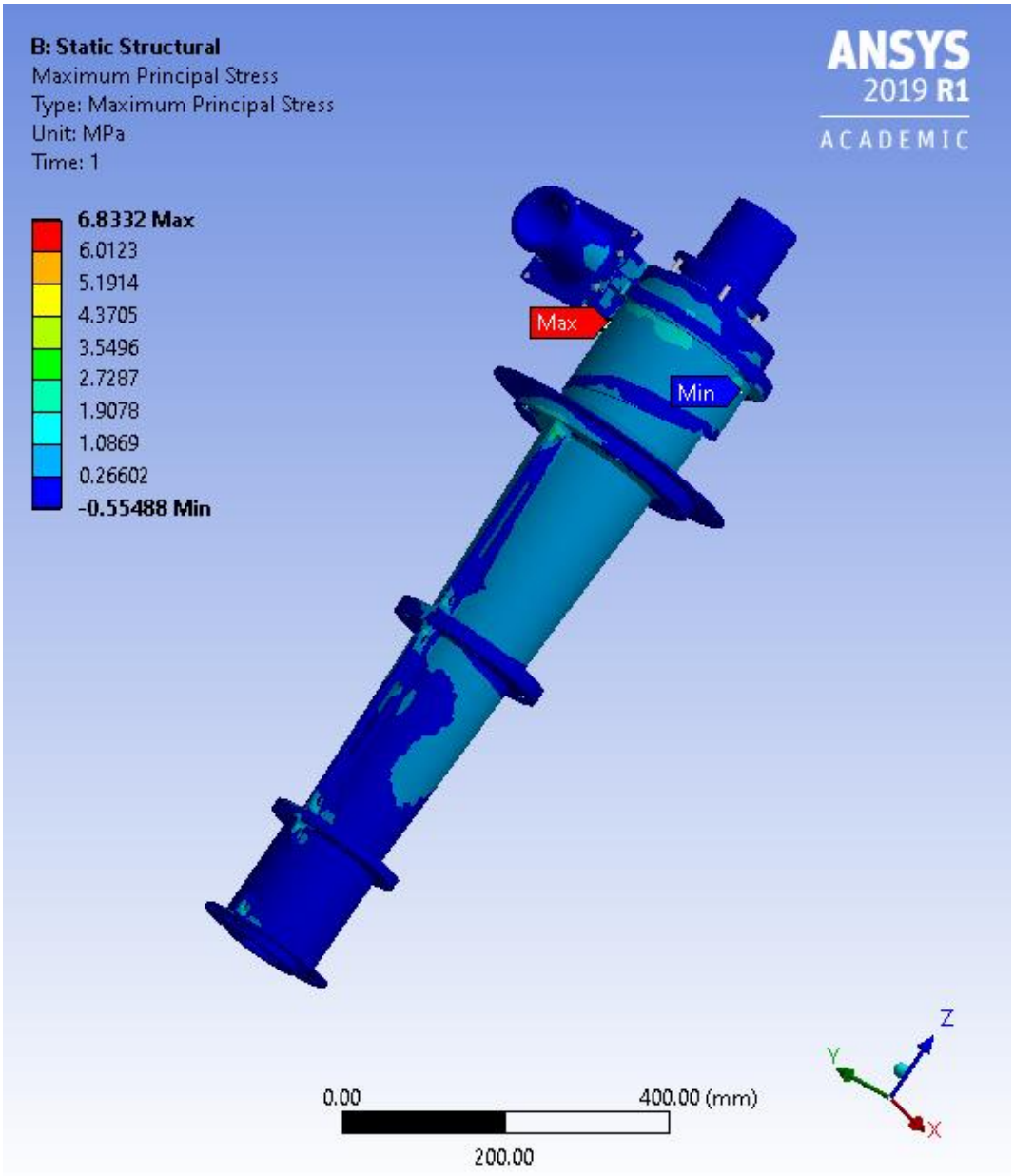

Figure 24. Maximum principal stress contour for hydraulically loaded 150 CVD.

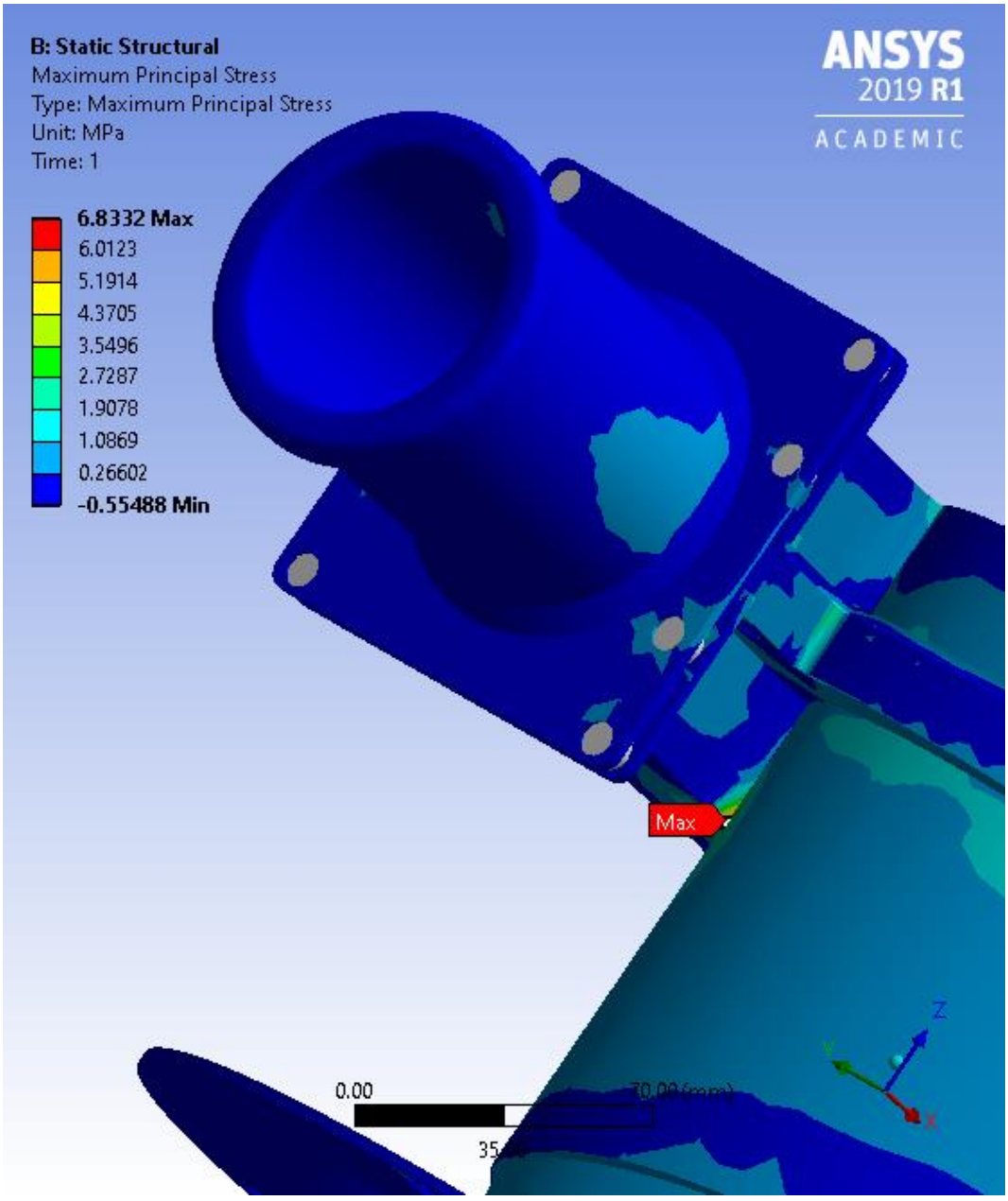

Figure 25. Location of maximum principal stress concentration for hydraulically loaded 150 CVD.

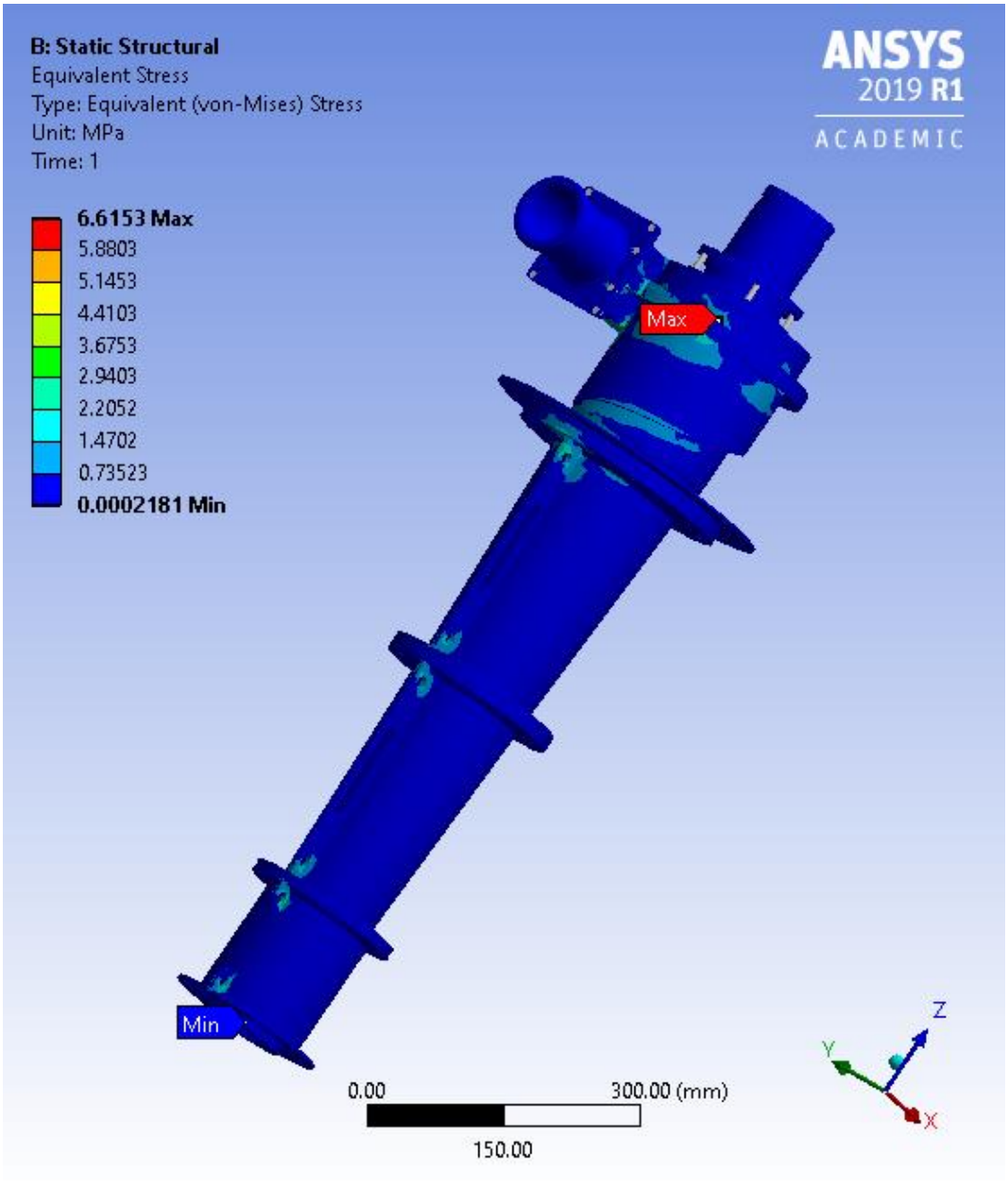

Figure 26. Von-Mises equivalent stress contour for hydraulically loaded 150 CVD.

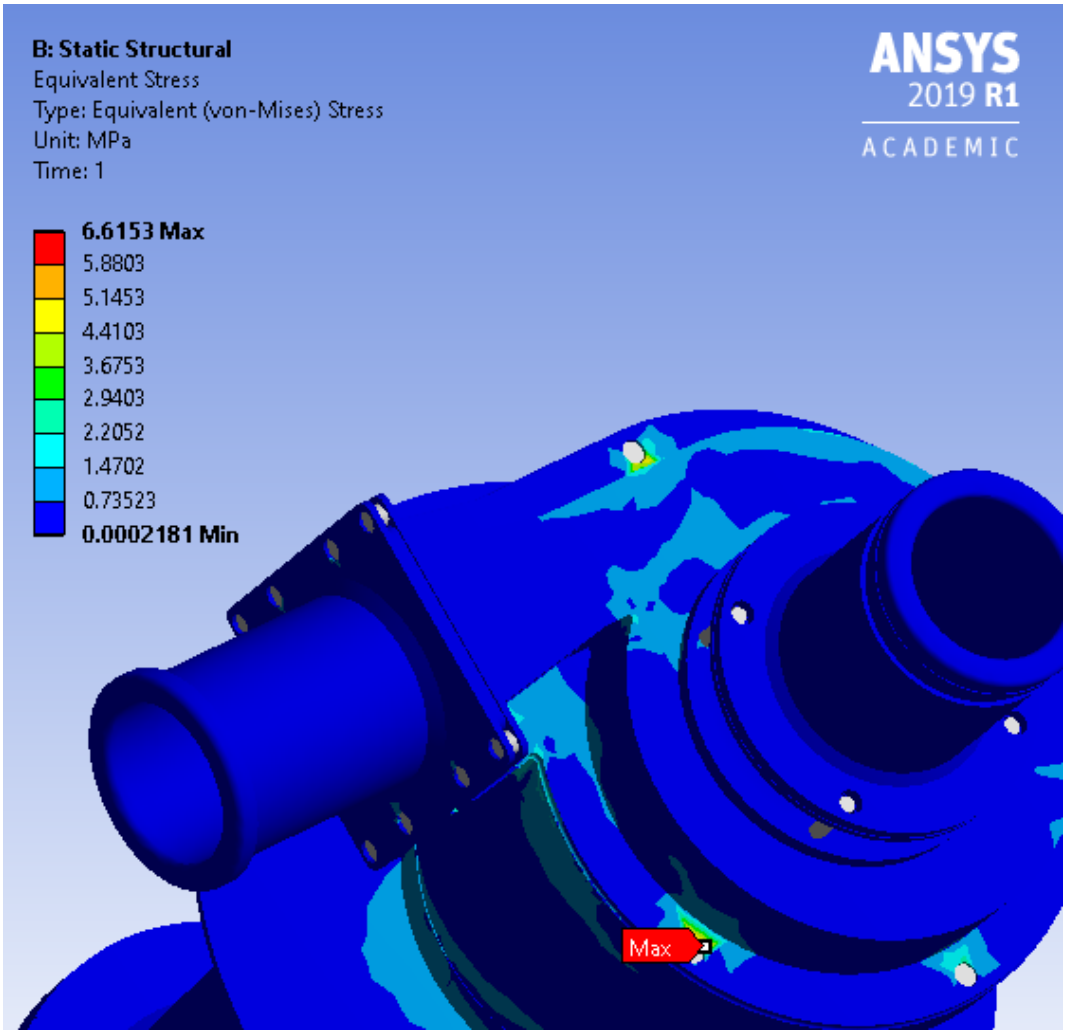

Figure 27. Location of maximum von-Mises equivalent stress concentration for hydraulically loaded 150 CVD.

The maximum stress found is quite low (< 7MPa in both cases) and experienced very locally. The far field stress remains even lower, proving that the loading due to hydraulic forces is not the driver for the material design of the cyclone. The deformation, shown in Figure 28, is also quite low (<1 mm) and was verified with the industrial sponsor.

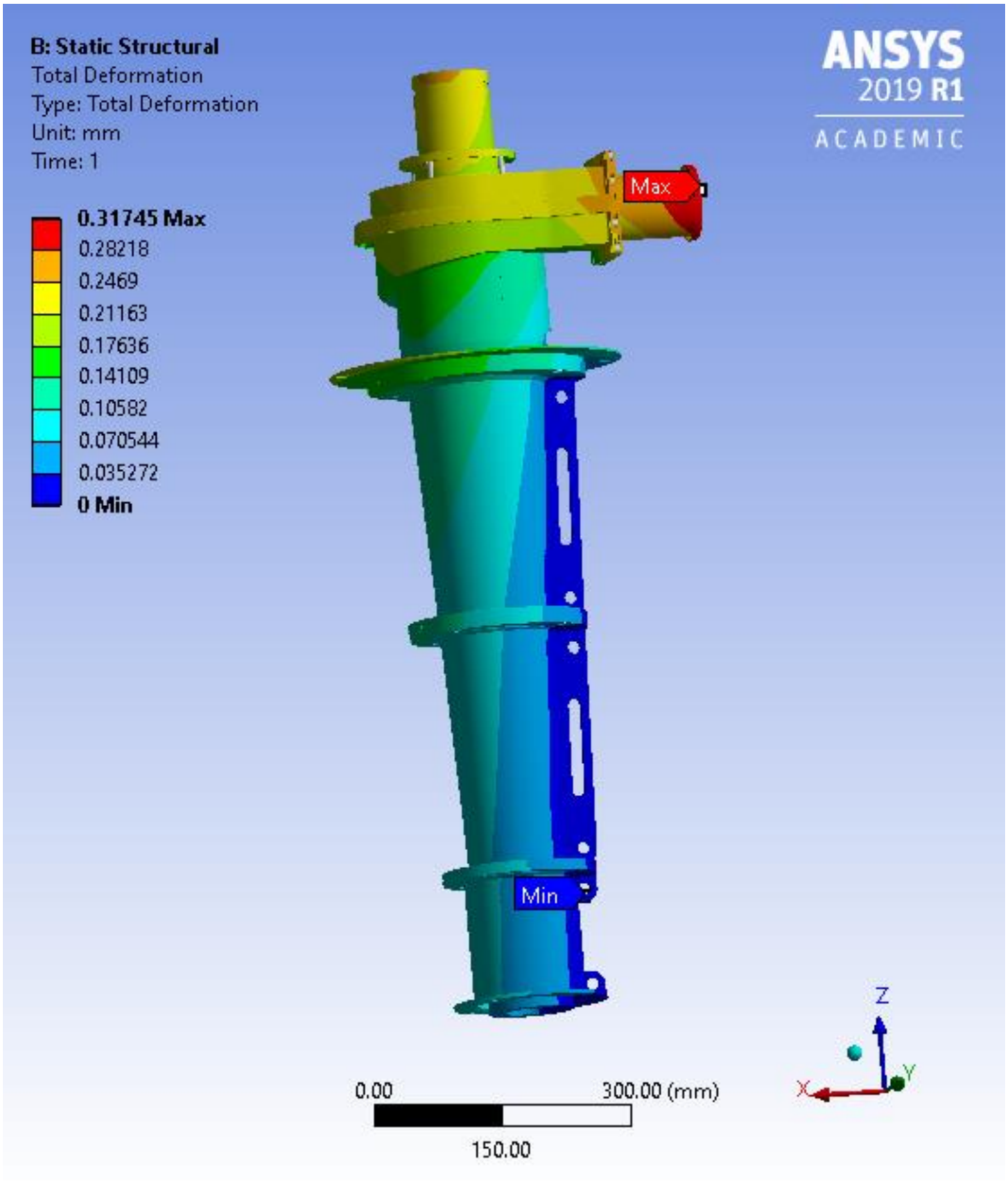

Figure 28. Contour of deformation for hydraulically loaded 150 CVD.

3.1.4 Analysis of the 150 CVD for 3 bar pressurisation without a rubber liner

To complete the material selection, analysis must also be completed for the 3 bar internal pressure condition. As discussed in Section 3.1.1, the function of the rubber liner is to provide wear resistance and is not considered to be a load bearing

component, thus it was omitted from this model. The material used was DMC, as in the hydraulic loading scenario. The fixed supports remained the same with the addition of an elastic support of 4 GPa at the inlet to represent the attachment which was decided after discussion with the industrial sponsor. In the field, there will be a hose attached that will provide a degree of support. The attaching hose material is determined by the operator, but for the purposes of this study it was assumed that a rigid polyvinyl chloride (PVC) piping is attached. In operation, depending on the application this could be steel piping thus using a modulus of 4 GPa is considered to be conservative. The mesh used was of a resolution of 5, however there was a reduction in the number of elements and nodes due to the removal of the rubber liner. The pressure of 300 kPa was applied to the inner surface of the parts and applied outward.

3.1.4.1 Results for DMC casing with 3 bar internal pressure

Figure 29 shows the contour for the maximum principal stress. The majority of the body of the cyclone remains between 28 MPa and -9 MPa. It is seen that most of the cyclone is in very low tensile loading while some parts along the flanged connections are experiencing compressive loading.

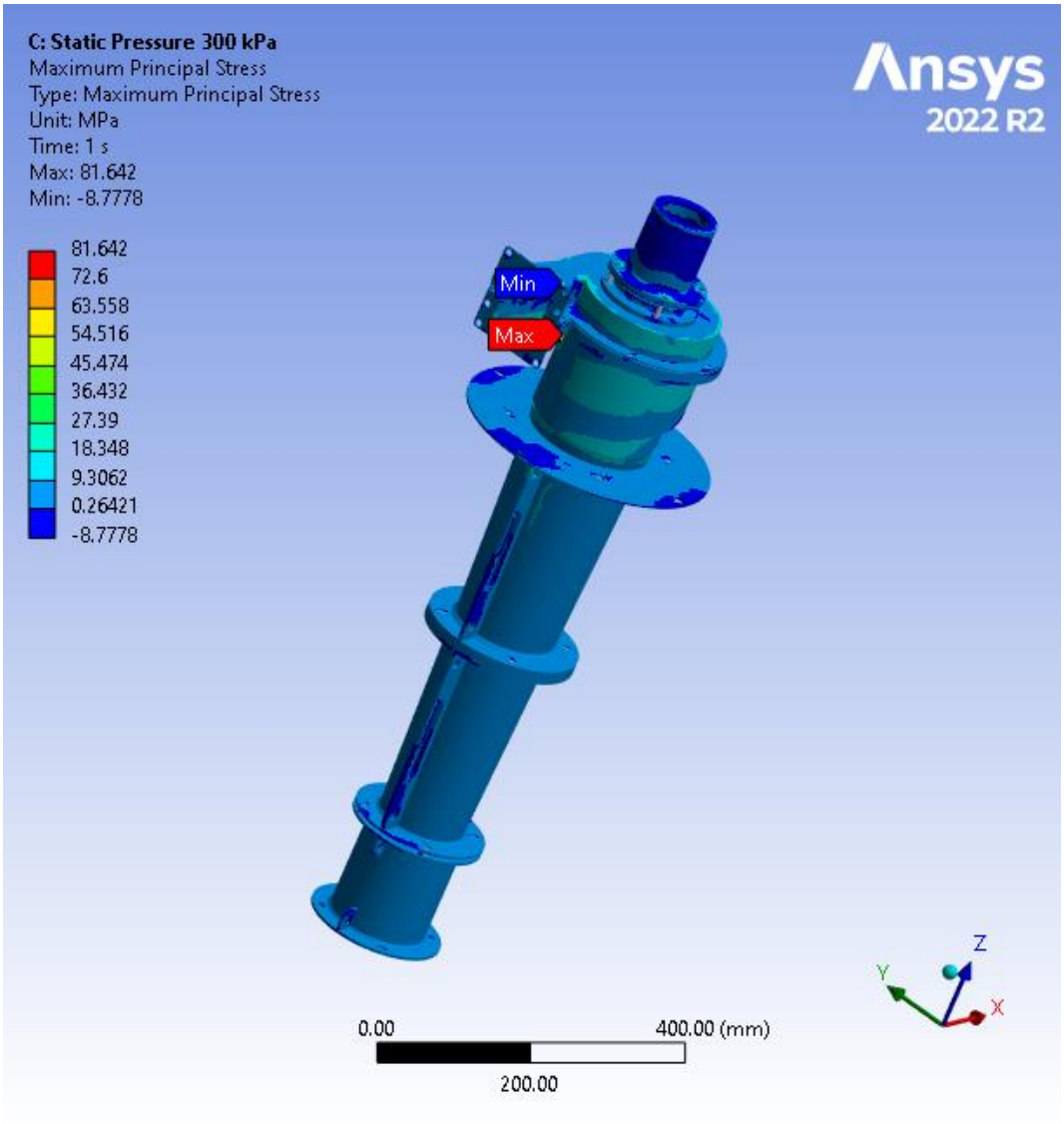

Figure 29. Maximum principal stress contour for 150 CVD pressurised to 3 bar.

The maximum stress is 81.642 MPa located at the corner where the inlet meets the feed chamber (Figure 30). This stress concentration appears to be highly localised and can be prevented in future design by creating a smoother transition. Keeping in mind that this current design was for fabricated steel which would require corners for welded joints. Utilising additive manufacturing could eliminate sharp transitions such as these [44].

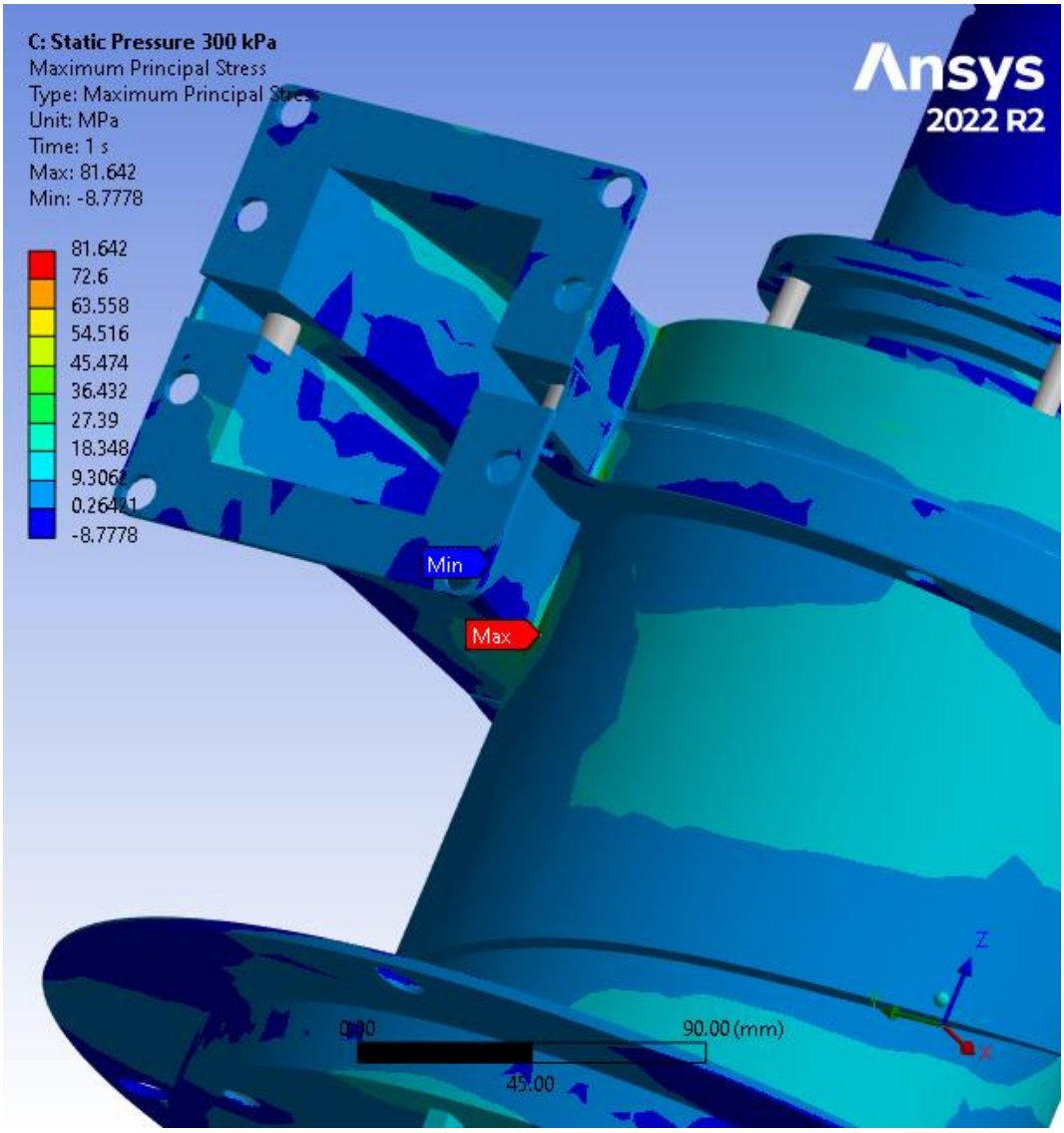

Figure 30. Maximum principal stress maximum stress concentration for 150 CVD pressurised to 3 bar.

The internal surface of the rubber liner is designed for the fluid interface in order to achieve maximum efficiency of the hydrocyclone. As seen in Figure 31, the cross section of the rubber liner of the feed chamber shows the surface that interacts with the slurry has smooth transitions. AM would be able to accommodate this and eliminate the welded joints of the steel component.

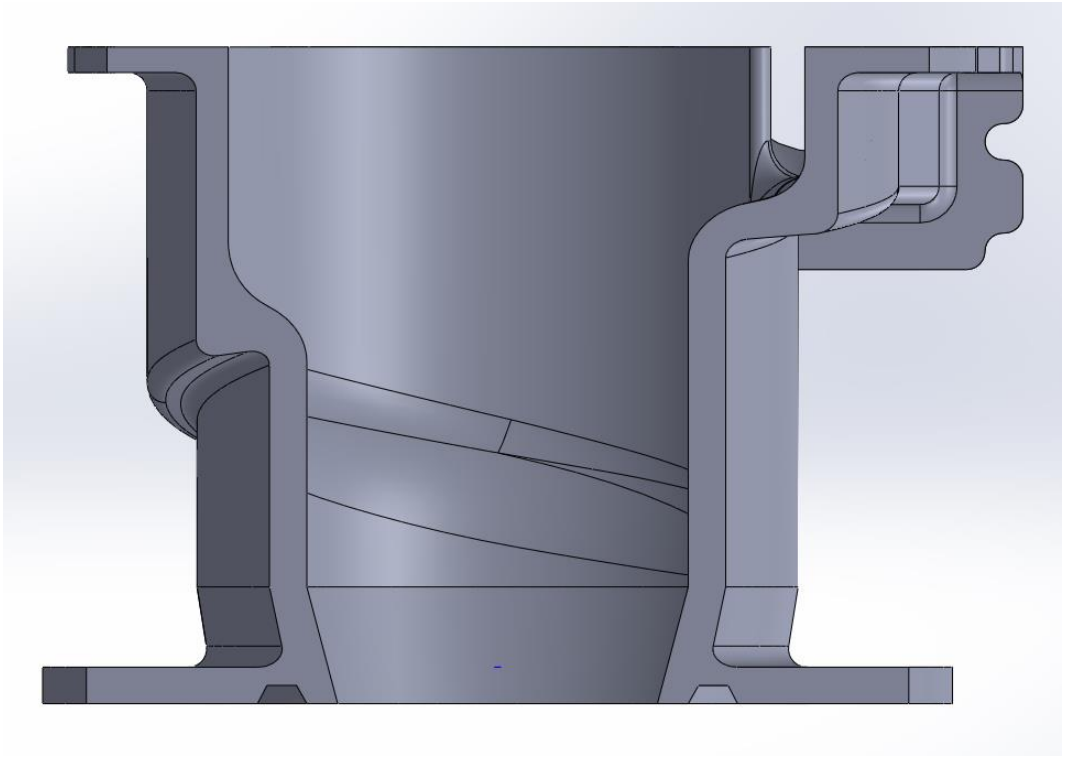

Figure 31. Cross section view of the rubber liner of the feed chamber showing smooth transitions for fluid interface.

A similar phenomenon is seen for the von-Mises contour in Figure 32, with no compressive stress on the body at all. This is attributed to the theory for von-Mises equivalent stress, which always results in positive stress values that are used to compare to the yield of ductile materials. The stress concentration in this scenario is found at a bolt hole on the feed chamber. Figure 33 demonstrates the higher stresses at the location of the bolt holes. This can be mitigated in future design as well to create further reinforcement at these locations. This is the advantage of using additive manufacturing as features can be redesigned and tested using rapid prototyping [35, 38].

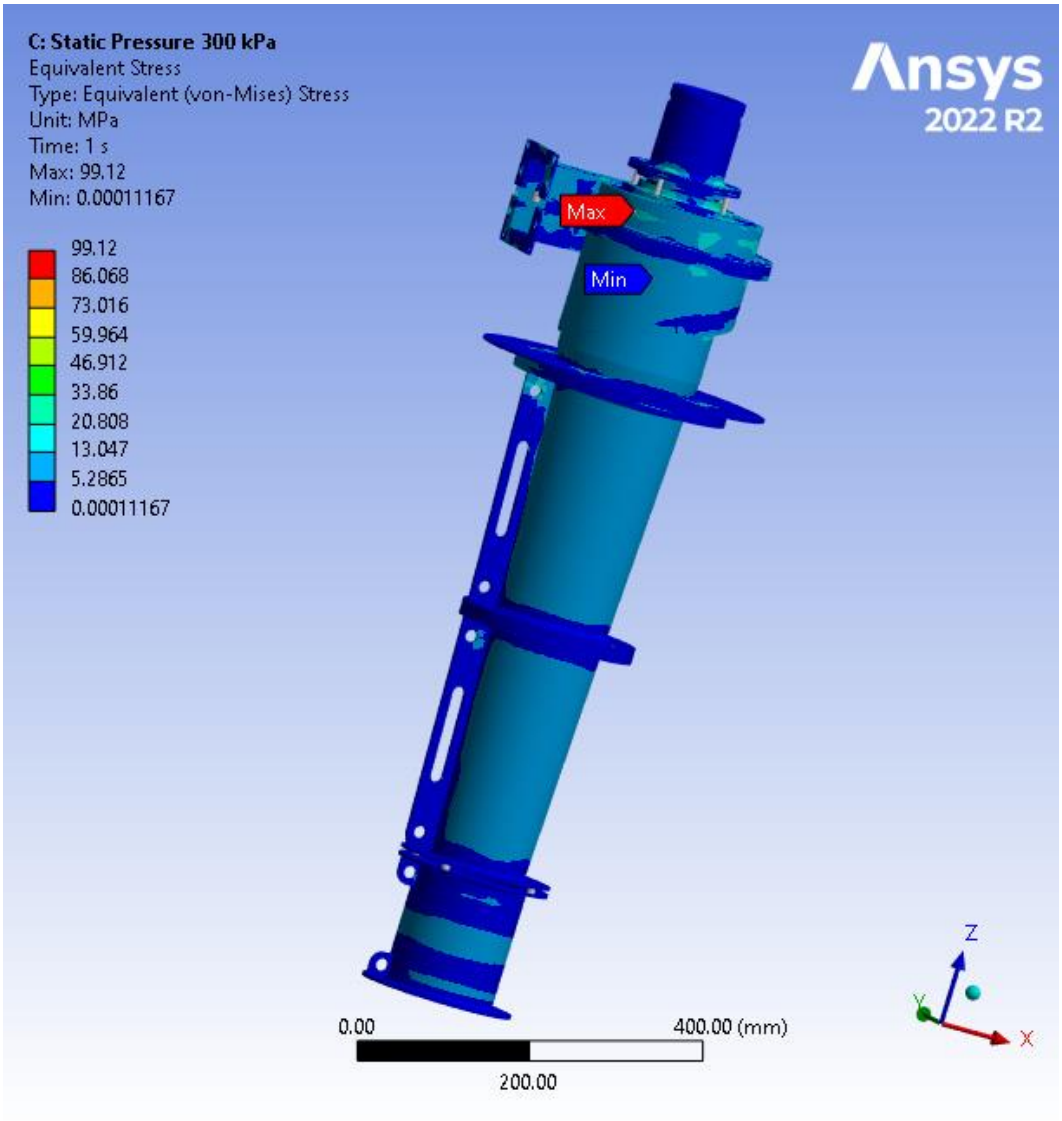

Figure 32. Von-Mises equivalent stress contour for 150 CVD pressurised to 3 bar.

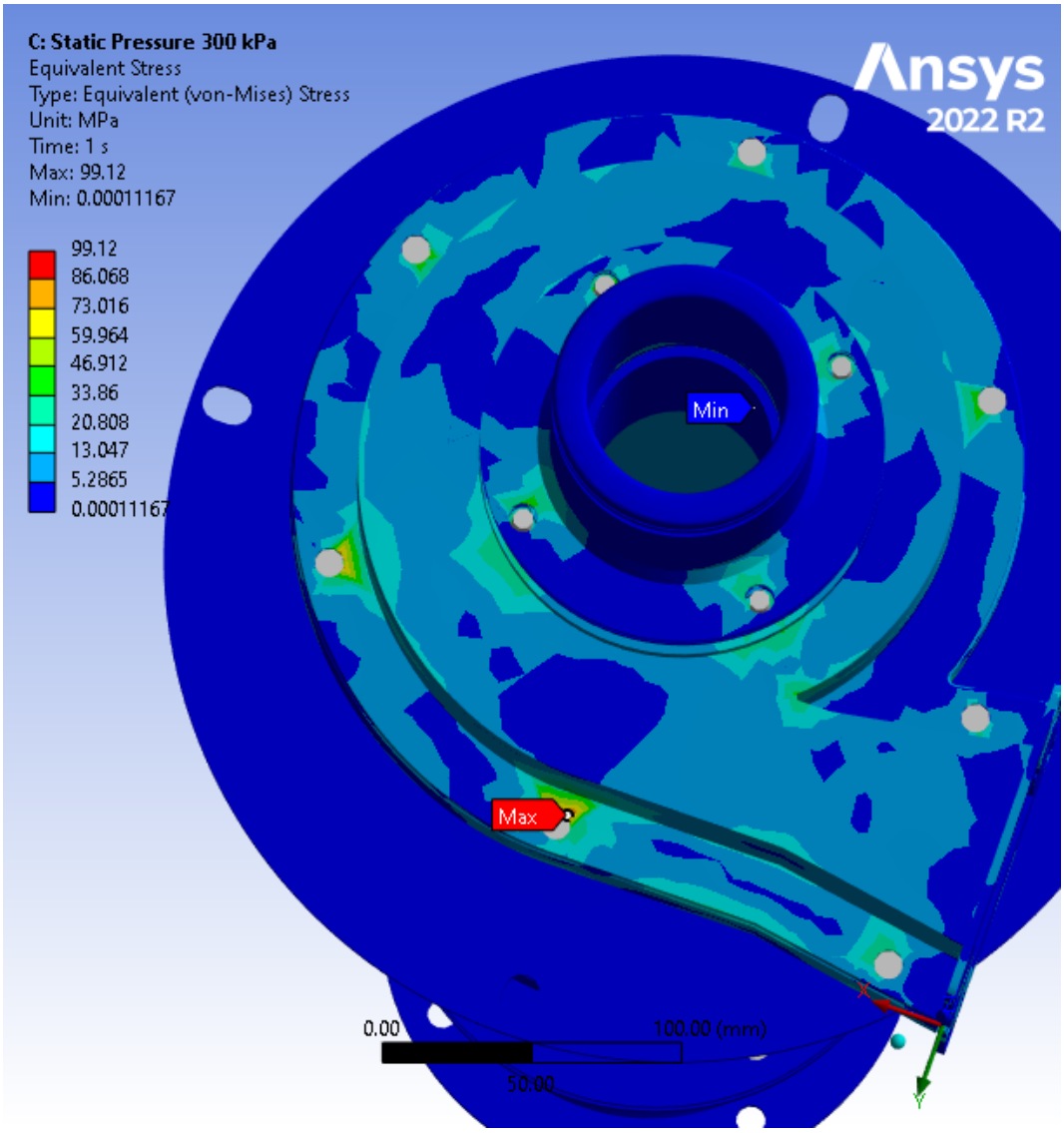

Figure 33. Von-Mises equivalent stress maximum stress concentration for 150 CVD pressurised to 3 bar.

3.1.4.2 Results for feed chamber component with redesign for AM

Per the analysis in Section 3.1.3, the highest stress concentration was found on the feed chamber of the hydrocyclone at the corner where the inlet meets the body. This is a sharp corner was originally designed to be a welded joint for the structural steel casing. In this section, a preliminary example of filleting some of the sharp edges for stress concentration reduction is shown.

The first step was to make changes to the design. Fillets of 10 mm were added to the outer edge of the feed chamber as shown in Figure 34. The details of the fillets on the corner of the body and inlet are shown in Figure 35. This is similar to the rubber liner of the feed chamber shown in Figure 31 in Section 3.1.4.1.

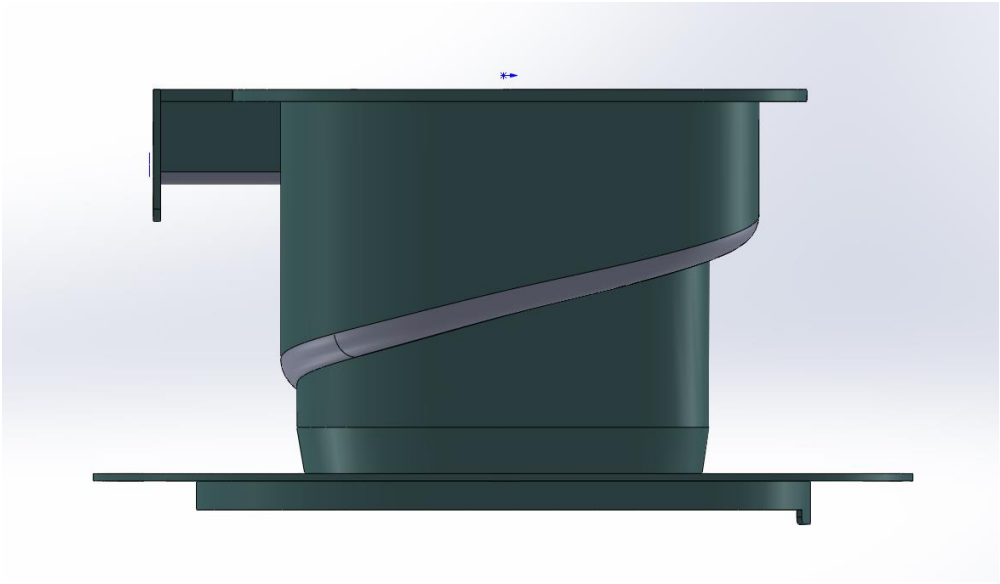

Figure 34. Filleted edge of feed chamber to reduce stress concentrations found during FEA.

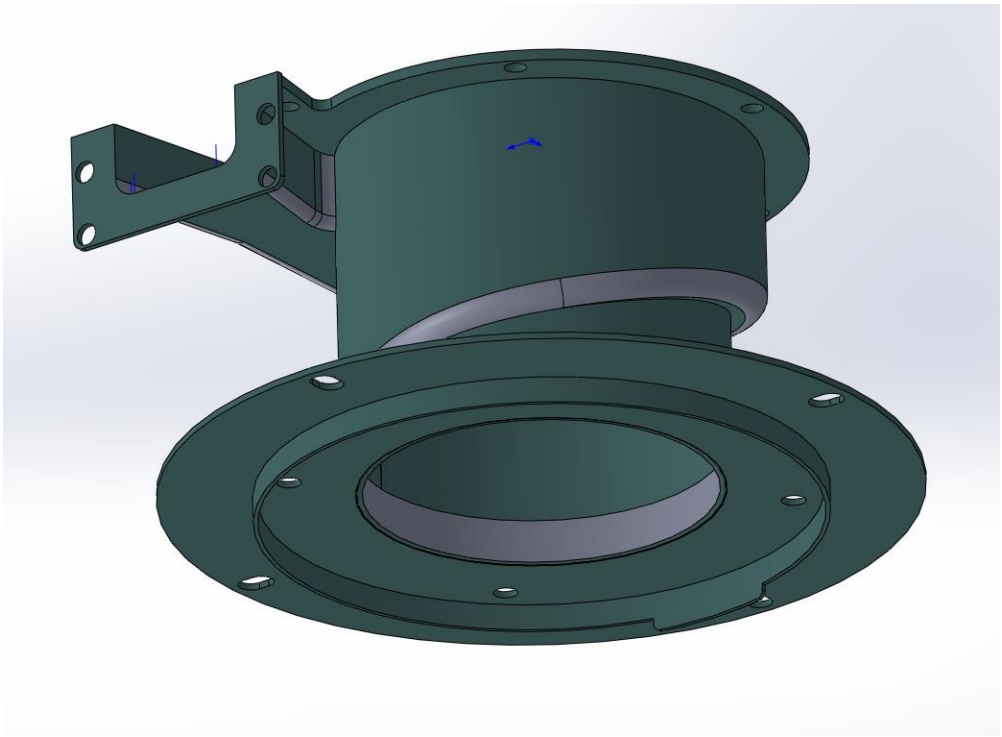

Figure 35. Another view of fillets added to the feed chamber to reduce the stress concentrations, particularly at the corn of the inlet and body.

The feed chamber was then constrained to match the analysis performed in Section 3.1.4.1. An internal pressure of 3 bar (0.3 MPa as denoted in ANSYS) was applied to all internal surfaces. The mesh was refined at the corner of interest and the adjacent fillet to a degree of 2 in order to obtain more specific results. As this study is focused on AM materials, ABS was chosen to enable material selection between the two AM materials of interest to the industrial sponsor. Using the static structural workbench, it was assumed that the behaviour of the material is isotropic and based on the weaker of the two orientations for ABS manufactured via Stratasys.

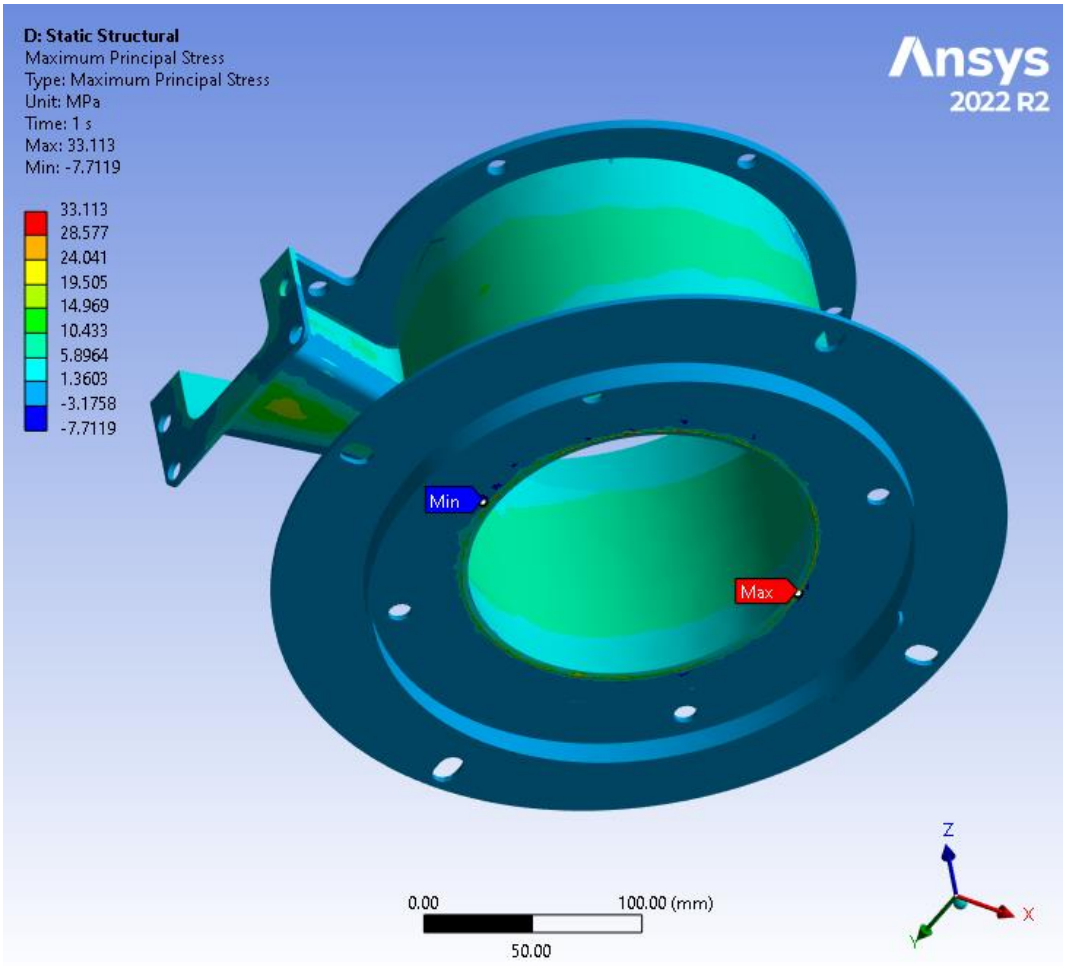

Figure 36. Maximum principal stress of feed chamber with an internal pressure of 3 bar showing the stress concentration has moved from the corner of the inlet.

Figure 36 shows the location of the maximum principal stress experienced on the feed chamber. Due to the filleting, this is now present at the connection of the bottom of the feed chamber to the flange. This component could be filleted to reduce this, as proven by re-designing the other edges of the feed chamber. Unfortunately, due to limitations with the model provided by the industrial sponsor some features could not be filleted due to overlapping solids and inconsistency in the boundaries as shown in Figure 37. This was mitigated and fixed where possible, however due to the constraints of the project and the experimental nature of the research this could not be done. For the purposes of this research and in combination with conservative estimates of

boundary conditions, it was determined that this location would benefit from the filleting, and this would reduce the stress concentration as shown for the inlet corner.

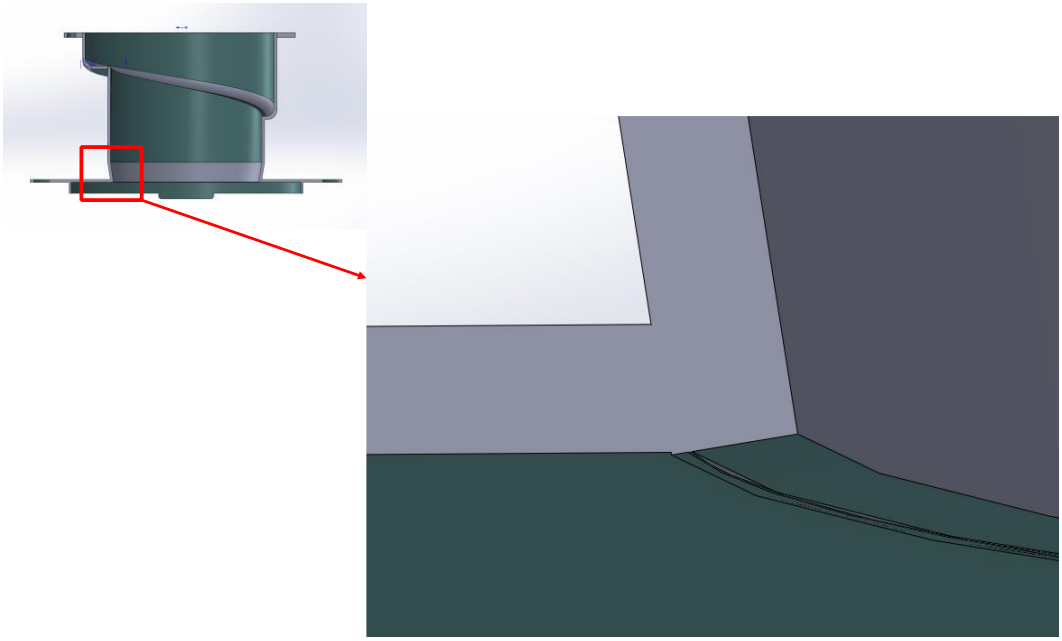

Figure 37. Example of issues with the joint of the body and flange of the feed chamber that prohibited filleting to reduce stress concentrations.

When examining the Von Mises equivalent stress, the maximum stress is seen at the internal corner of the inlet and body. However, this value is approximately 20 MPa which is lower than the ultimate tensile stress of ABS (26.8 MPa).

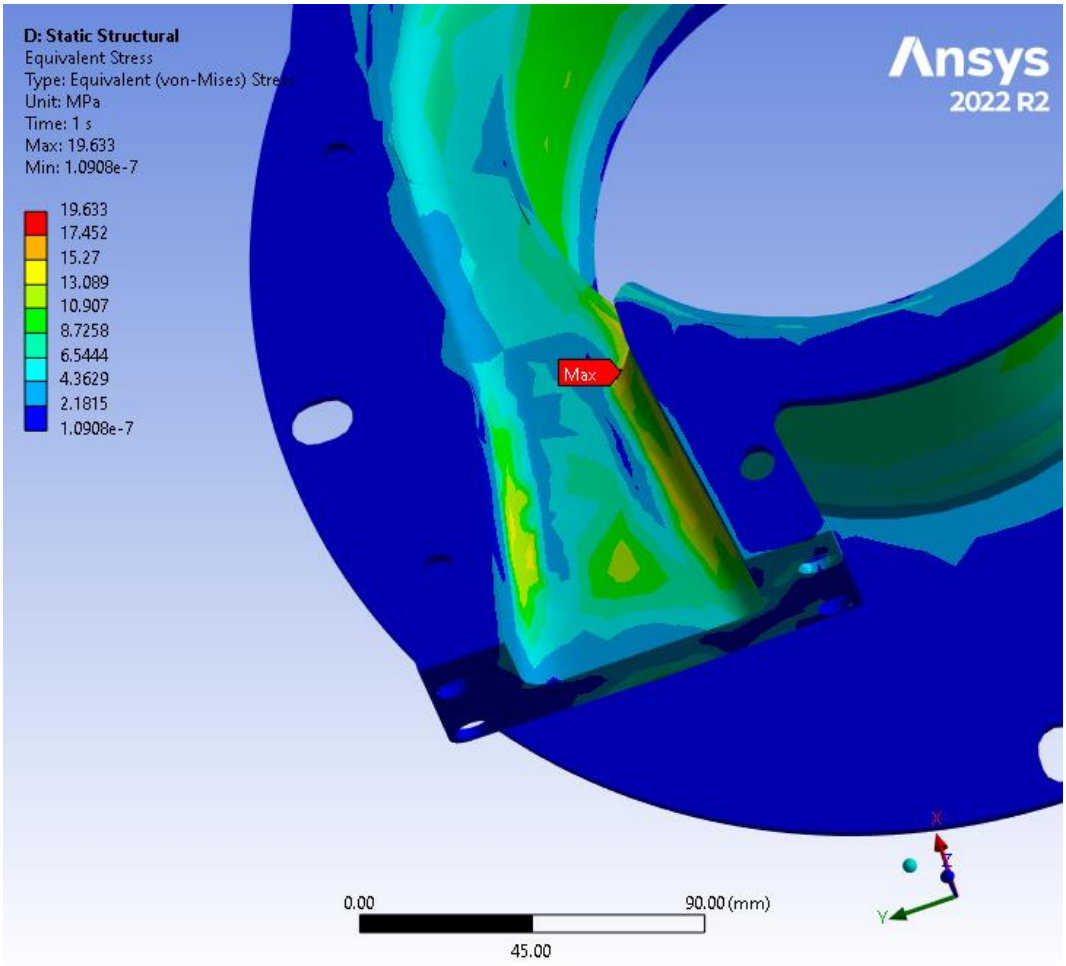

Figure 38. Von Mises equivalent stress contour showing the maximum stress for the re-designed feed chamber when an internal pressure of 3 bar is applied.

3.1.5 Material selection and the need for material testing

After reviewing the results of this finite element analysis and comparing to the material data provided from Stratasys, it was determined that ABS would be the choice material for further testing. The addition of filleted edges and corners alleviated the stress concentrations found during FEA of a DMC casing. The FEA on the ABS feed chamber showed that it is the choice material over Ultem 1010 as the structural requirements were met. However, this model cannot be used for predicting failure of the hydrocyclone because it assumes that the material is isotropic when in reality it is not. As seen in Chapter 2, little research has been done to understand the performance

of AM materials when pressurised. The greatest need, therefore, in determining if AM is suitable for this application is to test the material.

To understand the behaviour of the material without the interference of stress concentrations created by the geometry, the chosen vessel for this study was a cylinder with a hemispherical domed enclosure.

3.1.5.1 Design of a vessel for pressure testing

In order to understand the behaviour of the material when subjected to internal pressure, a demonstrative test of a cylinder was carried out. This largest conical component of the casing has a maximum internal diameter of 155 mm and a wall thickness of 3 mm. Before testing, it was necessary to make sure that this thickness was sufficient for a cylindrical pressure vessel by utilising the ASME code PD 5500 [76]. Equation (3-1) describes the thickness (denoted as 'e') required for a cylindrical vessel dependent on the design stress, internal diameter, and applied pressure.

$$e = \frac{pD_i}{2f - p} \tag{3-1}$$

Where 'p' is the applied pressure, 'D_i' is the internal diameter and 'f' is the design stress. The hoop stress, as shown in Equation (3-2), is the highest theoretical stress that will be seen by the vessel [77].

$$\sigma_{hoop} = \frac{pR}{t} \tag{3-2}$$

Where 'p' is the internal pressure, 'R' is the internal radius and 't' is the chosen thickness. In this case 't' is the design thickness of the hydrocyclone cones, 3 mm. If e << t, then use of the 3 mm design thickness is conservative and therefore permissible. However, if e >> t then re-design of the vessel will be required. The calculated thickness 'e' was found to be 3.06mm for a hoop stress of 7.75 MPa. These values were calculated using Equations (3-1) and (3-2) and the values in Table 6.

Table 6. Values used to calculate the highest hoop stress for the 150 CVD conical casing and the wall thickness per ASME code PD5500 [76].

Values used to calculate the highest hoop stress and wall thickness	
Pressure 'p'	300 kPa
Radius 'R'	77.5 mm
Thickness 't'	3 mm
Internal diameter 'D_i'	155 mm
Design stress 'f'	7.75 MPa

From this check, it is seen that 'e' is roughly equivalent to 't'. There is a 2% difference in thickness calculated by PD5500 from what was provided by the design of the hydrocyclone casing. It was determined that this was acceptable as the assumption that design stress 'f' was equivalent to the theoretical hoop stress was conservative.

In order to test the cylinder, access is required from one end in order to install an attachment for the pressurisation mechanism, a safety valve, and a pressure transducer which required the design of a flange and bulkhead. However, in order to reduce the number of flanges and locations of potential leaks due to bolted connections, a hemispherical end was designed. For a sphere, the stress experienced due to internal pressure is half of the hoop stress for a cylinder and equivalent to the longitudinal (or axial) stress of the cylinder. This is defined as:

$$\sigma_{sphere} = \frac{pR}{2t} \tag{3-3}$$

Per PD5500, the thickness required for a hemispherical end per 3.5.2.3.1 is the same equation as for a spherical vessel (equation 3.5.1-3). This is:

$$e_{sphere} = \frac{pD_i}{4f - 1.2p} \tag{3-4}$$

Using the same values for the radius, diameter, design thickness and internal pressure while substituting the spherical stress for the design stress we get:

$$\sigma_{sphere} = 3.875\ MPa$$

$$f = \sigma_{sphere}$$

$$\therefore e_{sphere} = 3.07\ mm$$

As this is roughly the same as the cylinder thickness calculation and with the same conservative assumptions, it was considered acceptable. Figure 39 shows the dimensions of the pressure vessel to be tested and Figure 40 is an overview of the geometry.

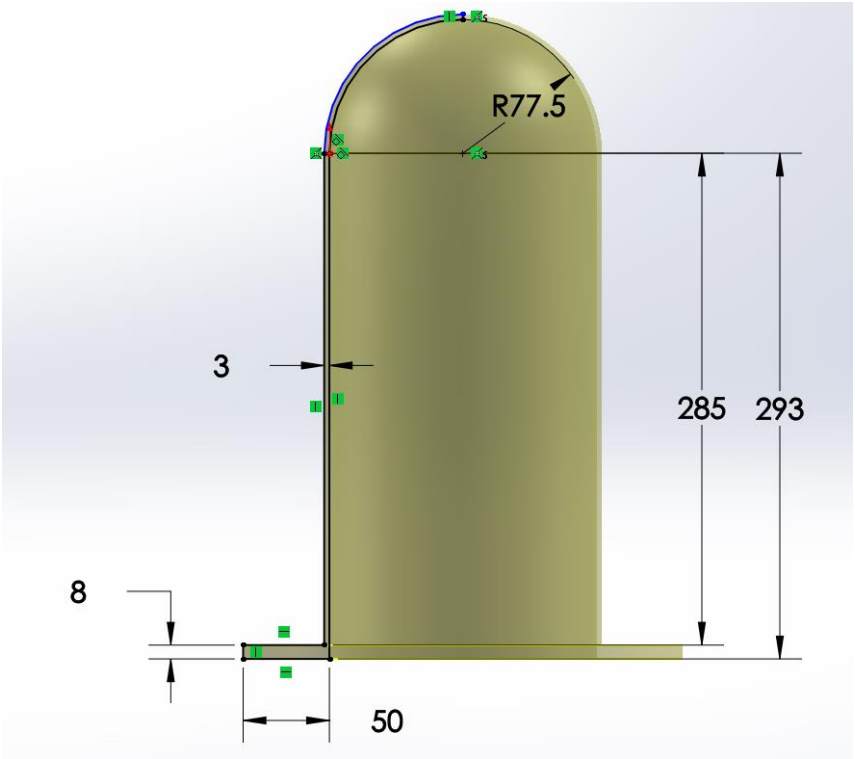

Figure 39. Dimensions (in mm) of domed cylinder for 3 bar pressure test.

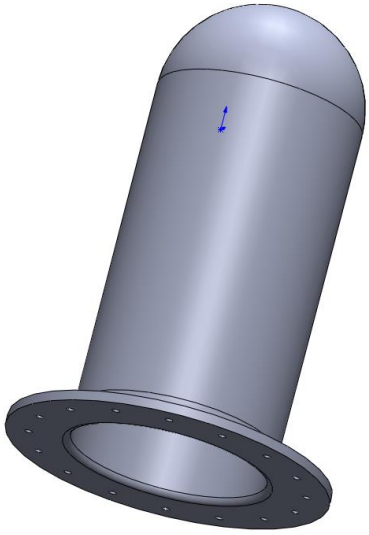

Figure 40. View of model for domed cylinder for testing.

A mating part encloses the open end; this is the bulkhead. The bulkhead design, shown in Figure 41, is made of steel and used for multiple tests. Since the tested vessel itself is a less rigid material than the bolts and the bulkhead, two measures were taken to alleviate bending of the flange of the vessel after clamping. The first is a steel clamping ring that fits on top of the flange which provided stabilisation and load distribution from the flange into the steel. The second is the use of 16 x M6 bolts, thus reducing the distance between holes which resulted in better resistance to bending. The bolts were checked by Professor David Nash using an in house code that incorporates the bolting requirements from Section 3.8 of PD 5500.

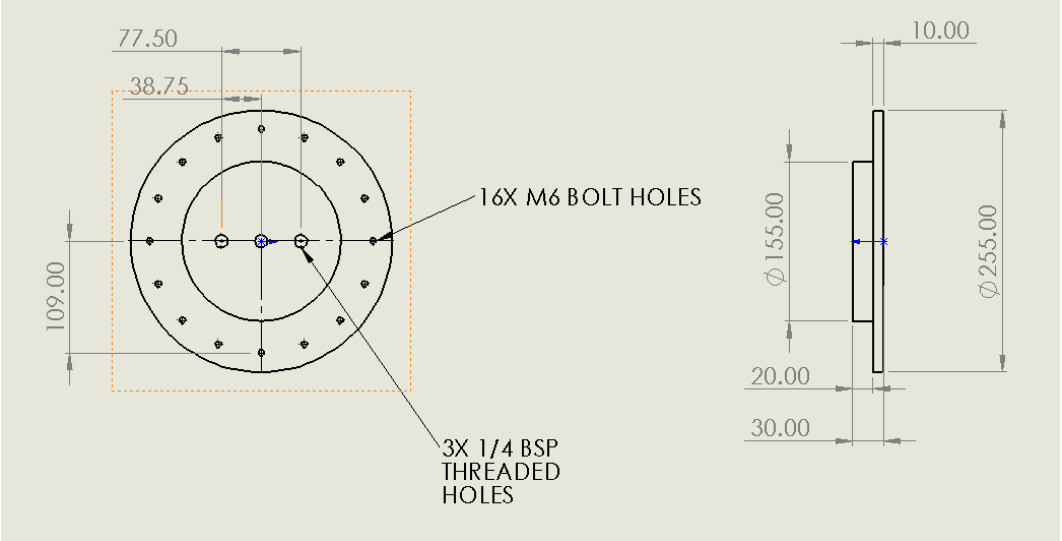

Figure 41. Dimensions of pressure head for the testing apparatus.

The three ¼ BSP threaded holes seen in the step of the head are for the pressure transducer, ball valve and hose to the pump. The test is set up so that the cylinder is vertical, with the domed end down. This takes advantage of the flange as a support and gives access to the bulkhead.

3.1.5.2 Experimental validation of cylinder for pressurisation up to 3 bar

The stress contour from the FEA analysis performed in ANSYS Static Structural workbench is shown in Figure 42. The cylinder was fully constrained at the flange, where it will be bolted to the steel bulkhead and clamped by a steel ring. The transition from the flange to the thinner wall will result in highest stresses seen towards the bottom of the cylinder.

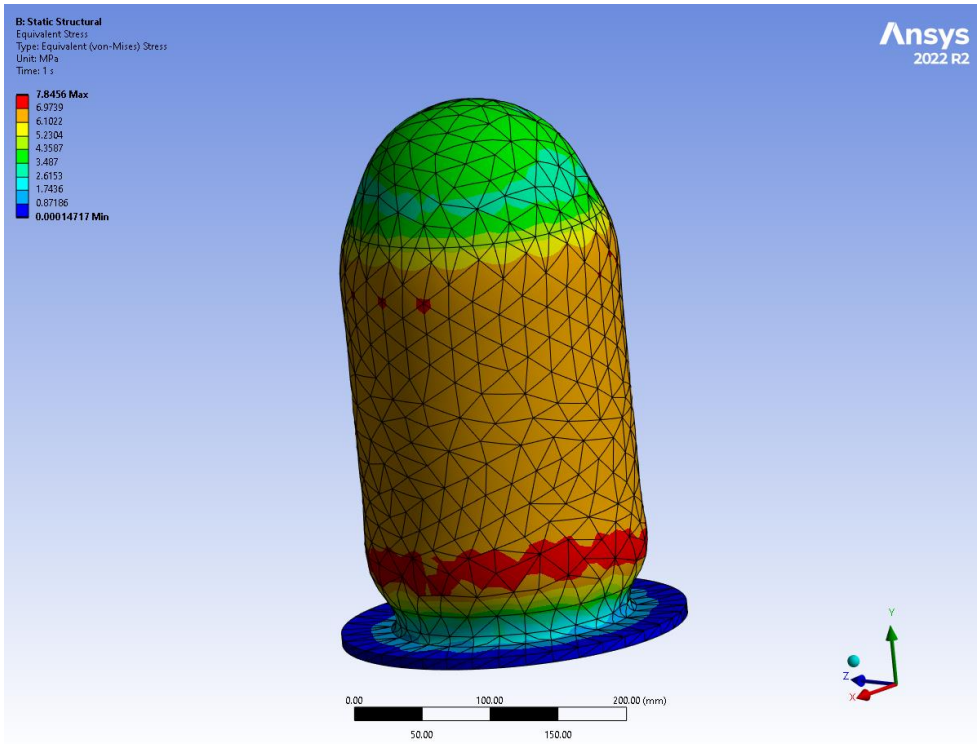

Figure 42. Equivalent elastic stress for ABS cylinder pressurised to 3 bar.

In order to create the most conservative estimate of strength, the ABS material was assumed to be isotropic with the interlaminar strength from the supplier input as performed for the feed chamber FEA as well. This would be the case in the axial direction as the layers are built up from the flange to the dome. In the hoop direction there will still be a seam where each layer meets the point at which it was initially laid down. Because of this, the vessel will be dependent on the interlaminar strength in both directions, with the highest loading in the hoop direction. Figure 43 shows the anticipated contour of the strain. This analysis informed the placement of the strain gauges on the vessel which is discussed in Section 3.2.

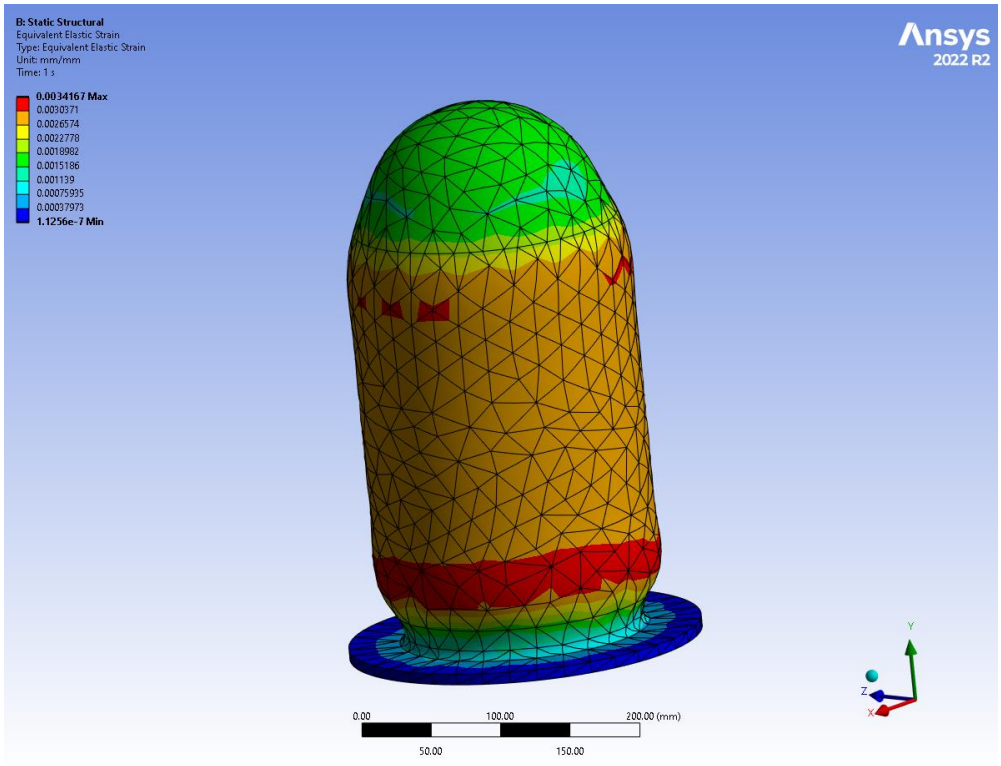

Figure 43. Equivalent elastic strain for ABS cylinder pressurised to 3 bar.

3.2 Experimental methodology for pressurisation up to 3 bar

3.2.1 Materials

After review of the structural requirements of the 150 CVD via FEA, it was determined that ABS had sufficient mechanical properties for this application. The material properties can be found in Table 5 in Section 3.1.1.

3.2.2 Epoxy sealing

Previous studies have found that FDM printed parts have a porous structure that is insufficient for holding internal pressure [78, 83]. A repeated pattern of porosity is created within the material, even at the 100% infill density setting of the printer. Considering the needs of the Weir Group, it was determined the most economical and accessible way to seal the parts at the university was by using epoxy resin which could be applied manually and did not require large investment in tooling.

A low viscosity epoxy, Epikote M135, was chosen in order for infusion into the voids to occur. The epoxy was cured with Epikure M134 & M137. All were supplied by PRF Composites. The epoxy and hardeners were mixed & cured according to the manufacturer's guidelines which recommended curing at room temperature (20-25°C) and a post-cure heat treatment at 40-150°C. The recommended weight ratio of epoxy to hardener of 100:30 (:15 for each hardener) was used. The combined viscosity at 25°C is 200 mPa s according to the manufacturer and has a pot life of approximately 45 minutes. PRF composites provides mechanical properties for the resin system when cured for 24 hours at 23°C and a post-cure of 15 hours at 60°C. This same curing procedure was used for the pressure vessel.

Table 7. Mechanical properties of RS-M135 epoxy with RS-MH134 and RS-MH137 hardeners (provided by PRF composites).

CURING : 24h @ 23°C + 15h @ 60°C		RS - M135 & RS-MH134 / RS-MH137
Density	g/cm³	1.18 - 1.20
Flexural strength	N/mm²	110 - 140
Tensile strength	N/mm²	70 - 80
Impact Strength	Nmm/mm²	40 - 50
Elongation	%	5 - 6.5
Compression strength	N/mm²	120 - 140
Modulus of elasticity	kN/mm²	3.3 - 3.5
Water absorption 24 hours / 23°C	%	0.10 - 0.20
Water absorption 7 days / 23°C	%	0.20 - 0.50
Shore Hardness	D	80 - 85
Fatigue under reverse bending stresses acc. DLR Brunswick	10% 90%	> 1 x 10⁶ > 2 x 10⁶

The epoxy was mixed and spread over the inside and outside surfaces of the pressure vessel were coated. The outside was coated by standing the vessel on the flange and pouring the mixture over the domed end. A brush was used in order to achieve more

uniformity on the surface. The entire vessel was left at ambient temperature for 24 hours then placed into the oven for 15 hours at 60°C.

In order to determine if the epoxy could stop leaking due to porosity at ambient conditions the vessel was suspended by the flange and filled with water. The vessel was then left for 24 hours, and visual inspections were performed to identify any leakage points. As the vessel could not be observed for the entire 24 hours and there was a risk of any leaks evaporating, the water within was dyed a deep purple so that evidence of a leak would be seen in residue left on the white ABS or in the pan below. If a leakage was found the vessel was emptied and dried by absorbing visible moisture with paper towels. Then the vessel was left at ambient temperatures for a minimum of 24 hours. After drying, another layer of epoxy was placed on the inside and outside of the vessel per the same process as stated previously with the removal of any excess after post cure. This was performed for a total of 3 times as the first two coats resulted in leaks. The third application ensured the vessel was watertight when at ambient pressure. The original weight of the pressure vessel was 0.8205 kg. The final weight was 0.8975 kg, corresponding to 8.6 wt% of epoxy.

Section 7.2.1 of Chapter 7 addresses concerns around the repeatability of this process and suggestions to mitigate this.

3.2.3 Testing apparatus

A manually operated pump was connected to the bulkhead via the blue valve in Figure 44 and used to pressure the vessel. The safety valve (red) was installed in order to immediately relieve pressure during the experiment in the event that the primary valve connected to the hose (blue) fails. The pressure transducer is installed in this location also (described further in section 0).

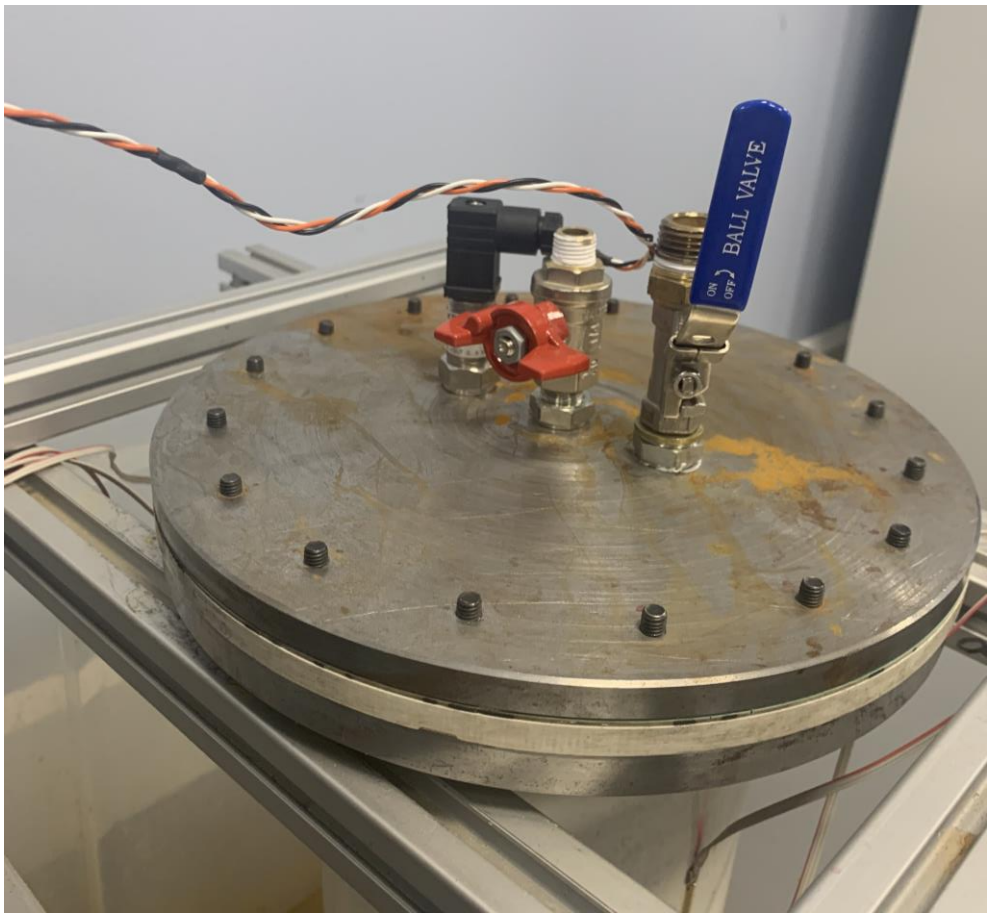

Figure 44. ABS cylinder with steel bulkhead and clamping ring.

3.2.3.1 Measurements during test

A 10 bar, 5 volt PR-21Y pressure transducer from Farnell was purchased and installed in the bulkhead. In order to measure the response of the material, strain gauges were placed in the hoop and axial direction. The direction of printing has been chosen so that the layers are hoop-wise as this is the largest stress. This means that the 'XZ' values are valid for this direction. The axial stress will be compared against the 'ZX' values. As the ratio of the 155mm diameter to the 3mm thickness is greater than 10, this is considered to be a thin walled vessel. Therefore, it can be assumed that the difference between the stress on the inside and outside of the wall is negligible [77]. The strain gauges are placed on the outside. A 350-ohm strain gauge specifically designed for inhomogeneous materials by Omega was chosen. A total of 6 strain gauges were applied in two groups of 3 symmetrically on the cylinder. Per Figure 45, one was placed in the hoop direction at the location of highest stress per the FEA and two were placed above this axially.

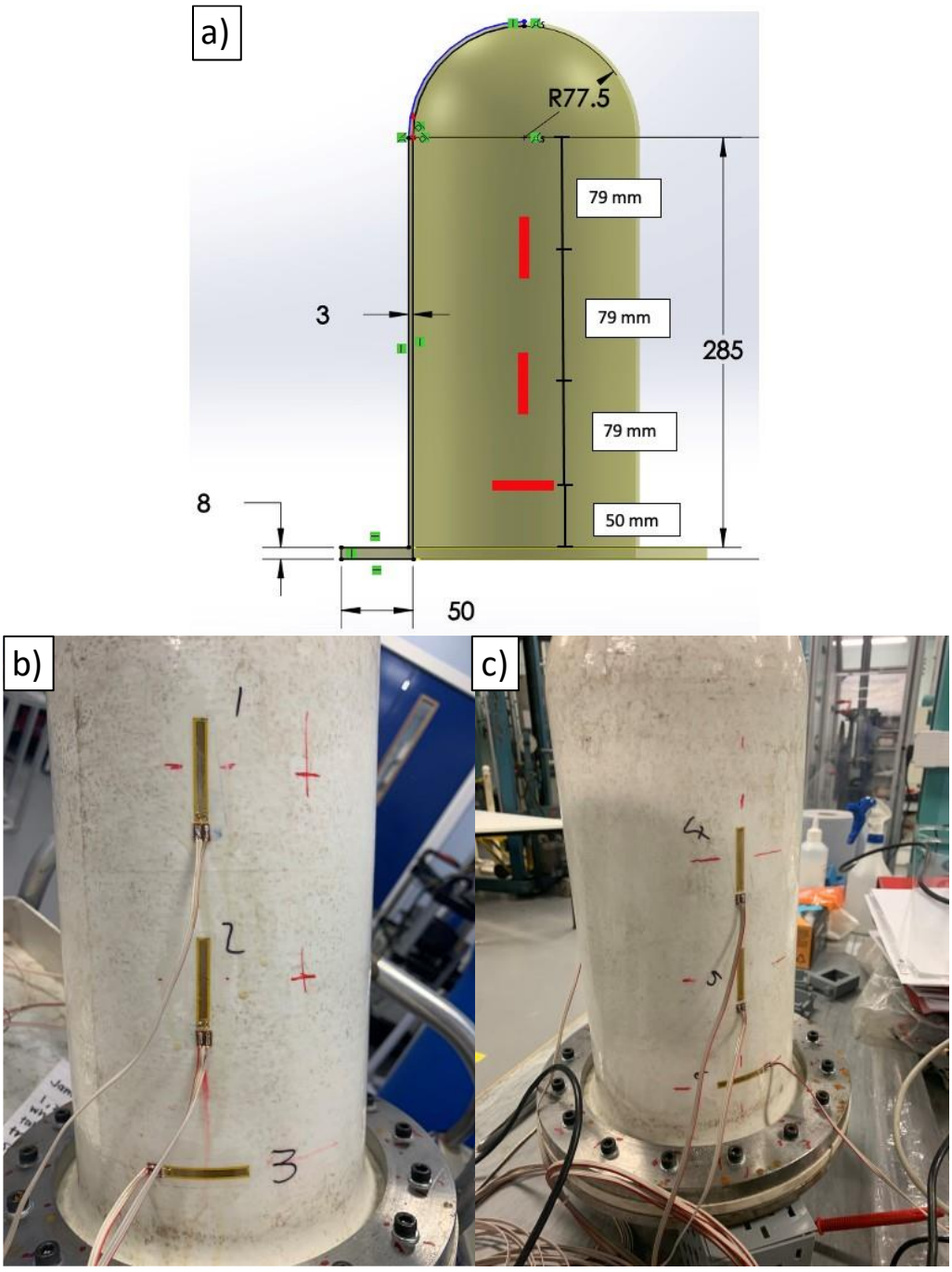

Figure 45. a) Placement of strain gauges for cylinder pressure testing; b) and c) the 6 strain gauges as installed symmetrically on the vessel.

The higher resistance will result in less current as strain is induced. This means that there will be less localised heating which could result in skewed strain values as the mechanical properties of thermoplastics will reduce at higher heats.

Pressures and any other data gathered were measured using Labview. The time, pressure and strain were recorded throughout the test and this data was translated to curves using Microsoft Excel and Origin.

3.2.4 Testing protocol

To create the methodology for this test ASTM D1599 [89] was used for reference, however a standard for testing of a polymer vessel exposed to longer term pressurisation and to measure any mechanical properties was not found.

The apparatus was placed on a support stand so that the cylinder could hang freely while supported by the flange as seen in Figure 46. The safety valve and blue valve connected to the manual pump are left open. The pump is operated until water leaves the safety valve. At this time the safety valve is closed, and pressurisation begins.

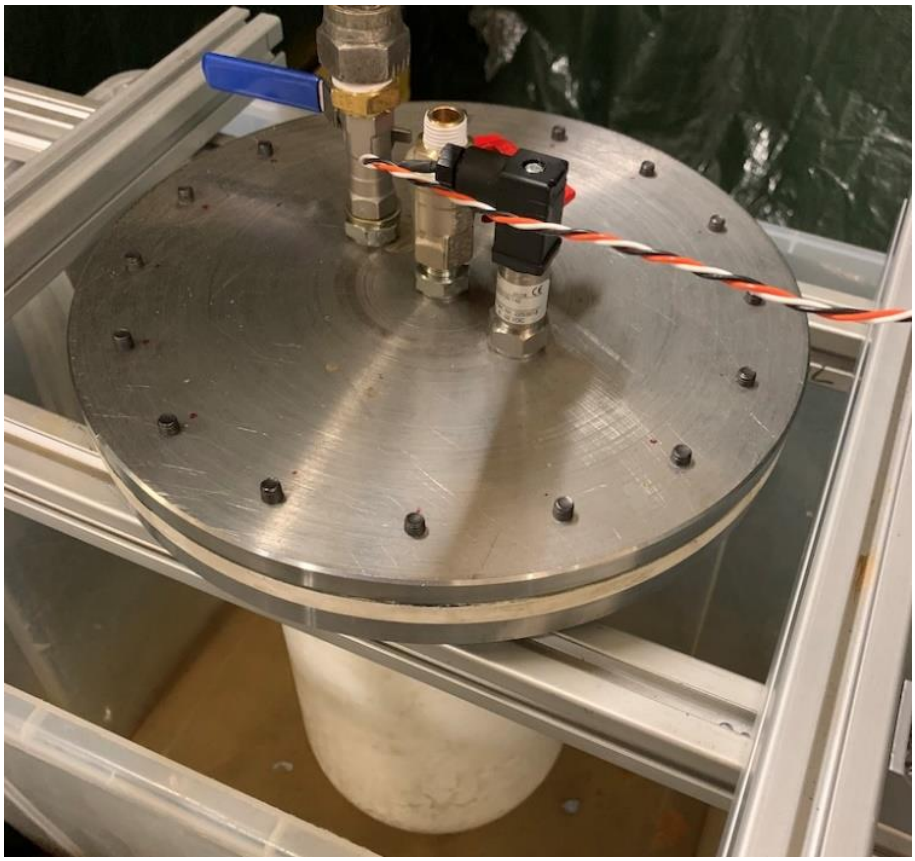

Figure 46. ABS cylinder sealed for pressure testing.

The vessel was pressurised in 0.5 bar increments and held for 24 hours at each pressure shown in Figure 47. Data from the pressure transducer and strain gauges were set to record via the LabView script. After a full cycle of testing to 3 bar the vessel was released back to ambient pressure and the testing schedule was run for a second time. The vessel was pressurised using a hand operated pump includes some overshooting & error involved in this process. To mitigate this the pump was operated slowly and the pressure was observed via Labview's readings from the pressure transducer. Any excess pressure was released from the system using by opening the safety valve.

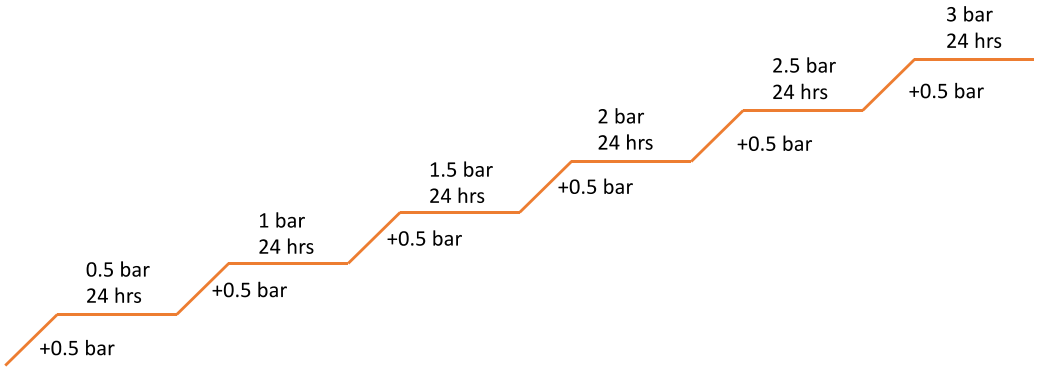

Figure 47. Schematic of pressurisation to 3 bar for cylindrical vessel.

After the vessel was sealed and deemed watertight, the strain gauges were installed. The programme in Figure 47 was run twice while recording strain measurements.

3.3 Experimental results and discussion of pressure testing to 3 bar

3.3.1 Leak rate

The leak rate at each interval was recorded, per the study by Al-Hasni and Santori [83], to determine if the vessel remained watertight above ambient pressure. In their study the acceptable leak rate was determined by the required performance of the thermally

driven chillers and heat pumps. For this study, the requirement of the vessel is that there is not catastrophic failure at a pressure of 3 bar or lower. Thus, the leak rate must be low enough that there is not a significant reduction in pressure so that the material response can be accurately studied. It was decided that for 3 bar, the acceptable margin of pressure loss would be 5%. A reduction in pressure from 3 bar to 2.85 bar would reduce the maximum equivalent stress from 7.8456 MPa to 7.4533 MPa as verified by the FEM. This is a 5% reduction in stress and both values represent approximately 30% of the ultimate tensile strength of ABS per Table 5 in Section 3.1.1. The corresponding leak rate was calculated using the following equation:

$$q = \frac{\Delta PV}{\Delta t} \tag{3-5}$$

Where 'q' is the leak rate in Pa m^3 s^{-1}, 'ΔP' is the change in pressure over the change in time 'Δt' and 'V' is the internal volume. The internal volume accounts for the cylinder and domed end and is calculated to be approximately 0.006 m^3. For 95% of the original 3 bar to be maintained, the allowable leak rate is 0.001 or 1x10^{-3} Pa m^3s^{-1}.

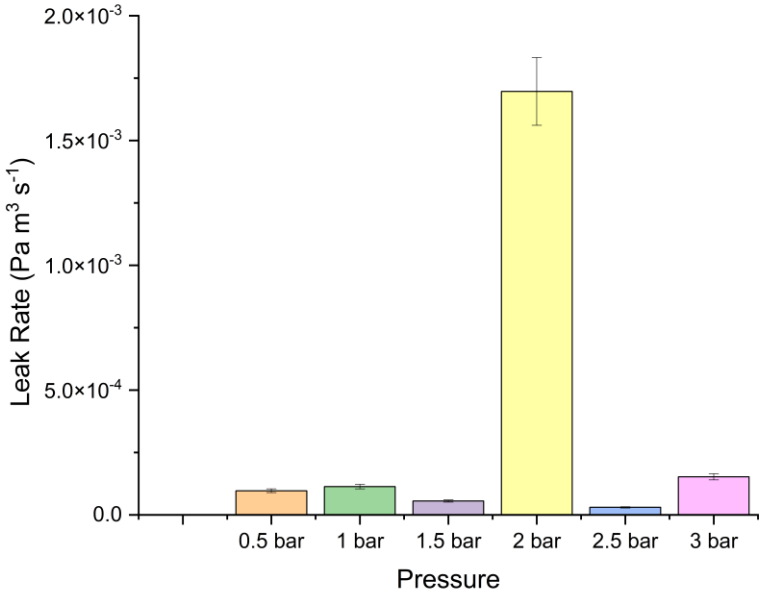

Figure 48. Leak rate of ABS pressure vessel when pressurised for 24 hours at each 0.5 bar interval.

The values for a 24 hour testing period are shown in Figure 48. A much higher leak rate than the subsequent higher pressures is shown for 2 bar which is outside of the allowable leak rate. The average leak rate of 1.7 x 10^3 Pa m^3 s^{-1} results in a change in pressure of 0.25 bar over the 24 hour period. As there were no visible leaks for this run and the higher pressures exhibited a tighter seal it was concluded that this was due to user error, most likely in the tightening of the safety valve. Further experiments with strain gauges proceeded with extra caution taken when securing the valves.

3.3.2 Analysis of mechanical behaviour

The behaviour of polymers is dependent on time with strongly non-linear stress-strain curves, even in early stages of deformation, and multi-axial creep observed [90, 91]. A previous study found that the mechanisms of yield and failure for FDM printed ABS are in line with the mechanics of traditionally manufactured counterparts [92]. The results in Figure 49 to Figure 60 exemplify the complexity of polymers when stressed over long periods of time which has been studied for ABS under tensile loading in the past [93-95]. This type of phenomenon, however, has not been studied for FDM printed ABS subjected to internal pressure as in this study.

Following is the pressure vs. time results from the experiment. Over the two runs there were no significant drops in pressure due to leaking that were observed.

In Figure 49 it is observed that the strain is very low overall for the first run at 0.5 bar and increases for all strain gauges from the second run in Figure 50. The highest strain is found above where it was anticipated at the A 2/2 axial strain gauge.

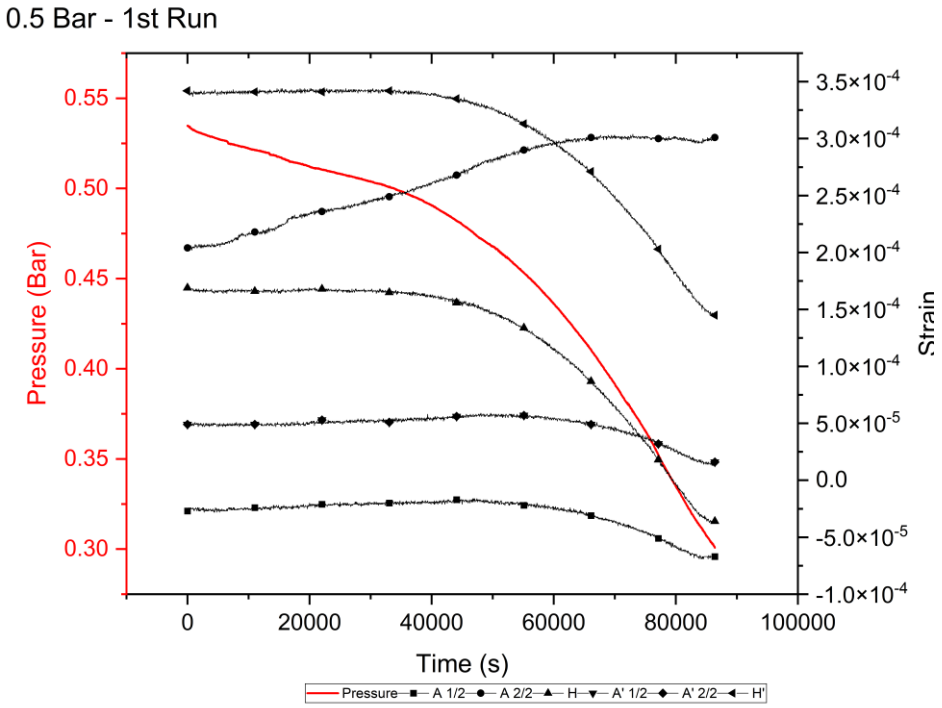

Figure 49. Pressure and strain response over time for the first run at 0.5 bar.

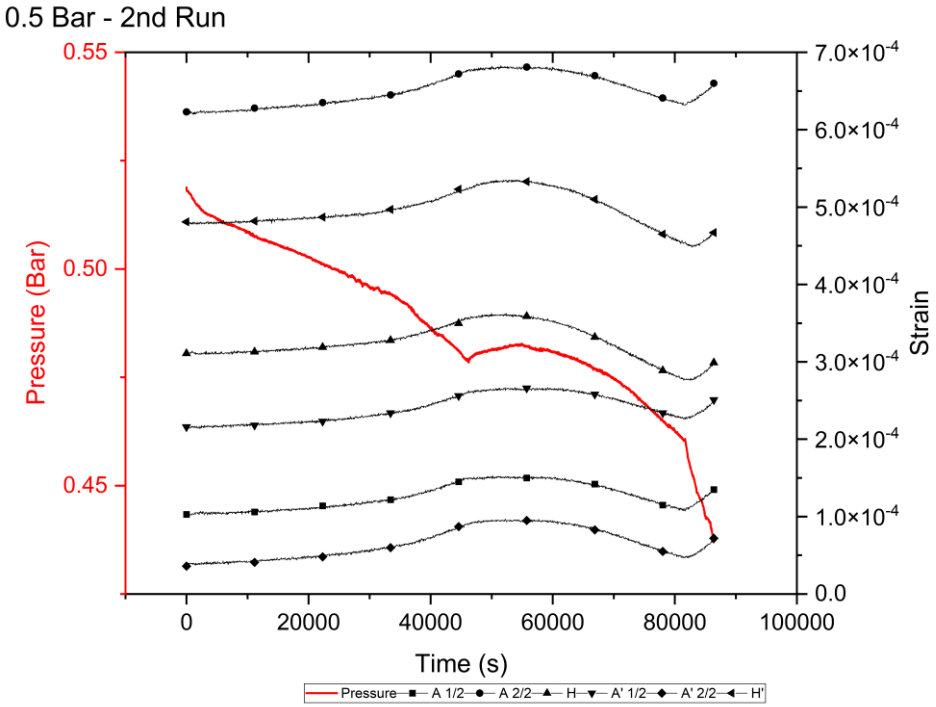

Figure 50. Pressure and strain response over time for the second run at 0.5 bar.

As the vessel is pressurised up to 1 bar, Figure 51 shows that for the first run the largest strain is from a hoop strain gauge with A2/2 following. There is some reduction in strain in the hoop direction while the strain for A 2/2 increases signifying creep. This was observed on the first run at 0.5 bar in Figure 49 as well. For the second run, shown in Figure 52, all strain gauges follow a repeated pattern as with 0.5 bar, however now the highest strains are seen in the hoop direction gauges as anticipated.

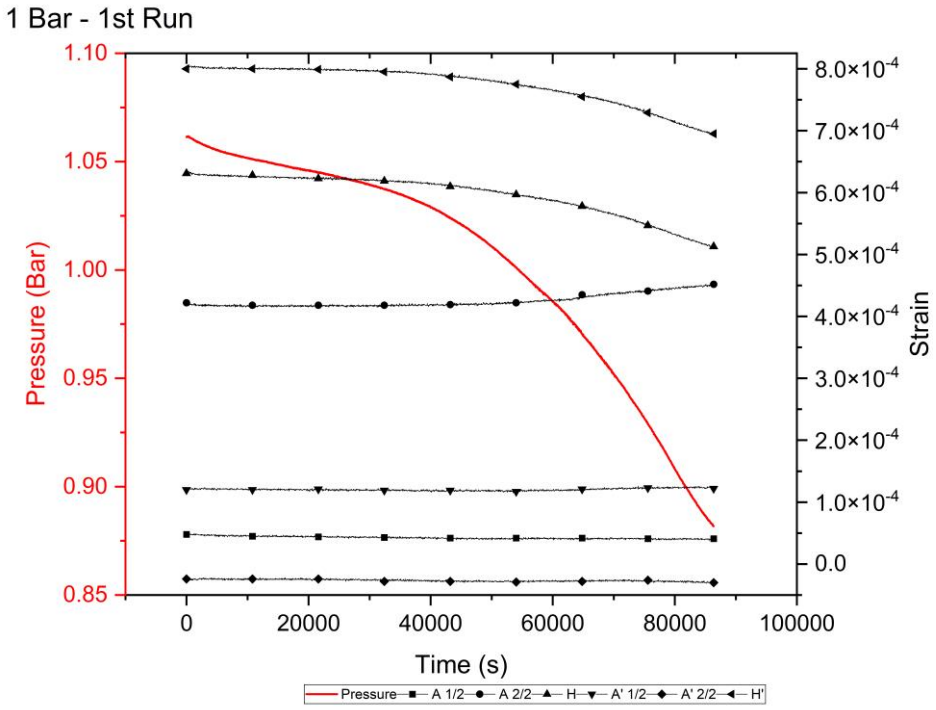

Figure 51. Pressure and strain response over time for the first run at 1 bar.

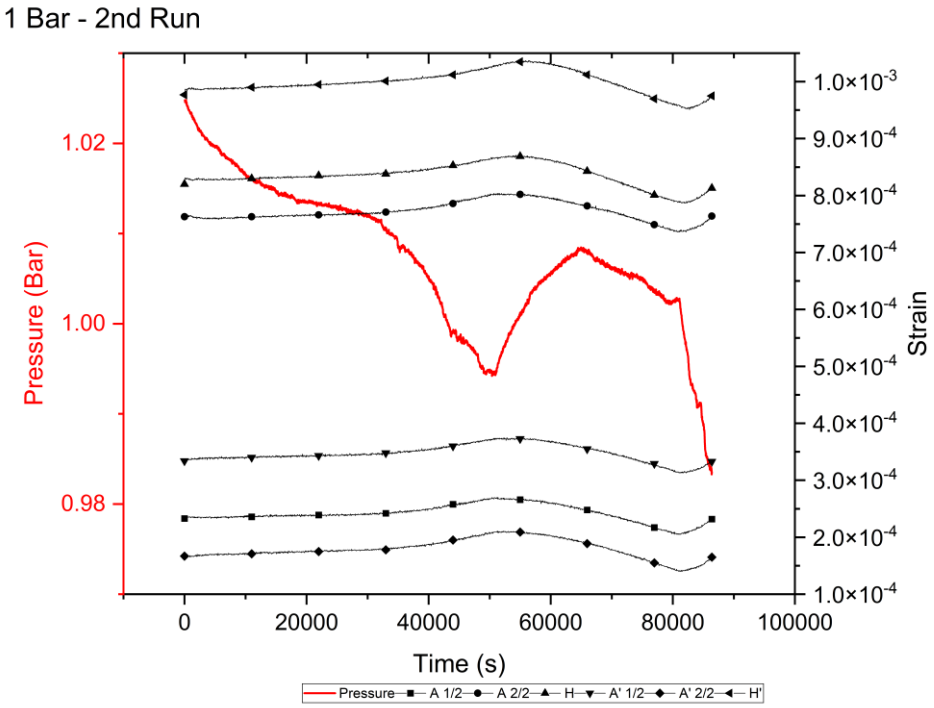

Figure 52. Pressure and strain response over time for the second run at 1 bar.

Once the vessel is pressurised to 1.5 bar the difference in strain from the first run to the second run starts to decrease for each location. In Figure 53 and Figure 54 the highest strains are always from the hoop gauges. For both runs there was a sharp decrease in pressure towards the end of the 24 hour cycles with an increase in strain. From this it can be assumed that there is some relaxation in the material's modulus creating further deformation.

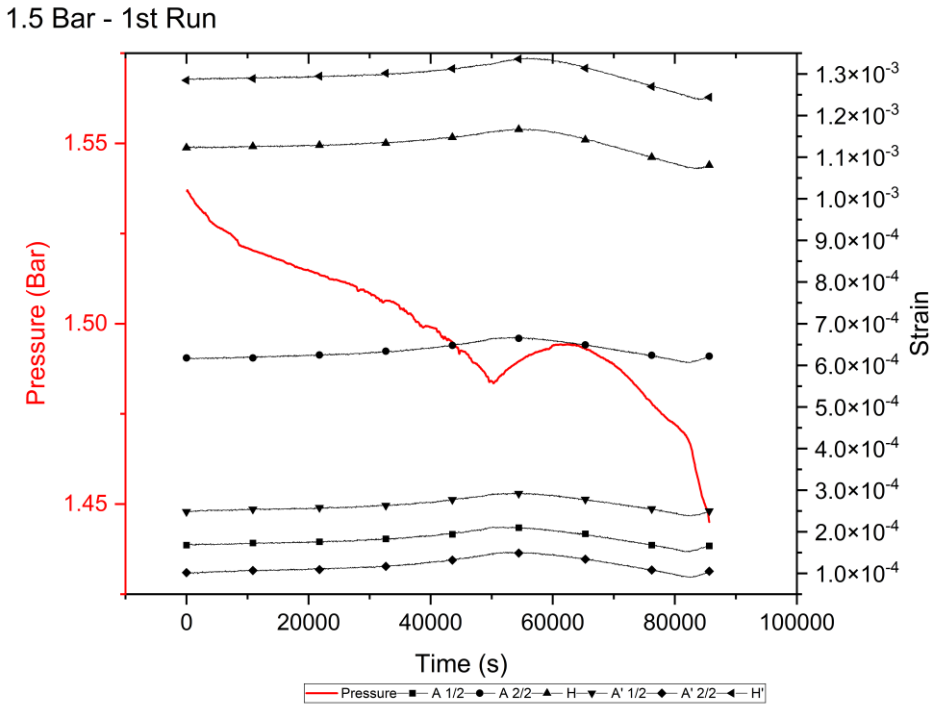

Figure 53. Pressure and strain response over time for the first run at 1.5 bar.

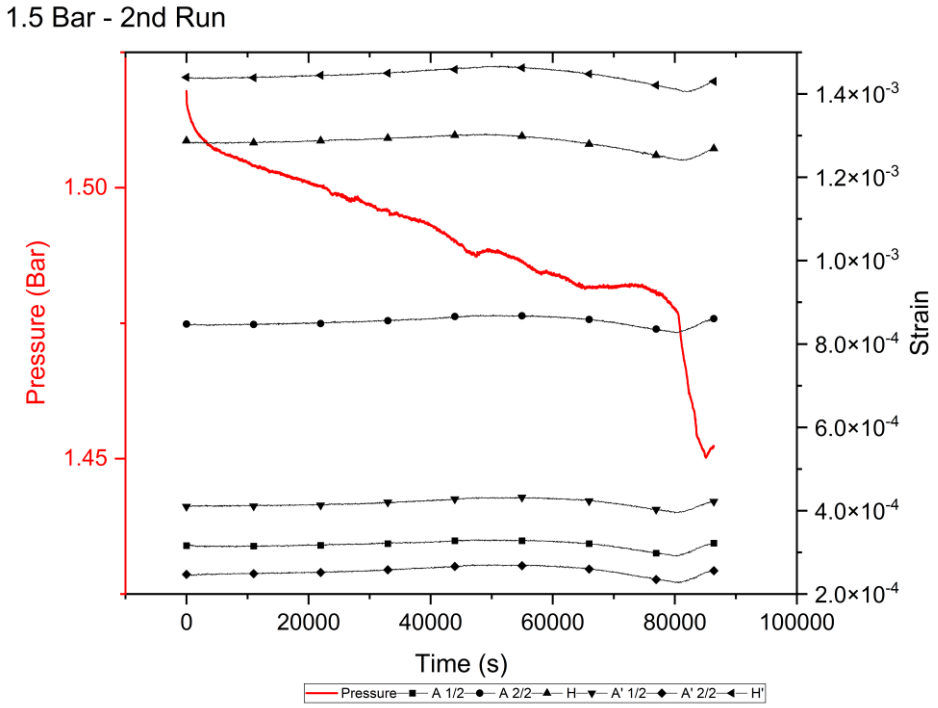

Figure 54. Pressure and strain response over time for the second run at 1.5 bar.

At 2 bar the strains have all increased with the difference between the strain in the hoop direction and that in the axial directions getting larger. Again, there is a dip in pressure towards the end with no apparent leaking from the vessel and some change in strain. Results for 2.5 bar, in Figure 57 and Figure 58, remain consistent with the 2 bar results.

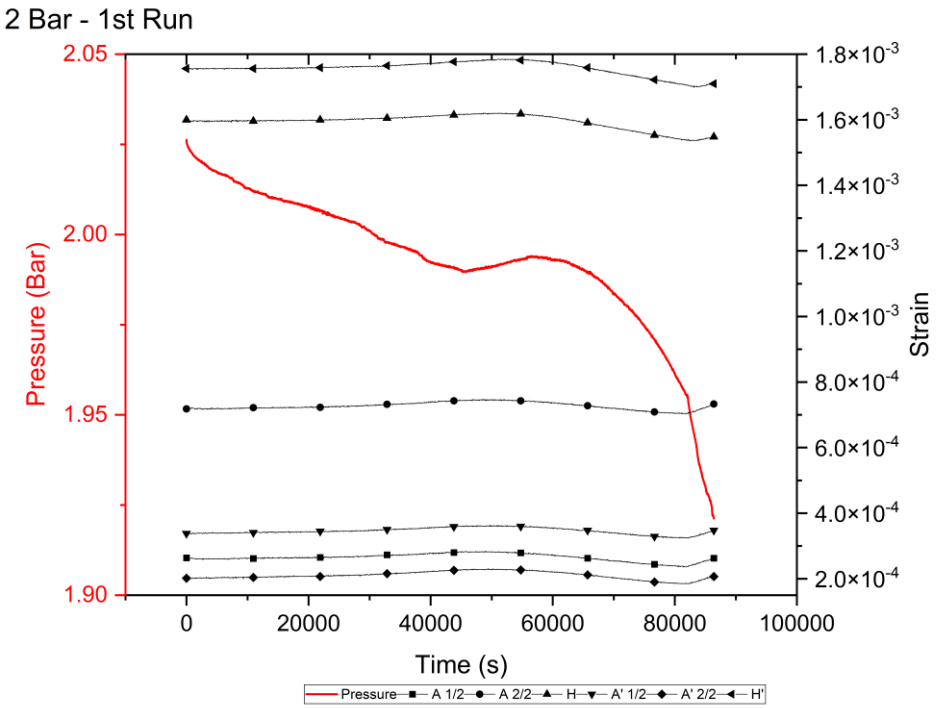

Figure 55. Pressure and strain response over time for the first run at 2 bar.

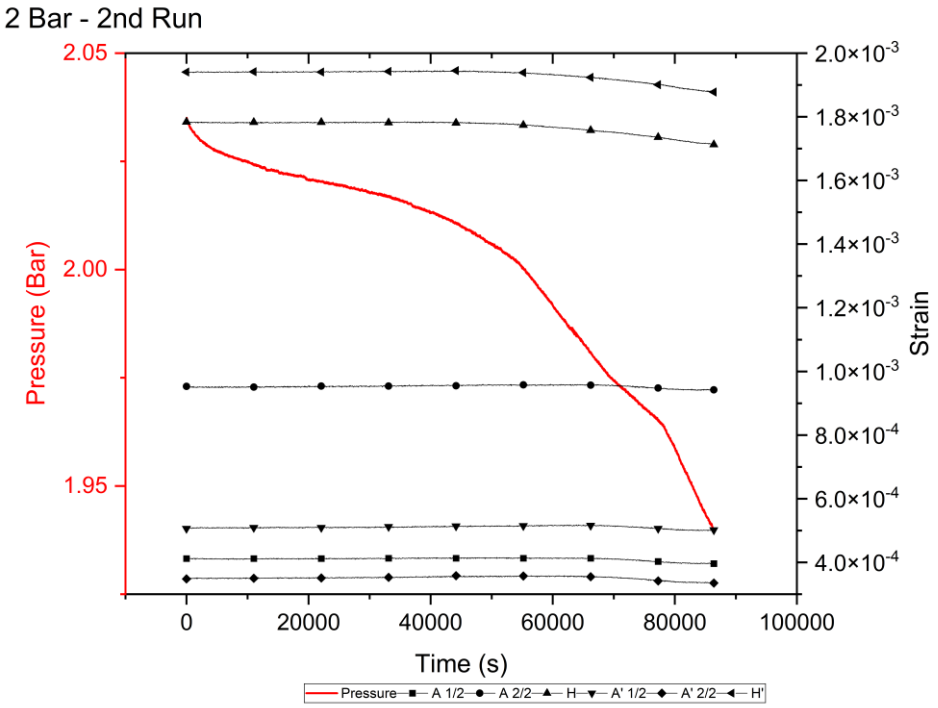

Figure 56. Pressure and strain response over time for the second run at 2 bar.

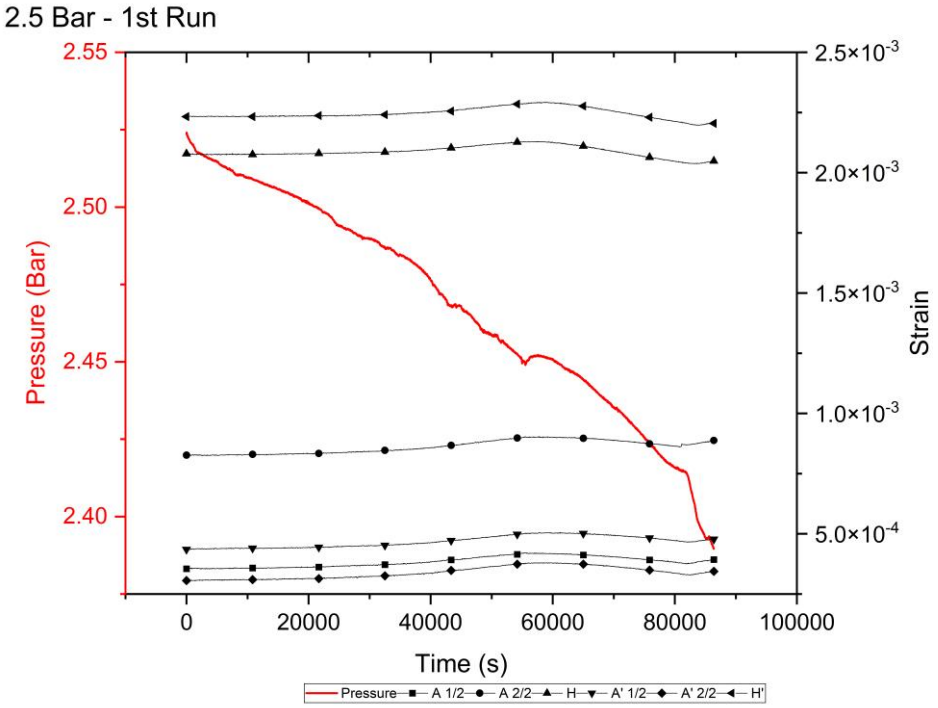

Figure 57. Pressure and strain response over time for the first run at 2.5 bar.

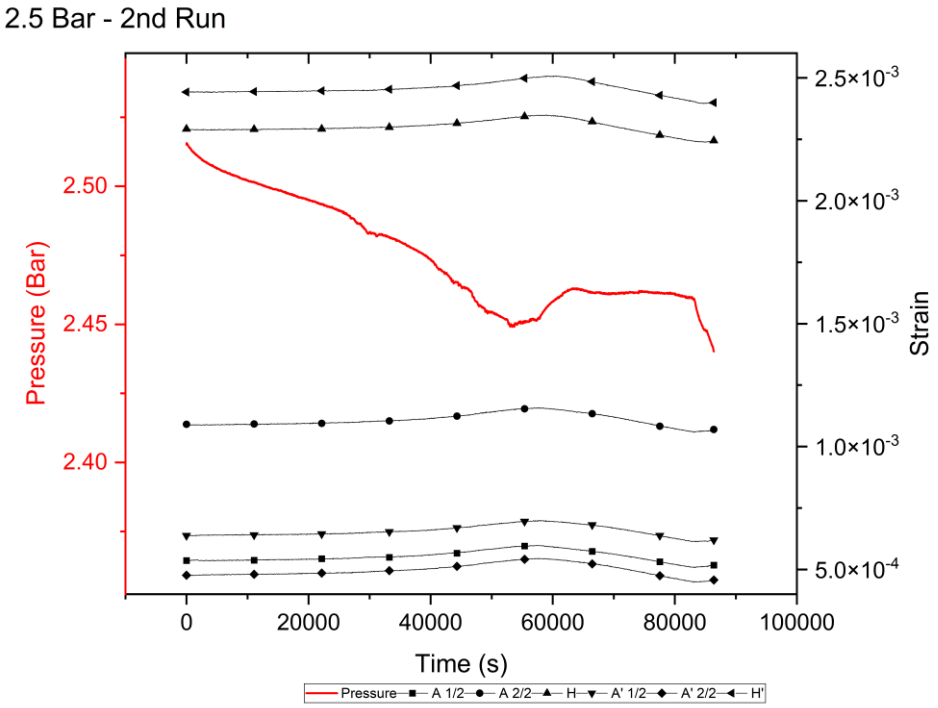

Figure 58. Pressure and strain response over time for the second run at 2.5 bar.

As 3 bar is the requirement for the certification of the hydrocyclone, these results are of the most importance. In Figure 59 and Figure 60, the strain remains very steady over the 24 hour period with a distinct difference in the hoop strain vs. axial strain. There is no visible failure of the vessel or apparatus. The vessel was able to successfully hold the 3 bar pressure for two separate 24 hour periods.

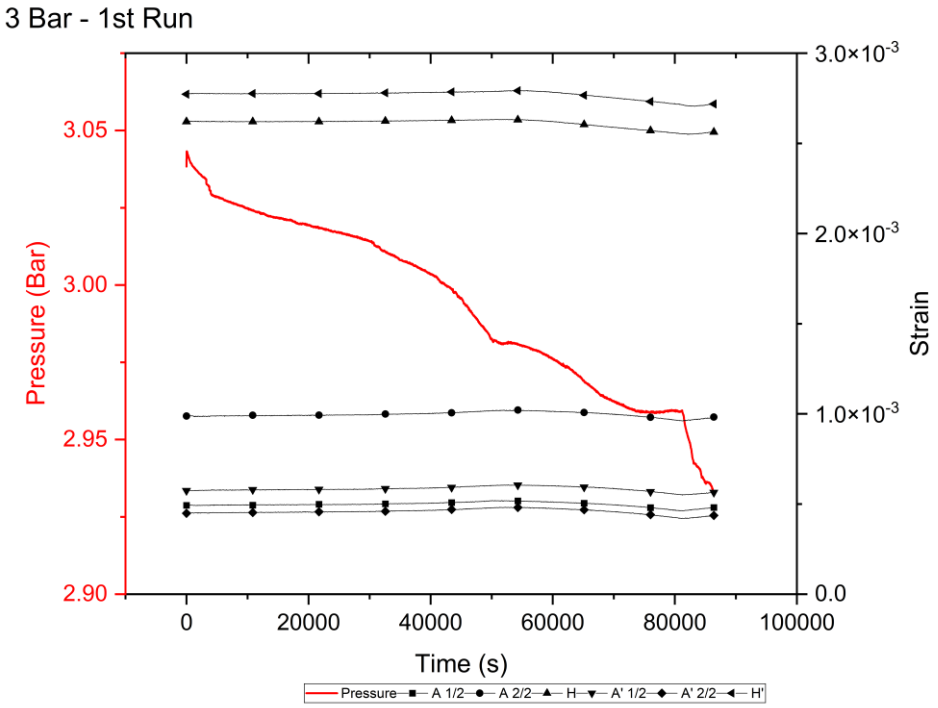

Figure 59. Pressure and strain response over time for the first run at 3 bar.

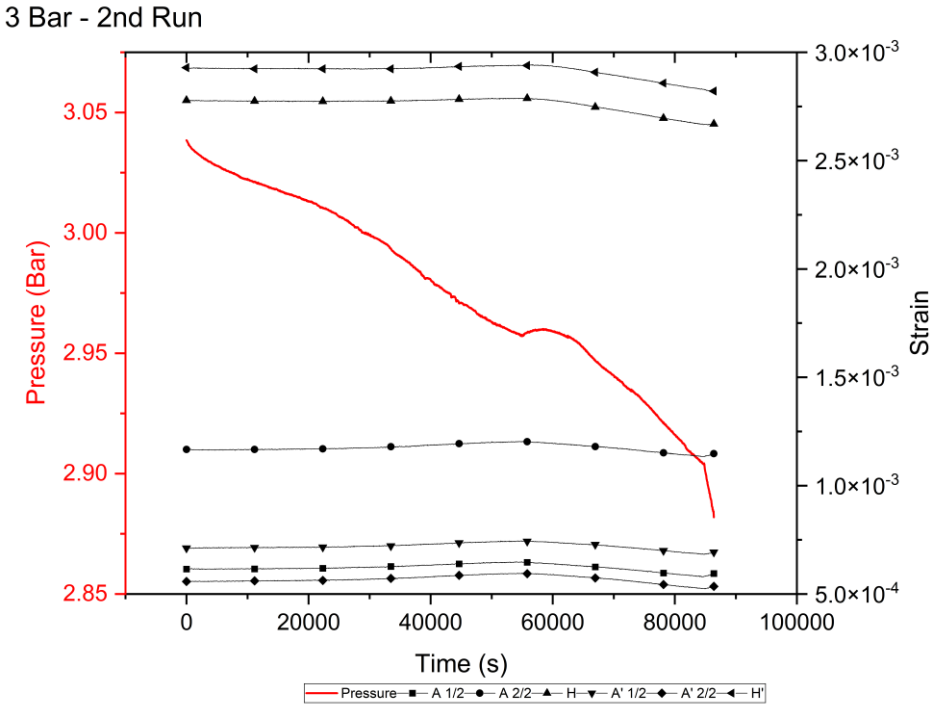

Figure 60. Pressure and strain response over time for the second run at 3 bar.

In Table 8, the highest strain values from both runs of the experiment are shown. In terms of strength and mechanical properties, the ABS is sufficient to hold the required 3 bar pressure for at least a 24 hour period. Comparing the results from the first run to the second run, there is an increase in strain in the latter. This is due to residual strain from previous pressurisation which is explored further in the following section.

Table 8. Measured strain from the 3 bar pressurisation experiments.

Strain	**1st Run**	**2nd Run**	**Percent increase**
A 1/2	0.05	0.06	20%
A 2/2	0.10	0.12	20%
H	0.26	0.28	8%
A 1/2’	0.06	0.07	17%
A 2/2’	0.04	0.06	50%
H’	0.28	0.29	4%

3.3.3 Creep response of the ABS pressure vessel

3.3.3.1 Creep during the 24 hour pressurisation tests

As seen in Section 3.3.2, there is non-linear behaviour in the material response with respect to time. At most pressures, there is a change in strain and pressure around 50,000 seconds (14 hours) into the test. In general, we see a rise in strain and a decrease in pressure followed by a decrease in strain and a rise in pressure. From the pressure hold tests, it is clear that the pressure drops over the duration, however there is no input into the system that would result in an increase in pressure.

Creep is a time-stress deformation response to a constant load which results in increasing strain due to the untangling of the chain-like molecules [96]. Simply, creep is the sum of the elastic instantaneous strain experienced by the material with the inelastic strain. Thus, it is dependent on the viscoelasticity of the material. Previous work found a universal viscoelastic model to be fairly accurate for ABS, however this does not consider the creep dependence on the parameters of 3D printing [94-98]. Creep is dependent on the entanglement between layers as it is a response at the

molecular level and literature has proven that the direction of the layers with respect to load influences the creep constants [95].

In a standard creep test, a constant tensile load will be applied to the specimen and the strain response would be recorded over time [99]. In the current study, the system is closed. There is no outside input during the 24 hour period, thus any load is resultant from the force of the water within the vessel. As an example, the data for 2.5 bar (2nd run) was chosen to examine this behaviour. The increase in strain with decrease in pressure followed by the inverse behaviour is shown in Figure 61.

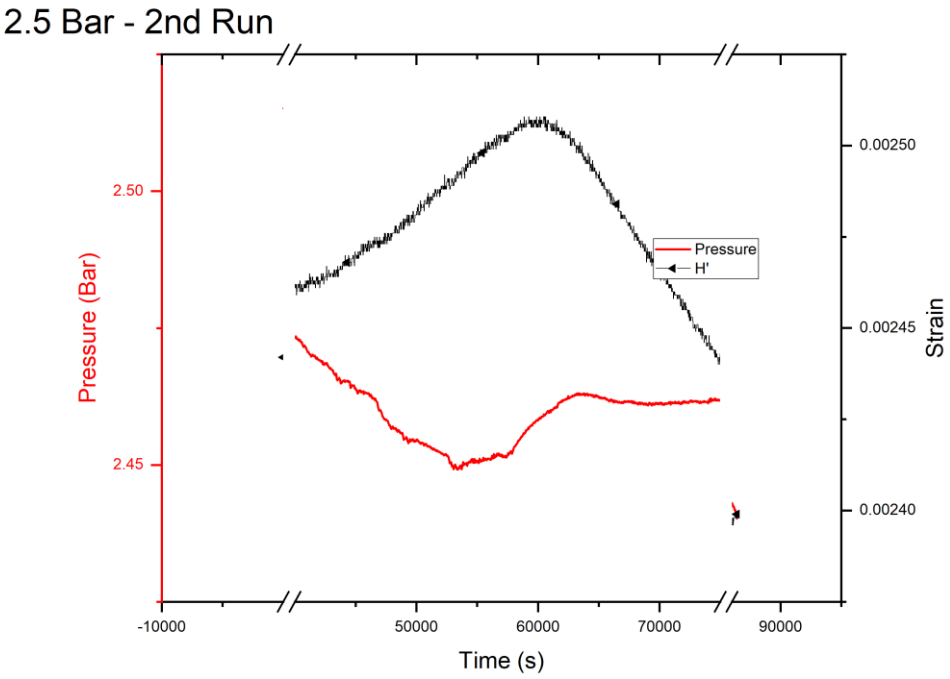

Figure 61. Area of strain rate change for 2.5 bar (2nd run).

Around 40,000 seconds the strain begins to increase indicative of creep behaviour. However, unlike previous studies and expectations [93, 98], the strain reaches a critical point at which the rate decreases before stabilising again. Inversely, the pressure drops in response to the change in dimension then begins to increase before resuming a steady state. Theoretically it is known that the stress in a pressure vessel is proportional

to the pressure applied as well as the radius and thickness of the vessel [77]. If the assumption is made that the stress response of the material is remaining constant and creep is occurring, it is expected that the percent change of the strain from the onset of the creep to the peak as well as the percent change of the pressure from the onset to the inverse peak to be similar. For 2.5 bar (2nd run) this is calculated to be 1.9% for the strain and 1% for the pressure.

In order to examine this over time, first derivative of a polynomial fit for the pressure and strain curve was calculated. Figure 62 and Figure 63 show the region selected as well as the polynomial fit with 30 decimal places used in order to calculate an accurate derivative. The first derivative with respect to time for each is shown in Figure 64.

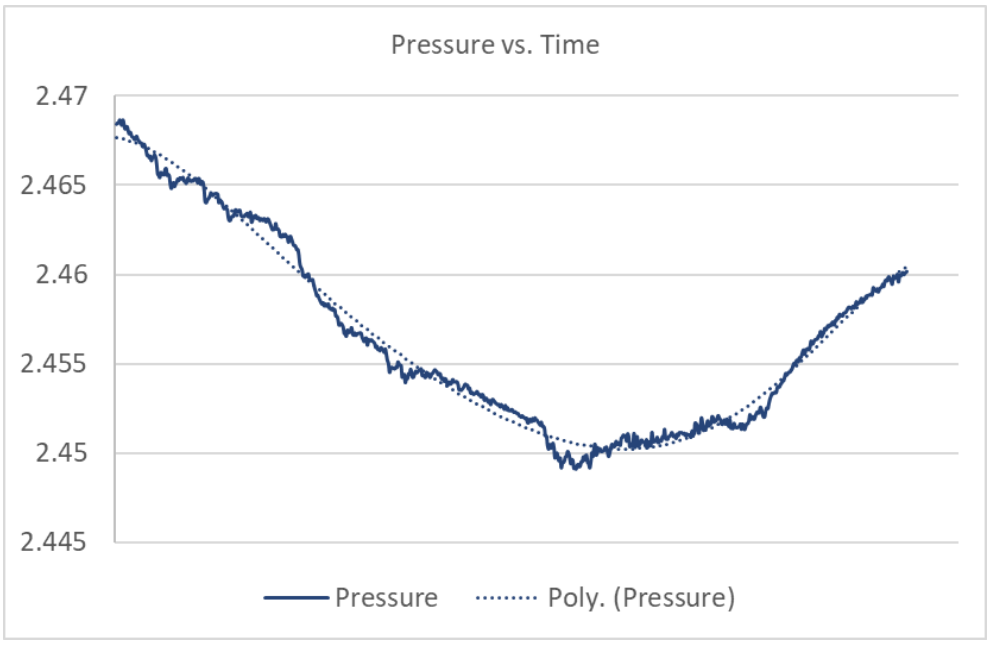

Figure 62. Pressure in creep region with polynomial fit showing decimal place used to calculate the first derivative.

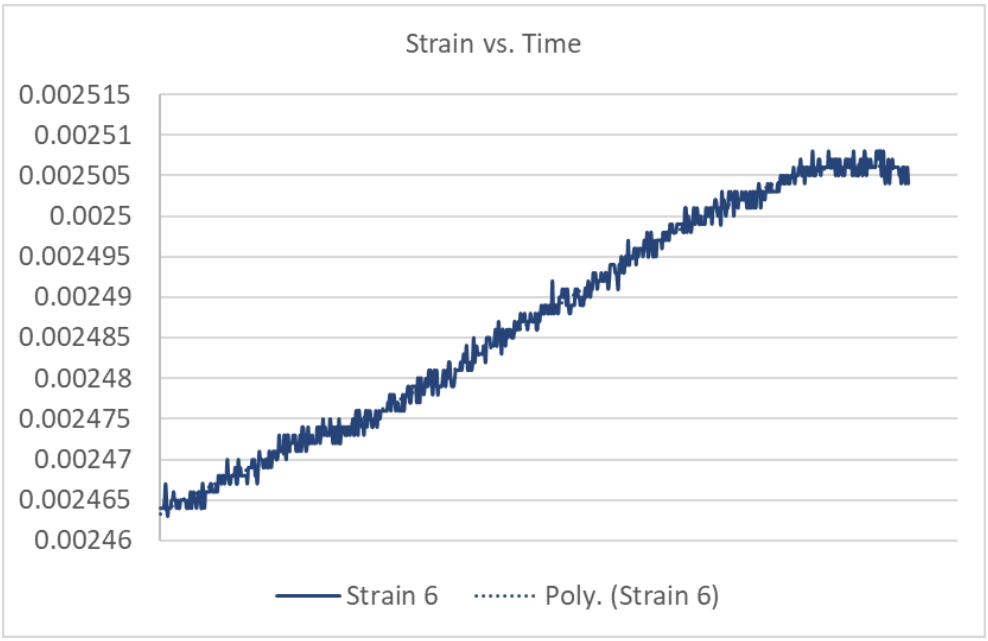

Figure 63. Strain in creep region with polynomial fit showing decimal place used to calculate the first derivative.

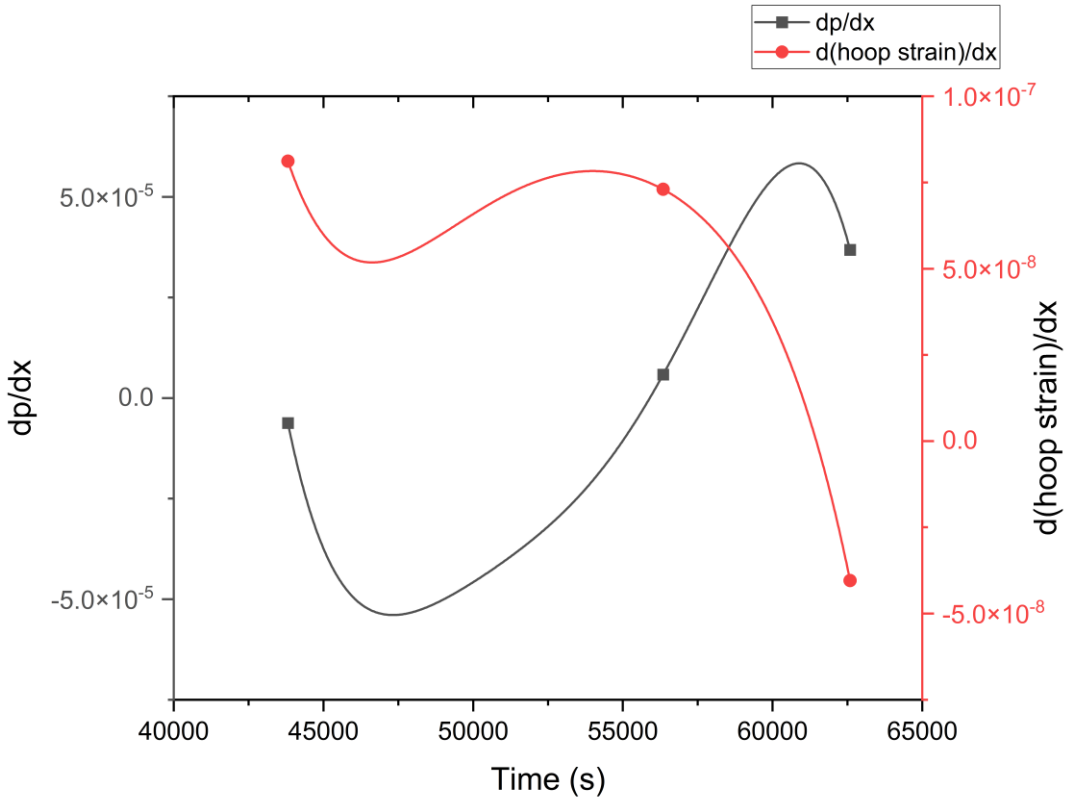

Figure 64. Rate of change of pressure and strain with respect to time during the creep region of the 2.5 bar (2nd run) test.

From the plot of the rate of change of the pressure and strain with respect to time, the rates follow a similar trend until about 52,500 seconds in which the pressure rate continues to increase while the strain rate starts to drop. At roughly the peak strain value seen in Figure 61, there is an intersection of the rates of change. After approximately 60,000 seconds, both rates continue to decrease. Because this is a closed system, it is expected that these lines will intersect as the system attempts to achieve equilibrium.

Looking at the entire 24 hour test and all strain gauges for 2.5 bar (2nd run) in Figure 65, from just after 60,000 seconds there is a stabilisation. Towards the end of the test, there is the beginning of a further creep event with a slight uptake in the strain visible and a decrease in pressure. Creep data in literature shows there is fluctuation in the strain over time creating peaks at different intervals before eventual failure [93]. Considering this in addition to the interaction of the closed system as described above, it can be expected that there will be multiple creep events before the failure of the pressure vessel if the test were to continue.

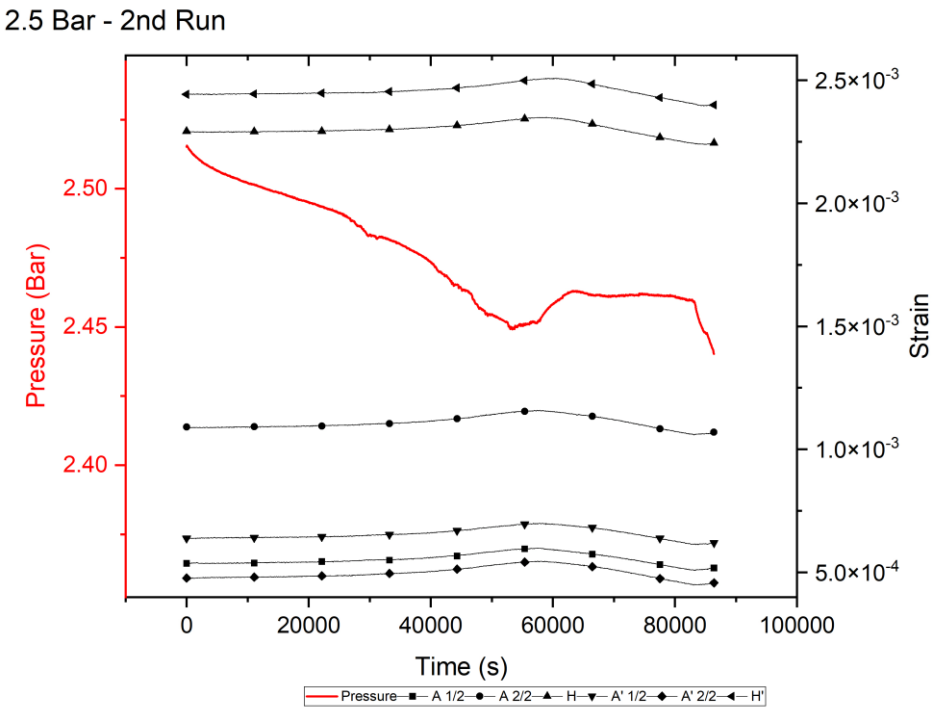

Figure 65. All strain measurements and pressure for 2.5 bar (2nd run) versus time.

3.3.3.2 Creep due to constant hydrostatic loading for 160 hours

Section 3.3.3.1 discussed the relation of creep to the induced pressure loading, however there will be a constant load due to the hydrostatic force of the water within the vessel. As an exercise in understanding the viscoelastic response of the vessel in an open system, the pressure was released, and the vessel was left with water inside for an extended period of time. The internal volume of the vessel is 6353 cm^3 which means there is 6.35 kg of water within the vessel. This corresponds to a hydrostatic pressure of 105 kPa acting on the domed end. The strain over time is shown in Figure 66 and the strain rate of the highest location (A2/2) is shown in Figure 67.

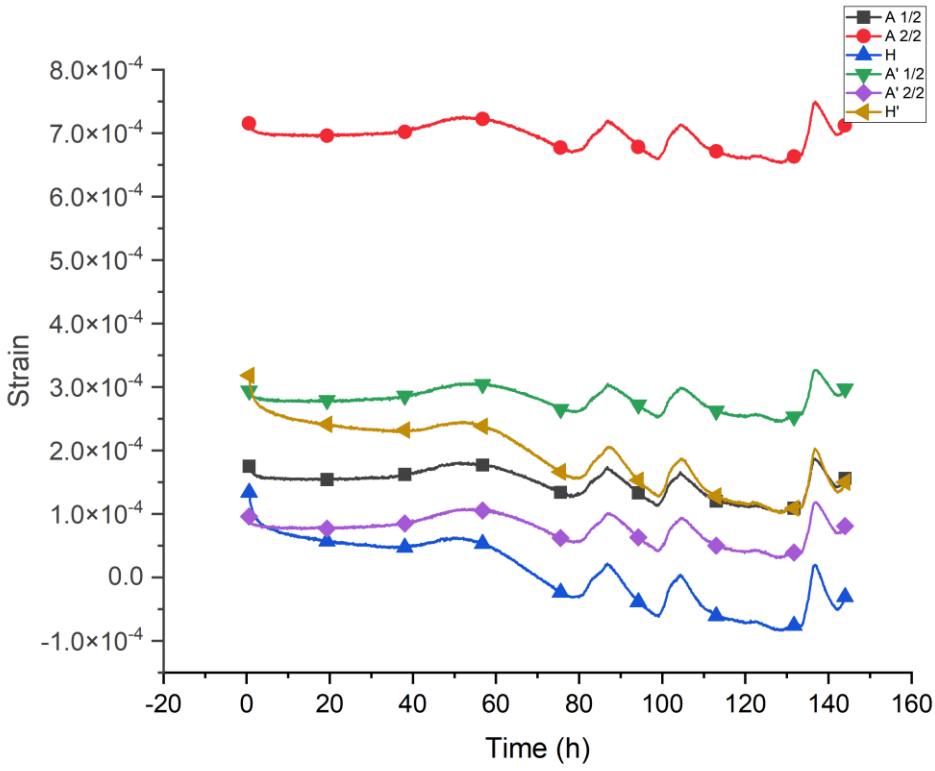

Figure 66. Long term strain for the ABS pressure vessel under a constant hydrostatic load of 105 kPa.

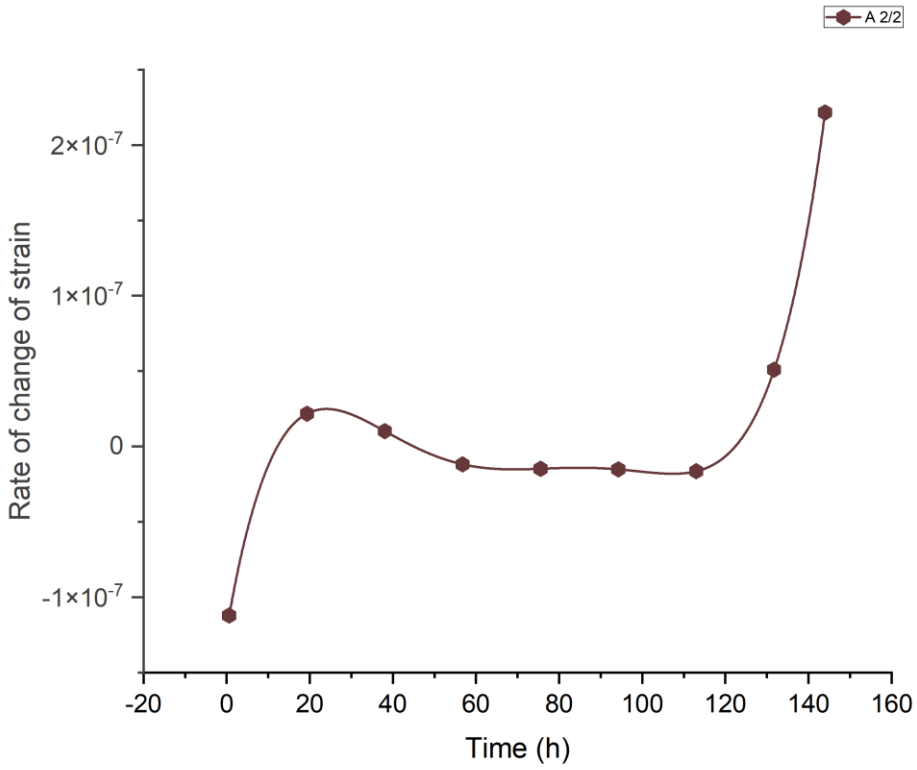

Figure 67. Strain rate of A 2/2 over the 6 day hydrostatic pressure test.

As seen in the study of longer term strain of PC-ABS (a polycarbonate blend of ABS), there are many peaks and troughs in the strain as creep occurs [93]. The strain appears to be changing at approximately the same rate for all locations. As this force is acting in the direction of gravity, it would be anticipated that the highest strain would be experienced at an axially oriented strain gauge. This is seen with the highest strain being at location A2/2. This curve was chosen to view the strain rate. A polynomial fit of the 6^{th} degree with an R^2 value of 0.51 of the strain curve was derived to obtain Figure 67.

From 0 to 20 hours the rate is increasing from the initial negative rates experienced by the recovery after the release of the 3 bar pressure. The rate remains steady until about 120 hours when there is a large increase. However, it must be considered that the polynomial fit was not an accurate representation of the multiple peaks that occurred

from 80 hours onwards. This demonstrates a general trend of the strain increasing over time but does not account for the multiple creep events taking place. After the 6 days, the part did not fail nor show any signs of visible elongation, as expected by the small values shown in Figure 66. Further work is necessary to understand this viscoelastic behaviour and the interaction between the hydrostatic force and pressurisation strains.

3.4 Failure of the pressure vessel

While the experimental study of the pressure vessel up to 3 bar provided insight into the mechanical behaviour of the additively manufactured ABS, the failure mechanism was not explored as failure did not occur within this pressure range. In order to determine the load at which failure occurs and how, a destructive test of the vessel was planned. This test took place at the industrial sponsor's site in Todmorden, UK in Figure 68.

Figure 68. Testing area at Weir Minerals, Todmorden, UK

3.4.1 Apparatus and methodology

The physical geometry of the cylinder and associated bulkhead did not change for this test. Two of the three ¼ BSP threaded holes in the bulkhead were plugged and the third

was used to connect to a pneumatic pressurisation system. The parts were assembled and placed into a steel cylinder for safety.

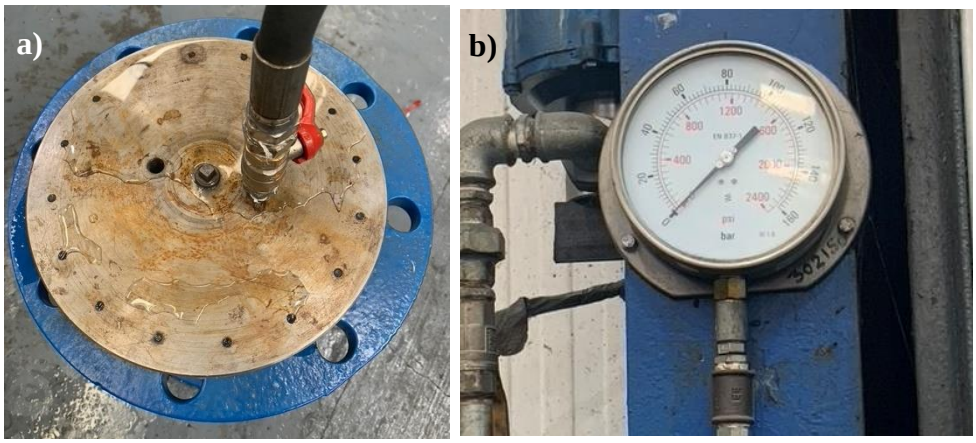

Figure 69. a) Bulkhead of ABS cylinder after filled with water prior to pressure testing to failure; b) Gauge used to determine pressure in vessel.

The mainline of the pneumatic system was water at a pressure of 6 bar. Once the cylinder was filled with water at ambient pressure, the part was pressurised in 1 bar increments. At each increment the pressure was held for one minute to ensure it was stabilised. For pressures above 6 bar, the pneumatic system used compressed air to raise the pressure. The initial pressure was 3 bar. This set up can be seen in Figure 69.

Upon first run of the test leaking was found at the connection between the flanges and the bulkhead when pressurised to 3 bar. The pressure was released, and all bolts were tightened. The second run resulted in no leaks until it reached 6 bar, at which point there was an immediate drop in pressure. Visible leaks between the flanges and at the bolt holes were apparent. Per ASTM D1599 for hydraulic pressurisation of plastic pipes, leakage at the end enclosure is considered an invalid test and not a failure of the vessel [89]. Pressure was released and the parts were dissembled. A liquid rubber (see Figure 70) was applied between the ABS flange, gasket paper and bulkhead in a ring. The part was then resealed, and the liquid rubber filled the gap between the flanges.

Figure 70. Application of liquid rubber to aid in sealing ABS cylinder for pressure testing.

Testing resumed from 6 bar and the pressure was still dropping. It was then apparent that there was a leak from one of the plugs. This was tightened and no further leaks were found. Pressurisation continued in one bar increments until failure.

3.4.2 Results and discussion

Failure of the ABS cylinder was anticipated to be around 12 bar and occur between 45 and 50 mm from the flange per the FEA. Figure 71 shows the stress contour when 12 bar is applied to the inside surface of the cylinder. The red area about 50 mm from the flange shows the highest stress which has reached 31 MPa approximately. The ultimate interlaminar tensile strength for ABS is 26.8 MPa.

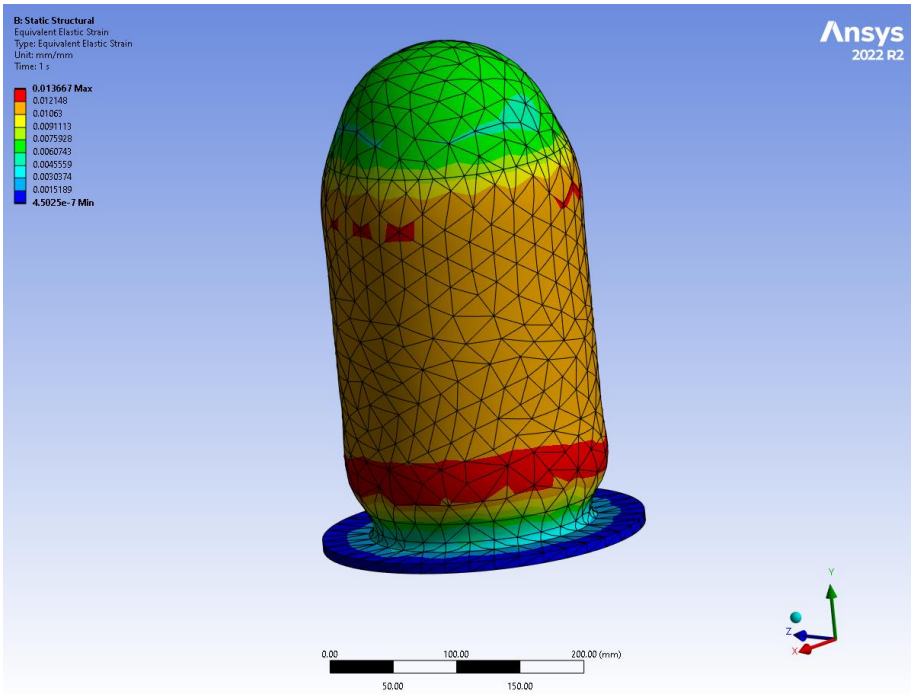

Figure 71. FEA for failure of ABS cylinder.

During the experiment the vessel burst at a pressure of 11 bar. Failure is seen along the seam where each layer that creates the height of the cylinder meets in Figure 72. This was a weak point on the vessel due to the connection point of the contours and failure was anticipated to be at the interface of printed material due to its lower mechanical strength.

Figure 72. ABS cylinder crack along axis.

The initial location of failure can be observed better from the inside of the cylinder. Point A in Figure 73 shows what has been interpreted as the point of initial failure at the interface of layers. The crack then propagates towards the seam and continues to the flange. The flange was supported by the steel bulkhead and clamping ring; therefore, the crack does not propagate further. In the opposite direction the crack continues down the length of the cylinder and dome. Because the vessel was kept in a steel drum for safety, this cannot be verified. It is recommended for future tests to have a testing apparatus that allows for visual detection of failure.

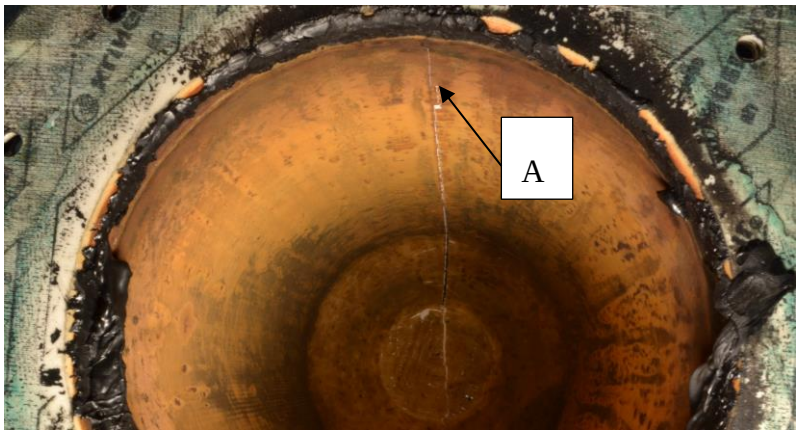

Figure 73. Entire crack in ABS cylinder as seen from the inside.

A closer look at the point of failure better shows the phenomenon described. The scale in the photo starts approximately 10 mm from the edge of the flange, showing that the point of failure is at approximately 45 mm from the flange.

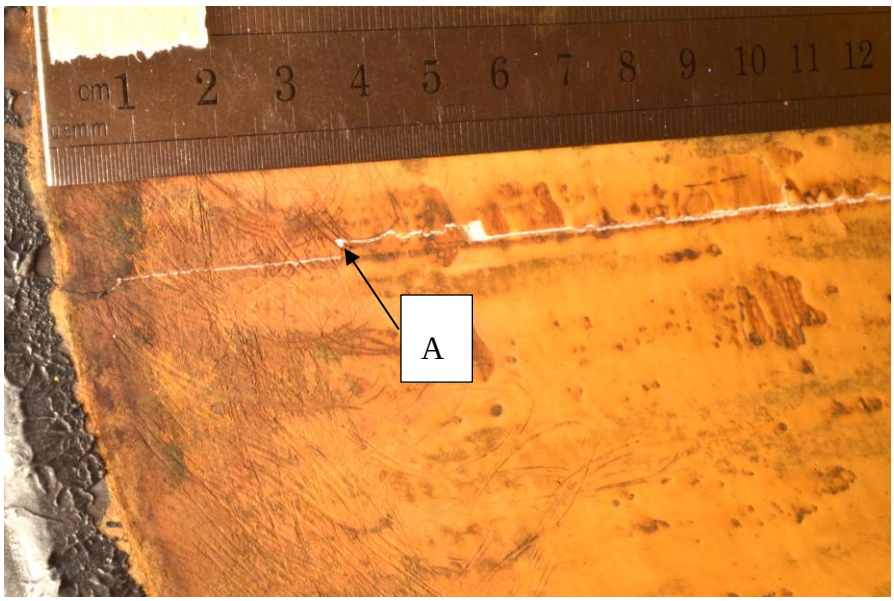

Figure 74. Close up of point of failure and crack propagation in ABS cylinder.

Examination of the damage from the outside of the cylinder, in Figure 75, shows regions of failure where material has cracked and flaked off the cylinder. This is similar to stepped failure seen in previous studies of the failure of 3D printed ABS [70]. ABS is a rubber-modified amorphous polymer, and thus the failure mechanisms will be driven by the amount of the rubbery phase of butadiene present in the material [66, 100]. Due to the material colour, it is difficult to see the crazes (plastic deformation) that occurs which would result in a lighter coloured area. It has been found that ABS experiences this type of fatigue striation and crack growth during failure [101]. Overall, the failure exhibited was considered to be predictable after consideration of the known behaviour of additively manufactured materials. However, it is known that defects in the material due to the printing process have an impact on the fracture strain so this would need to be accounted for in the future [102].

Figure 75. Image of brittle failure on the outside of the ABS cylinder.

3.5 Conclusions

Initial analysis work was performed in order to understand the behaviour of the existing 150 CVD hydrocyclone under hydraulic loading and 3 bar pressurisation with the absence of a rubber liner using the existing DMC material. This informed a study on the performed of AM materials for pressurisation to 3 bar and to failure. The significant findings are:

1. For hydraulic loading, the structural requirements of the 150 CVD casing are very low. For 3 bar pressurisation there are some locations of stress concentrations, however the majority of the structure exhibits lower stress.

2. The design of the 150 CVD analysed was initially for welded steel sheets, therefore there are areas of stress concentrations that could be optimised for a design that was tailored to additive manufacturing.

3. ABS is a suitable material for the structural requirements of the 150 CVD hydrocyclone. After 3 bar pressurisation and pressurisation to failure it exhibited adequate strength and did not fail until 11 bar (almost 4 times the requirement of the 150 CVD).

4. Catastrophic failure can be anticipated to occur at locations where deposited material rasters meet, as shown in Section 3.4 where the crack propagated along the length at the intersection of each circumferentially deposited raster.

5. If ABS or a similar thermoplastic are to be used for the 150 CVD, design work in order to eliminate stress concentrations and create more robust thicknesses where needed is required.

6. ABS exhibits creep behaviour. The response of the material is dependent not only on the conditions of the loading, but also time. In a closed system, this will create feedback between the expansion of the vessel and the pressure within. The data shows that the system will attempt to achieve equilibrium, however it is anticipated that eventually the material will fail. After 6 days with only hydrostatic force applied, there were further creep events however the material did not fail or show significant signs of elongation or dilation.

Currently, the 150 CVD design includes a rubber liner for wear resistance. In order to fully assess the feasibility of an entirely additively manufactured hydrocyclone, a fundamental study of the erosion resistance of FDM materials was needed. Chapters 4-6 cover the background, methodology and assessment of the erosion behaviour of additively manufactured polymers and polymer composites relevant to the hydrocyclone.

4. Literature review of wear of polymer and polymer composites

4.1 Introduction

Processing technology, such as the 150 CVD hydrocyclone, often uses a slurry for the transportation of solids. A slurry can be defined as a liquid with suspended solids of varying size that have a specific gravity greater than 1 [103]. The effect of wear due to solid particle erosion is a topic of great interest due to the potential cost of replacing these parts [104].

Predicting the rate of material removal from solid particle erosion does not have a general solution due to the wide range of properties of commercially available materials [105]. There are many variables that affect the erosion of a material. The main categories are properties of the target material, erodent properties and experimental conditions [106]. The target material is affected by composition, microstructure, reinforcement and respective interface, mechanical properties, fibre orientation and surface roughness. The erodent can vary in shape, size, hardness, type, the rate at which it is fed and the temperature. The experimental conditions, such as angle of impingement, impact velocity, temperature, particle flux and erosion media can be varied.

For fibre reinforced composites there are three processes that the material undergoes during erosion [107]:

- Removal of material in resin rich zones.
- Erosion of fibre zones associated with the breaking down of fibres into small fragments.
- Erosion of the interface zones between the fibres and the adjacent matrix.

Neat polymers are known to undergo some degree of brittle failure for mineral processing applications [108]. Sharp abrasives, such as angular sand, prove to have higher erosive properties than rounded erodent [109]. This chapter will provide an

overview of literature to support the study of FDM polymers and polymer composites for equipment subjected to erosion. Additionally, a study of the current state of the art for wear of 3D printed polymers and polymer composites has been conducted to provide context for the novelty of this area of study.

4.2 Erosion of traditionally manufactured polymers and polymer composites

4.2.1 Background on erosion testing

Ian Finnie is considered one of the pioneers of the study of erosion of materials. His 1960 publication 'Erosion of surfaces by solid particles' [110] provides a foundation for understanding the mechanisms of wear for ductile and brittle materials. This describes the cutting and displaced material expected with a ductile response contrarily to the network of interlinking cracks that lead to failure for brittle materials.

The design of a jet impingement slurry erosion test rig was studied by Zu et al. with varying test parameters (impact velocity, solid particle concentration and impact angle) [111]. A schematic of the rig is shown in Figure 76. The particles used in the slurry were rounded silica sand with two ranges of diameters: 425-600 μm and 600-1000 μm. The specimen tested were rectangular and made of aluminium, copper, mild steel, and alumina. The study concludes that use of this rig resulted in reliable test results over extensive periods of continuous experimentation.

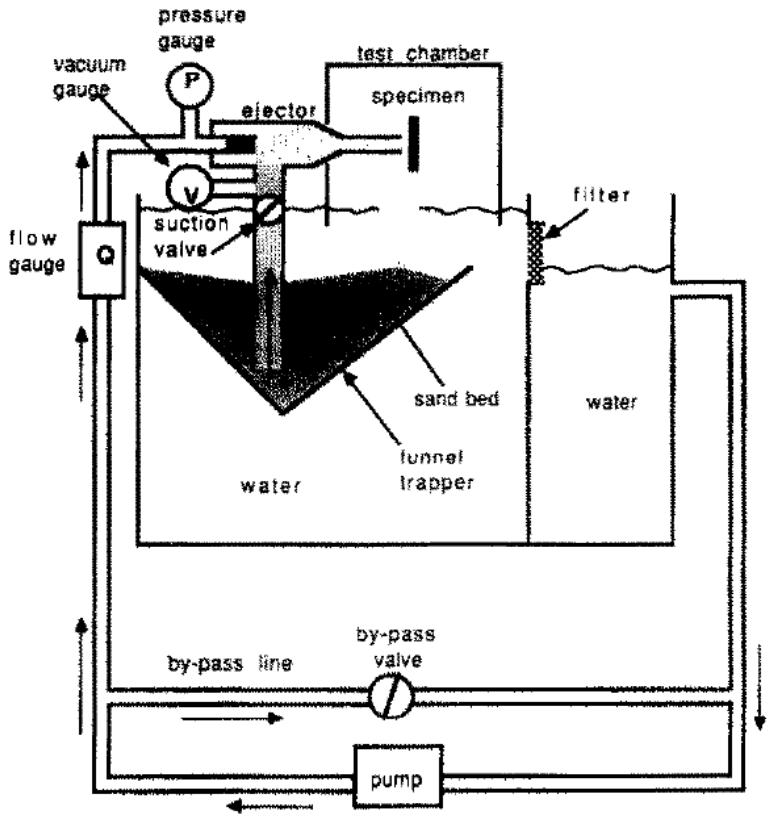

Figure 76. Schematic of slurry erosion test apparatus [111].

The effects of erodent recycling in solid particle erosion testing was investigated by Sparks et al. [112]. As particles circulate in a testing apparatus (e.g. in a rig similar to that studied by Zu et al. [111]) the particles will experience rounding or fracture into multiple particles. Over the duration of the test this will result in varying conditions. Sparks et al. set out to examine these changes due to impact with one another and a glass-ceramic target material via air-blast erosion. The erodent materials were soda-lime glass spheres and silica sand, both sieved to 125-150 μm. Experiments were carried out at velocities of 44 m/s and 89 m/s with impact angles of 30° and 90°. Images of the particles after cycles of impact are shown in Figure 77 and Figure 78. The study concluded that extensive fragmentation was observed for both types of erodent for a velocity of 89-98 m/s at normal impact angle however, at lower velocity (44 m/s) and 30° impact angle no fragmentation was observed and therefore no change in erosion

rate with recycled particles was found. Where fragmentation is present, progressive changes in erosion rates were found.

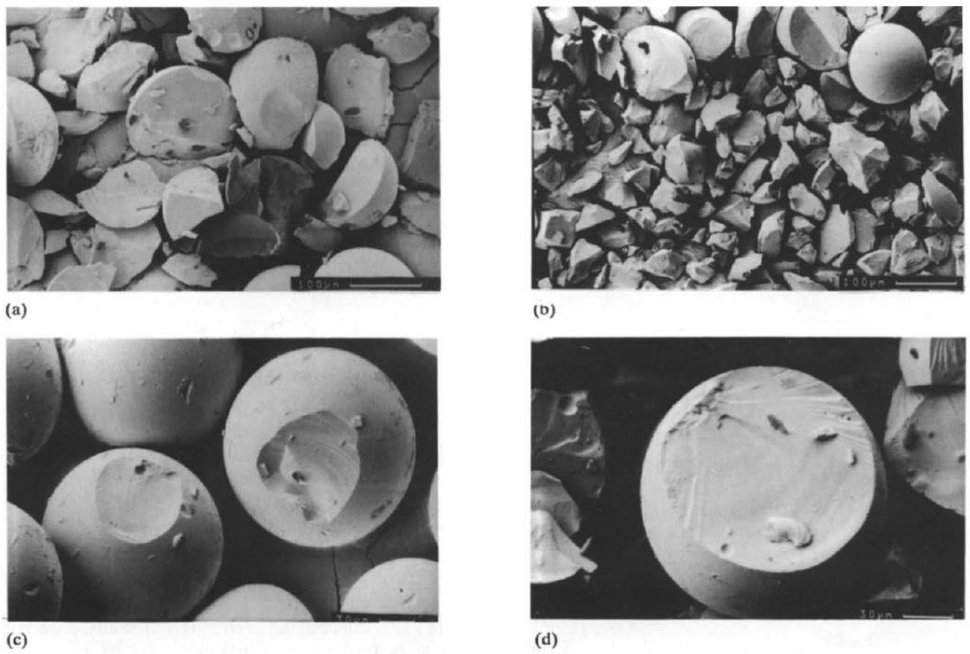

Figure 77. SEM images of soda-lime spheres after impact at 89 m/s (a) after 5 cycles, (b) after 10 cycles. (c) a typical cap fracture and (d) a split particle [112].

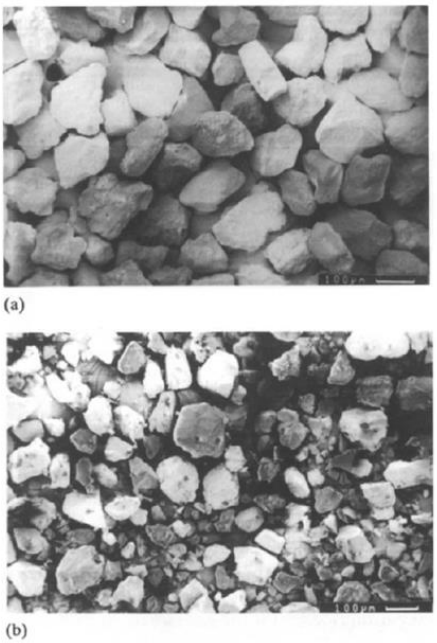

Figure 78. SEM images of silica sand after impact for (a) 5 cycles at 44 m/s at 30 ° and (b) 5 cycles at 98 m/s at 90 ° [112].

One of the determining factors in erosion rates is the size of the particle as explored by Stack et al. [113]. Alumina and silicon carbide particles ranging from 250-1000 μm were used in a rig similar to Zu et al. [111]. Circular disc specimens made of iron, aluminium, stainless steel, alumina, and Teflon were tested with a slurry at a temperature of 25°C and impact angles ranging from 22.5°-90°. The study found that at the peak erosion rate, particle size varied as a function of the velocity and shape as well as with the material properties of the specimens and flow environment. Larger particle size results in a greater maximum erosion depth, however smaller particles result in more widespread damage over the surface of the specimen. For the polymer, Teflon, the peak in erosion rate was found at smaller particle sizes than the metallic samples when eroded by alumina. It was concluded that this was due to impacts causing plastic deformation and a lower coefficient of restitution for the material.

Aquaro and Fontani [106] investigated the fundamental mechanisms of solid particle erosion for brittle and ductile materials. After reviewing existing theories and models of erosion, experiments using gas jets for impingement were conducted to reproduce results from the theories the authors deemed most valuable. The authors state that although erosion is a complex phenomenon, a simplified approach results in three main variables that effect erosion: impingement variables that describe particle flow, particle variables and material variables. Velocity, angle of impact and particle concentration make up the particle flow variables. Shape, density, and size are the particle variables. Mechanical properties, hardening behaviour, hardness, toughness, and microstructure form the material variables. For ductile mode the Bitter model was examined. This model hypothesises that material is lost via plastic deformation and cutting. Using Hertzian theory for pressure distribution as a starting point, brittle erosion was concluded to be due to the formation of cracks which form when a critical hydrodynamic tensile stress is reached. The authors developed an approach to predict erosion based on the finite element method and found that the influencing factors were mechanical properties as a function of temperature.

Wensink and Elwenspoek [114] explored the ductile-brittle transition in soda lime glass, Pyrex glass and crystalline (100) silicon (all brittle materials) when exposed to

solid particle erosion. As discussed in previous studies [106, 110, 113], brittle erosion occurs via crack formation and is most prevalent at normal impact angle (90°) while ductile behaviour results in cutting and ploughing of material with maximum erosion at oblique angles (usually 30°). For these three brittle materials, erosion rates and failure mechanisms were studied with 45° and 90° impact angle and two different kinetic energies of the particles (6×10^{-10} and 6×10^{-7} J). Alumina particles of size 3-29.2 μm at speeds of 75 and 200 m/s were used as the erodent. The study found that an 'erosion classification value' (E_{cv}) could be calculated as the ratio of the erosion rate at 45° and 90°. When $E_{cv} \approx 45$ brittle erosion is present, while $E_{cv} > 1$ represents ductile erosion.

$$E \propto (\sin(\theta)\, v)^k \tag{4-1}$$

Where 'E' is erosion rate, 'θ' is the impact angle, 'v' is the particle velocity and 'k' is the velocity exponent.

$$E_{CV} = \frac{E_{45^\circ}}{E_{90^\circ}} \approx (0.707)^k \tag{4-2}$$

The derivation above results in the erosion being dependent on only the kinetic energy. A larger kinetic energy exponent will result in a decreasing E_{CV} and therefore more brittle behaviour.

4.2.2 Solid particle erosion of polymers

Friedrich et al. [115] studied the erosive wear of polymer surfaces by steel balls at 57 m/s in an air blast rig. The target material was soft polymers (polyethylene, polypropylene, polybutene-1) and brittle polymers (polystyrene). It is known that ductile polymers have high dependence on the angle of erosion similar to ductile metals [116] with wear rates peaking at 30° impact angle. Brittle materials experience highest wear rates at normal impact however [117]. In the experiment conducted by Friedrich et al. [115], the softer polymers exhibited an incubation period before the erosion rate (reduction in thickness per testing time) stabilised while the brittle polymer has no incubation and the highest erosion rate. This is influenced by morphology of the semi-crystallinity, finding that spherulitic microstructure wears faster when coarse versus fine. Additionally, decreasing testing temperature will result in increased wear rates. A schematic of this can be seen in Figure 79. A brittleness index is useful in predicting erosion resistance of polymers. Increase in hardness (H) of the target material signifies more brittle behaviour while an increase in fracture energy (G_{lc}) usually results in better erosion resistance, therefore high brittleness index (H/G_{lc}) yields lower erosion resistance.

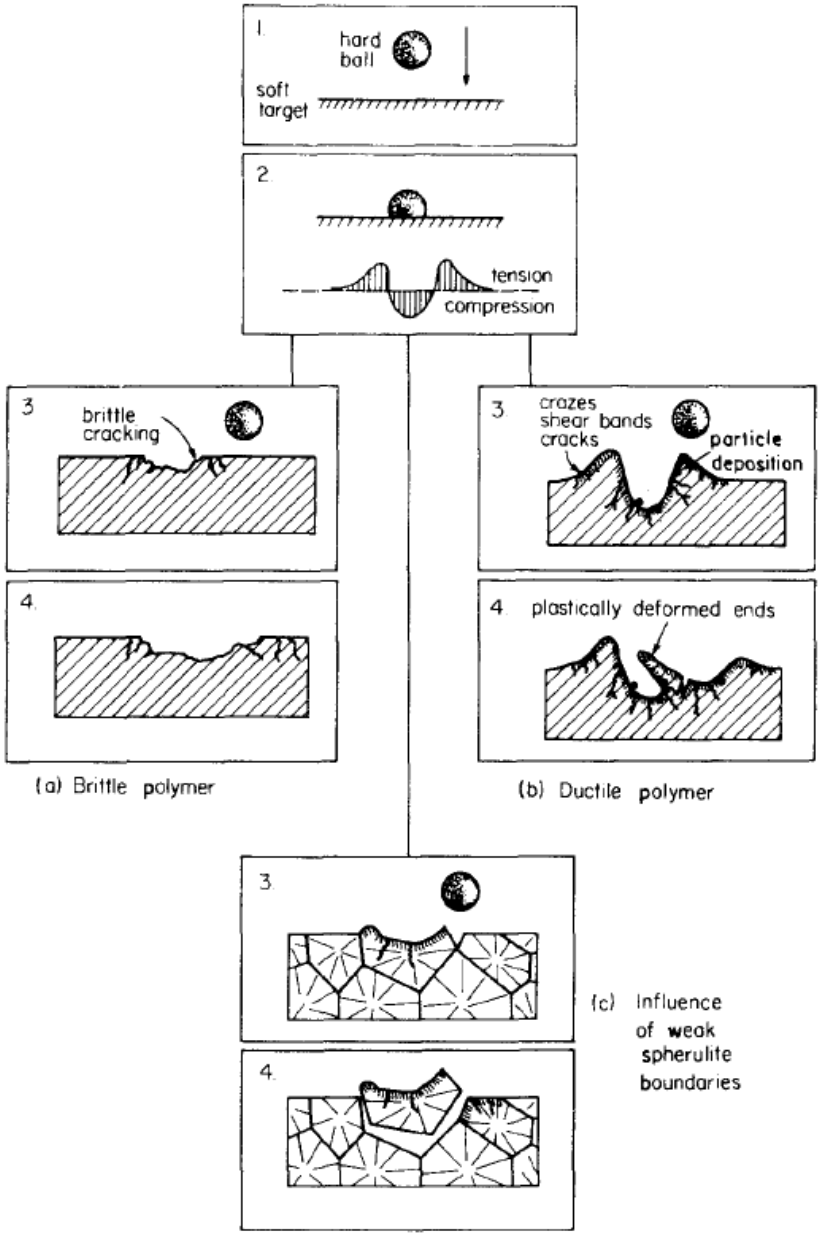

Figure 79. Schematic sketches of sequential surface damage as a result of repeated particle impact on brittle and ductile polymer targets [115].

Hojo et al. [118] examined the erosion damage of polymethylmethacrylate (PMMA) by a slurry. The slurry was made of glass beads with a diameter of 176 μm and a density of 2.48 g/cm^3 in neat water. The PMMA specimens were cylindrical with dimensions of 6mm diameter and 27 mm length. Before the test the specimens were

immersed in 30 °C water for 100 hours to eliminate further water absorption. The slurry impinges the length of the specimen with the flow travelling around the diameter. The authors found that the main erosion mechanism for a cylindrical specimen differs as the fluid moves around the diameter of the specimen. Brittle damage was observed, even on the stagnant side of the specimen, and it was suspected that fatigue occurs.

Larsen-Basse et al. [109] studied the slurry abrasion of high density polyethylene, polypropylene, PVC, PMMA, Delrin and polytetrafluoroethylene (PTFE) in relation to submarine power cables linking to the Hawaiian Islands. At the time the research was conducted, this was a novel application. The experiment was based on ASTM G75-82 test method for slurry abrasivity [119]. The abrasives used were silica sand, crushed coral, and lava in order to simulate the conditions of the seabed. The slurries were created with both fresh and sea water. Abrasives were sieved to 250-420 μm in size. The authors found that the shape of the abrasive has a great effect on the wear rate. Rounded particles were found to create shallow grooves with material pushed away while sharper abrasives created deep grooves with cracking. The wear rate from sharper particles was orders of magnitude higher than that of rounded particles. Significant differences were found in the behaviour of brittle vs. ductile polymers.

Barkoula et al. [120] studied the solid particle erosion of epoxy resin modified with hygrothermally decomposed polyester-urethane. Impact angles of 30°, 45°, 60°, and 90° were investigated using a sand blasting chamber with sharp angular corundum particles of size 60-120 μm. The nozzle was 220 mm from the sample with a constant speed of 70 m/s. Epoxy resin is known to be brittle and therefore would be expected to have the highest rates of erosion with normal impact, while the polyester-urethane would exhibit more ductile behaviour [121]. The addition of the polyester-urethane resulted in less cross-linking in the epoxy network. Because of this, the nature of the material when subjected to solid particle erosion changed. Samples with higher mean molecular weight between cross-links exhibited behaviour more similar to ductile materials with peak erosion at and impact angle of 30°. With low molecular weight

between cross-links typical brittle behaviour was exhibited. As the fracture energy increased there was a linear increase in erosion resistance.

Rajesh et al. [122] studied two polyamides (PA6 and PA12) for erosive wear at 30 and 90° impact angle. Polyamides, also called Nylon, are known to absorb water and swell. The authors sought to determine whether this has an effect on the erosive wear and mechanical properties of the Nylon. The samples were created by compression moulding and cut down to 30 mm x 30 mm x 6 mm specimens. The sample were submerged in water and weighed every two hours to track water absorption as a function of time. After 24 hours the samples were removed for erosion testing. The study found that PA6 absorbed 1.13% of its mass while PA12 absorbed 0.15%. The erodent used was 90-180 μm silica sand and compressed air was the medium to which the erodent impacted the target material at 80 m/s for 20 minutes via a 6 mm nozzle that was 10 mm from the surface. The tensile strength, elongation to break and hardness of PA12 increased with water uptake and PA6 decreased for all. For Izod impact, PA6 improved after absorption while PA12 did not. Thermal degradation was suspected after inspection of the main crater created by the erosion. Untreated PA12 samples exhibited marginally better wear resistance than PA6. Where there was a deterioration in strength properties, a deterioration in erosive wear performance was also observed. Therefore, water treated PA6 performed worse than untreated PA6 and PA12 experienced an improvement in erosion resistance after water treatment. The benefit for PA12 was seen at both impact angles but was less significant for normal impact. The difference in steady state erosion rate of treated and untreated PA was much higher for oblique impact than normal impact overall.

Arjula and Harsha [121] studied the erosion efficiency of polymers and polymer composites by reviewing existing data from a collection of studies. Erosion efficiency was first introduced by Sundararajan et al. to identify the dominant micromechanism present for metallic and ceramic materials [123]. In this study [121], Arjula and Harsha apply this parameter to the polymers. The erosion efficiency is defined as follows:

$$\eta = \frac{2EH}{\rho v^2} \tag{4-3}$$

Where 'η' is erosion efficiency, 'E' is the erosion rate (defined as mass loss of target material over mass of the erodent used), 'H' is hardness of the target material, 'ρ' is density of the target material and v is the velocity of the erodent at impact. If a modified erosion rate, 'E_v' which is the ratio of volume loss of the target material over mass of erodent, is used the equation simplifies to:

$$\eta = \frac{2E_v H}{v^2} \tag{4-4}$$

A study conducted by Harsha and Thakre [124] on the solid particle erosion behaviour of polyetherimide and its composites produced the data used by Arjula and Harsha. In this investigation neat PEI and three composites were tested; randomly oriented short E-glass fibres, carbon fibres and solid lubricant (Molybdenum disulphide, graphite, and PTFE) filled PEI. The experiment was conducted by using compressed air to direct silica sand of 150-300 μm to the target material via a 4 mm diameter nozzle. The study found that the behaviour of the material strongly depended on the impingement angle. Which material performed best was heavily dependent on this. Peak erosion for neat PEI occurred at 60° with semi-ductile behaviour. The worn surfaces of the PEI showed evidence of micro-cracking, sand particle embedment, chip formation, exposure of fibres, fibre cracking and removal of fibres. The addition of fibres to PEI provided no benefit in relation to erosion resistance. A further study by Arjula, Harsha and Ghosh showed that neat PEI exhibits maximum erosion rates at 30° impingement angle (ductile behaviour) while the addition of unidirectional carbon fibres peaks at 60° due to the brittle nature of the fibres [125].

Using this data, Arjula and Harsha found that the erosion efficiency for PEI is 0.65 for a velocity of 30 m/s, 0.21 for a velocity of 52 m/s and 0.21 for a velocity of 60 m/s. The magnitude of the efficiency can be used to describe the mechanisms of the erosion. Ideal microploughing results in displacing material without fracture. In this case no

material would be removed from the surface so η=0. Contrarily, ideal microcutting results in complete removal of material so η=1. When η is very low it can be assumed that erosion is due to lip or platelet formation and subsequent fracture due to repeated impact which is indicative of ductile behaviour. Erosion by failure due to linked micro-cracks resulting in removal of material is expected to have an efficiency greater than 1 and is indicative of brittle behaviour. Use of this parameter gives a good indication of material behaviour that can then be further validated by post-analysis techniques.

Adding to the knowledge already demonstrated, Arjula et al. [126] conducted a study of solid particle erosion of seven high-performance thermoplastic polymers. The thermoplastics studied were PEI, PEEK, PEK (polyetherketone), PPS (polyphenylene sulfide), PES (polyethersulfone), PSU (polysulfone), and UHMWPE (ultra-high molecular weight polyethylene). The steady state erosion at impingement angle of 15-90° and velocities from 25-66 m/s was recorded. The erodent used was 200 μm angular silica sand accelerated via compressed air and then through a 4mm nozzle to the target material. It was found that impingement angle and velocity have the greatest influence on the erosion rate, however material properties do play a role as well. Higher hardness was associated with a decrease in erosion resistance due to less ability to absorb impact energy of the erosive particles. This leaves the particles with more energy to induce plastic deformation, crack initiation and fracture.

Frosell et al. [104] investigated the effect of slurry particle concentration on the erosion rate and profile of ABS. Commercially available ABS sheets were subjected to a slurry flow test loop in which glass spheres were impacted with the coupons using a jet impingement rig. The flow rate ranged from 20-55 L/min with slurry concentrations between 2.1% and 11.4% by volume (4.6-22.4% by weight). The mean particle diameter was 150 μm. The Stokes number was used to determine particle entrainment, trajectory, and profile of the erosion. Stokes number is defined as:

$$St = \frac{\tau_p U}{D} \tag{4-5}$$

Where 'St' is the Stokes number, 'U' is the average exit velocity, 'D' is the nozzle diameter and 'τ_p' is the characteristic time of the particle defined as:

$$\tau_p = \frac{\rho_p d_p^2}{18\mu_f} \tag{4-6}$$

Where 'ρ_p' is the particle density, 'd_p' is the particle diameter, and 'μ_f' is the fluid viscosity. Stokes numbers between 1 and 40 indicate that the particles were predominantly entrained by the fluid. By increasing particle size, higher Stokes number can be achieved resulting in less entrainment as seen in previous studies [127]. The erosion profiles investigated are shown in Figure 80.

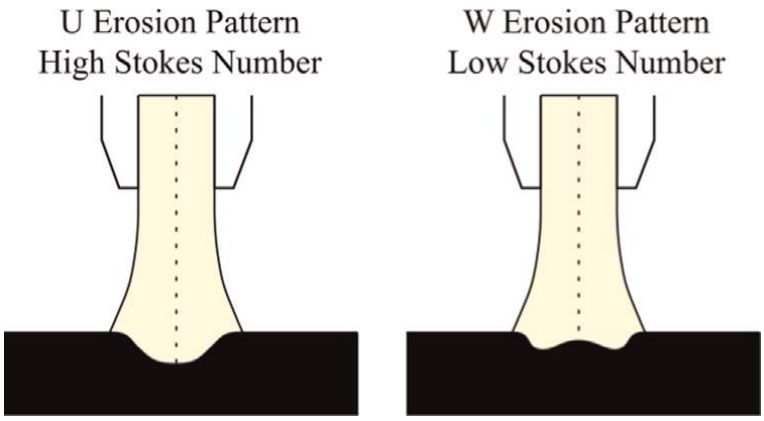

Figure 80. U erosion profile (left) and W erosion profile (right) [104].

After testing it was concluded that the erosion rate change as the volume of the erosion profile changes. Erosion patterns will initially have a 'W' shape with high initial erosion rates. The height of the hump seen in the middle will increase as the material around it is eroded. A transition to the 'U' shape is seen as the minimum erosion rate occurs. Beyond this the erosion rate will increase and the highest erosion rates will be observed. The rate of erosion relative to the depth does not change with the slurry concentration, however the point of transition from 'W' to 'U' will shift.

Lima et al. [128] studied the slurry erosion and corrosion behaviour of three types of flame spray-deposited polymer coatings. The deposition occurs by heating the coating material and accelerating it by high temperature jet through a nozzle. The droplets of material then impact the substrate material where they spread, cool, and solidify to form the coating. Polymer coatings are used on metal substrates in order to help inhibit corrosion, as they are non-conductive. The polymers are in powder form before undergoing the thermal spray process. Those used for this study are PEI, PEEK, and PA12. The substrate used is AISI 1020 carbon steel. For slurry testing the samples were 32 x 15 x 3 mm in size. Slurry testing was conducted in a slurry pot tester with distilled water and quartz particles of 300μm at a concentration of 300 g/L. The impingement angles studied were 30° and 90° at a velocity of 41.5 m/s for 360 minutes. Erosion resistance was determined by mass loss. The performance of the three coatings was found to be very similar at 30°, however at 90° PA12 and PEEK performed better than PEI. Erosion rates were found to be higher at 30°, as expected for more ductile materials [115]. Defects in the coating were found for PEI and are thought to be the reason for poor performance at normal incidence.

The erosion performance of Nylon 12 (PA 12) with varying experimental conditions was investigated by Debnath et al. [129]. The specimens were subjected to sand (SiO_2) particles with sizing ranging from 300-355 μm, 355-500 μm and 500-600μm. The particles impinged the surface at angles ranging between 15° and 90° with velocities between 30-50 m/s. The distance between the source and the material varied from 15-25mm. All tests were performed at ambient temperature. As there were many experimental characteristics being varied, an analysis of variance (ANOVA) was implemented to understand the significance and interactions of the individual variables. It was seen that the maximum erosion was exhibited at 30°, in line with ductile behaviour. Increasing velocity resulted in greater erosion, while increasing distance resulted in lower rates of erosion. Morphological analysis was performed for images captured on the SEM. It was found that the mechanisms of wear were micro-cutting, micro-ploughing, micro-cracking, and plastic deformation as shown in Figure 81. Micro-cutting and micro-ploughing which are plastic deformation due to tangential

force are denoted as 1 and 2. In (c) and (d), the wear is via plastic deformation and propagated cracks from repeated impact (denoted as 3). As also shown in (e) and (f), this does not result in extensive material removal as the cutting and ploughing do.

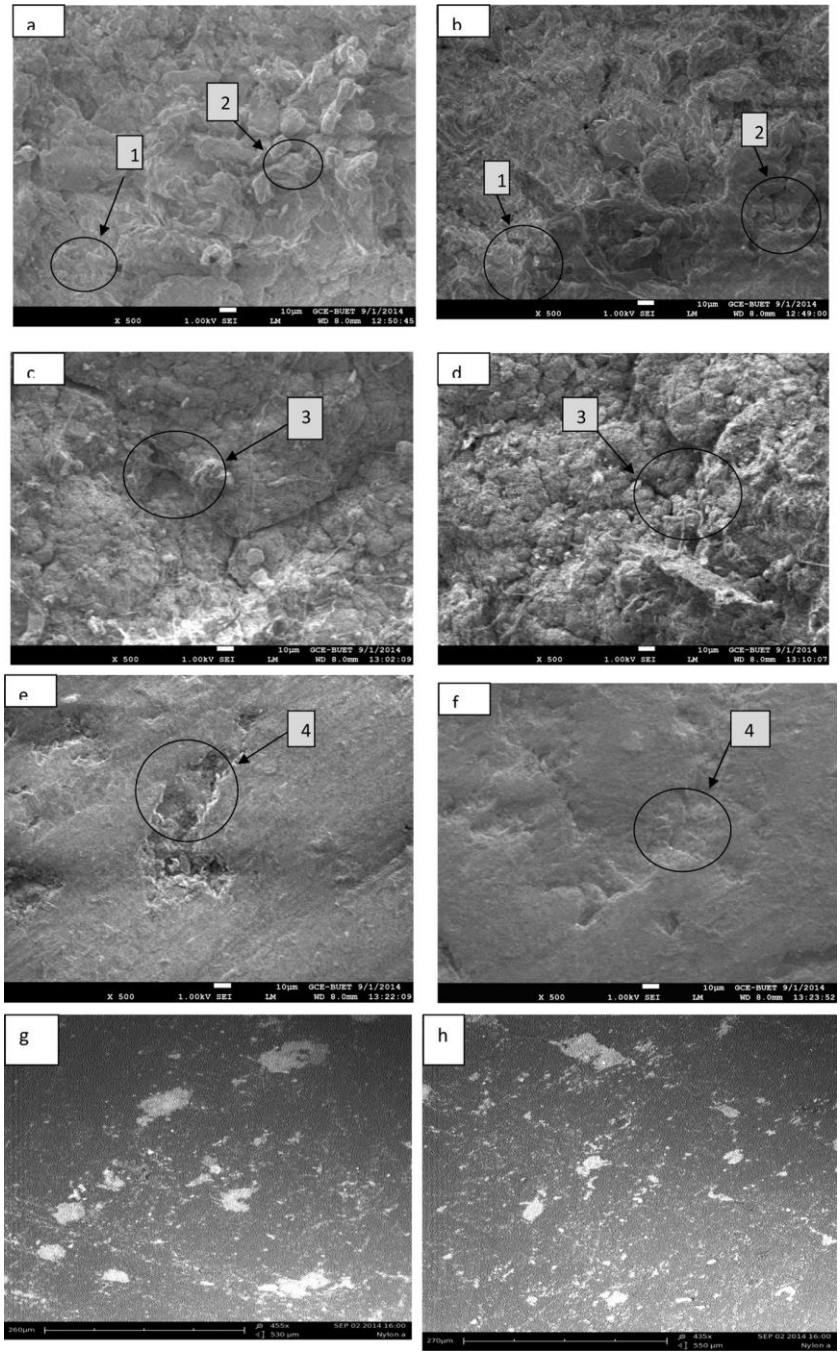

Figure 81. SEM micrograph (x500) of eroded Nylon 12 at impingement angle: (a) and (b) 30 °, (c) and (d) 60 °, (e) and (f) 90 °, and (g) and (h) before test [129].

For the minerals processing industry, equipment is in direct contact with abrasive slurries requiring the material to possess good erosion resistance [108]. Koskela et al. [108] studied the performance of low-density (LDPE) and high-density (HDPE) polyethylene (PE) manufactured by either rotational moulding or extrusion under these conditions. The experiments were conducted in a slurry pot tester with a rotational speed of 520 rpm so that the outer edge of the rectangular sample experienced impact at 5 m/s and the inner edge a velocity of 3.2 m/s. The erodent used was quartz sand with a nominal particle size of 100-600 μm. The water was supplied from a nearby riverbed and the slurry had 30 wt% solids content overall. The samples were dried and weighed before and after the experiment in order to record the amount of mass loss due to erosion. Each experiment ran for 24 hours and 72 hours at temperatures varying from 35-65° and impact angles from 15-90°. This study was novel in that it is the first time slurry erosion of PE had been studied at temperatures higher than ambient. It was found that the manufacturing method of the PE resulted in varying erosion resistance. Extruded PE exhibited better erosion resistance than rotational moulding, however between rotational moulded LDPE and HDPE there was not a significant difference. It is concluded that this difference is due to the residual stresses and orientation of material characteristic to each type of manufacturing. At an impact angle 45°, increasing temperature resulted in a significant erosion increase in erosion damage, however, this had no effect at 90° impact.

4.2.3 Solid particle erosion of composites

Wear characteristics of filled composites when impacted by solid particles has been extensively studies as shown in the review of literature by Patnaik et al. [130]. This review defines two distinct modes of erosion: brittle and ductile. More ductile matrix composites are seen to wear via cutting and chip formation while brittle matrix composites exhibit failure by crack formation [131]. The damage of the two types of materials is predicted in different ways [132, 133]. For ductile matrix, damage accumulation and impact damage are most present. In brittle materials the subsurface lateral crack propagation dominates. There are 6 main parameters that effect erosion

[121, 132, 134]: fibre material, fibre content, reinforcement type, fibre orientation, fibre treatment and interface, and testing conditions.

Zahavi et. al investigated the solid particle impingement of uncoated composite materials using sand [107]. The composites studied were quartz-polyimide, glass-epoxy, and quartz-polybutadiene. The target materials were impinged with sand via compressed air at 42 m/s with impact angles of 90°, 75°, 60°, 45° and 30°. The study found that mass loss increased with increasing impact angle with a maximum at 75°. With a constant impact angle, it was found that mass loss increased with an increase of mass of impacting sand in the range of 200-600 mg. Erosion in the resin rich zones, breakdown of fibres into small fragments (10-30 μm in length) and at the interface of the matrix and fibres was found. Erosion resistance improved by nearly an order of magnitude when the composite had a larger percentage of fibre reinforcement with good adhesion to the matrix and low porosity.

Lhymn et al. [135] investigated the slurry erosion of polyphenylene sulphide reinforced with glass fibres as a function of sand particle velocity and sand particle size. This thermoplastic composite was chosen in order to compare to conventional cast iron erosion rates. Rectangular specimens were manufactured via injection moulding and subjected to a slurry at an impact angle of 45°. A previous study by Ruff et al. [136] indicates brittle behaviour from this material. The Lhymn et al. study [135] concluded that the slurry erosion rate under the conditions was much lower compared to cast iron. Subsurface crack propagation and debris that forms from this control the failure of the material. After derivation of an equation to describe the effect of particle size and velocity on erosion rates the following was determined: erosion rate increases as the particle mass increases, as the velocity of the impacting particles increases, is inversely proportional to the fracture energy, and is a function of the fracture toughness. This research reinforces what was describes by Friedrich et al. [115] as the brittleness index.

Bahadur et al. [137] investigated the mechanical and tribological behaviour of glass fibre reinforced polyester with weight percentage of fibres varying from 0 to 50%. Pin-

on-disc tests were performed to evaluate the friction and wear resistance of the material. The sliding speeds were 1, 1.5, 2 and 2.5 m/s with a normal load of 9.8N on a steel disk. A coupling agent to assist with the interface of the fibres and the polyester matrix was applied. It was found that this improved strength, however it resulted in insignificant effects on wear rate. The addition of fibres did have an effect on wear resistance; the authors found that neat polyester wears at a higher rate than its composite counterpart. Wear rate and coefficient of friction are lowest at 10 wt% glass fibres, and both increase with decreasing and increasing fibre proportions. Increasing sliding speed increases the wear rate, however this had no effect on the coefficient of friction. Increasing sliding speed results in higher temperatures which enables oxidation of the polyester.

Bijwe et al. [138] investigated the friction and wear behaviour of polyetherimide composites for adhesive, abrasive, three-body abrasion, fretting and erosive wear modes. The materials investigated were neat PEI and two composites (20 wt% short glass fibres and a commercially available bearing material with 25 wt% glass fibres and three solid lubricants). Adhesion tests were done via pin-on-disc machine. Abrasive wear was tested via single pass and multi-pass against silicon carbide (SiC) papers and a rubber wheel abrasion tester. For erosion testing, a sand blasting machine was used with 80 μm silica sand at 1 kg/min. The amount of erodent varied from 3, 6, 9, 12 and 15 kg with impact angles of 15, 30, 45, 60 and 75°. The 3 mm nozzle was placed 12 cm from the sample. A polymer pin was fretted against a stationary mild steel disc with loads of 70, 80, 90 and 100 N. A main finding was that the addition of fibres deteriorated the performance of the neat polymer, with the addition of fibres and fillers proving detrimental. Wear was found to increase linearly with an increase in the amount of erodent. The maximum effect of impact angle was found at 30°.

The erosion behaviour of PEEK reinforced with unidirectional carbon fibres was investigated by Tewari et al. [134]. The material was evaluated at impingement angles from 15-90° with fibre orientations of 0, 45, and 90°. The erodent used in the tests were steel balls with a diameter of 300-500 μm and impact velocities of 45 and 85 m/s. The particles were accelerated along nozzle of 80 mm in length and 8 mm in diameter

using compressed air. The feed rate was 15 g/s with a distance of 160 mm from the nozzle to target material. The authors found that semi-ductile behaviour was exhibited by the composite. The maximum erosion rate was seen at an impingement angle of 60°. When the steel ball impact the fibres normally, greater erosion rates are seen compared to when the impact occurs parallel to the fibres. At normal impact to the fibres, there is more breakage due to less resistance to bending as the steel ball impacts the fibre (or bundles of fibres). Matrix removal, exposure, cracking, and removal of fibres are found to be the cause of most of the wear.

Kim and Kim [139] investigated the behaviour of carbon fibre reinforced epoxy composites when subjected to solid particle erosion. Unidirectional and multidirectional continuous fibre reinforced epoxy with orientations of ‘0’, ‘0/90’ and ‘0/60/-60’ were tested at various angles of flow to fibre direction (displayed in Figure 82 and Figure 83).

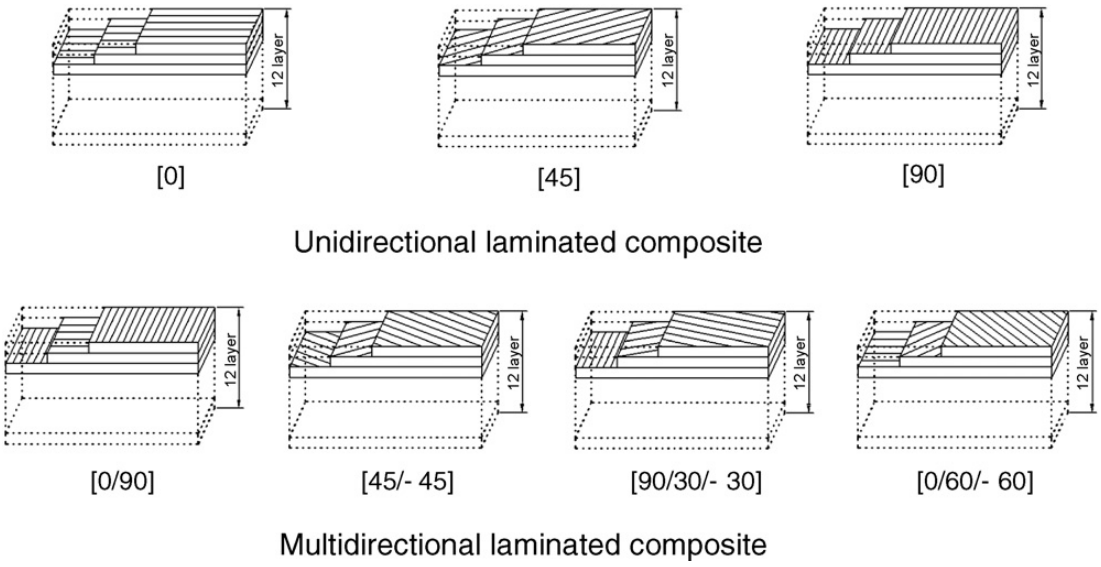

Figure 82. Fibre orientation for tests [139].

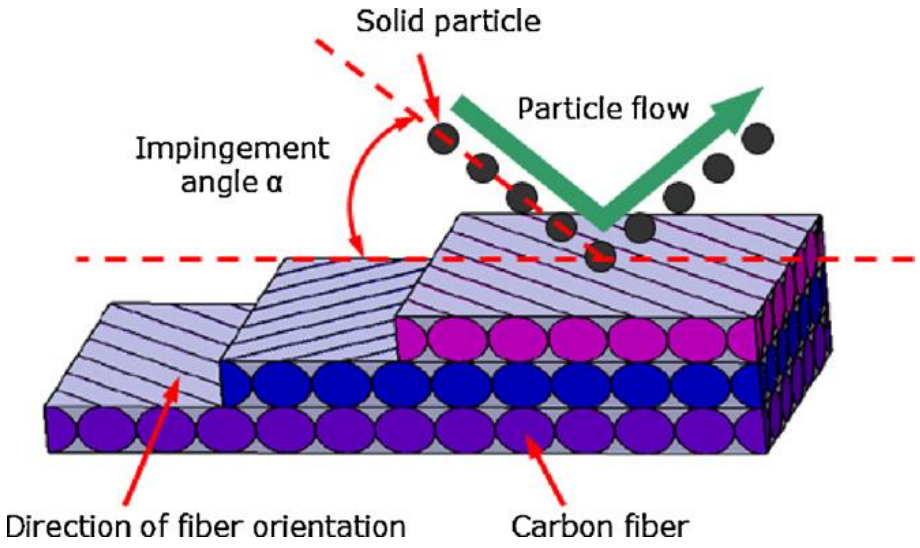

Figure 83. Schematic of particle flow over target material [139].

Impingement angles from 15-90° were used with an erodent velocity of 70 m/s (controlled by compressed air). The previous study by Tewari et al. [134] explored the dependence of fibre orientation on erosive wear finding clear dependence. For unidirectional composites, higher erosion rates were found at 90° orientation than 45° or 0° at acute impingement angles. At 90° impingement angle there is much less effect of fibre direction which aligns with previous work [140]. Multidirectional composites exhibit less erosion at acute angles, likely due to the stabilising effect of crossed fibres. Fibre cracking and removal of fibres were found to be the most critical mechanisms of erosion.

Akinci et al. [141] studied the slurry erosion of low density polyethylene filled with basalt at 10, 30, 50, and 70 wt%. The samples were exposed to slurry media composed of 50 wt% Aluminium oxide (Al_2O_3) particles with a size of 500 μm and 50 wt% distilled water. The slurry impacted the samples at 1m/s at angles of 15, 30, 45, 60, 75 and 90° for 30 minutes. The authors found that the addition of basalt particles improved the hardness of the material but did not increase the tensile strength and fracture strain. For impingement angles above 60° and basalt concentrations above 30 wt%, the erosion rate sharply increased. This is due to the increasingly brittle nature

of the material and is in accordance with behaviour noted in previous studies [131, 142].

Ahamed et al. [143] conducted a study on the impact angle effects on erosion maps for glass fibre reinforced polymers (GFRP) by investigating a G-10 grade fibre-reinforced epoxy composite laminate. The erodent was irregular silica sand at impingement angles of 15-90º. The erosion rig used is seen in Figure 84. Using SEM, the erosion was evaluated. Semi-ductile erosive wear was found at 60º impingement angle. By using salt water with the erodent, a synergistic effect was also observed which increased the depth of penetration and in turn extended crack propagation.

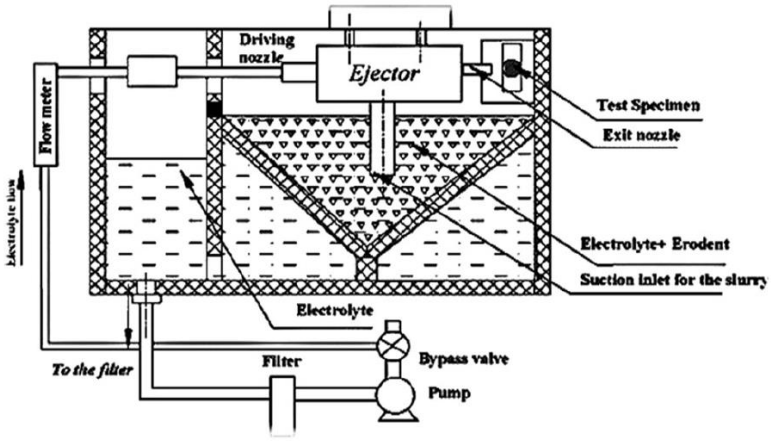

Figure 84. Schematic diagram of slurry impingement jet rig [143].

4.3 Current studies in wear of 3D printed polymers and polymer composites

4.3.1 Effect of surface texture

The surface texture is known to have an influence on the performance of polymers for wear, for example, the creation of undulations can trap wear particles, therefore reducing further wear [144, 145]. In biological applications, texture is useful in protecting animals from harsh environments such as desert sandstorms. In two studies,

Han et al. investigated how this texture improves anti-erosion properties [146, 147]. One study found that the biological coupling of surface morphology and flexibility of the material was the leading factor in erosion resistance [146]. While the second study found that the micro-texture and curvature of the surface resulted in superior erosion resistance because of the relative impact angle [147].

Depressions can act as channels for lubricants which assist with friction between sliding surfaces [144]. In a number of applications, wear resistance is the primary concern for material performance. These applications include processing equipment for industries such as mining, renewable energy, marine infrastructure and more. Polymers and polymer composites are suitable in these applications due to their inherent corrosion resistance [7]. The lack of electro-chemical response to water and other corrosive mediums means that wear is induced mechanically. Additionally, due to self-lubrication and low friction behaviour, these materials have become increasingly desirable [148].

The surface finish on the 3D parts is textured, which is dependent the printing parameters chosen by the user. With traditional polymer and composite manufacturing, the surface finish will often be much smoother than that of additive manufacturing. This will have an impact on the wear resistance of the materials. The addition of texture has also been known to improve friction performance under certain conditions [149]. Coblas et al. [145] have investigated wear resistance of materials with surface texture induced in order to increase the wear properties. The findings show that there are three major roles that the texture can play: debris trapping, lubricant reservoirs, and micro-hydrodynamic bearings. Further studies found that in order for the hydrodynamic lubrication to be effective the grooves or pockets must be narrower than the contact width for sliding wear [150]. However, there is still little literature available on the wear resistance of materials manufactured by FDM [151].

There were varied, but limited, types of wear investigated in literature at the date of writing Sections 4.3.2, 4.3.3 and 4.3.4 that follow. The majority of existing studies are focused on the friction performance of the printed polymers and polymer composites. This can be either in the form of dry or lubricated sliding, or the performance of gear

teeth. Currently, there are minimal publications concerning the performance of printed polymers exposed to solid particle erosion.

4.3.2 Sliding wear and friction performance: 3D printed polymers

Sood et al. [152] studied the effects of sliding wear on parts built by FDM by five printing parameters: layer thickness, part build orientation, raster angle, raster width, and air gap. Due to the number of parameters, the relationship of FDM parts with wear is complex. During the FDM process, layers are put down on the printing bed at temperature above melting [153]. As the layers cool, they are reheated by subsequent layers. Due to this, there is distortion in the bottom layers of the part. Since sliding wear is dependent on the internal structure of the material as well as the surface finish, it was suggested by the authors that controlling this distortion could also control the wear response. ABS coupons were tested by a rotating disc at a speed of 1 m/s for around a contact path diameter of 120 mm. There was a 25N load parallel to the axis of the specimen. The wear volume was then determined by multiplying the cross-sectional area with the loss in height of the specimen along the sliding distance. The main findings were that localised melting between layers resulted in strong bonding which in turn meant increased strength and wear resistance.

Mohamed et. al [154] conducted a parametric investigation of the friction performance of PC-ABS (polycarbonate-acrylonitrile butadiene styrene) parts created by FDM. Similarly, to Sood et al. [152], different process parameters were compared to the wear performance. These parameters were: layer thickness, air gap, raster angle, build orientation, road width (denoted as raster width by other authors) and number of contours. Samples were 35mm long cylinders with a 6mm diameter and tested per ASTM G99 ‘Standard Test Method for Wear Testing with a Pin-on-Disc Apparatus’ [155]. After testing it was found that the most important factor to wear resistance was layer thickness. The coefficient of friction rapidly increases with layer thickness. This is due to the fact that the surface roughness increases with layer thickness. Images taken via SEM shows that there are cracks and a large number of grooves at the highest layer thickness (0.332 mm). However, it was found that the coefficient of friction decreases with a decrease in the value of all process parameters. SEM also shows that

thicker layers and road widths are not recommended as 'they caused fracture, deep permanent grooves, debris and cracks in the part microstructure'[154]. The ideal process parameter set was found to be 'layer thickness = 0.127 mm, air gap = 0.0, raster angle = 0.0, build orientation = 90.0, road width = 0.4572 mm, and number of contours = 1.0'.

The studies discussed thus far considered the effect of the surface finish created by the manufacturing process, however, Hong et al. [156] investigated the use 3D printing to create textured surfaces specifically for wear resistance. By printing coupons with convex and concave surface texture (Figure 85) as well as rectangular channels, the wear resistance was examined for dry sliding and compared to a flat printed surface. Depressions have been shown to trap debris and reduce the ploughing component of friction [144]. They have also been shown to feed lubricant and increase the load carrying capacity of a surface under sliding [144].

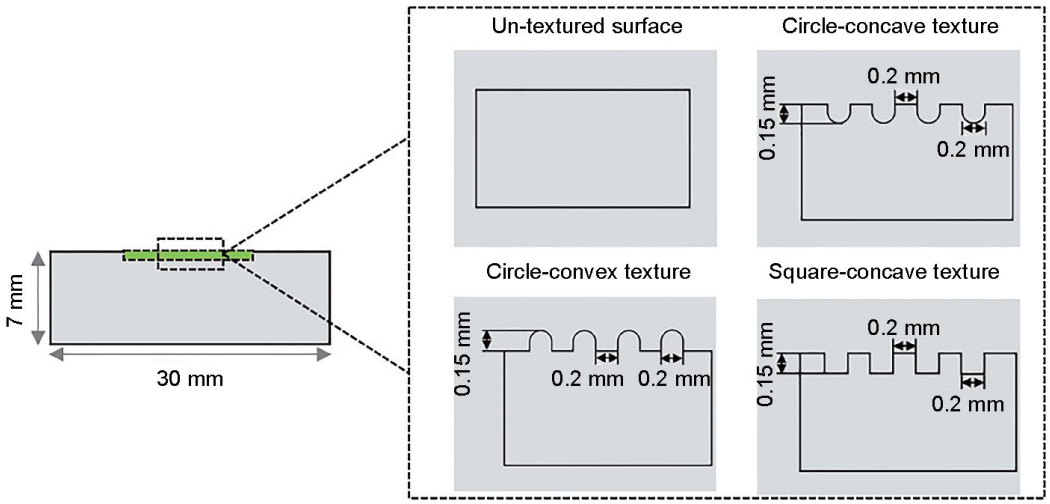

Figure 85. Surface textures for samples [156].

Two load cells were used to continuously measure the friction force and applied load as a steel ball was slid over the surface for a distance of 10 mm with an oscillation frequency of 3 Hz. The sliding cycle was set to 10,000. The results conclude that the

shapes do affect the friction performance of the material with wear loss being lower for circular concave surfaces than untextured.

The self-lubrication and friction performance of 3D printed journal bearings has been studied by Lee et al. [157]. The difference here is that a specific type of application is explored as well as two types of printing (FDM and SLS). 'Plastic materials' is specified for the FDM parts, while nylon and aluminium SLS parts were examined. The coupons were 10 mm in thickness with an inner diameter of 30 mm and a length of 40 mm. Micropores were included for permeation of the lubricant. The uptake of oil after the heat of rotation was measured. The FDM parts were tested at speeds of 500 and 700 RPM with 30 N loading. The SLS parts were tested at the same speeds but with only 10 N of loading. It is concluded that the FDM parts resulted in the best oil uptake and therefore self- lubrication.

Table 1 Amount of oil content for the FDM specimen

	Weight of specimen (g)		Weight of immersed specimen (g)		Weight of oil content (g)	
Thickness of layer (mm)	Avg.	σ	Avg.	σ	Avg.	σ
0.09	13.68	0.030	13.78	0.046	0.10	0.062
0.14	14.17	0.036	18.06	0.023	3.89	0.220
0.19	14.28	0.047	19.33	0.090	5.05	0.172

Table 2 Amount of oil content for the SLS specimen

	Weight of specimen (g)		Weight of immersed specimen (g)		Weight of oil content (g)	
Type	Avg.	σ	Avg.	σ	Avg.	σ
Nylon	19.86	0.041	20.05	0.035	0.19	0.058
Aluminum	53.33	0.064	53.45	0.051	0.12	0.042

Figure 86. Tables from Lee et al. for FDM and SLS oil uptake [157].

Hanon et al. [158] investigated the tribology behaviour of ABS and PLA printed by FDM. Cylindrical parts with a diameter of 7.5 mm and length of 10 mm were tested via reciprocated linear sliding friction with a steel counterpart and no lubrication. It was concluded that any distinction in wear was due to the inherent characteristics of the material, not the manufacturing method. There was no clear conclusion on the effect of 3D printing settings and further research was suggested.

Abdollah et al. [159] studied the effect of load and speed on the behaviour 3D printed ABS subjected to dry sliding. The printed specimens were pins with different internal geometry: solid structure and internal square, rectangular, circular, triangular, and flipped triangular structure. They were printed using FDM with a printing speed of 60 mm/s, layer height of 0.10 mm, nozzle temperature of 234 °C and 100% infill density. Pin samples were slid against a 72 mm diameter carbon-chromium-steel discs per ASTM G99-05 at 27°C. The flipped triangular internal structure proved to have the lowest coefficient of friction and wear rate, however when the tribological performance of each internal structure was compared to its respective mechanical properties there is not a significant correlation. Delamination, abrasion, and fatigue wear were the main mechanisms.

Aziz et al. [160] conducted a study on the friction behaviour of 3D printed PLA with a pattern of circular surface texture printed by FDM. Samples were tested using ASTM G99 at a speed of 100 and 500 RPM with loads of 10, 20, 30, 40, and 50N both lubricated and dry. The lubricated tests used SAE 20W40 oil. The texture types are shown in Table 9.

Table 9. Types of texture on the samples [160].

Representation of 3D printed samples.

Type	Texture Depth	Texture diameter	No of specimen
T_1	1 mm	1 mm	20
T_2	1 mm	1.5 mm	20
T_3	1 mm	2 mm	20

The minimum coefficient of friction was found for texture T2 for both speeds with dry sliding and it exhibited less entrapment of wear debris. When lubricated, T3 possessed the lowest coefficient of friction at low speed and T1 at high speed. The wear was due to adhesion and abrasion. Overall, the coefficient of friction is reduced by 80% with the addition of lubrication.

4.3.3 Sliding wear and friction performance: reinforced 3D printed polymers

There has been a number of investigations for sliding and friction for 3D printed polymers with reinforcement in the form of fillers and short fibres.

Boparai et al. [161] investigated the tribological properties of Nylon6-Al-Al_2O_3 and ABS parts printed via FDM. For the Nylon 6, three different proportions of Al and Al_2O_3 were used. All parts were tested for dry sliding conditions under loads of 5, 10 ,15, and 20 N with a sliding velocity of 1.36 m/s for a duration of 5 and 10 minutes. It was found that the composite materials with the Nylon 6 matrix had better performance than the ABS parts due to the presence of Al and Al_2O_3. The main mechanisms of wear for ABS were delamination and abrasion, while the composite was dependent on adhesion as well. Singh et al. have conducted two separate studies on Nylon-6 with Al_2O_3 powder and SiC-Al_2O_3 additives [162]. In both studies the samples were printed using FDM and tested per ASTM G99. The first study in 2016 on Al_2O_3 proved that the reinforced Nylon-6 can be produced with the Al_2O_3 and the industrial benchmark for such was set. The second paper in 2017 looked at creating filament with SiC added in addition to the Al_2O_3. This study found that abrasion and adhesion are the greatest factors in wear of these materials. The authors concluded that a feedstock filament with reinforcement could be made that would enhance the wear properties when tested for pin on disc wear. The particle size distribution plays a role in the wear resistance with a wider range providing better resistance.

Bustillos et al. [163] studied PLA and PLA filament with graphene. The parts were printed with FDM on MakerBot replicator 2. The filament has a diameter of 1.75 mm and density of 1.25 g/cm3. Both materials were printed at 220°C, extrusion speed of 110 mm/s with a layer height of 0.2 mm and 100% infill. Nozzles of 0.4 mm (PLA) and 0.6 mm (PLA-graphene, larger to prevent clogging) were used. Rectangular strip coupons of 85 x 10 x 2.5 mm were made with a scaffold of 20 x 20 x 3 mm with pore size gradient of 400-850 μm. Nanovea ball-on-disc tribometer was used to test the specimens. A 3 mm stainless steel ball with loads of 5, 10 and 20N was used with a linear speed of 16 mm/s for a duration of 30 min. PLA-graphene showed 65% decrease

in coefficient of friction and 14% increase in wear resistance when compared to PLA (Figure 87). The authors found regions of delamination which was to be expected in adhesive wear. Frictional heat created by the process thus inducing shear and encouraging the formation of debris. In the PLA-graphene, weak interface of the two materials contributed to small debris sizes as each could break away more easily. It was predicted via Archard's equation that the increase in hardness from PLA to PLA-graphene would result in 34.2% increase in wear resistance. In reality the authors found that this was actually only 14%.

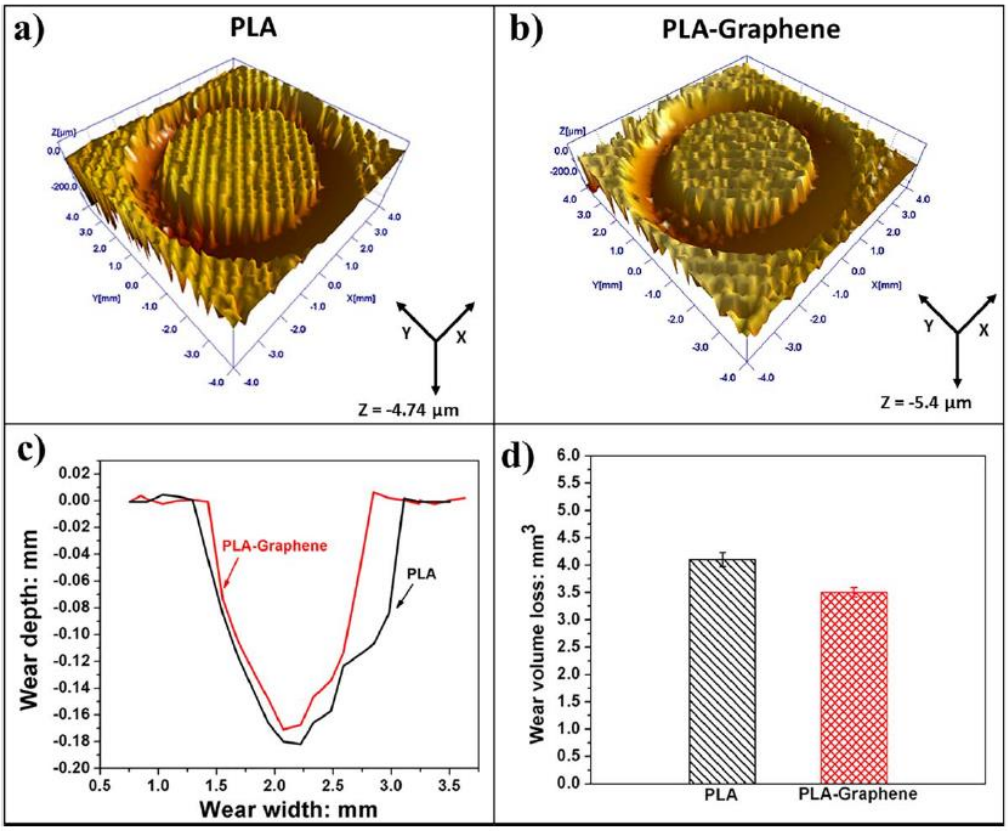

Figure 87. 'Wear tracks profiles of 3D printed: (a) PLA (20 N, 30 min) and (b) PLA-graphene (20 N, 30 min). (c) 2D line profiles showing width and depth of the wear track obtained in Figure 8a and b. (d) Wear volume loss comparison of 3D printed PLA and PLA-graphene.' [163].

A study performed by Ertane et al. [164] explored the wear properties of PLA reinforced with biocarbon in order to make a completely biodegradable composite.

The cylindrical specimens were printed using FDM with a diameter of 24 mm and a thickness of 7.8 mm. The printer had a build volume of 20 x 20 x 20 cm and a brass nozzle with an opening of 0.4 mm. The material was extruded at 220°C onto a bed with a temperature of 80°C. The specimens had a layer thickness of 0.30 mm. Translatory oscillation was used for tribological testing. Four proportions of biocarbon were tested, neat PLA (0 vol%), 5 vol%, 15 vol% and 30 vol%. After dry sliding against an Al_2O_3 ball the 30 vol% had the lowest wear volume. Overall, increasing the amount of reinforcement decreased the wear volume. The coefficient of friction is about 0.5. The 30 vol%, however, was the hardest to produce via FDM.

Lin et al. [165] investigated the impact of nanosilica on a PEEK/CF composite coating printed via FDM and subjected to sliding against a steel ring. The specimens were printed using a modified Ultimaker 2 FDM 3D printer with a 0.3 mm diameter nozzle with a temperature of 420°C, platform temperature of 150°C, layer height of 0.2 mm and 100% infill density. The filament was TECAFIL PEEK 450 with 30 wt% carbon fibre. Dry sliding was performed per ASTM G77-98. A carbon (100 Cr6) steel counter-body ring was used with a sliding velocity of 1 m/s and force of 50N. Tests were conducted parallel and normal to the printing direction. In the second test, nanosilica was fed into the interface of the specimen and the steel ring. The friction and wear properties are strongly dependent on the fibre orientation with perpendicular sliding resulting in better wear resistance. Friction was greatly reduced when the nanosilica was introduced to the sliding interface as it reduced adhesion, however the PEEK matrix was susceptible to abrasive wear from the particles and wear was not seen to be reduced by the addition of nanosilica.

Prusinowski and Kaczyński [166] studied FDM printed fibre reinforced thermoplastics for sliding wear in both air and water. The ABS matrix was fed via two nozzles with the continuous carbon fibre fed by the die head along the extrusion axis. Pin on disc tribological tests were performed with a rotating counter-body of 40 HM steel with a sliding speed of 1 m/s. The surrounding media was air or water. Varying forming temperatures with constant layer height of 0.350 mm and fibre content of 9.43 vol% were studied in the first stage, with a constant forming temperature of 235°C and

varying layer height and fibre content (from 6.6-11 vol%) for the second stage of research. For dry conditions it was found that fibre content above 9 vol% results in lower wear intensity (ratio of the change in layer height to the original volume [166]) when compared to neat ABS. The composites displayed 10 times greater wear in dry air conditions vs. water and two times more friction. Neat ABS results in greater material wear irrespective of environment.

4.3.4 Solid particle erosion of 3D printed polymers.

At present, only two studies on the behaviour of 3D printed polymers subjected to solid particle erosion exist. The first study reviewed was by Abdelaal et al. [167] in which effect of water-silica slurry on 3D printed PLA was investigated. The PLA samples were manufactured by FDM on the XY printing plane with an infill density of 100%. The printing temperature was 200°C with a bed temperature of 60°C. Three-layer thicknesses were investigated: 0.1, 0.2, and 0.3 mm. Each of these were investigated for the ‘X’, ‘Y’ and ‘45°’ orientation as seen in Figure 88.

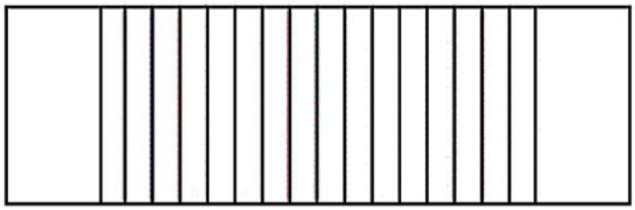

a) X- Orientation

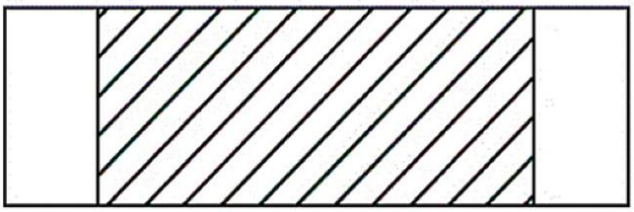

b) 45°- Orientation

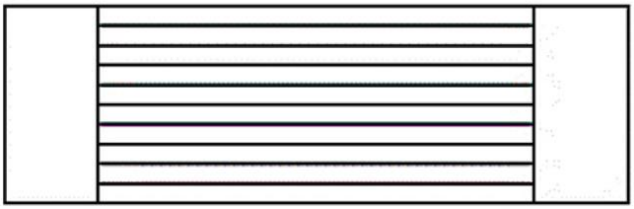

c) Y- Orientation

Figure 88. Orientations of the printed specimens for slurry erosion testing [167].

The impact angles investigated were 15 ,45, and 90° and corresponded to specific layer thicknesses and building orientations. The following table from the study shows each specimen and corresponding data.

Table 10. Experimental layout. using the Taguchi L9 design [167].

Specimen	Building orientation (BO)	Layer Thickness (LT)	Impact Angle (IA)
S1	Y- orientation	0.1	15
S2	Y- orientation	0.2	45
S3	Y- orientation	0.3	90
S4	45°- orientation	0.1	45
S5	45°- orientation	0.2	90
S6	45°- orientation	0.3	15
S7	X- orientation	0.1	90
S8	X- orientation	0.2	15
S9	X- orientation	0.3	45

The erodent used was natural silica sand ranging in size from 355-500 μm. A whirling arm slurry erosion test (WASET) was used to perform the experiments. The slurry was created with tap water and 1 wt% silica sand at room temperature. Due to the nature of polymeric materials and the voids created by the FDM process, there was a weight gain observed by the specimens. In addition to uptake of water, sand was found to be embedded in the specimens after testing. After ANOVA analysis of the parameters and results, it was found that the layer thickness and the impact angle had the most influence on water gain. However, this was not true for the embedment of sand particles in which only the layer thickness was a significant factor. The most weight gain due to water was seen in specimen S6, which has the largest of the three layer thicknesses. This was followed by S9 and S8 which have layer thicknesses of 0.2 and 0.3 mm respectively. The authors postulated that the effect of the pores created by the FDM process effect the water gain of the specimens. Further work is proposed to investigate this and the embedment of particle fragmentations.

Sınmazçelik et al. [168] investigated the effects of 3D printed surface texture on erosive wear of ABS. The ABS samples were subjected to solid particle erosion with air as the medium. The 40 x 40 x 3 mm specimens were made on a Zortrax M200 Plus 3D printing system. The layer thickness was 0.19 mm with a solid infill. The texture created by the printing process is denoted in the study as ‘micro-texture’, in which the

peaks and valleys of the layers are small compared to the size of the erodent. This resulted in a measured roughness of 2.95 μm when measured normal to the raster orientation. For comparison, specimens had texture printed onto the surface that were larger than the erodent. This is called ‘macro-texture’. Examples of all sample types are shown in Figure 89 with the orientations of flow also denoted.

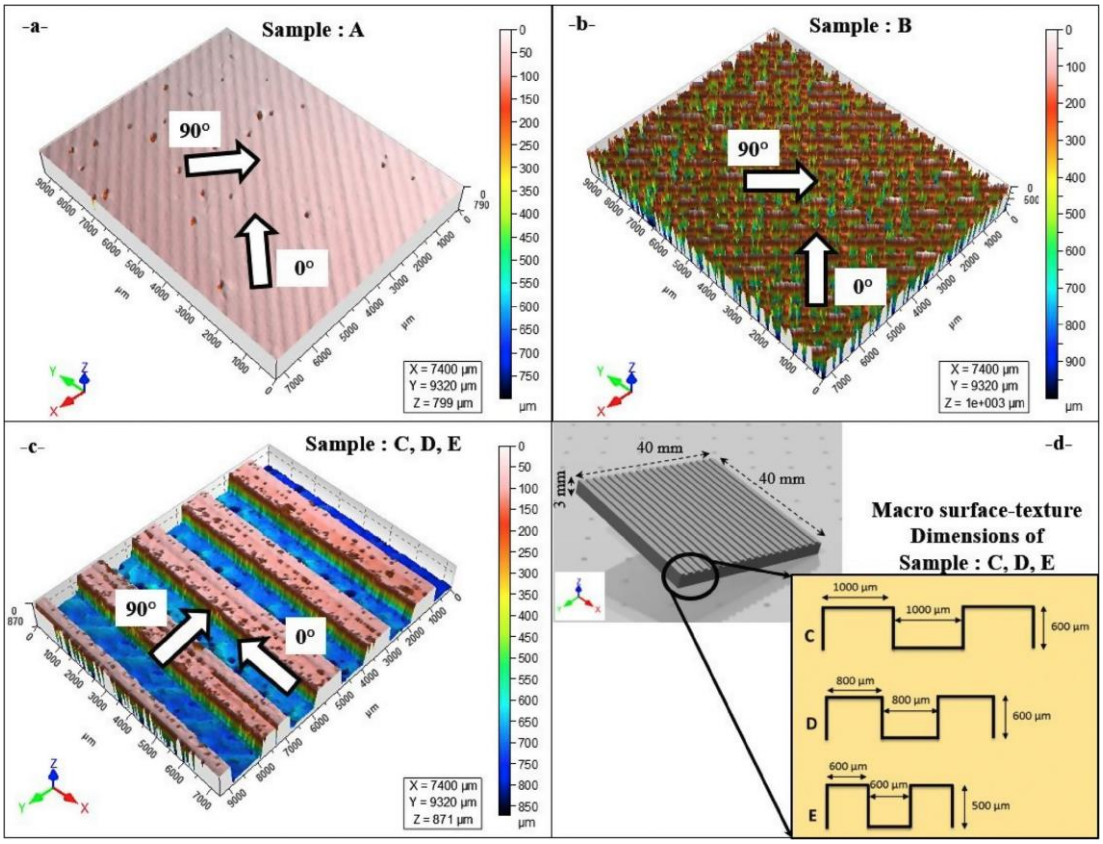

Figure 89. Types of surface textures tested by Sınmazçelik et al [168] : 3D printed ABS test coupons. Micro-textured surface (Sample A) (a). Micro-textured surface (Sample B) (b). Macro-textured Sample C, D and E (c). Surface geometry details of macro-textured Sample C, D and E (d).

The erosion tests were carried out at room temperature with compressed air and alumina oxide abrasive particles impacting the samples from a distance of 20 mm using methodology from a previous study performed by Zhou et al. [169]. The particles had an average size of 250 µm. The impingement angle was held constant at 45° as it results in significant material loss and allows for the study of localised impingement as the particles interact with the textured surface. The velocity of the particles was controlled by the compressed air and set to 56 m/s for this experiment. The results of the erosion tests are shown in Figure 90.

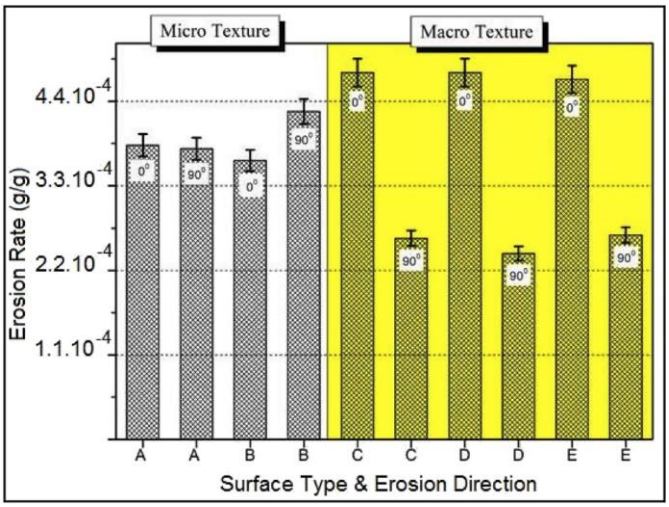

Figure 90. Mass loss from solid particle erosion of ABS [168].

The study concluded that the micro-texture designed for particle erosion direction can reduce the damage caused by particle erosion. The orientation of the flow with respect to the raster orientation has a significant effect on the erosive damage for micro and macro textured surfaces. For the micro-textured samples, the difference in erosion rate between the orientations ranged from 1.15-15%. The macro-texture showed much lower wear for the 90° orientation when compared to 0° and compared to the results for the micro-textured surfaces. When looking at individual orientations, the macro-texture had 28% more erosion damage for the 0° orientation than the micro-texture. However, for the 90° orientation the macro-texture was 71% lower than the micro. The authors of the study assumed that the loss of kinetic energy after first impact has an effect on the erosion. At 90° orientation, the particles are obstructed by the rebounded particles and could be contributing to the lower erosion rates.

5. Methodology for erosion characterisation

5.1 Introduction

This chapter will discuss the materials, protocol, and post-test analysis techniques for assessing the performance and behaviour of polymers and polymer composites under slurry flow conditions.

5.2 Materials

The focus of the study was to investigate the material loss due to erosion and mechanism for specimens printed using FDM while under slurry conditions. In order to understand this phenomenon two commercially available materials were studied at the request of the industrial sponsor: Ultem 1010 and Nylon 12CF. Ultem 1010 is the trade name for polyetherimide (PEI), which is an amber translucent thermoplastic that exhibits good strength, high glass transition temperature and high modulus [170]. Nylon 12CF is a polyamide with chopped carbon fibres in the filament. This material was chosen in order to study the behaviour of a composite under slurry conditions. The properties of Ultem 1010 and Nylon 12CF are shown in Table 11 and Table 12.

Table 11. Mechanical and thermal properties of Ultem 1010 provided by Stratasys.

Ultem 1010 Mechanical Properties	**XZ Axis**	**ZX Axis**
Ultimate Tensile Strength (MPa)	79.2	28.2
Tensile Modulus (MPa)	3040	3000
Elongation at Break (%)	4	1.1
Yield Compressive Strength (MPa)	245	438
Glass transition temperature (°C)	209.37	

Table 12. Mechanical and thermal properties of Nylon 12CF provided by Stratasys.

Nylon 12 CF Mechanical Properties	**XZ Axis**	**ZX Axis**
Ultimate Tensile Strength (MPa)	53.4	28.8
Tensile Modulus (MPa)	7515	2300
Elongation at Break (%)	1.9	1.2
Yield Compressive Strength (MPa)	N/A	N/A
Glass transition temperature (°C)	41	

Table 13. Mechanical and thermal properties of injection moulded Ultem 1000 provided by Sabic.

Ultem 1000 Mechanical Properties	**XZ Axis**
Ultimate Tensile Strength (MPa)	85
Tensile Modulus (MPa)	3200
Elongation at Break (%)	60
Yield Compressive Strength (MPa)	N/A
Glass transition temperature (°C)	217

As a means of validating the experimental apparatus and methodology as well as comparing the FDM printed Ultem 1010 to a more traditional manufacturing method, injection moulded Ultem 1000 was chosen. This is a PEI that has nearly the same mechanical properties as ULTEM 1010, per Table 13, therefore the primary difference between the two will be their manufacturing method and the impact this has on surface finish, strength, and any other physical/mechanical properties. These results could then be directly compared to those for the Ultem 1010 printed specimens. For Nylon 12CF, there is no literature or traditionally manufactured equivalent to compare to. Neat polyamides have been studied for wear properties and provide some basis for comparison [129, 161, 171], however it would be anticipated that the brittle nature of the carbon fibres will deviate from the results found in literature for neat Nylon. Because of this, the literature results for other polymeric based composites in addition to studies done on PA12 are used.

The final material used is the austenitic stainless steel UNS S31600 (chemical composition shown in Table 14) which was used as a reference material in order to ensure calibration of the closed loop submerged jet impingement rig. This steel was chosen due to its generally good corrosion resistance and ensured consistency across all tests [172]. The specimens are 38 mm in diameter with varying thickness. This is because the samples are grinded down and reused for future calibrations.

Table 14. Nominal chemical composition (wt%) of UNS S31600 [172].

	C	Cr	Ni	Mn	Si	Mo	S	N	P	Fe
UNS S31600	0.08 max	16-18	10-14	2 max	0.75 max	2-3	0.03 max	0.1 max	0.045 max	Bal

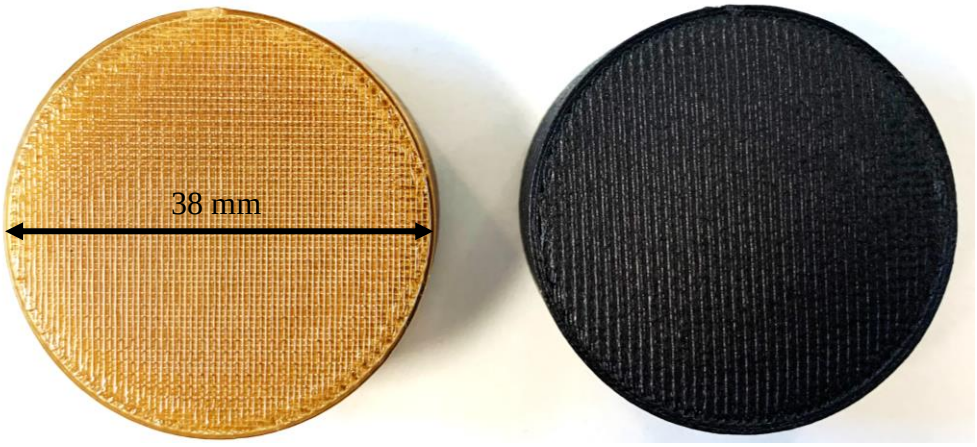

Figure 91. Photo of the surface of Ultem 1010 and Nylon 12CF specimens used for erosion testing.

As in the hydrocyclone case study, the specimens were printed using FDM on the Stratasys F900. These were provided by the industrial partner and SYS Systems. All parts were printed with 100% infill density and 0.254 mm layer thickness. The specimens were printed to dimensions of 38 mm diameter with 17 mm thickness. The specimens were printed with an XY orientation, meaning that the diameter was flat on the bed and the thickness was built up with 0° and 90° alternating layers and a circumferential contour.

According to the manufacturer, Nylon 12 CF consists of 35 wt% carbon fibres with an average length of 6 mm. Due to the method of printing, there is repeated roughness created on the surface. This roughness consists of parallel lines of material that have been deposited by the nozzle. Figure 92 shows a photo of the surface in which a grid-like pattern is visible. Because of the translucent nature of Ultem 1010 layers below the surface are able to be seen as well, in comparison to the opaque Nylon 12CF.

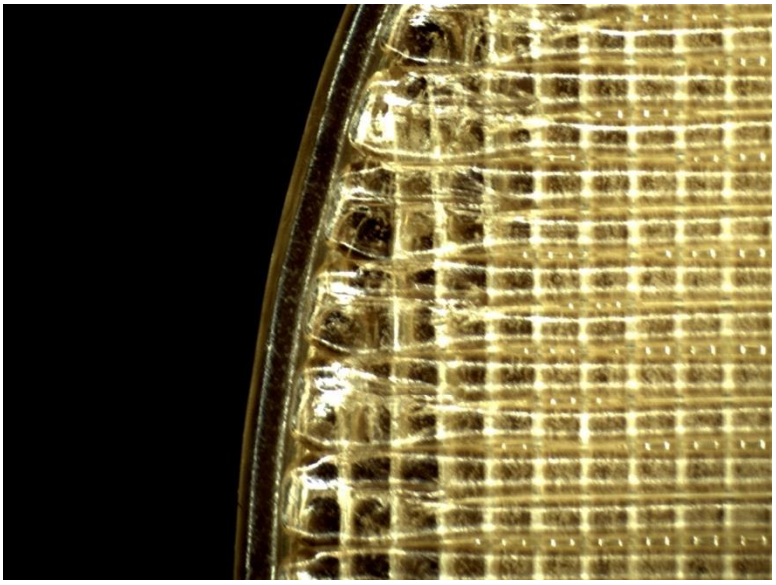

Figure 92. Photo from optical microscope of the surface of an Ultem 1010 wear specimen.

This roughness is repeated on both sides of the specimen, however because the cylinder shape was printed to build thickness one of the sides was in contact with the printing bed. This side contains damage due to manually removing the material from the printer. This is apparent via visual inspection. Because of these flaws, only the surface that was printed last was used for testing.

The injection moulded PEI (manufacture by Protolabs) via injection moulding Protolabs utilises injection moulding in order to make sample placards that are distributed to potential customers in order to demonstrate the differences in surface finish for their available manufacturing methods. The front of the placard has ridges, as shown in Figure 93, and the back of the placard has a smooth surface created by the injection moulding. Specimens with a 38mm diameter were then cut from the placards using a water jet.

Figure 93. Ultem 1000 injection moulded placard showing water jet cut specimen for wear testing.

The experimental apparatus and basis for the testing methodology were originally developed by Giourntas [3] to test metallic materials. For the testing of erosion and corrosion this method was validated and further used for research [172]. In order to validate this testing apparatus for erosion of polymeric materials, the ability to adequately compare back to literature was necessary. Erosion rates are highly dependent on the parameters of the test; however, literature is used as a baseline to compare general behaviour. At the time the experiments were conducted there was no literature found in which the performance of additively manufactured materials subjected to slurry erosion were available in order to replicate testing methodology. In the time after, two papers exploring solid particle erosion of FDM printed materials were published [167, 168] and could be used as a basis of comparison for the analysis of results. For traditional methods of manufacturing (i.e., injection moulding) there is a wealth of knowledge on the behaviour of polymeric materials as demonstrated in Chapter 4.

5.2.1 Material Characterisation

The roughness of the surface was measured using the Mitutoyo SurfTest apparatus. The measurement was in accordance with BS EN ISO 4288 which specifies that the stylus move over a minimum of 4mm of the surface [173]. For these readings the stylus moved over 7.5 mm of the surface at a speed of 0.1 mm/s with a maximum

height/depth range of 800 μm and 18000 points. A minimum of four readings were taken for all specimens and then averaged to calculate the average roughness (Ra) for each material prior to testing.

The hardness of the material was measured using the Sauter HBD 100-0 Shore D Durometer. The precision is 3% of the 100 Shore D maximum.

5.3 Epoxy sealing

As discussed in Chapter 3, any materials used in the application of hydrocyclones are required to pass a certification by pressurising to 3 bar. Due to the intrinsic nature of materials manufactured via FDM, a repeated pattern of porosity is created within the material. Epikote M135, cured with Epikure M134 & M137 hardeners, was used to seal the FDM printed specimens to be tested under the same conditions as all other specimens. The epoxy and hardeners were mixed & cured according to the methodology in Chapter 3. The specimens were submerged in the resin for 10 minutes and then removed. As the goal is to seal the internal porosity, any epoxy on the surface was removed manually by wiping excess away. As with the sealing of the vessel for pressurisation experiments, it was necessary that a method for sealing that was simple and accessible was employed. By submerging and manually removing excess, the process can be completed quickly and with minimal investment in tooling. This method resulted in a surface that inevitably maintained some surface roughness due to the nature of the printed material as well as variation due to the manual removal of liquid uncured epoxy. As the purpose of this process is to seal the internal porosity, the epoxy in pores below the surface is the priority for the industrial sponsor. The purpose of exposing these specimens with remnants of the epoxy remaining is to understand how this will affect the erosion rate and mechanisms if this method of sealing were to be employed on the hydrocyclone prior to service.

Figure 94. Submerged FDM printed Ultem 1010 specimens in epoxy resin.

5.4 Pre-test methodology

5.4.1 Preparation of specimens

Before the specimens are tested a visual inspection of the material is necessary. Due to the XY printing orientation, the FDM printed specimens have two distinct sides; that which was in contact with the printing bed and that which was the final layer printed. That which was in contact with the printing bed has a higher degree of consolidation and existing flaws due to interaction with tools when removing the specimens from the bed. Due to the differences in consolidation of layers, only the top surface was tested to ensure consistency. This approach was also used for the sealed FDM printed specimens. As discussed in Section 5.2, the Ultem 1000 injection moulded samples only have one side suitable for testing.

5.4.1.1 Calibration specimens

In order to create a smooth surface free of major scratches and defects the stainless-steel calibration specimens were grinded using three increasingly finer grits: 500, 800 and 1200 SiC grit papers. This resulted in a finish of 0.07μm Ra. This was done to all calibration samples in order to maintain continuity. After grinding, the specimens were cleaned with methanol to remove debris and dried.

5.5 Erosion testing procedure

5.5.1 Testing protocol and apparatus

After any necessary surface preparation was performed the specimens were cleaned and weighed before testing was conducted. The specimens were stored in sealed bags at ambient temperature and humidity. Each specimen was weighed five times on the Sartorius Entris mass balance with an acceptable tolerance of ±0.5 mg. The balance was calibrated to an accuracy of ±0.3 mg prior to use.

Once the weight before the test was recorded, the specimen was placed into the holder for the erosion rig shown in Figure 95. In order to ensure consistent distance between the nozzle and the specimen, a 5 mm thick Perspex disk was placed between the edge of the nozzle and the surface of the specimen. This was removed prior to testing. A spirit level was used to ensure that the nozzle holder was balanced. Polytetrafluoroethylene (PTFE) tape was used to ensure that there is no gap between the specimen and the cavity of the holder. This guarantees that the specimen did not move during testing and that sand from the slurry did not become entrapped in the cavity. This can be seen as the white layer in Figure 95.

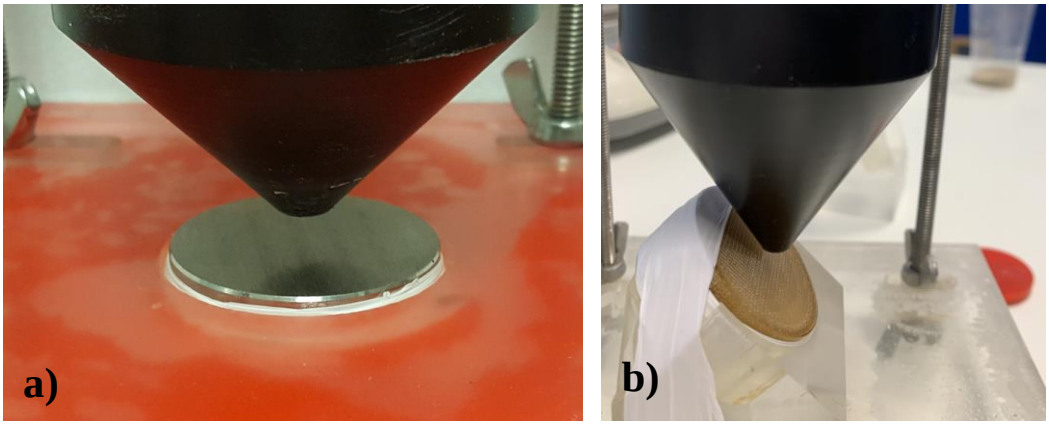

Figure 95. a) Specimen for 90 degree testing in holder showing distance from nozzle [172]; b) Ultem 1010 specimen in holder for 45 degree impingement test.

For Ultem 1010 and Nylon 12 CF at 45° and 20° impingement angles the specimens were also rotated so that the tangential component of the slurry flow to the rasters of the top layer of printed material was 0° and 90° as shown in Figure 96. This placement was done by visual inspection as the direction of the top layer of the material is apparent.

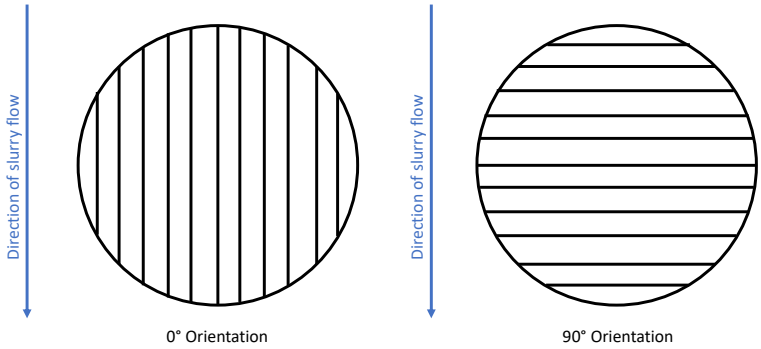

Figure 96. Schematic of 0° and 90° orientation of flow to top layer used for 20° and 45° impingement angles.

Once the specimen was secured in the holder the rig is prepared for the test. The tank of the recirculating rig is filled with 33L of water pre-heated to 40°C. The water was pre-heated in order to keep the temperature consistent throughout the duration of the

test. The pump generated heat as it operated, and it was found that by using water at 40°C the effect was eliminated. All testing parameters are shown in Table 15 followed by the matrix of tests for each material in Table 16.

Table 15. Wear testing parameters.

Parameter	Value
Velocity	19 m/s
Type of sand	400-500 µm angular silica sand
Nozzle diameter	4 mm
Sand Concentration	0.34 g/L
pH	7
Temperature	40°C
Impingement angle	20°, 45°, 90°
Test duration	1 hour

Table 16. Materials for slurry erosion testing.

Material	**Impingement angle**	**Type of test**
ULTEM 1010	90°	1 hour slurry erosion test
Nylon 12CF	45° & 0° w.r.t. raster	
ULTEM 1010 (epoxy sealed)	45° & 90° w.r.t. raster	
Nylon 12CF (epoxy sealed)	20° & 0° w.r.t. raster 20° & 90° w.r.t. raster	
ULTEM 1000	90°, 45°, 20°	
Stainless steel UNS S31600	90°	

The specimen holder was then attached to the piping and submerged within the water. A single speed pump was used to circulate the water. Once the pump was turned on and the water is circulating the necessary amount of sand based on the calibration of the rig is added to create a slurry. The schematic in Figure 97 shows the set up for the impingement rig and Figure 98 shown an example of a submerged specimen. The pump designated as ‘P’ recirculates the slurry and impinged the sample designated as ‘S’. The pump used was an Ebara JESX M5 single phase pump with an operating head range of 11.5-32 m and a potential flow rate of 5-45 L/min. The attached piping and tank were made from commercially available prefab polyvinylchloride (PVC).

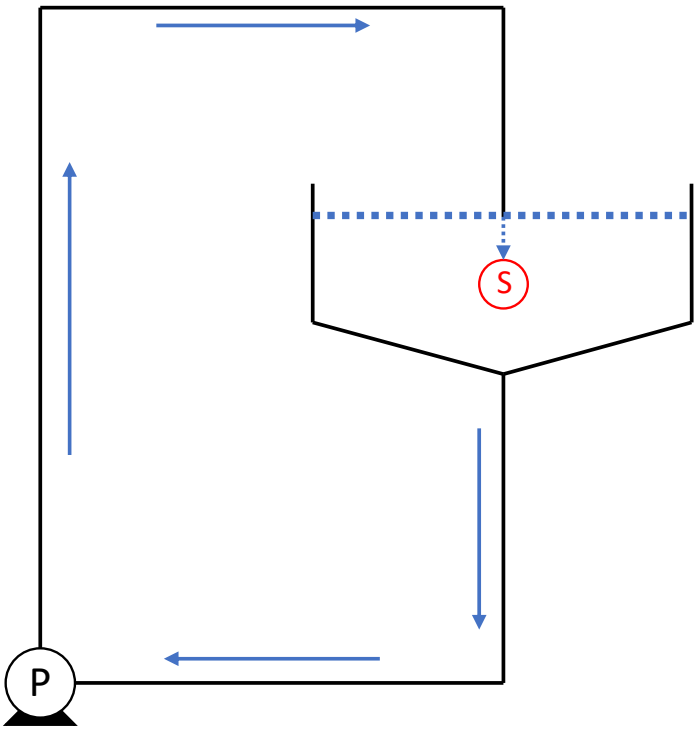

Figure 97. Schematic of recirculating slurry impingement rig.

Figure 98. Sample submerged in impingement rig.

After the completion of the 1 hour test, the specimen was removed and weighed per the protocol above for pre-test measurements. Due to the porosity created by the FDM process, the printed samples underwent a drying protocol that is detailed in Section 5.5.1.1. This was then compared back to the initial weight to determine the amount of material lost.

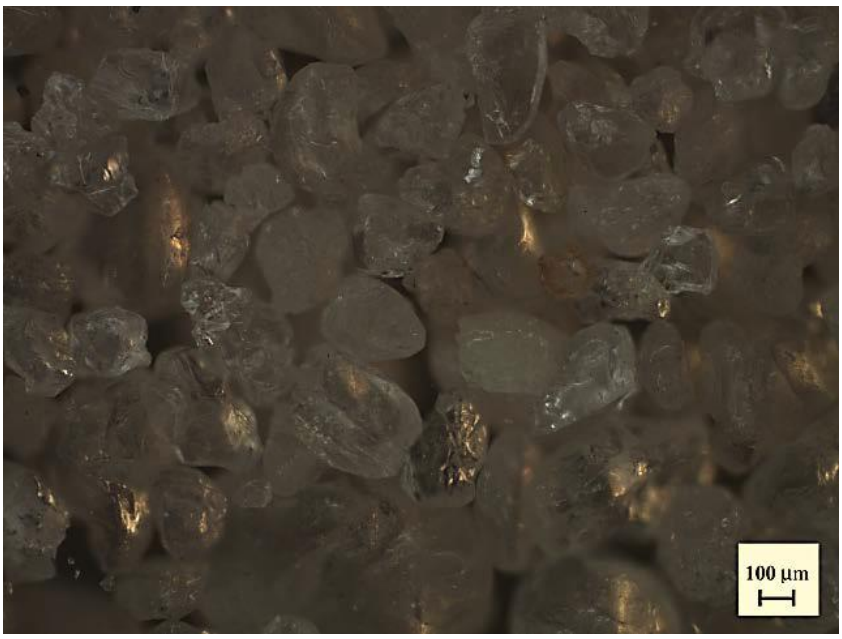

Figure 99. Angular silica sand used for testing with a size range of 355-500 µm [3].

.

Figure 99 shows the sand prior to testing. This will degrade during the test into finer particles. After each test the rig is completely cleaned of all slurry to ensure there is no interference with future tests.

5.5.1.1 Drying of specimens

The mass of the specimens after testing was higher than initial mass. In order to determine if this was due to water uptake, either due to internal porosity from FDM or the hydrophilic nature of the polymers, or sand that had become embedded two steps were taken. The first was drying the samples at elevated temperatures to see if the mass

reduced and the second was examining the specimens using X-ray computed tomography (XCT) which will be described in Section 5.6.

The first study to understand the water uptake was to place the samples in an oven at 60°C for a period of 4 hours. The results of this are seen in Figure 100. As shown the mass does reduce for both the Ultem 1010 and Nylon 12CF specimens, however at this temperature and for this duration the mass does not go below the initial mass before testing.

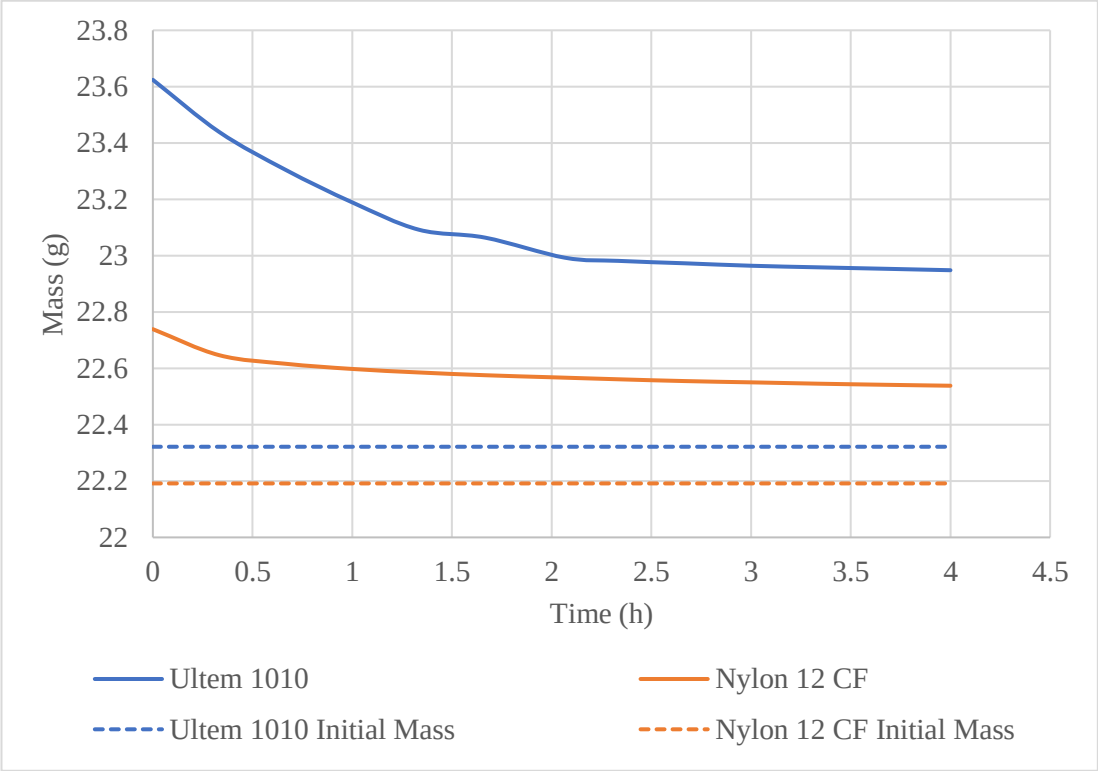

Figure 100. Mass of specimens during drying at 60℃ over 4 hours.

In order to ensure all water was removed, the specimens were dried in an oven at 120°C for 24 hours. The specimens were then left to return to ambient temperature and humidity over a period of 7 days (the conditions at which the specimens were weighed

pre-test). After this drying regime the Ultem 1010 samples were, on average, 100 mg lighter while the Nylon 12CF were 66 mg lighter than the post-test mass.

5.5.1.2 Calibration of testing rig

The stainless steel specimens were subject to the same testing protocol as the polymer samples, with the exception of the post-test drying. As the stainless steel is not porous nor does it exhibit uptake of water during testing, the specimen was cleaned and dried before weighing.

The rig was calibrated by running an initial 1 hour test in the test rig with 40 g of sand. This resulted in an initial mass loss of 6.8 mg which was considered the baseline for all future tests. After every 5 tests the rig was recalibrated. If the mass loss went down, more sand was added until the mass loss of the steel specimen was within ±0.5 mg of the 6.8 mg baseline. The rig was calibrated this way to keep consistency with the erosive properties of the initial test so that the slurry's effect is consistent throughout all tests.

The single speed pump used loses efficiency over time as its own impeller degrades. When sand beyond 3 g of the original 40 g was needed the efficiency of the pump was considered to be too low to continue to use and it was replaced with a new pump. This was then recalibrated to determine the amount of sand needed to achieve the 6.8 mg baseline. Because of this the sand concentration provided in Table 15 is an estimate and will slightly change after each calibration.

5.5.1.3 Flow velocity and sand concentration measurements

The flow velocity was measured per the protocol for use of the erosion rig [172]. The tank is filled with 33 L of water and the amount of sand used for the test (approximately 40 g). The pump is run for 15 minutes to move the slurry. After this point, a hose is attached to the nozzle and the slurry is collected in a separate vessel for 20 seconds. The vessel used is a large 10 L beaker so that the volume collected can be calculated. From this, the velocity of the slurry at the nozzle was calculated using the equation below.

$$v = \frac{Q}{20 \times \pi r_n^2} \quad (5\text{-}1)$$

Where v is velocity (m/s), Q is the volumetric flow rate (m^3/s), and r_n is the radius of the nozzle (m). The slurry collected was then passed through a sieve in order to separate the sand. This sand was thoroughly dried then weighed on the Sartorius Entris balance. From this, the sand concentration per litre was be calculated. This was performed with each calibration test in order to maintain consistency throughout the experimental phase.

5.6 Post testing analysis techniques

5.6.1 Macro examination

Macro examination included visual inspection of the specimens and review of photos to determine the main wear zones. Specimens exhibited a main wear scar and a secondary wear zone after the sand has left the main scar and slides over the remaining surface. The wear scar shape was distinctive for each impingement angle, irrespective of material. However, the size and depth of the scar differed between materials. Images were taken of the surface using a single-lens reflex (SLR) camera.

5.6.2 Study of material loss

As described in the testing protocol the specimens were weighed prior to the erosion test and then again following the drying protocol. The mass loss was calculated outright by subtracting the final mass from the initial mass. For a specific material the volume lost was calculated by dividing the mass by the density of the material. These values were compared to the material properties or used to calculate further values such as erosion rate and erosion efficiency using the equations introduced in Chapter 4, Section 4.2.2. This will be further discussed in Chapter 6, Section 6.2.2.

5.6.3 Surface topography

As with the surface roughness measurements, the Mitutoyo SurfTest was also used to obtain a 2D visualisation of the depth of the wear scar. This was done by selecting the

Ry depth measurement as the parameter of interest. The stylus measured a length of 7.5 mm at a speed of 0.5 mm/s measuring 16600 points. This was performed for the 90° impingement angle specimens in order to compare the shape of the crater to the calculated Stokes number to verify the experiment was in line with expectations from literature [104]. The depth of all impingement angles was then analysed and used for characterising the material loss in the wear scar after testing.

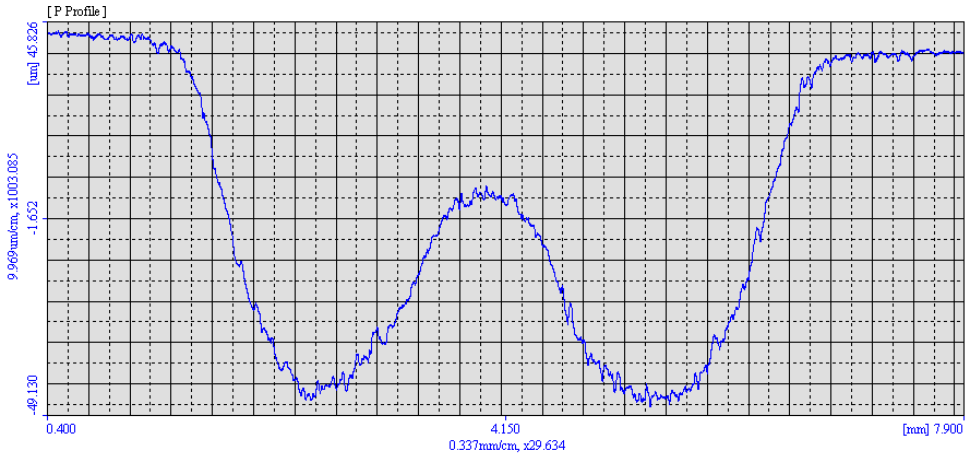

Figure 101. Example of wear scar depth 2D topography for 90 ° impingement angle as measured on the Mitutoyo SurfTest.

5.6.4 X-ray computed tomography and image analysis software.

For further analysis of the internal structure of the specimens and to determine if sand had become embedded in the material a Nikon XT H 225 LC X-ray computed tomography scanner (XCT) was used to create 3D data sets of chosen specimens. This XCT uses 225kV X-ray source of reflection and transmission in order to create a stack of images. These slices were then reconstructed to form a 3D volume that can be used for analysis via software such as Image-J, Dragonfly or Avizo. The resolution of the images is dependent on the size of the specimen. Smaller specimens will result in higher resolution.

Images obtained via XCT will contain data in the form of varying brightness on a grey scale. The brighter a section of the image, the higher the density. For example, air would be displayed as black while a solid material such as sand would be displayed as a light grey or brighter white depending on the limits of the thresholding. In the data analysed for the purposes of this study there were 3 or 4 materials present: air, target material (Ultem 1010, Nylon 12 with CF) and silica sand. By thresholding the image and isolating the bright areas that correlate to sand, the volume of sand was calculated. This was provided in the form of voxels (3D pixels) and can be translated to area in μm^3 via the resolution of the image.

The main functions of the software that were used were thresholding and image segmentation. Segmentation is the process of partitioning an image into sets of pixels. The sets can then be analysed separately from the whole image. Segmentation is done with respect to a characteristic of the pixels such as colour or intensity. Because of the nature of the images produced by XCT (grey scale), intensity (or brightness) is used to segment the sand from the specimen material and air.

Image-J is an open source software used for image processing. It can display the stack of images and create 3D visualization. Segmentation in Image-J is done by creating a binary image where the desired range of intensity can be isolated via thresholding. The two constituent parts (pixels that fall inside the threshold area vs. everything outside) are then assigned as either white or black. Initial visualisation of the data was completed using Image-J, however due to the size of the data a more robust software was used for computation.

Avizo is an image analysis software used for visualisation and computation of data sets. This software was used to analyse the amount of sand that was present on the specimens after testing. Imaging of the cross section of the material, which can provide insight to the manufacturing method and the anticipated porosity due to the behaviour of the material during printing, was also produced.

The first step for analysis in Avizo is loading the data and inputting the resolution. In order to calculate the volume of sand within the sample it must be separated from the

air and specimen material via thresholding. As the image contains a large volume of air and some scatter a 3D cropping tool is used to eliminate as much air as possible and isolate the specimen. Once this is done the interactive thresholding tool is used to isolate the sand. The distribution of intensity of pixels is displayed as a histogram. Using the tool, sections of the histogram can be chosen to be displayed while everything outside of the region will be displayed as black which is synonymous with 'void'. The density of the sand is much higher than that of the Ultem 1010 or Nylon 12CF, therefore is it easy to visualise as the histogram is narrowed. A new data set containing only sand is created. This is then used as a mask to apply over the data set containing all solid materials (sand and specimen). From this the sand particles can be visualised as coloured elements overlayed on the total volume. Using label analysis, the sand particles' volume and diameter are calculated and provided in the form of a .csv file. The output of this analysis is therefore any visualisation that aids in understanding the material and wear as well as the calculation of volume of sand.

5.6.5 Microscopy

Two optical microscopes were used to examine the surface of the specimens. The first was a Yenway stereo microscope which was used to view the worn surface of the specimens and perform distance calculations on the accompanying software. This microscope only provided magnification up to x135, however, was capable of viewing a larger surface area. The second is the Olympus GX51 light optical microscope which provided magnification up to x1000. It was used for specimens that were cut along the length of the wear scar in order to observe any cracking that occurred below the surface. An example of these specimens is shown in Figure 102. Once cut, they were cast in a clear epoxy that could then be polished. This kept any fragmented material in place. Sealed samples were cut and polished, but were not set in additional epoxy, in order to determine the penetration of the epoxy sealing.

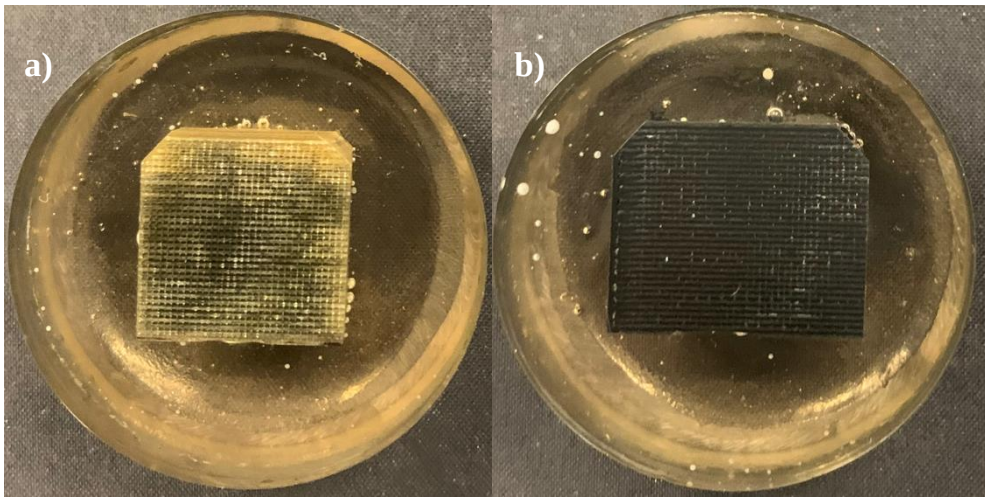

Figure 102. a) Ultem 1010 and b) Nylon 12 CF specimens cut to view cross section and cast in epoxy.

The Hitachi S-3700 scanning electron microscope (SEM) was used in order to determine wear mechanisms present at magnifications beyond the capability of the Olympus GX51. Additionally, use of light optical microscopes results in lower quality images for the reflective materials such as Ultem 1010.

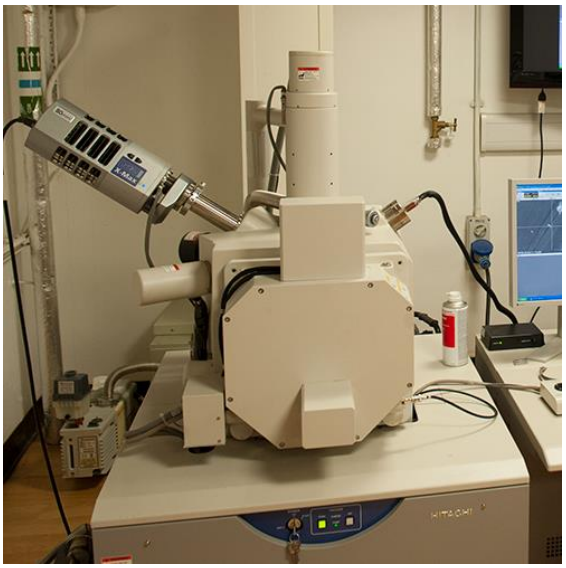

Figure 103. HITACHI S-3700, a variable pressure, tungsten filament, large chamber 300mm x 110mm, scanning electron microscope.

SEMs work by using the conductivity of the sample. Sputter deposition is used to cover the specimen with a thin layer of gold. This is done by placing the specimen in a chamber where a pump is used to create a vacuum. The chamber is then filled with argon and the sputtering gas is released in order to create the film. The sputter coating protects the material from being charged by the electron beam of the microscope. For the majority of images, the secondary electrons were used in order to perform topographical analysis of the worn surface. When sand was observed, backscattered electrons were used for elemental analysis, however, the XCT images and analysis provided a better understanding of where sand was present on the surface.

6. Assessment of the erosion behaviour of additively manufactured polymers and polymer composites

6.1 Introduction

The durability of mineral processing equipment, such as the hydrocyclone, is dominated by the wear of the material [174]. In order to better understand the potential of additively manufactured materials in these applications without erosive protection, such as natural or synthetic rubber liners, a fundamental study of the behaviour of materials under slurry wear conditions was undertaken. This chapter will discuss the results of the experiment and post-test analysis performed using the methodology presented in Chapter 5.

6.2 Validation of experimental methodology

The experimental methodology and materials used for this study were pre-determined by the industrial partner. As seen in literature, the erosion rate of a material is highly dependent on not only the physical properties of the erodent and target material, but also the experimental parameters [110, 132, 175]. For this reason, it was necessary to keep these parameters consistent with previous work done by the industrial partner in order to compare the results back to the existing body of work for metallic, ceramic and rubber materials [3, 127, 172].

The methodology was validated by Giourntas and used in successive projects investigating slurry erosion [3]. The basis for the validation was on the erosion corrosion of metallic materials, therefore further validation was necessary in order to assure that the protocol created comparable results for polymeric materials.

6.2.1 Trajectory of sand particles

In Chapter 4 the Stokes number was introduced for describing particle entrainment, trajectory, and profile of the erosion. The value of the Stokes number will indicate whether the erosion profile will have a 'W' or 'U' shape [104, 176]. It is entirely dependent on characteristics of the fluid flow, apparatus and particle used for erosion as seen in the equation (6-1).

$$St = \frac{\tau_p U}{D} \tag{6-1}$$

Where St is the Stokes number, U is the average exit velocity, D is the nozzle diameter and τ_p is the characteristic time of the particle defined in equation (6-2).

$$\tau_p = \frac{\rho_p d_p^2}{18\mu_f} \tag{6-2}$$

Where ρ_p is the particle density, d_p is the particle diameter, and μ_f is the fluid viscosity. The Stokes number is not dependent on characteristics of the material that is impacted. Therefore, if this number is calculated for a given experiment it should predict the shape of the damage created by erosion for any given material at normal impact. As shown in Figure 104, a low Stokes number would result in a 'W' shaped erosion profile.

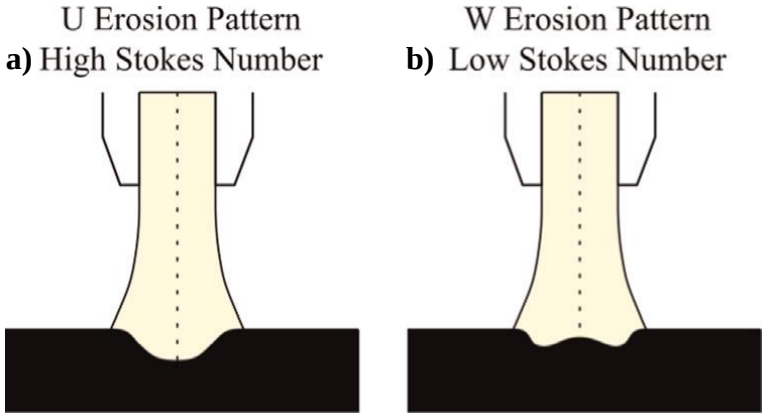

Figure 104. a) U erosion profile and b) W erosion profile [104].

When the Stokes number << 0.1, particles will closely follow the streamlines of the fluid with acceptable flow tracing accuracy errors below 1% [177]. For this experiment the following parameters were used to calculate the Stokes number as 2.17E-7. This value is very low, thus a 'W' shaped erosion profile in which the particles follow the streamline of the flow as they exit the nozzle and impact at the outer edge of the nozzle is expected (see Figure 105).

Table 17. Parameters of experiment for calculation of Stokes number.

Parameter	**Value**
Particle density (ρ_p)	2.65 g/cm^3
Average particle diameter (d_p)	450 μm
Dynamic viscosity of water at 40°C	0.6531 mPa s
Characteristic time of particle (τ_p)	4.56E-11 s
Average exit velocity (U)	19 m/s
Diameter of nozzle (D)	4 mm
Stokes number	2.17E-7

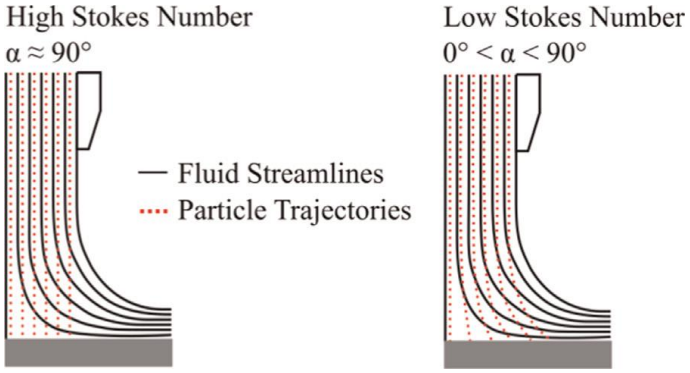

Figure 105. Fluid streamlines and particle trajectories [104]

In order to determine the profile of the wear scar, the Mitutoyo SV-2000 Surftest profilometer was used as described in Chapter 5. Figure 106 to Figure 110 display typical profiles for 90° impact for each polymeric material tested.

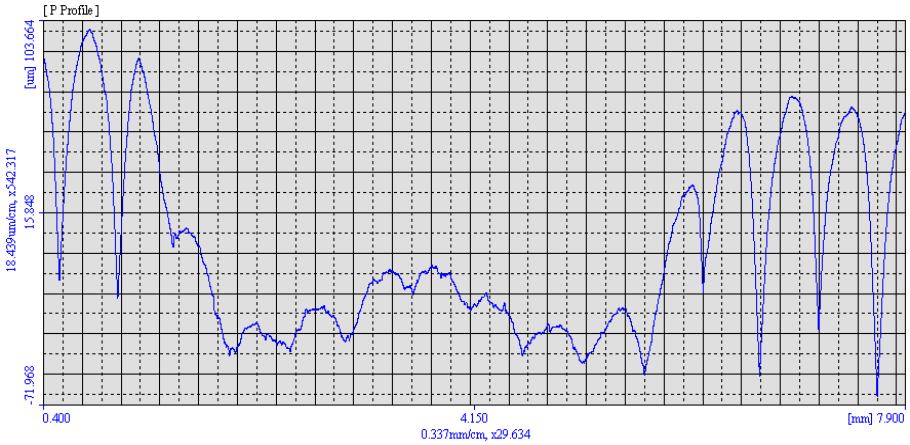

Figure 106. Wear scar profile of Ultem 1010 at 90° impact angle.

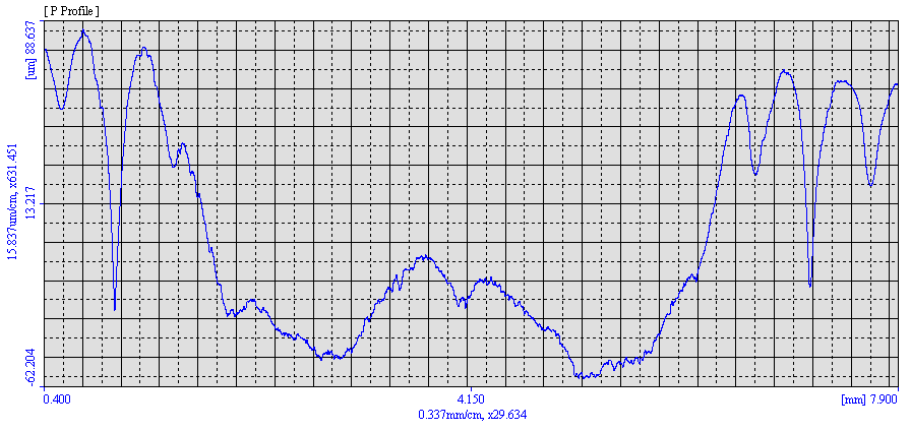

Figure 107. Wear scar profile of Ultem 1010 sealed with epoxy at 90° impact angle.

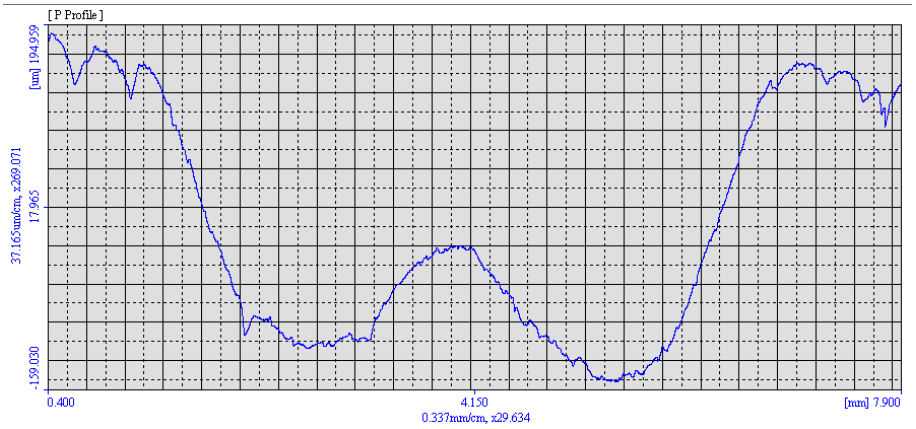

Figure 108. Wear scar profile of Nylon 12CF at 90° impact angle.

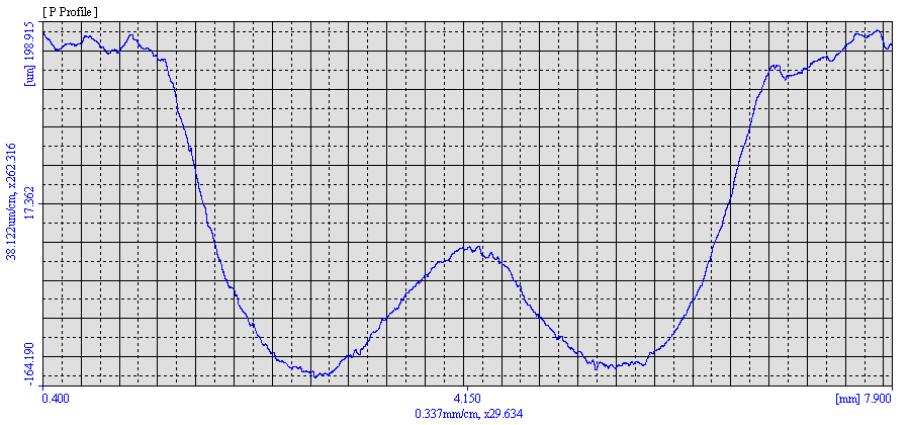

Figure 109. Wear scar profile of Nylon 12CF sealed with epoxy at 90° impact angle.

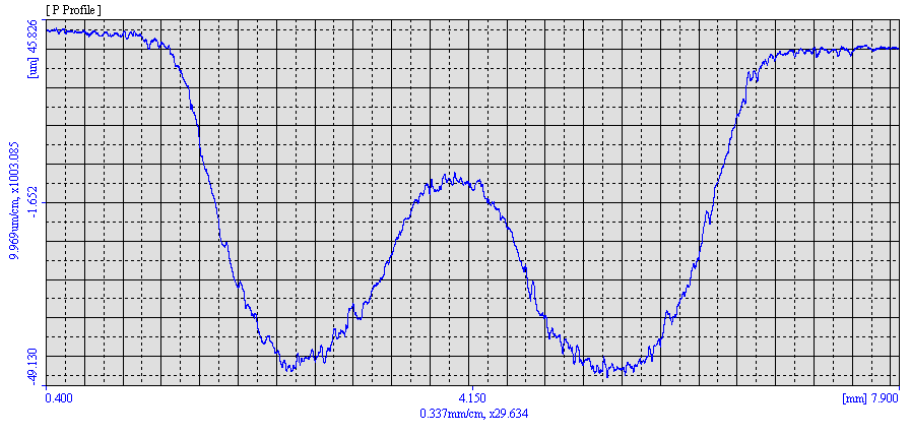

Figure 110. Wear scar profile of Ultem 1000 at 90° impact angle.

A clear 'W' shaped profile can be seen in all examples. The nozzle was designed to reduce turbulence in the flow by ensuring that the length of the nozzle was 10 times the diameter of the nozzle [178]. This design results in a stagnation point approximately at the centre of the flow. Previous research conducted on these erosion rigs at the University of Strathclyde yielded the same erosion profile [3, 172].

For the additively manufactured specimens, the profile was measured by dragging the stylus at a 90° orientation to the rasters of the top layer, thus the influence of the printing pattern on the wear scar profile is visible. This is in comparison to the Ultem 1000 specimens which were manufactured by injection moulding and therefore have a smoother finish.

Comparing the profile of the wear scar for all materials at 90° impact angle to the anticipated profile from the calculation of the Stokes number, it is clear that the experiment is behaving as expected with particles impinging the target material normal to the surface and the anticipated stagnation point present.

6.2.2 Erosion Efficiency

As discussed in Chapter 4, there is a wealth of knowledge on the behaviour of traditionally manufactured polymers and polymer composites [110-143] when subjected to solid particle erosion. As the conditions for each experiment varied,

authors [121, 123] found that it was necessary to find a way to interpret the results across literature in order to create substantiated claims about the wear mechanisms exhibited. One such technique was the use of the erosion efficiency parameter.

Erosion efficiency was first introduced in 1990 by Sundararajan et al. for metallic and ceramic materials [123]. In 2006, Arjula and Harsha used this method and applied it to existing data for erosion of polymers and polymer composites in order to map the efficiency value that correlates to different material behaviour [121]. The erosion efficiency is defined in equation (6-3).

$$\eta = \frac{2EH}{\rho v^2} \tag{6-3}$$

Where η is erosion efficiency, E is the erosion rate (defined as mass loss of target material over mass of the erodent used), H is hardness of the target material, ρ is density of the target material and v is the velocity of the erodent at impact. The hardness (H) is in MPa over the projected area and calculated by multiplying the Vickers hardness by a factor of 9.807.

For neat PEI, Harsha and Avinash found that the main wear mechanisms were micro-cutting and micro-ploughing at low impact angles and micro-cracks at normal impact with peak erosion rate at 60° [124]. Peak erosion occurring between 45-60° for thermoplastic polymers indicates semi-ductile behaviour [125]. The study of the erosion efficiency of polymers and polymer composites found that efficiencies between 1-10% were associated with ductile behaviour and erosion mechanisms involving the displacement of material (i.e., micro-ploughing). Brittle behaviour is associated with erosion efficiency of 100% where interlinked micro-cracks results in complete removal of the material. Values that lie between 10-100% are indicative of semi-ductile behaviour in which a combination of mechanisms are present.

In order to validate the experimental apparatus and methodology, the erosion efficiency of the Ultem 1000 specimens (injection moulded PEI) was calculated to find

if it was in line with the expectation from literature of semi-ductile behaviour. The erosion rate was calculated by dividing the mass loss by the mass of erodent used. The velocity was measured to be 19 m/s and the hardness and density were provided by the manufacturer as 140 MPa and 1.27 g/cm^3 respectively.

Table 18. Erosion efficiency calculated for Ultem 1000 injection moulded specimens at corresponding impact angle.

Angle	Erosion efficiency
90	15%
45	16%
20	8%

The highest erosion efficiency, which corresponds to the highest erosion rate for Ultem 1000 specimens is seen at 45°. For both 45° and 90° impact, the efficiency falls within the bounds for semi-ductile behaviour. At the most acute impact angle of 20°, the efficiency is within the ductile range, however at the upper end of this. This is in line with evidence found at a similar angle of 30°, where the dominant mechanism was abrasion [126].

As the values calculated were found to be in accordance with anticipated behaviour of traditionally manufactured PEI, the methodology is considered to be valid for use with polymeric based materials.

6.3 Effect of velocity component and local impingement angle

Velocity components, V_0 is 0° from the surface of the specimen and V_{90} is normal to it as defined in equations (6-4) and (6-5).

$$V_0 = V \times \cos(\alpha) \tag{6-4}$$

$$V_{90} = V \times \sin(\alpha) \quad (6\text{-}5)$$

For an exit velocity of 19 m/s the following values are obtained:

Table 19. Velocity components in the tangential and normal direction for impact angles of 45 ° and 20 °.

Velocity component	**α = 45°**	**α = 20°**
V_0	13.44 m/s	17.85 m/s
V_{90}	13.44 m/s	6.50 m/s

At 90° impingement the wear mechanisms are highly dependent on the inherent brittle or ductile nature of the material. Brittle behaviour will result in the formation of cracks while ductile behaviour results in plastic deformation and flake formation [106]. At 45° and 20° the mechanisms of wear will be dominated by the velocity component. For 45° it is seen above that these components are equivalent, therefore there will be a combination of effects of cracking and plastic deformation as seen at 90° impact as well as the effects from low angle impact in which erosion rate will depend on the influence of surface texture and roughness. The effect of this roughness and texture will play an even more significant role at 20° where the V_0 component is larger than the V_{90}.

In addition to the global impingement angle, there is an effect due to the local impingement angle. As shown in literature, the printed filament does not achieve a perfectly flat surface and there is curvature maintained in the printed raster [156, 168, 179, 180]. A schematic of this is shown in Figure 111.

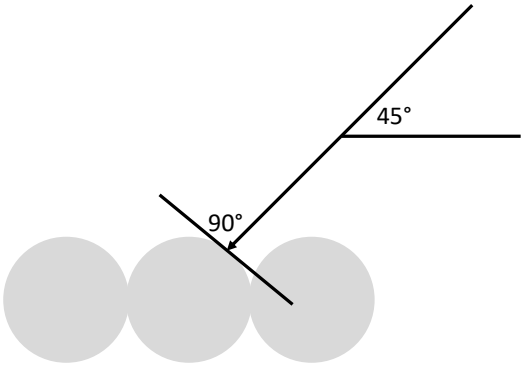

Figure 111. Orientation of sand particle to surface of printed layer at 45,90 orientation.

This local impingement angle will have an effect on the specimens that are tested at the 90° to raster orientation. This was confirmed when the 2D topography performed to measure the maximum depth of the wear scar. This was especially visible at 20°,90° orientation as shown in Figure 112. The worn left-hand edge of the rasters is clearly visible and the effect of this was considered when analysing the quantitative data from the experiments.

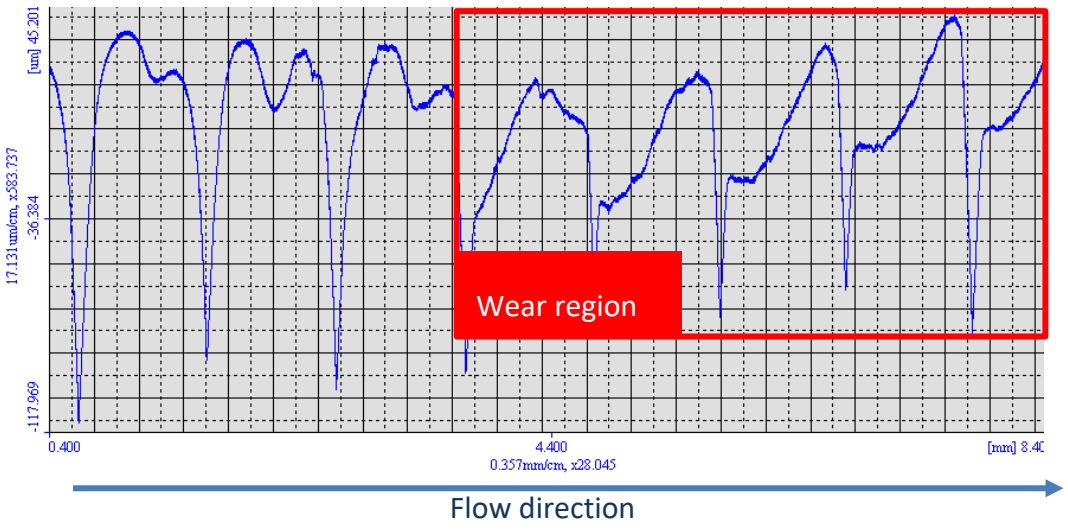

Figure 112. Example of effects of local impingement angle for orientations normal to the raster length from 2D profilometry.

6.4 Presence of epoxy within the specimens

To understand if the epoxy would have an effect, the Ultem 1010 and Nylon 12CF specimens were examined to determine if epoxy was present. After curing the specimens were weighed and it was found that the FDM printed Ultem 1010 specimens had a greater uptake of epoxy than the Nylon 12 CF counterparts as shown in Figure 113. This is because larger pores are seen in the Ultem 1010 material than the Nylon 12CF due to differences in melting temperature (this will be discussed further in Section 6.6.2).

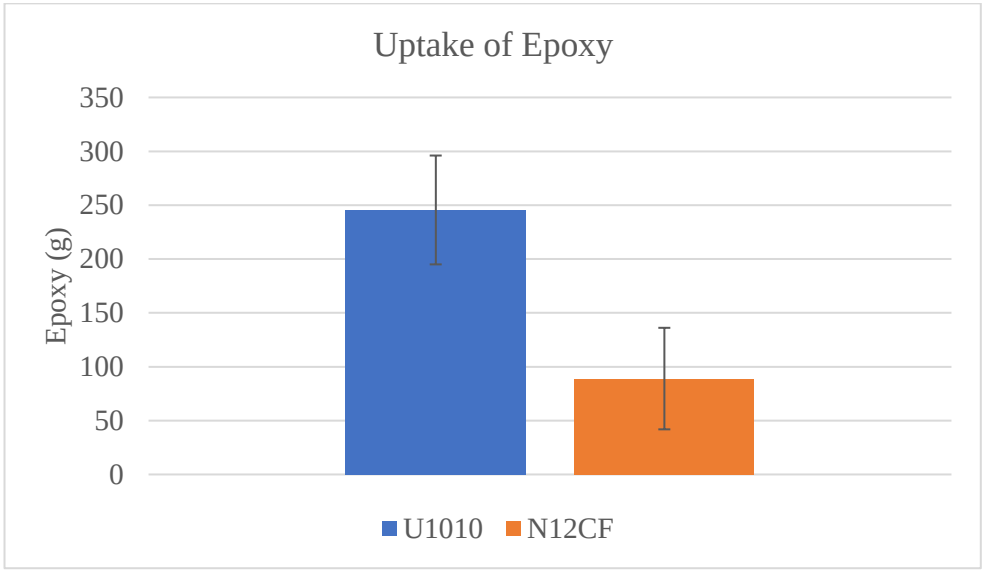

Figure 113. Uptake of epoxy in grams for FDM printed specimens for wear testing.

A sealed Ultem 1010 and Nylon 12CF specimen were cut in half perpendicular to the raster orientation of the top layer. These specimens were then ground and polished to view under the microscope as described in Chapter 5. Figure 114 shows epoxy that has penetrated approximately 4 layers of the Ultem 1010 with Figure 115 showing a close up of this.

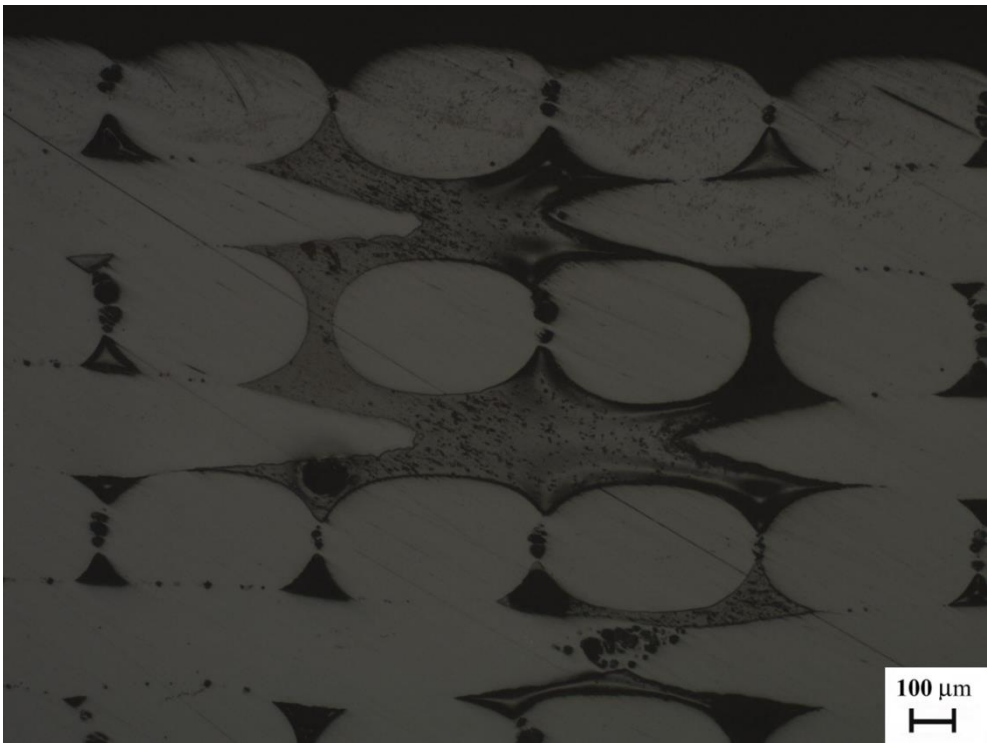

Figure 114.Sealed Ultem 1010 with epoxy visible between layers at x50 magnification.

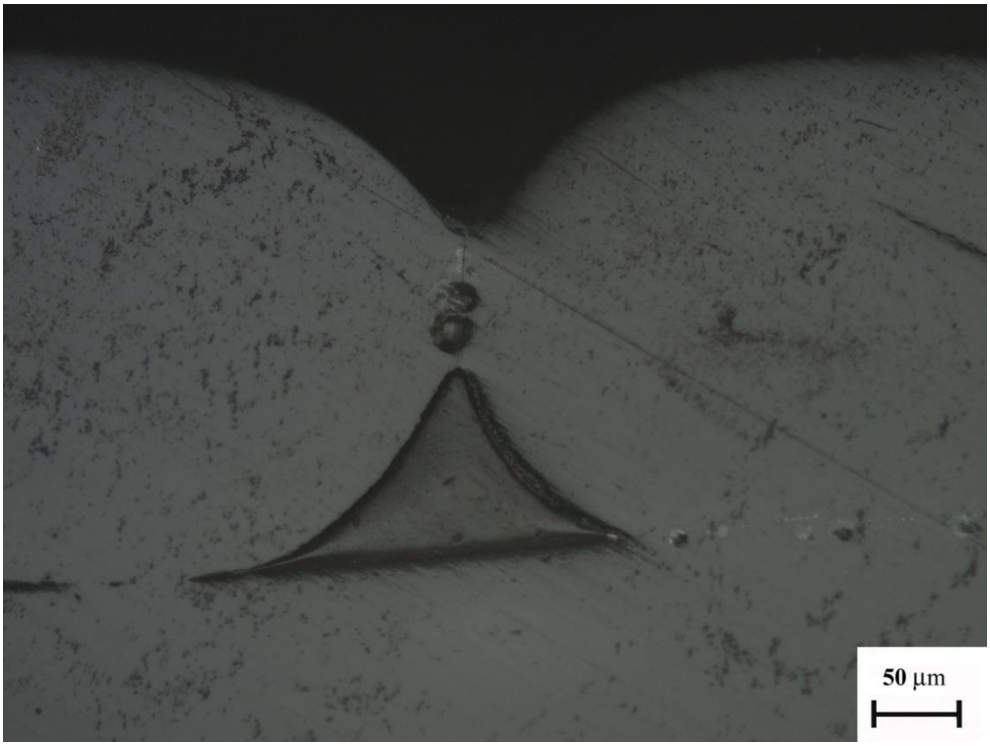

Figure 115. Sealed Ultem 1010 with visible epoxy between two rasters at x200 magnification.

The Nylon 12CF also had epoxy present between layers, but it was much harder to visualise in some areas due to the tighter network of porosity compared to the Ultem 1010. In areas where the rasters had some distance between them it is easily visible because the epoxy will not emit brightness compared to the Nylon 12CF filament in which the fibres appear very bright. This is shown in Figure 116 and Figure 117.

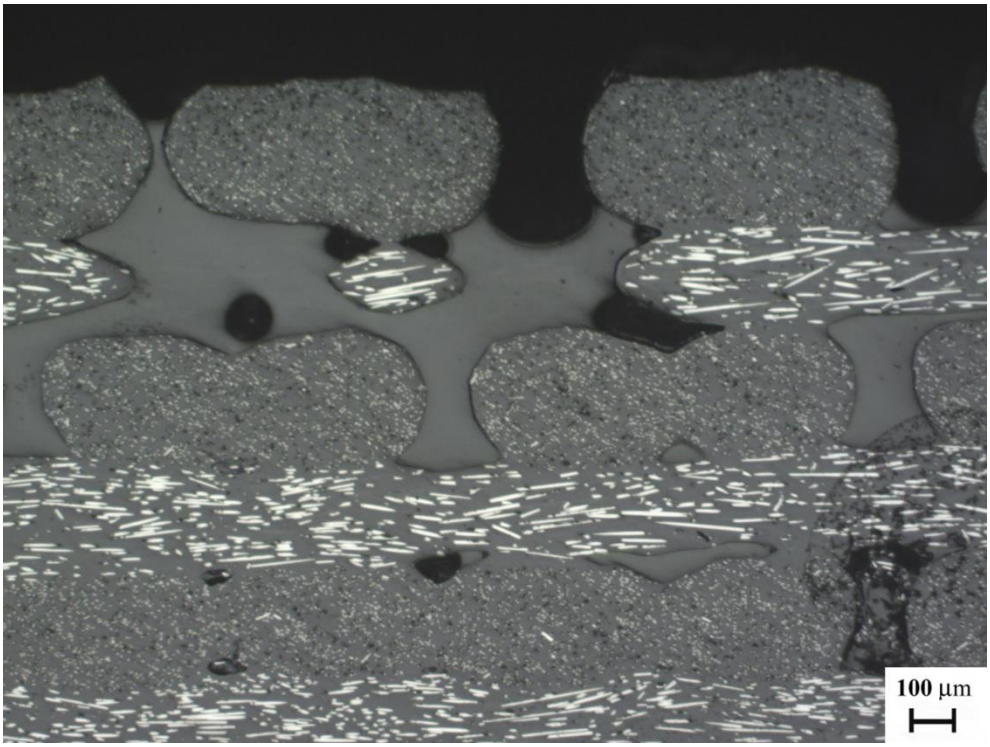

Figure 116. Sealed Nylon 12CF with epoxy between layers at x50 magnification.

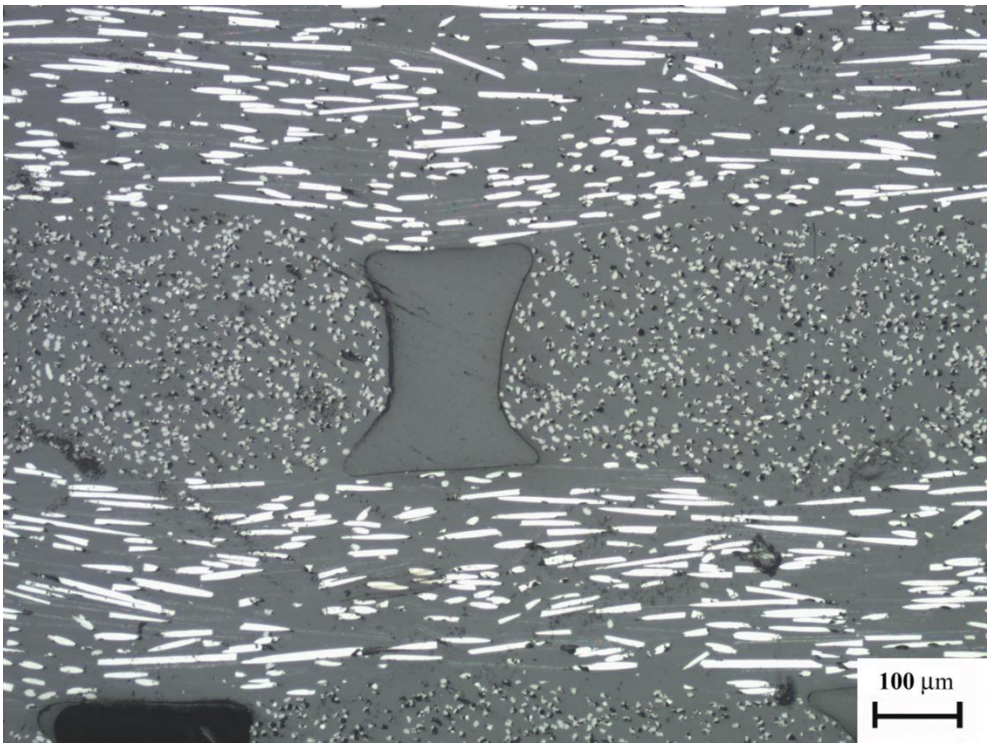

Figure 117.Example of epoxy between rasters of sealed Nylon 12CF at x100 magnification.

6.4.1.1 A model for behaviour of epoxy sealed specimens

After presence of the epoxy was confirmed, a conceptual model was developed in order to assist with examining the erosion of the specimens. As seen in the studies of textured surfaces in literature, the orientation to the rasters on the surface layer will change the erosion behaviour. At 0° the sand will be unobstructed by the surface texture and can bore through the gap between rasters, while at 90° to the raster orientation it will impact with the edge of the raster as seen in the schematic in Section 6.3.

Contrarily, from the limited studies conducted on erosion of FDM printed materials the highest erosion is found when the flow is parallel to the raster orientation, while for composite materials the highest erosion is found when the flow is normal to the fibre orientation. It has been hypothesised that this is due to the higher susceptibility of the fibres to become broken when impacted normally versus along the length [134].

For the epoxy sealed specimens, the discussion in Section 6.6 will consider the epoxy to be acting a composite matrix while the raster acts as the reinforcement.

6.5 Macro Examination

The physical damage created by the impinging sand particles will have different characteristics dependent on the angle at which impact occurs. At 90-degrees the phenomenon shown in Figure 118 is observed. The solid particles immediately hit the material and as they lose energy are pushed outside of the impingement zone causing sliding and abrasive wear.

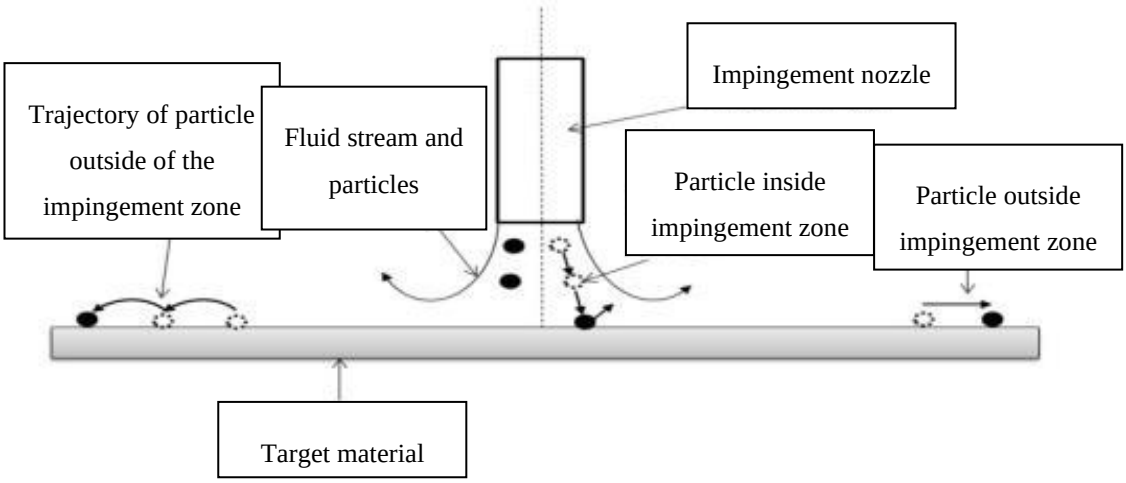

Figure 118. Particle Trajectories (made by F. Brownlie for the Weir Group)

At 45° and 20° elongated wear scars are observed. This was consistent across all materials but was most obvious in photographs for the Nylon 12CF material. Therefore, an example of each wear scar shape is shown in Figure 119 with Nylon 12CF.

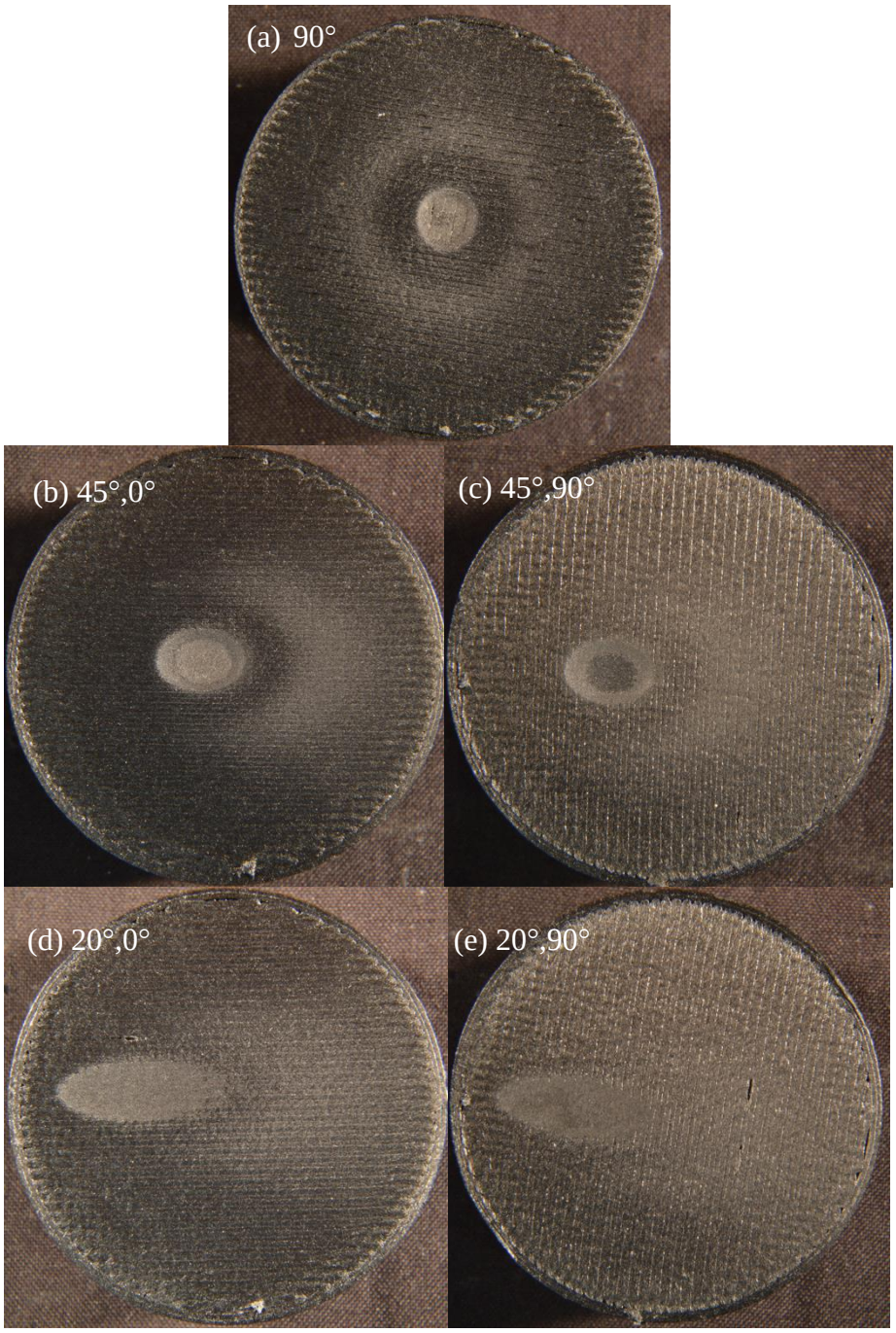

Figure 119. Erosion wear scar shapes shown on Nylon 12CF for (a)90, (b)45,0, (c)45,90, (d) 20,0 and (e) 20,90 orientations.

The 90° impact angle, denoted as (a), shows mostly circular wear scar with the secondary impingement zone clearly visible concentric to the wear scar. Figures (b) and (c) show the wear scar for 45° impact. The scar is symmetrical across two primary axis and takes on an oval shape. The secondary impingement zone is also visible, however instead of occurring all around the scar as it does for the 90° impact angle, it is trailing behind the main scar in the direction of the flow. The region outside the impingement zone in which the sand particles fan out is visible. Figures (d) and (e) are examples of 20° impact and exhibit similar behaviour to 45° in that the main scar is oval with a trailing secondary impingement zone, however, the wear is much shallower over a larger area. Scatter of the sand particles is more likely at this lower angle.

6.6 Results and discussion

6.6.1 Material Loss

The mass of the specimens after drying, per the protocol in Section 5.5.1.1, were compared to the initial pre-test mass. As the materials tested have varying densities, the mass was converted to volume loss by dividing by the density of the respective materials in order to normalise the data and compare between materials. The density and mass loss data are shown in Table 20 and Table 21 respectively. The volume loss is presented in Figure 120 and the depth of the main wear scar as measured by 2D profilometry is shown in Figure 121.

Table 20. Density of materials tested for slurry erosion.

Material	**Density (g/cm^3)**
Ultem 1010	1.27
Nylon 12CF	1.15
Ultem 1000	1.27

Table 21. Average mass loss results for all materials at all impingement and raster orientation angles.

Material	**90°**	**45°,0°**	**45°,90°**	**20°,0°**	**20°,90°**
Ultem 1010	40.5 mg	64.4 mg	56.8 mg	32.8 mg	21.7 mg
Ultem 1010 Sealed	29.7 mg	21.0 mg	44.7 mg	32.0 mg	38.8 mg
Nylon 12CF	112.2 mg	78.7 mg	68.4 mg	60.4 mg	77.2 mg
Nylon 12CF Sealed	62.9 mg	69.2 mg	91.0 mg	75.9 mg	75.5 mg
Ultem 1000	9.7 mg	10.5 mg		5.2 mg	

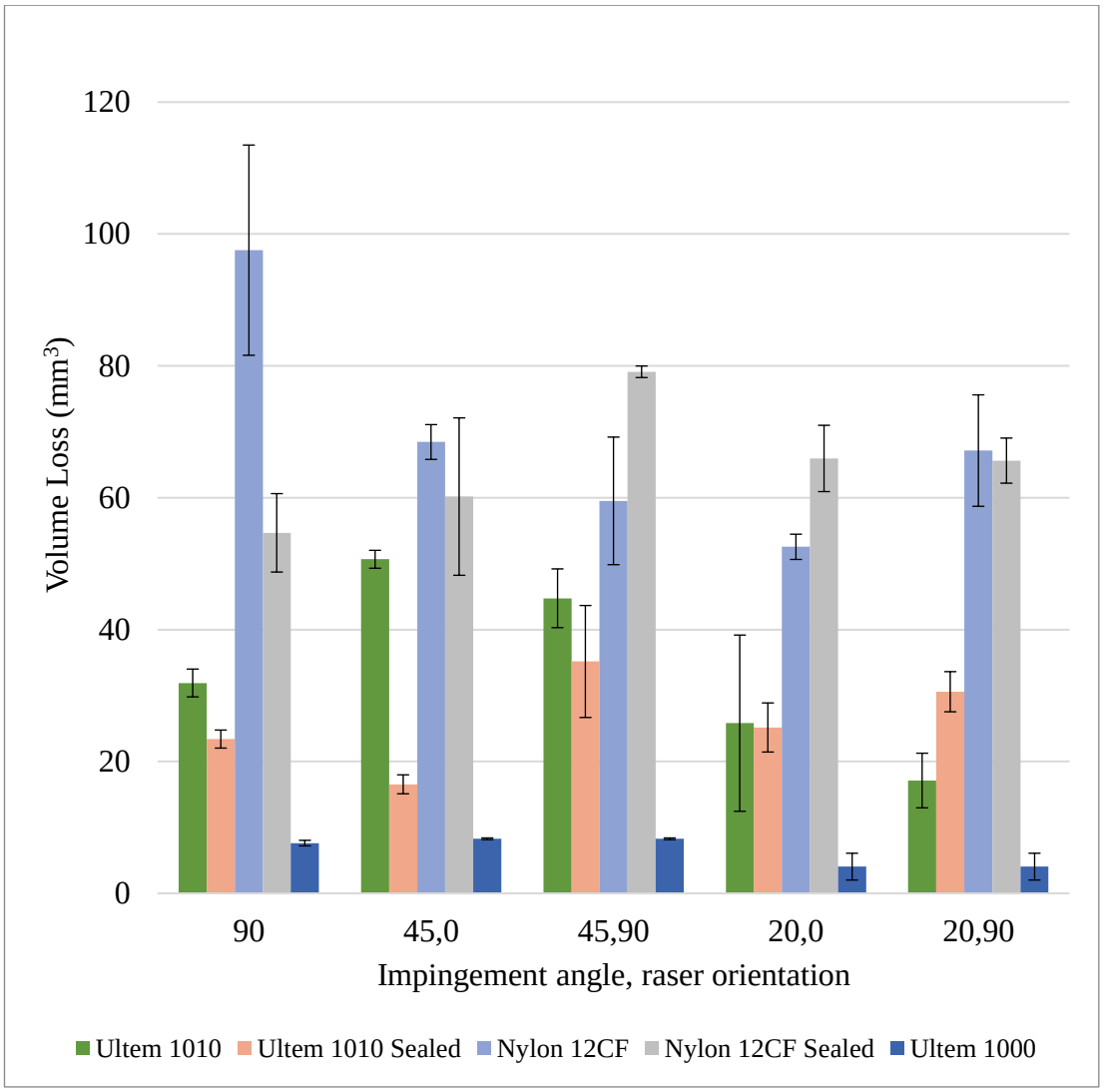

Figure 120. Volume loss vs. impingement angle for all materials tested.

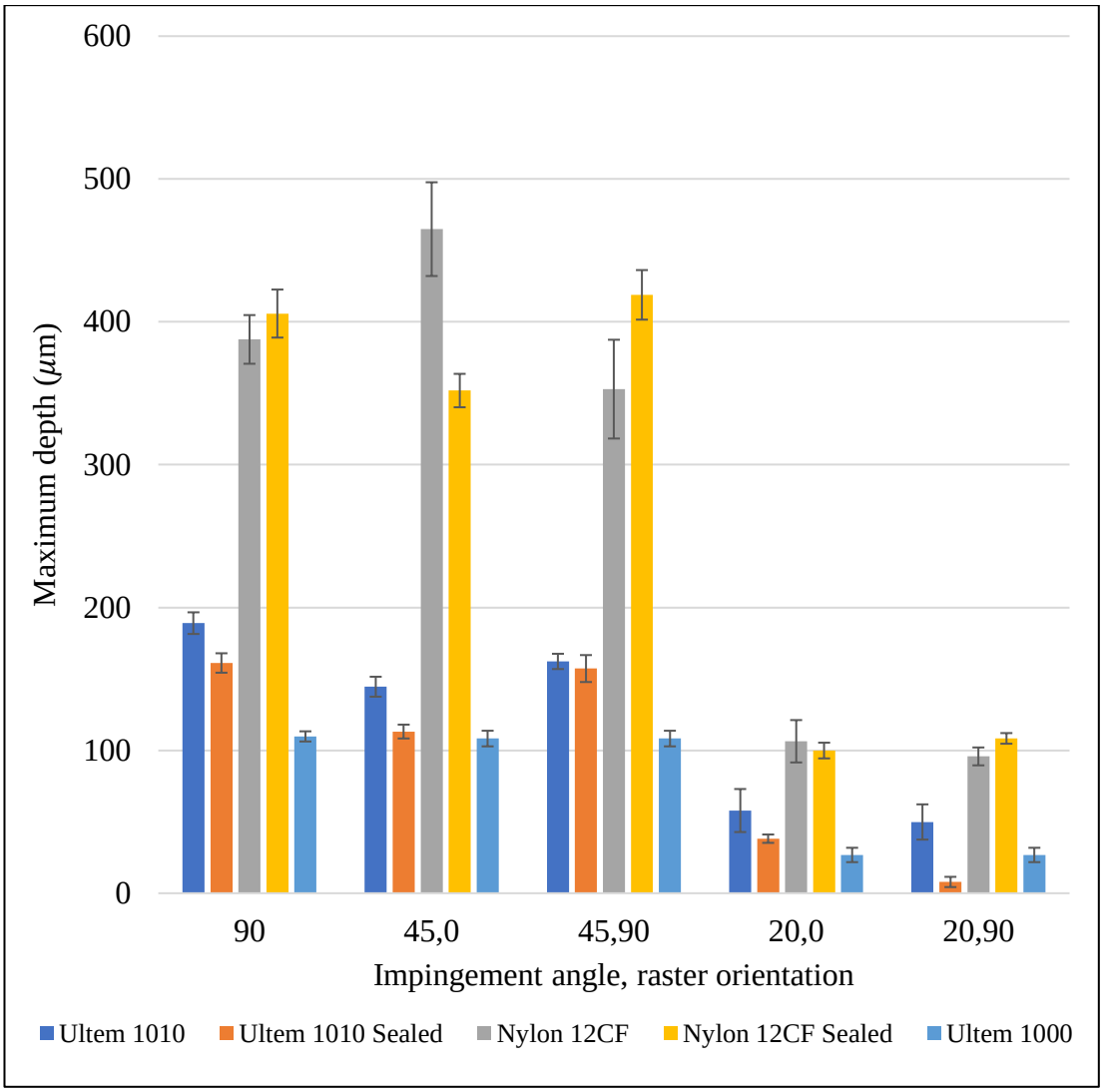

Figure 121. Average maximum depth as measured by 2D profilometry for all materials at all impingement angle and raster orientations.

The first impression of the volume loss readings in Figure 120 is that there is no apparent advantage from the additively manufactured surface in terms of erosion resistance. The Ultem 1000 outperformed the Ultem 1010 printed specimens. When comparing the Ultem 1010 to Nylon 12 CF, the Ultem has outperformed the Nylon 12CF. For all additively manufactured specimens, when compared to the traditionally manufactured Ultem 1000, the standard deviation of values is larger for many data points. This indicates that manufacturing method results in greater variety in the

response of the material within the parameters of the experiment. The layer height for both printed materials is 0.254mm. The depth of Ultem 1010 does not exceed this meaning that all material lost is from the top layer from both the unsealed and sealed specimens. This means there will not be an alternating effect from the raster orientation as the material is removed. From the examination of sealed specimens, it was shown that the epoxy penetrates beyond the top layer of Ultem 1010, thus the epoxy will influence the wear behaviour. For Nylon 12CF all angles except 20° exceed the layer height. This has two implications, the first being that at acute angles the raster orientation will change during the erosion process within the wear scar. Secondly, the presence of epoxy beyond the first layer of Nylon 12CF could not be confirmed across the specimen due to the lack of airgap in some locations. Thus, the effect of epoxy will be limited to the top layer.

For Ultem 1000, the highest mass and volume losses are seen at the 45° impingement angle followed by 90° and then 20°. As seen in the literature review, traditionally manufactured PEI exhibits semi-ductile behaviour and it would be anticipated that the peak rate of erosion would occur between 30° and 60°. The mass loss at 90° is 9.7 mg and at 45° is 10.5 mg. The mass loss at 90° is 9.7 mg, which is only 0.8 mg less than the mass loss measured at 45°, implying that the material is on the more brittle end of the semi-ductile spectrum and thus is more susceptible to normal impact. Understanding this baseline material's behaviour for this experiment contributes to the understanding of the Ultem 1010 results as it will help distinguish what responses are due to inherent material characteristics or the manufacturing process.

Comparing all angles for Ultem 1010, the trends follow the Ultem 1000 results implying that material characteristics are still a significant factor for erosion. Comparing the trends for volume loss to those of the maximum depth of the wear scar a shift is seen in which the depth decreases with decreasing impingement angle. As observed in the macro examination of the specimens, for all angles there will be a secondary wear zone in which the sand particles erode the surface after leaving the wear scar. The expected mechanism here would be abrasion as the particles have lost

a large amount of energy after the initial impact. Lower depths at 90° vs. 45° with opposite trends for volume loss indicates that there is significant abrasive wear at 45° in the secondary wear zone. When comparing this to the Ultem 1000 injection moulded results, it is observed that the depth of the wear scar follows the same trend as the volume loss. This indicates that for Ultem 1010 the manufacturing has an effect on the behaviour of the material with respect to impingement angle, especially for abrasive mechanisms.

Comparing the raster orientations at 45° for Ultem 1010, higher volume and mass loss was observed at the 0° orientation. This was expected as the particles of silica sand would be unobstructed by the surface roughness created by the rasters. The opposite effect is seen for the depth measurements, with 90° having a slightly higher depth. This implies that the effect of abrasive wear is less severe at this orientation, but the erosion in the wear scar is more extensive than at parallel orientations. However, at parallel orientation the rasters will not provide protection by reducing the energy of the sand particles in the abrasive zone as in the normal orientation. At 20° the volume loss follows the trend with higher rates at parallel orientation to the raster. It can be seen that there is a more significant difference between the volume losses at the two orientations than the depths, however both follow the same trend. Greater loss at parallel orientation that is not correlated to a significantly greater depth suggests that as with 45° a shallow abrasive region outside of the main wear scar has driven higher material loss. From the most recent literature, it is anticipated that for the additively manufactured samples the greatest erosion will occur at the 0° to layer orientation which supports these hypotheses [168].

When Ultem 1010 is sealed with epoxy, the behaviour switches at 45° with greater volume loss at the 90° orientation. For sealed specimens, the highest volume loss is seen at 45°,90° but the second highest is not at the 45° impingement angle as observed for unsealed Ultem 1010. It is instead seen at 20°,90°. Using the composite laminate conceptual model described, the interface of the epoxy matrix to the Ultem 1010 reinforcement and the presence of any defects such as voids in the material will

contribute to the wear. For both acute impingement angles the epoxy does not provide more protection from erosion at the normal raster orientation when compared to the parallel direction. In the case of 20° impingement it accelerates it. The literature review in Chapter 4, Section 4.2.3 showed that composite laminates have higher rates of erosion with 90° fibre orientations [134]. At normal impact the fibres (in this case raster) will be more prone to impact from cracking. In areas where the raster is removed, the matrix will be left un-reinforced and more susceptible to wear. In areas where the matrix is weakened by the impact, rasters will be exposed. At parallel impact, the previously present air gap is now filled with epoxy which helps to inhibit erosion between rasters. At 20° this results in less extensive abrasive wear outside the wear scar for parallel impact than normal impact as shown by the higher depth at 0° orientation despite a lower volume loss. At all impingement angles the addition of epoxy results in a lower volume loss with the exception of 20°,90°. Comparing the depths of the unsealed and sealed specimens at this angle and orientation, while the volume loss is higher for the sealed the depth is much lower than the unsealed specimen. Therefore, abrasive secondary wear is more critical for the sealed specimen. This volume loss even exceeded the 90° impingement angle for sealed specimens, further exemplifying the effect of sealing on widespread abrasive wear.

Nylon 12 is known to experience highest rates of erosion at 30° impact angles indicative of ductile behaviour [122]. There are a number of factors that will influence the behaviour of a composite material such as wt% of the fibre reinforcement, orientation of the fibre and strength of the interface between fibre and matrix [132]. For the Nylon 12CF specimens without epoxy sealing, the highest erosion rates are seen at 90°. This implies that the erosion is dominated by the brittle carbon fibre reinforcement. In literature, PEEK matrix with carbon fibres exhibited a similar phenomenon in which the erosion rate at 90° impact angle was higher than that at 45° and the overall behaviour of the composite was semi-ductile [134].

From the optical microscope images of the cut and polished sealed Nylon 12CF (Figure 116 and Figure 117) presented to show the epoxy resin, it is clear that the

chopped fibres tend to lay quite parallel to the raster orientation. From the literature review, it was observed that impact at acute angles in parallel to fibre direction resulted in less erosion [139]. At 20° this is observed with a slightly lower volume loss at the parallel raster orientation. The depth of the parallel orientation however is greater than the normal orientation implying that in the abrasive region the fibres could be accelerating wear for the normal orientation. Wear at this impingement angle does not exceed the layer height, thus the effect of raster orientation is the same throughout the depth of the wear scar.

The trends for volume loss at 45° are more in line with what is expected from the FDM induced surface texture, as seen with Ultem 1010. For the depth, the parallel orientation shows much higher values than the normal orientation. This is opposite to the Ultem 1010 results and further indicates that the fibres' susceptibility to normal impact are a main driver of erosion in the secondary wear zone. Additionally, there will be a synergistic effect of the raster orientation in the wear scar as the depth exceeds the layer height. At 90° impingement this will have little to no effect in the wear scar however it will affect the secondary wear zone where the particles will be impacting the material at acute angles. Because the particles are impacting the surface symmetrically, the orientation angle will range from 0-90°. The greatest depth is seen at 45°,0° confirming that the abrasive wear is contributing to the higher volume loss value at 90° impingement.

Sealed Nylon 12CF has even more complexity as it is essentially a composite laminate in which the reinforcement is a discontinuous fibre composite. Thus, the behaviour of the material is reliant on two interfaces. Thermosetting polymers can exhibit semi-ductile behaviour with erosion rates peaking at acute angles [121]. This will only be exhibited in the top few layers due to the tighter network of pores in Nylon 12CF. At 90° and 45° impingement angles, the wear scars that are greater than the 0.254mm layer height and the presence of epoxy cannot be guaranteed beyond this. The greatest volume loss and depth is seen at 45°,90° for the epoxy sealed Nylon 12CF. With both the discontinuous carbon fibres and the entire raster acting as a reinforcement to the

epoxy, this is the anticipated behaviour as both forms of reinforcement are now susceptible to the normal impact. Sealing results in greater volume loss and wear scar depth at 45°,90° compared to the unsealed specimen supporting this. There is a very clear advantage to sealing the parts at 90° in terms of volume loss. When comparing the depths of the unsealed and sealed specimens at this angle, the sealed specimen exhibits a deeper wear scar despite the much lower volume loss. This signifies that the epoxy has coated the surface and protected the carbon fibre reinforced rasters from the abrasive wear in the secondary wear zone. At 45°,0° the volume loss and depth for the sealed specimen are lower than the unsealed specimen indicating that filling the air gap provided erosion resistance.

For 20° impingement the depth does not exceed the 0.254 mm layer height, therefore it is anticipated that epoxy is present throughout the depth of the wear scar. At 20°,0° the volume loss was reduced by sealing the specimen; however, this had a negligible effect on the depth which suggests that the greatest benefit of filling the air gap was found in the secondary wear zone. For 20°,90° degrees there is only a slight advantage to sealing the part when viewing the volume loss. The depth of the sealed specimen is marginally higher than the unsealed. The small differences for both make it difficult to decipher whether there was any positive or negative impact by sealing.

6.6.2 XCT and image segmentation

XCT scans show the internal structure of the specimens and allow for a 3D reconstruction of the part for visualisation. FDM results in porosity which was known after exploration of the 3D printing technique via literature and experience with pressure testing. Additionally, after slurry testing, water was getting trapped within the internal pore structure which resulted in the protocol for drying specimens in Chapter 5, Section 5.5.1.1. As the slurry circulates within the rig it will impact the specimen and the sand particles will also collide with one another, resulting in sand particles smaller than the original 400-500 μm nominal size. It was hypothesised that sand was getting trapped within the material as some could be seen in initial microscopy. In

order to determine if this was significant enough to affect the mass loss calculation, XCT scanning was performed, and then further image segmentation was done using Avizo to calculate the volume of the trapped sand.

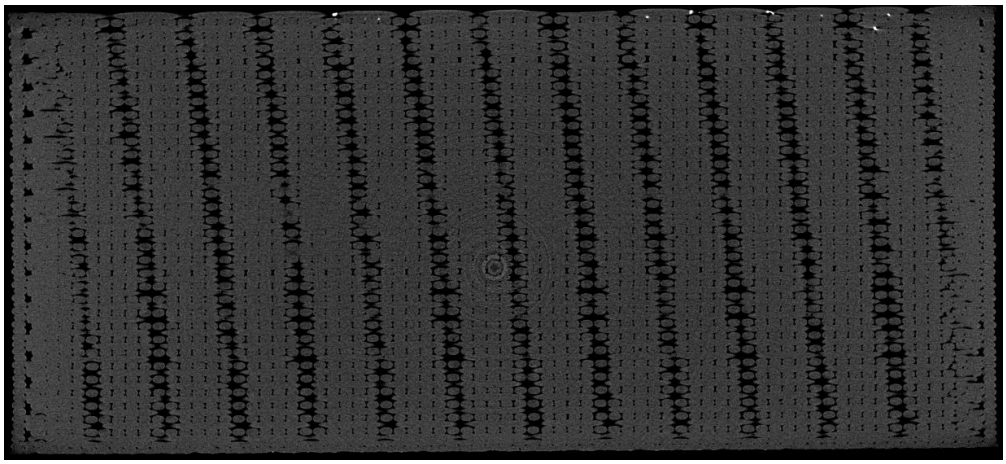

Figure 122. XCT scan slice of unsealed Ultem 1010 showing sand particle as brighter objects when brightness is adjusted for density.

Figure 122 shows a number of very bright particles at the top of a randomly selected slice. After interactive thresholding of the scans the sand could be separated from the specimen material due to its higher density (which results in brighter appearance from the X-ray).

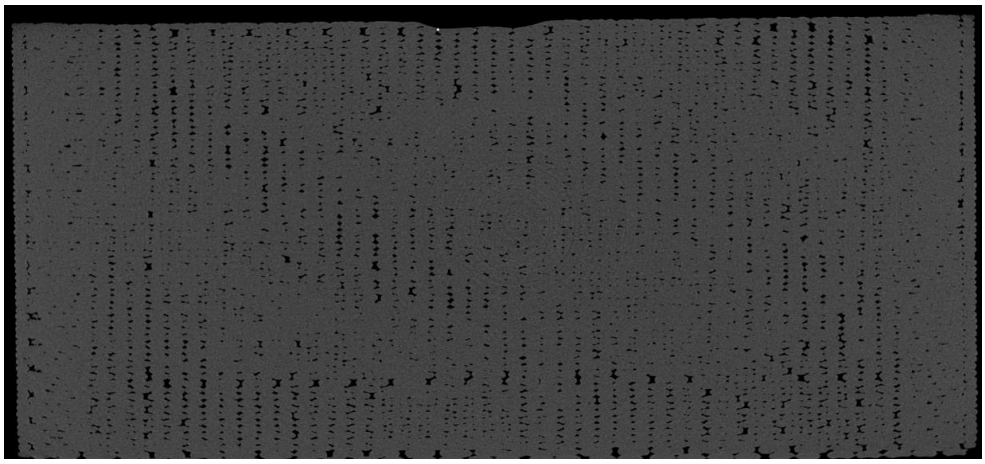

Figure 123. XCT slide of unsealed Nylon 12CF showing porosity and small instances of sand embedded in the wear scar (top centre of slice).

Figure 123 shows an example of a slice from the Nylon 12CF in which a sand particle is visible at the top of the scan in the area of the wear scar. Using thresholding to isolate the sand particles and creating a label analysis for them in Avizo, images were created to help visualise the sand. Figure 124 shows sand (blue particles) embedded in the wear scar of Nylon 12CF. It is seen that these are in voids exposed by the erosion process. Figure 125 shows small particles of sand (yellow and pink) embedded between the rasters of the surface of Nylon 12CF as well.

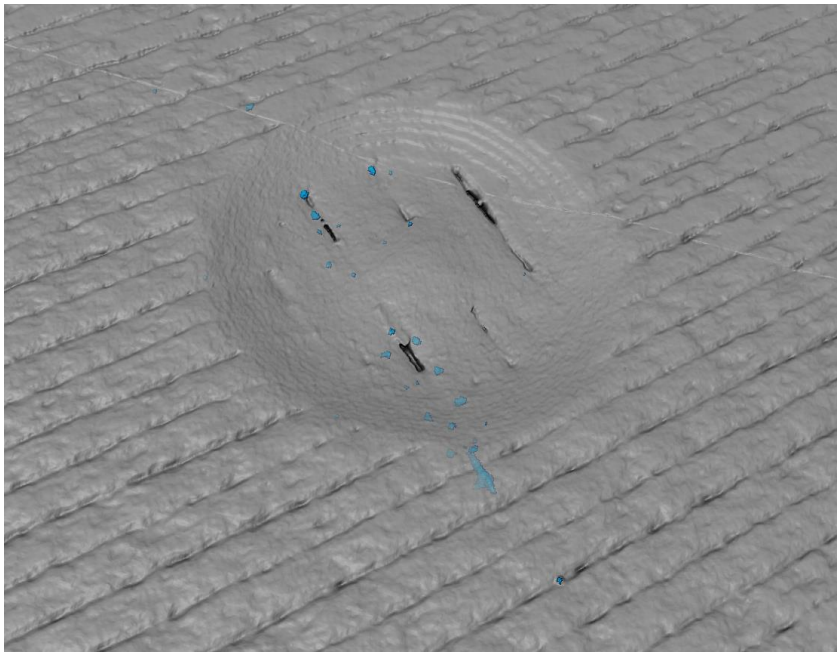

Figure 124. Sand embedded in the wear scar of unsealed Nylon12CF sample after 90° slurry impingement.

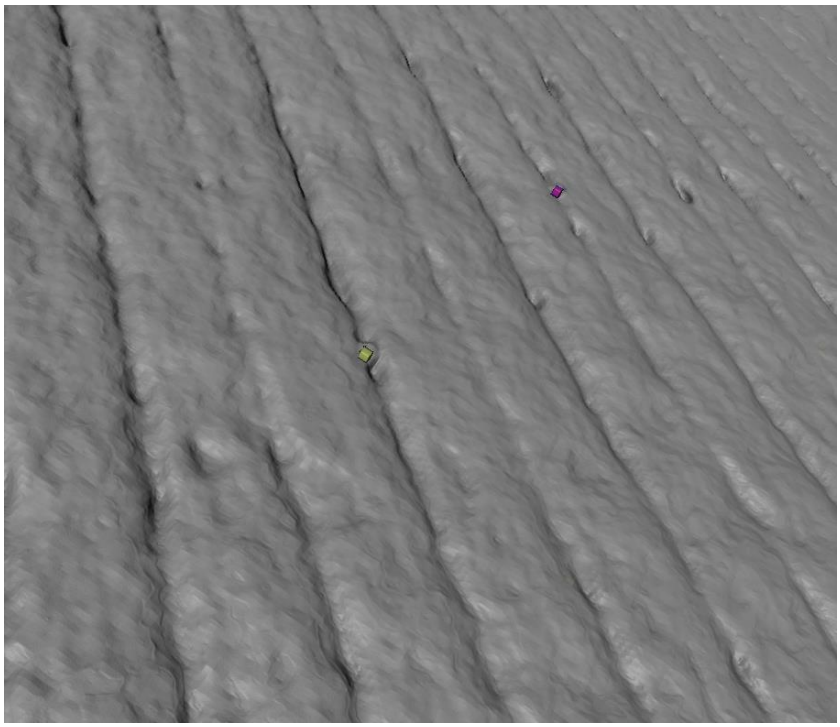

Figure 125. Sand between rasters of unsealed Nylon12CF after slurry erosion testing.

For Ultem 1010, the distance between rasters is larger due to a lack of neck growth between the rasters, thus the sand has become trapped between these rasters rather than becoming embedding in the material itself via force. Figure 126 shows that sand particles are embedded in the surface at the lower edge of the wear scar rather than within it. In this example the flow impacted the material at 45° from the top of the image downwards, therefore the sand was getting trapped as it left the main wear crater and fanned out over the surface. The particles that do not get trapped will create abrasive wear in the region outside the scar. Figure 127 provides a closer view of the sand between rasters.

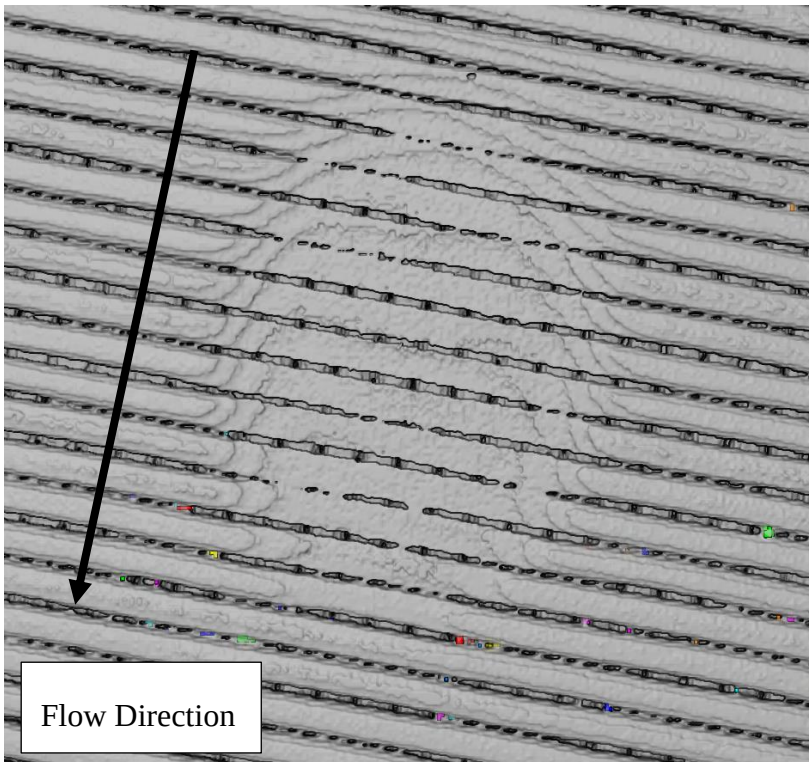

Figure 126. Sand embedded in between rasters of Ultem 1010 after 45,90 degree slurry impingement.

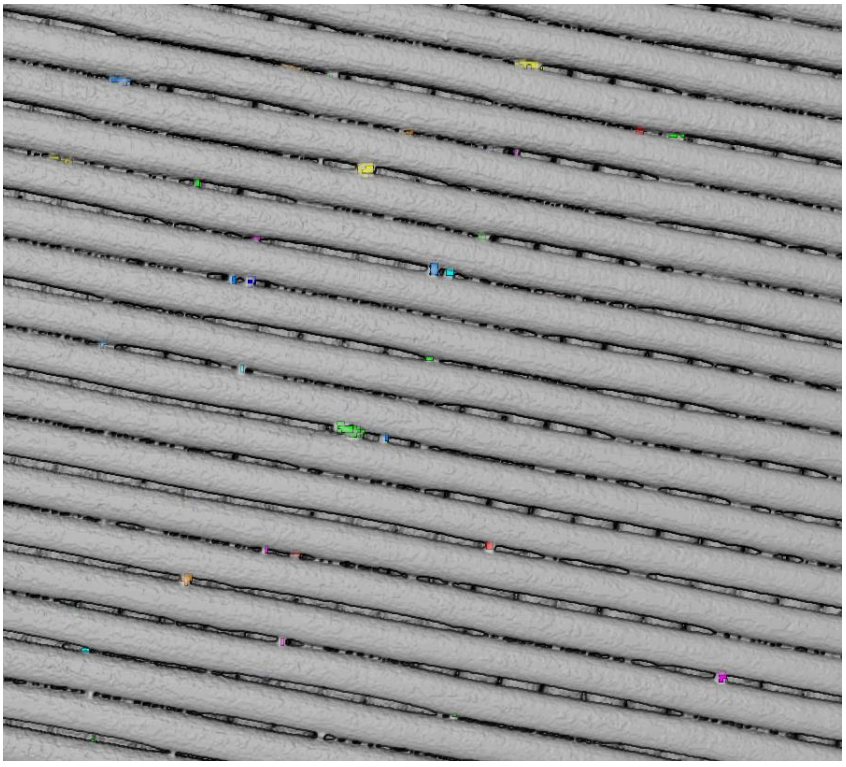

Figure 127. Sand embedded in between rasters of Ultem 1010 after slurry erosion testing.

Calculation of the mass of sand in the Ultem 1010 and Nylon 12CF specimens was found to be 1.44 mg for Ultem 1010 and 0.15 mg for Nylon 12CF. This accounts for approximately 3% of the average mass loss for Ultem 1010 and 0.2% of the mass loss for Nylon 12CF. Because both of these values fall within the error bars presented for either material in Section 6.6, they were considered to be negligible when considering the overall material loss due to erosion.

In addition to calculating the volume of sand, the scans provided important information into the internal porosity structure and the consolidation of the material overall. Nylon 12CF has a melt temperature of 178°C and a glass transition temperature of 41°C. Ultem 1010 has a melt temperature of 340-360°C and a glass transition temperature of 215°C. In the cross-sectional images above, it is apparent how these differences in thermal properties contribute to the internal structure. Because Ultem 1010 requires twice the amount of heat to create flow from the nozzle to print compared to Nylon 12CF. Furthermore, the glass transition temperature is more than five times that of Nylon 12CF. When examining the internal structure, Ultem 1010 has visibly larger pores with more areas of pore connection than Nylon 12CF. Additionally, the circular shape of the filament used to feed the nozzle to print is still very apparent in the Ultem 1010. For Nylon 12CF the layers appear much more flattened and consolidated. For both materials better consolidation is seen on the bottom layer and at the edges. This contributed in turn to the epoxy uptake seen and to the size of the air gap created.

6.6.3 Images of the surface of specimens after testing

For purposes of efficiency, most of the samples observed were from the 45° impingement angle as exhibit regions of direct impingement and regions of abrasive wear are exhibited.

6.6.3.1 Ultem 1010

For all Ultem 1010 SEM images shown the direction of flow is from the top of the photo downwards.

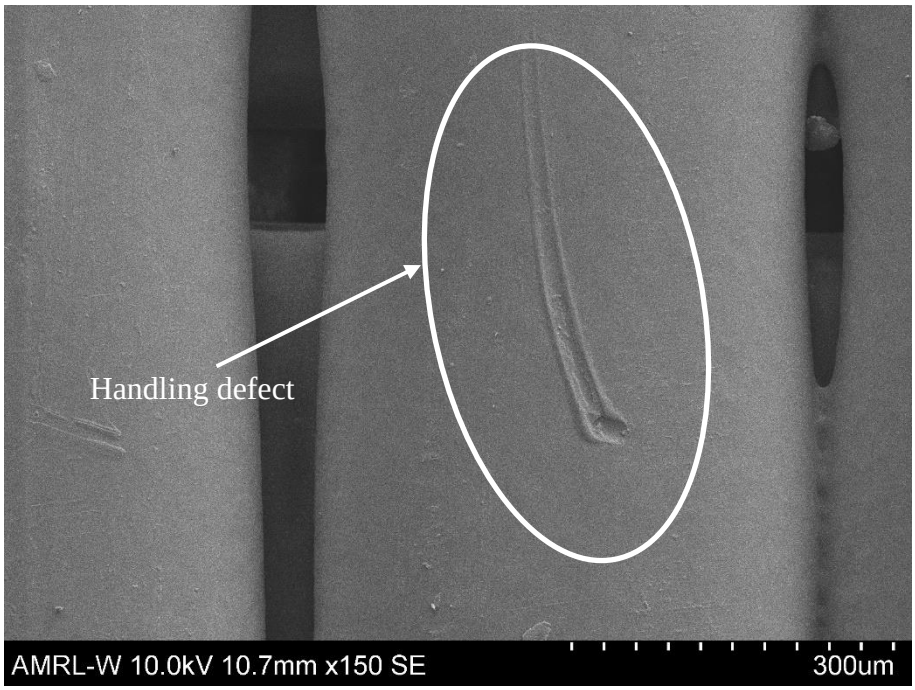

Figure 128. Ultem 1010 as deposited surface, x150 magnification.

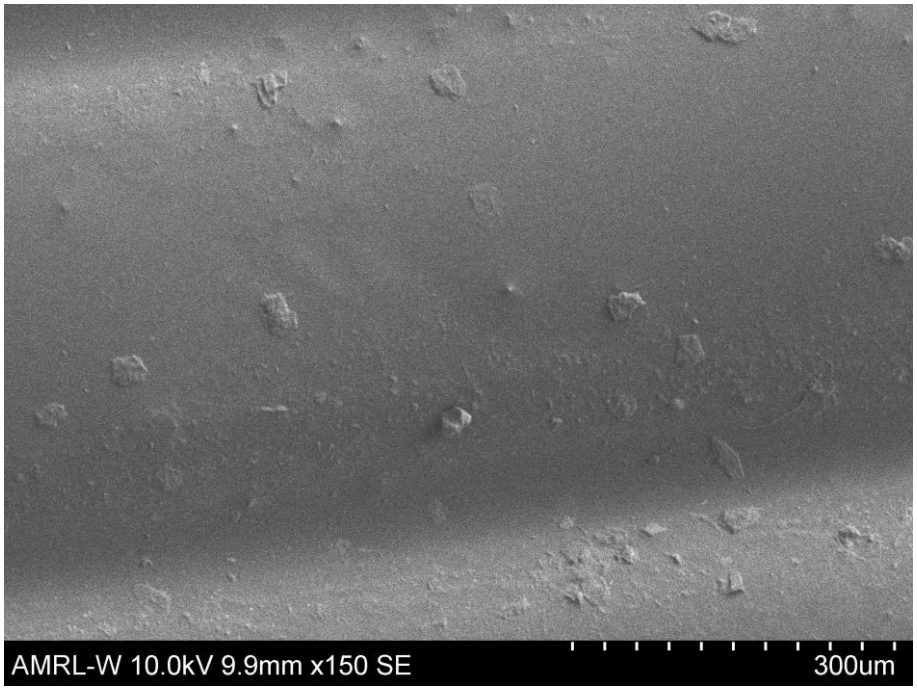

Figure 129. Ultem 1010 epoxy sealed surface, x150 magnification.

In Figure 128 and Figure 129, the as deposited surface and the epoxy sealed surface of an Ultem 1010 specimen is shown respectively. The as deposited surface shows a mostly smooth texture with some defects due to handling the specimens after printing. This is to be expected as there is no surface treatment for the additively manufactured samples. Surface treatment such as grinding would results in the reduction of layer height, and it was desired to understand the materials as they are printed. The epoxy sealed surface however does show deposition of the epoxy with smooth material underneath. The epoxy was manually removed from the surface, per Section 5.3, but material will remain as this is not a precise removal.

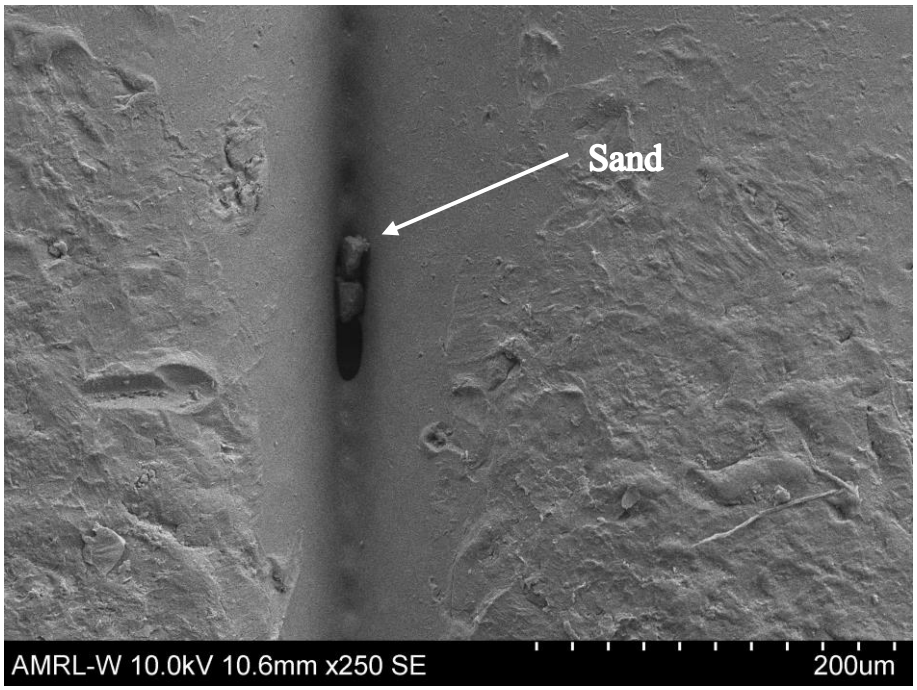

Figure 130. Onset of wear for Ultem 1010 45,0 degree impingement angle, x250 magnification.

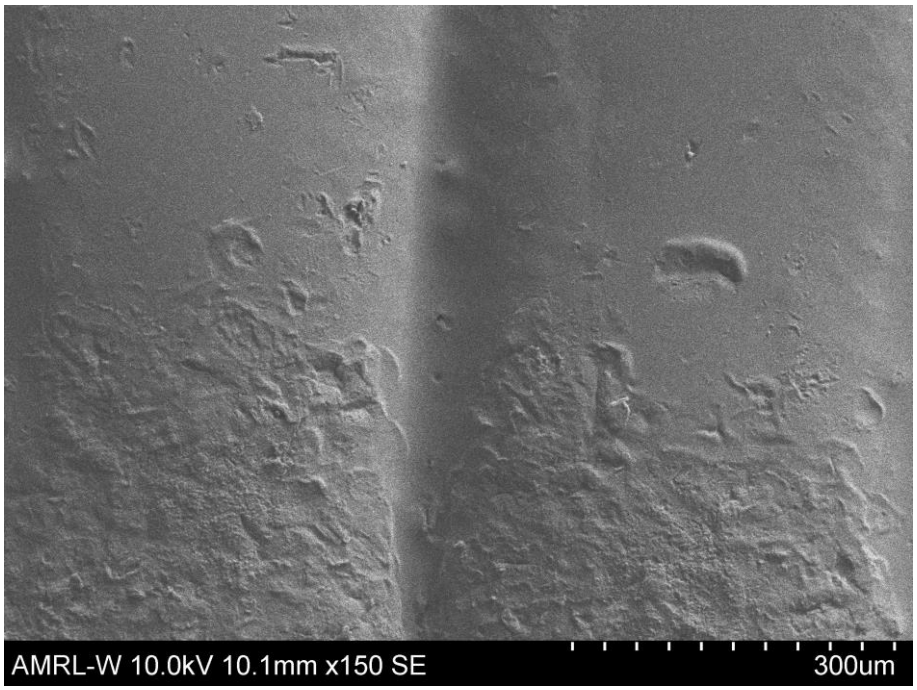

Figure 131. Onset of wear for Ultem 1010 45,0 degree impingement angle with epoxy sealed surface, x150 magnification.

Figure 130 and Figure 131 display the difference between as deposited and epoxy sealed specimens at the onset of wear for the 45,0 degree impingement angle. The as deposited surface has a visible gap between rasters with particles embedded in the air gap. The epoxy sealed part does, however show that there has been effective sealing of the air gap with the epoxy. ,

At 45°,90° it is expected that the onset of wear will occur along the curvature of the layer that is 90° to the flow. While the flow is 45° to the average surface of the specimen at a macro level, the particles will be impacting the edge of the raster at approximately 90° (per Figure 112) which should result in the observance of mechanisms more similar to normal impact at the edge.

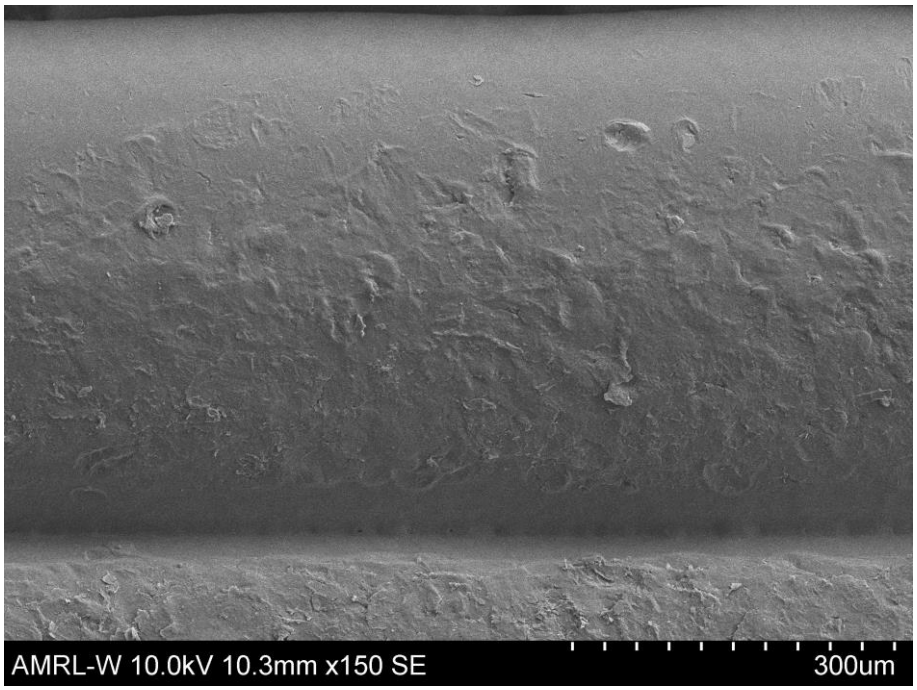

Figure 132. Onset of wear for Ultem 1010 45,90 degree impingement angle, x150 magnification.

Figure 132 shows the onset of wear for the corresponding 45°,90° angle with as deposited and epoxy sealed surfaces. Evidence of flake formation indicative of micro-ploughing and micro-cutting is present. Opposed to the 45°,0° impingement angle, the sand particles will not be able to bore through the air gap as the direction of flow is perpendicular to the rasters.

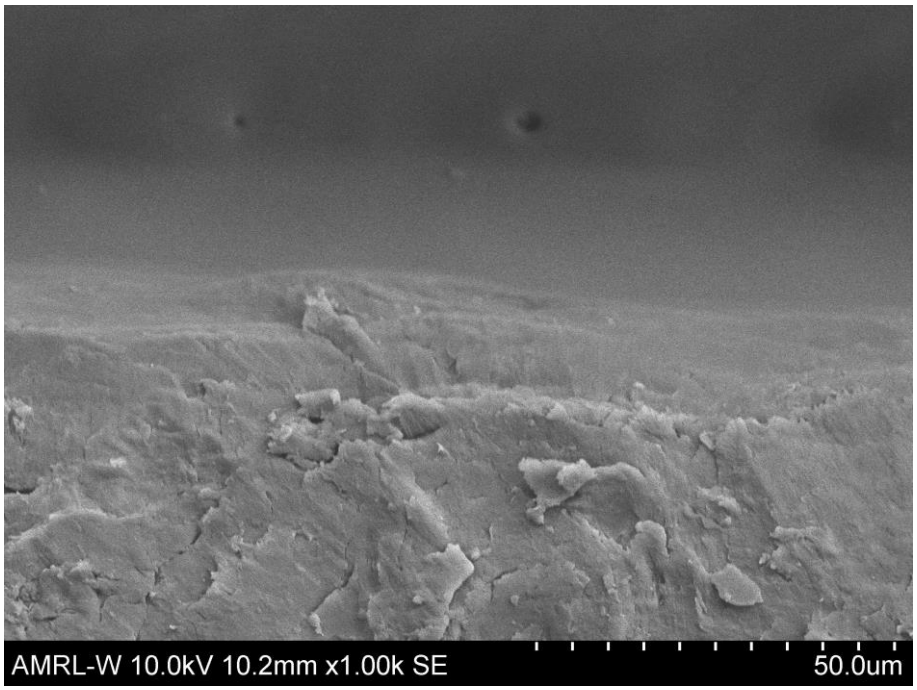

Figure 133. Edge of the wear scar for Ultem 1010 45,90 degree impingement angle, x1.00k magnification.

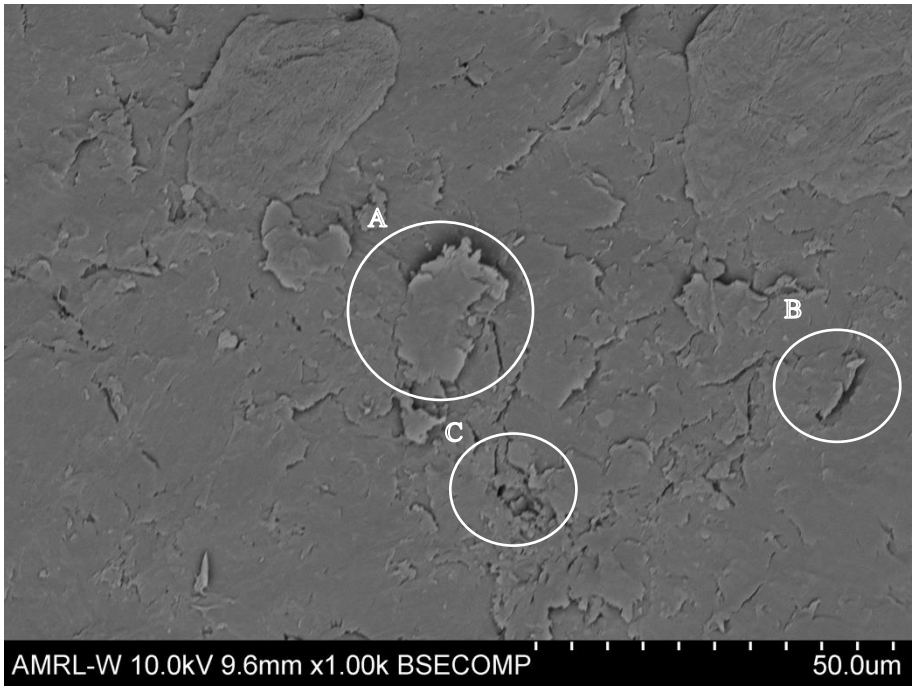

Figure 134. Edge of the wear scar for Ultem 1010 45,90 degree impingement angle with epoxy sealed surface, x1.00k magnification.

Figure 133 and Figure 134 show further details of the edge of the wear scar for the 45°,90° impingement angle. There are flakes formed at the layer boundary on the as deposited surface at x1.00k magnification. This was not as apparent in previous photos which were only at x150 magnification. This surface appeared smooth at lower magnification, however here there is evidence of erosion. The top half of the image shows the depth of the channel which remains smooth as the sand skips over and impacts the curvature of the raster. The rasters are acting here as asperities. In Figure 134, 'A' denotes a flake formed from plastic deformation. 'B' is a crack formed from brittle behaviour after impact, and 'C' shows an area where fragments of material have been removed creating a cavity. For both the as manufactured and the epoxy coated surface widespread cracking is apparent which was expected at the micro level due to the actual orientation of the flow to the edge of the raster.

At 45°,0° and 45°,90° impingement of Ultem 1010 the worst levels of wear are observed. This phenomenon is most apparent at the edge where the material has not been removed in large quantities and we can observe the difference between uneroded and eroded surface. For as deposited Ultem 1010, the mass loss for 45°,0° is higher than 45°,90°. As discussed, the as deposited surface has deeper channels in which the sand can bore through the air gap and remove material deeper down when the flow is 0° to the raster. Although, at 90° to the flow, the layers will create more asperities it will also result in the loss of energy of the sand as the particles impact the edge of the raster. This in addition to the absence of sand particles boring through the air gap results in better wear resistance for as deposited Ultem 1010 at 45°,90° than at 45°,0°.

This changes however for the epoxy sealed specimens. At 45°,0° Ultem 1010 tends to achieve a better wear resistance when sealed than at 45°,90°. The depth and width of these channels will be reduced due to the epoxy that is deposited there. With the absence of manufactured asperities created by the angle to the flow and filled channels there is overall less wear than in the 45°,90° orientation where the sand will continue to remove the tops of the layers. Additionally, the resistance of the rasters (now acting

as fibres with an epoxy matrix) to the bending induced by the impact will be reduced. Removal of the epoxy matrix will expose the Ultem 1010 rasters to further wear.

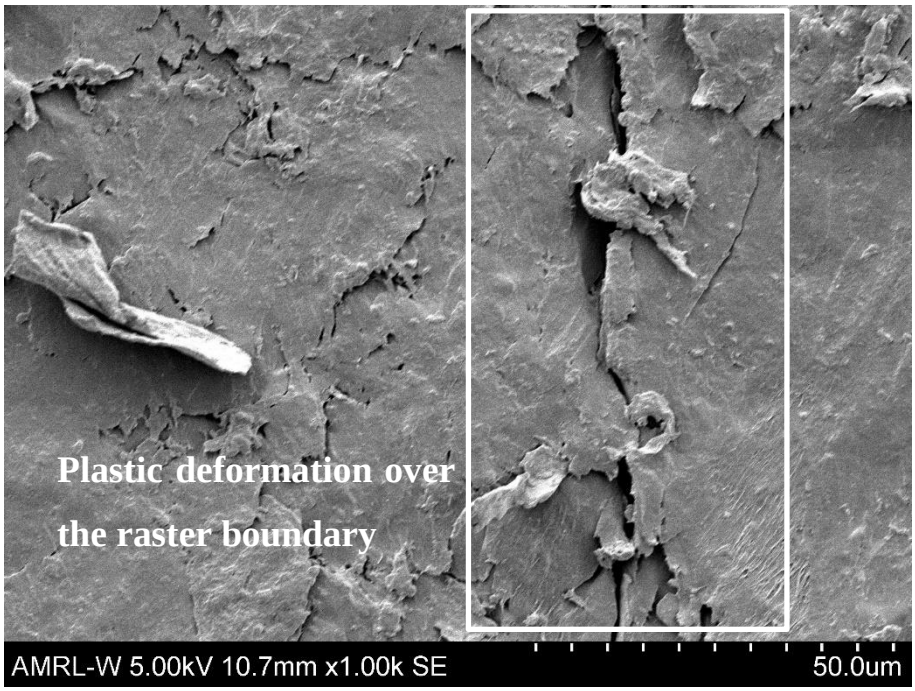

Figure 135. Wear scar at layer boundary Ultem 1010 45,0 impingement angle, x1.00k magnification.

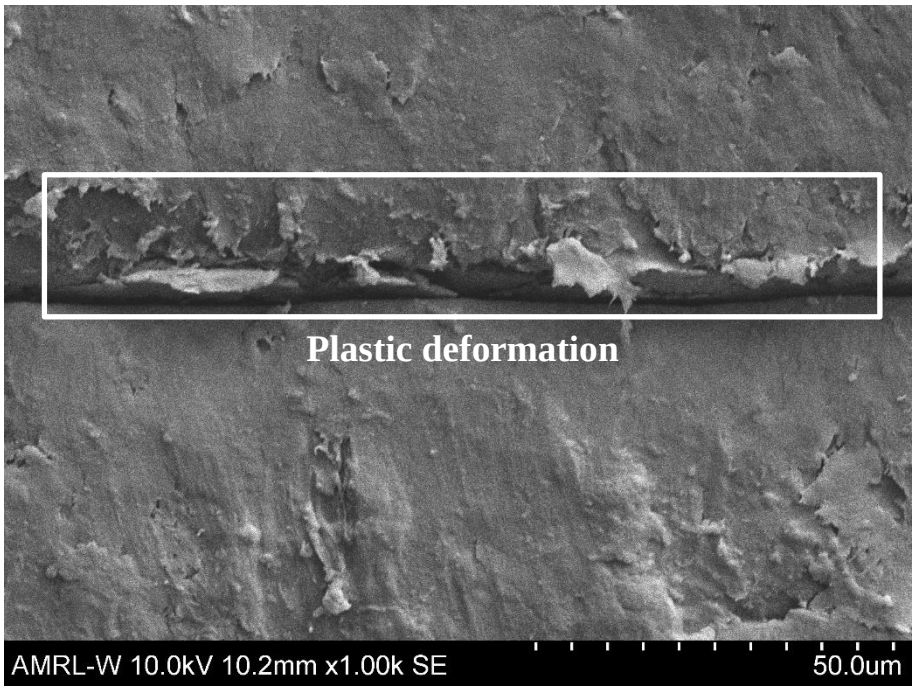

Figure 136. Wear scar at layer boundary Ultem 1010 45,90 impingement angle, x1.00k magnification.

Figure 135 and Figure 136 compare the details within the wear scar at the raster boundary for the 45°,0° and 45°,90° orientation. Within the wear scar, we continue to see flake formation suggesting plastic deformation as the main wear mechanism. Both samples were tested 'as deposited'. On the left of Figure 135, the 0° raster boundary is shown to be worn down with flakes and debris now covering the boundary. On the right, the 90° raster boundary is still quite distinct suggesting that less material is removed. There is evidence of areas of plastic deformation and material removal for both orientations.

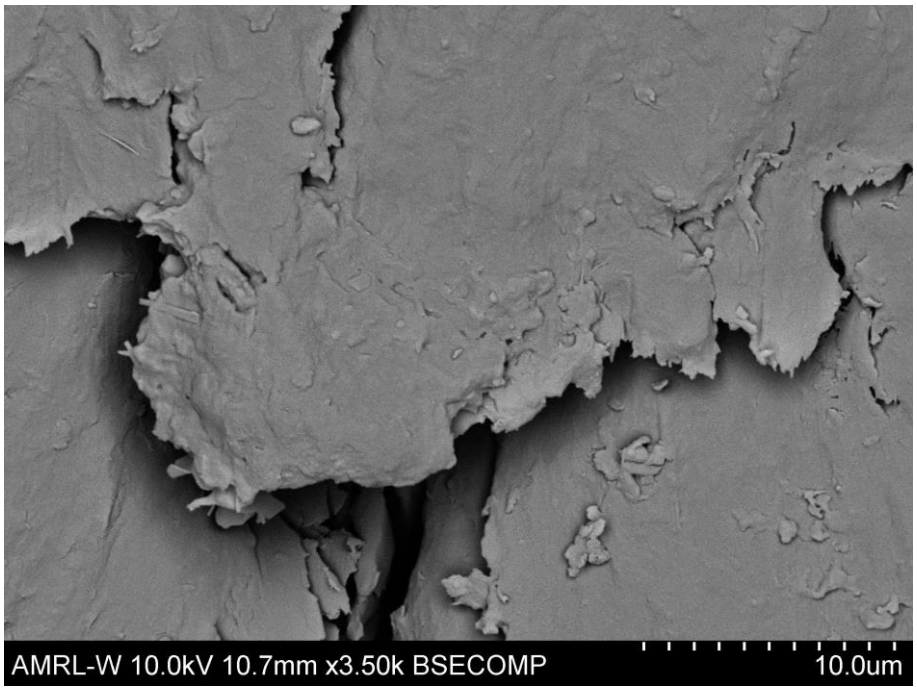

Figure 137. Details within wear scar Ultem 1010 45,0 degree impingement angle, x3.50k magnification.

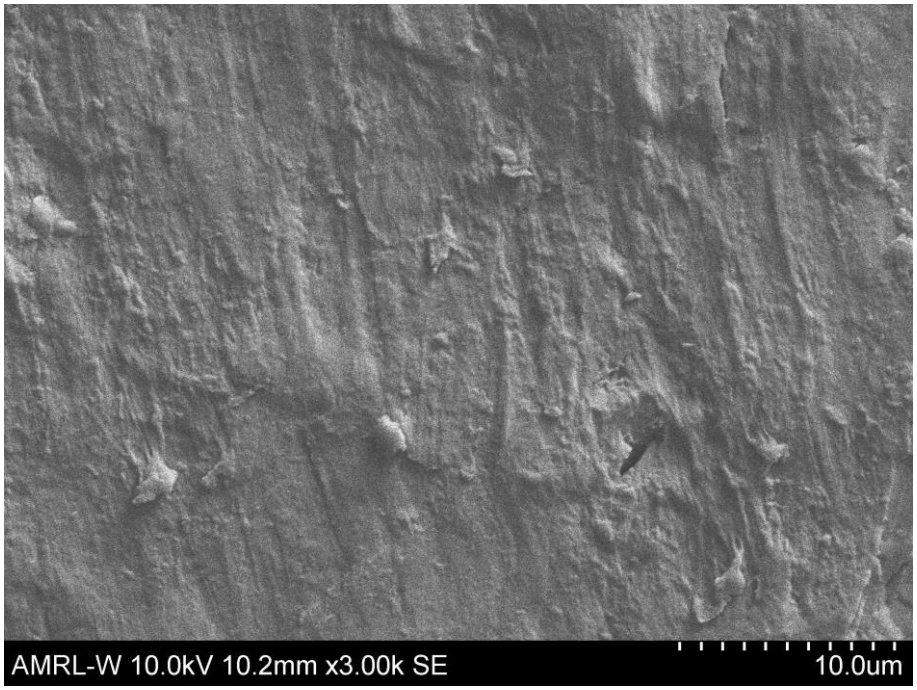

Figure 138. Details within wear scar Ultem 1010 45,0 degree impingement angle with epoxy sealed surface, x3.00k magnification.

Figure 137 and Figure 138 compare the 45°,0° as deposited and epoxy sealed specimens within the wear scar. Large flake formation is found at x3.50k magnification for the as deposited surface with a crack propagated below. The epoxy sealed surface shows there were large regions with wear more consistent with extensive plastic deformation and propagation of cracks similar to a previous study for thermoplastic materials subjected to erosion [129]. This does not as effectively remove material as the micro-ploughing that is evident from flake remnants. This combination of effects (crack propagation, micro-ploughing, and plastic deformation) is consistent with semi-ductile behaviour which was anticipated from literature and the erosion efficiency study performed for Ultem 1000 (the injection moulded counterpart to Ultem 1010) [121].

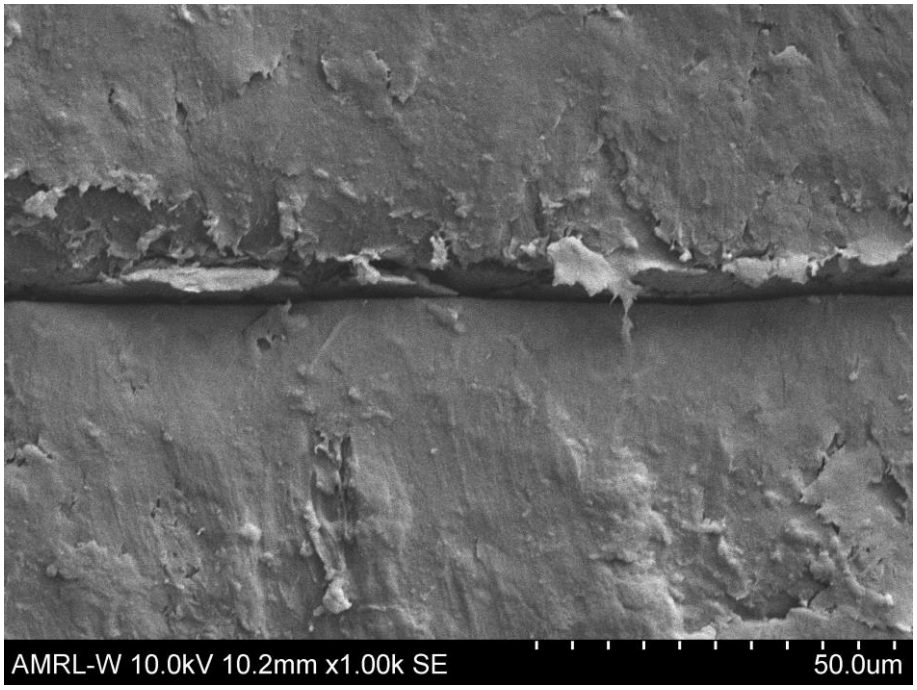

Figure 139. Details within wear scar Ultem 1010 45,90 degree impingement angle, x1.00k magnification.

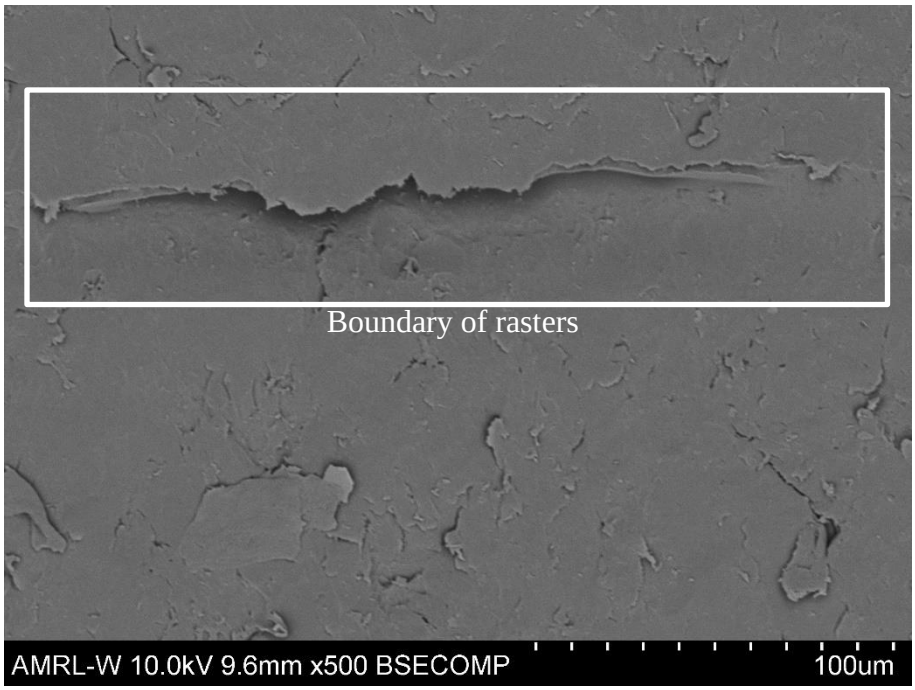

Figure 140. Details within wear scar Ultem 1010 45,90 degree impingement angle with epoxy sealed surface, x500k magnification.

Figure 139 and Figure 140 compare the 45°,90° impingement angle for as deposited and epoxy sealed specimens within the wear scar at a raster boundary. The as deposited surface shows areas of flake formation due to micro-ploughing as well as areas of plastic deformation. The raster boundary is still clearly visible, however for the epoxy sealed surface the raster boundary is not as visible due to the permeation of the epoxy. This smoother surface will reduce the energy loss of the particles. In Figure 140 there is some flake formation, but also cracks can be seen across the surface. The epoxy is a thermoset polymer and therefore will have exhibit more brittle behaviour due to the cross-linking of the molecules.

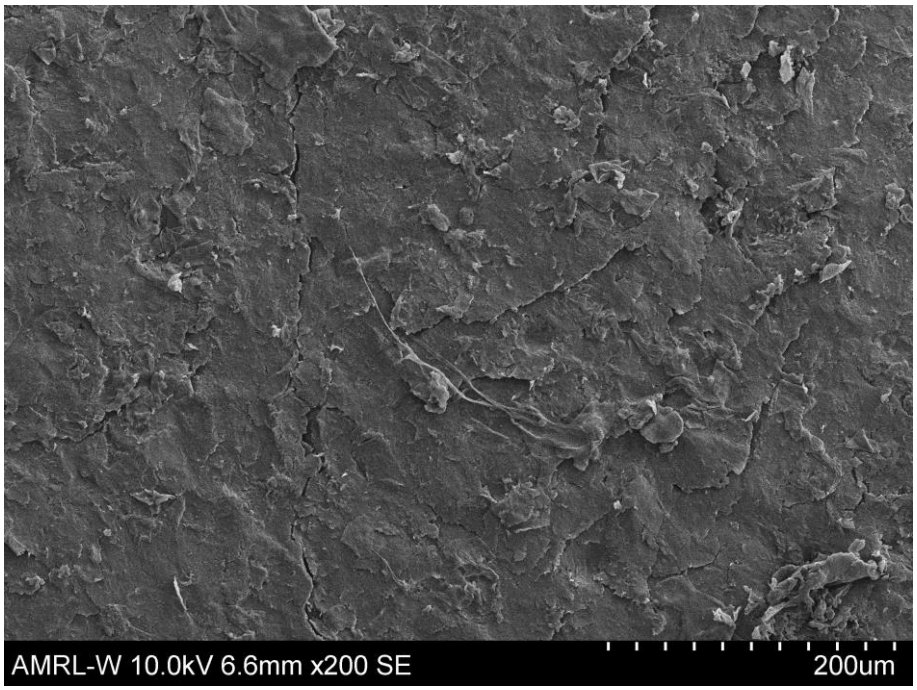

Figure 141. Details within wear scar Ultem 1010 90 degree impingement angle, x200 magnification.

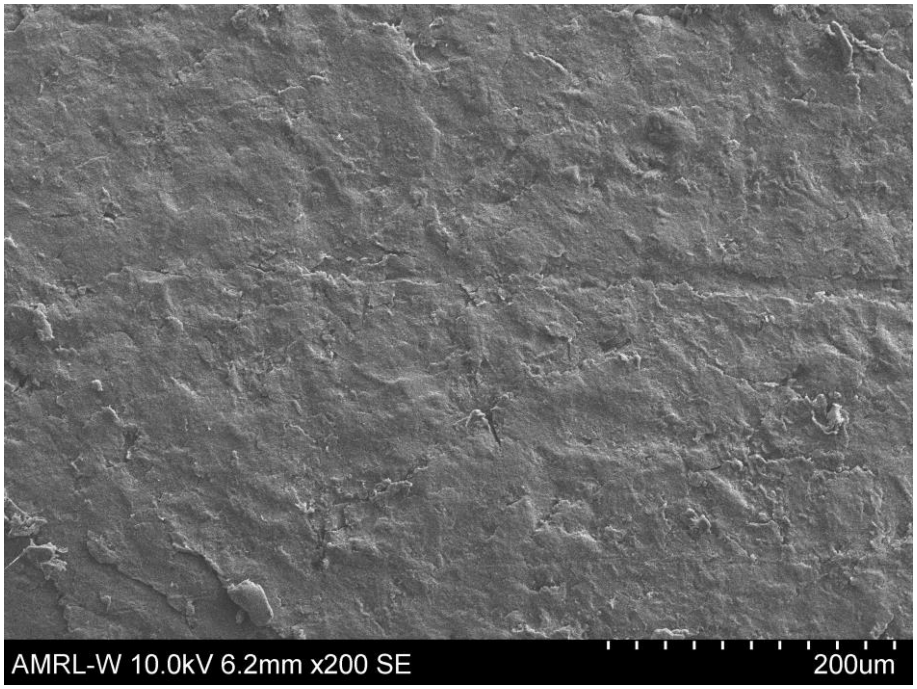

Figure 142. Details within wear scar Ultem 1010 90 degree impingement angle with epoxy sealed surface, x200 magnification.

Most images were taken for the 45° impingement angle as Ultem 1010 exhibited the highest erosion rates at this angle. For comparison some images were taken of the 90° impingement angle to compare the wear mechanisms present within these wear scars.

Figure 141 and Figure 142 compare the as deposited and epoxy sealed specimens that underwent erosion at 90° impingement angle. For the as deposited Ultem 1010, there are regions of cracking consistently over the surface with flakes and threads of material present as well. This indicates plastic deformation characteristic of ductile polymers but also cracking and the influence of weak spherulites of brittle polymers [115]. The epoxy sealed specimen exhibits less formation of flakes with more widespread cracking, this is due to the influence of the brittle epoxy. This mechanism is not as effective at material removal as the formation and removal of plastically deformed flakes which is reflected in the lower material loss found for the epoxy sealed specimen at normal impact.

Outside of the direct impingement zone, the secondary wear does not result in a deep wear scar but rather areas that are worn via abrasion. As shown in Section 6.6, this can have a significant contribution to the material loss of the specimen. This occurs downstream of the 45° and 20° wear scars and in a circumferential pattern around the wear scar for 90° impingement. As the sand loses energy and is moved out of the main wear scar by the incoming flow and particles, the particles experience an upward movement away from the material where they are then forced back down and come into contact with the surface [3, 172]. Because these particles have lost energy and have possibly been reduced in size due to impact with the surface and with one another the secondary wear does not result in as much material removal as the primary wear as shown in Figure 118.

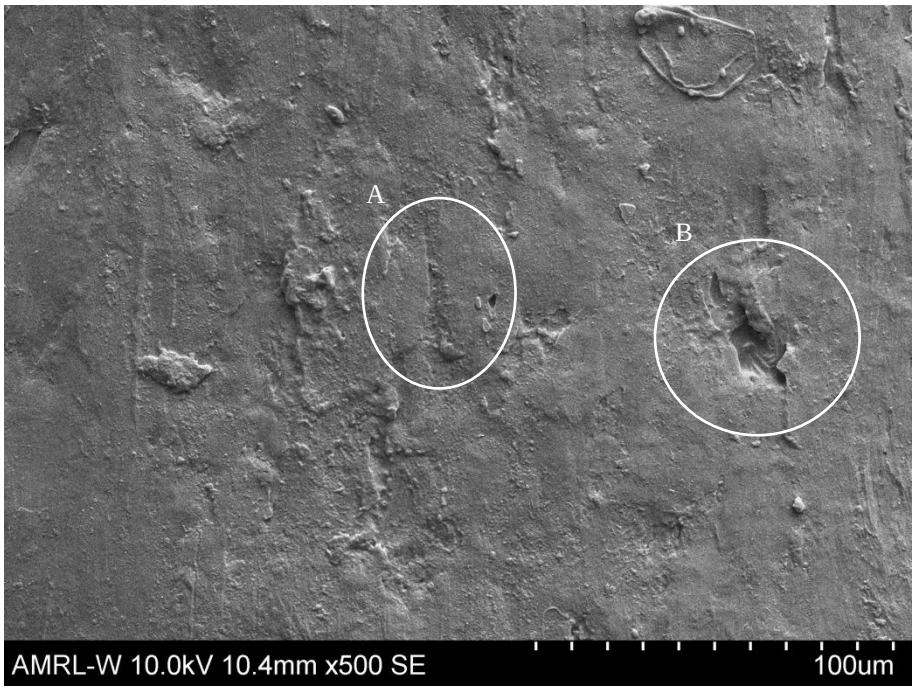

Figure 143. Details of secondary wear Ultem 1010 45,0 impingement angle, x500 magnification.

Figure 143 shows the secondary wear at 45°,0° for as deposited Ultem 1010. Here the dominant wear mechanism appears to be removal of the material via cutting (denoted as 'A'). There is debris remaining on the surface with areas that have undergone more extensive material removal (denoted as 'B').

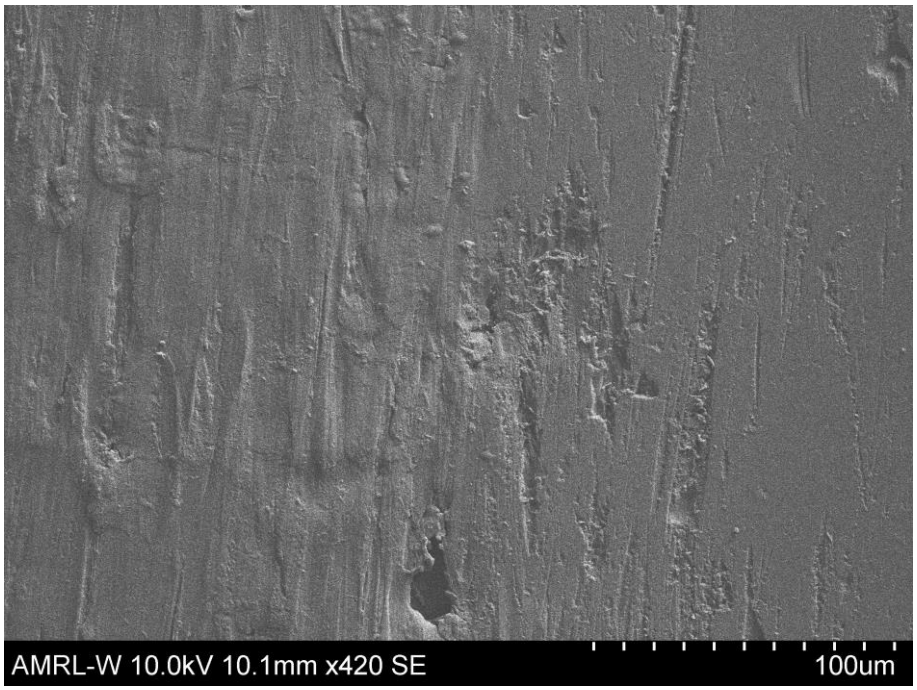

Figure 144. Details of secondary wear Ultem 1010 45,0 impingement angle with epoxy sealed surface, x420 magnification.

Figure 144 displays the secondary wear at the same angle, 45°,0°, but for an epoxy sealed specimen. Here striations due to cutting are much more apparent over the surface and there is less debris on the surface. This removal mechanism is not as effective due to the addition of the epoxy and displays similar morphology to a previous study for epoxy exposed to solid particle erosion at varying angles [143].

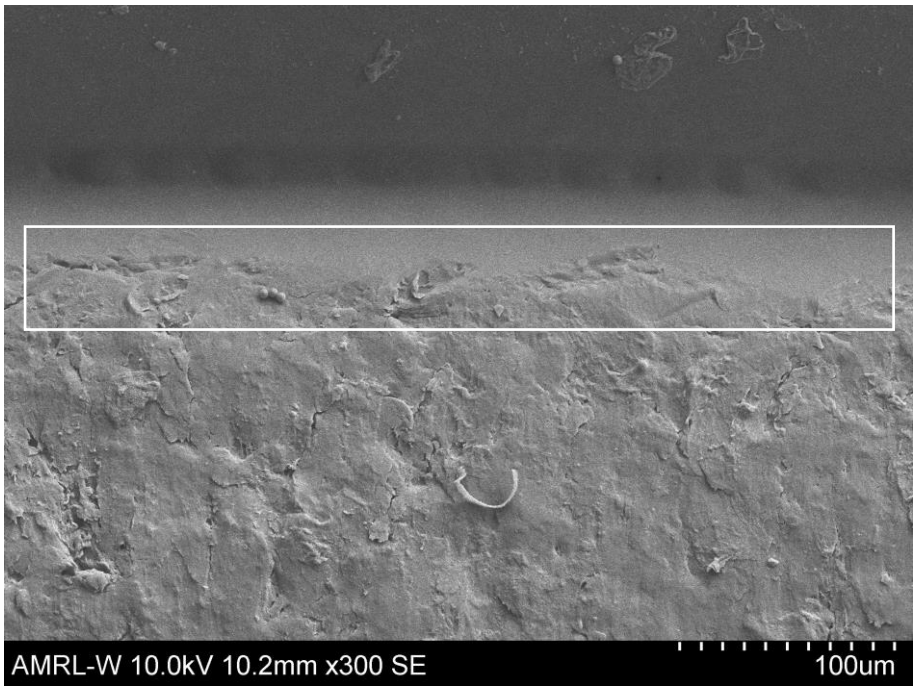

Figure 145. Details of secondary wear Ultem 1010 45,90 impingement angle, x300 magnification.

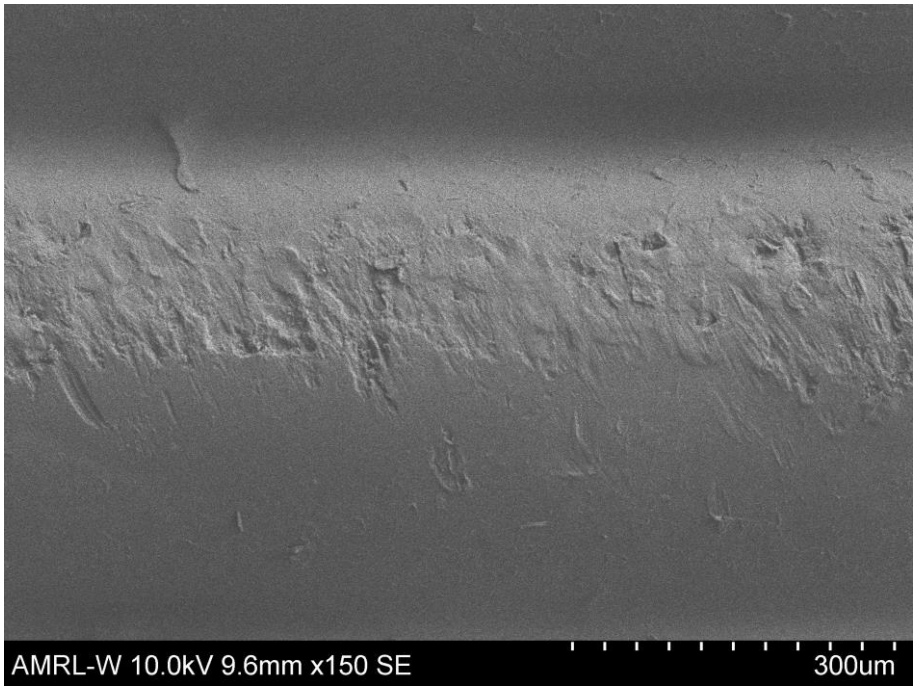

Figure 146. Details of secondary wear Ultem 1010 45,90 impingement angle with epoxy sealed surface, x150 magnification.

Figure 145 shows the side of a layer subjected to impact from the 45°,90° orientation for as manufactured Ultem 1010. Here similar mechanisms to the onset of wear are present with widespread cracking and flake formation from plastic deformation, however the damage is less extensive. In the white box, material removal due to normal impact is seen with cavities present. Figure 146 shows the same location of wear for the epoxy sealed specimen. Linear striations from cutting are present and show signs of the brittle behaviour of the epoxy similar to the 45°,0° orientation seen in Figure 144. Damage is isolated to the flow facing edge of the raster as below it is observed that the material retains a smoother undamaged surface.

SEM images provide a great understanding of the wear mechanisms present on the surface. Figure 147 compares the cracks observed from SEM with the optical microscope. The images in a) and b) are from the Ultem 1010 sample shown in Chapter 5, Section 5.6.5, Figure 102.

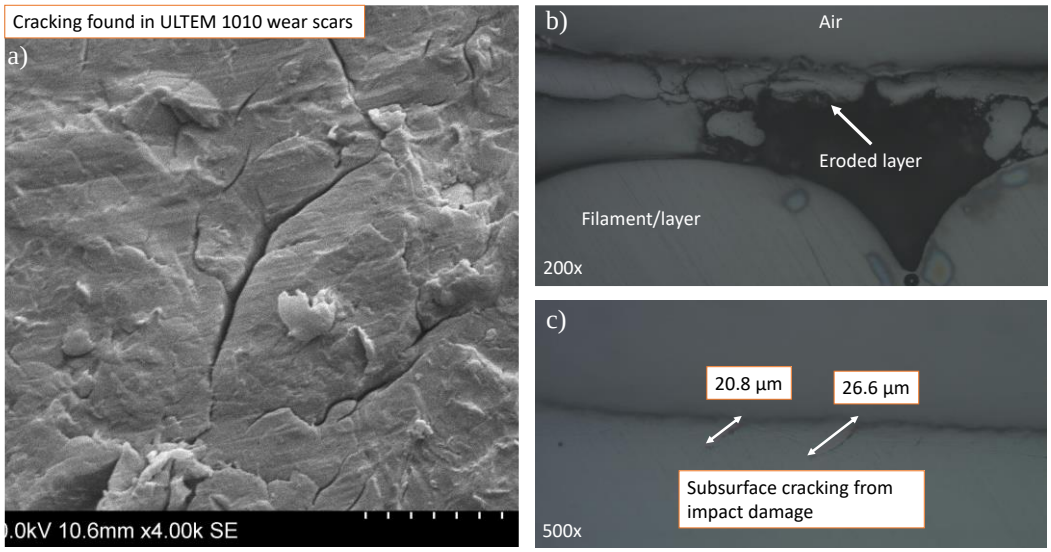

Figure 147. Cracking found in Ultem 1010 wear scars: a) SEM image x4.00k magnification, b) optical microscope image x200 magnification of cut Ultem 1010 specimen, c) optical microscope image x500 magnification of cute Ultem 1010 specimen with measured cracks.

In a) it is shown that via SEM cracking can be seen at high magnifications. In b) the uneroded layer below is visible. This shows that erosion is occurring on the 0.254 mm top layer. In c) cracks that were found in the cross section of the material and layers of erosion that resulted in fragmented material from the top layer. These cracks and fragments signify that in addition to plastic deformation, brittle fracture is occurring within the material as well. This brittle fracture will result in fragments that can be carried away by the recirculating flow resulting in mass loss. This further corroborates the semi-ductile nature of the material as determined by SEM image and analysis of the erosion vs. impact angle.

6.6.3.2 Nylon 12 CF

Similar phenomena are found for Nylon 12CF with the exception of fibre pull-out as this is a reinforced polymer. Overall, Nylon 12 is a more ductile material than Ultem 1010, however the carbon fibres will exhibit brittle behaviour upon impact. Previous studies of Nylon 12 (PA12) examined erosion behaviour and found that extensive plastic deformation is to be expected [122, 129]. The images that follow are in line with this literature.

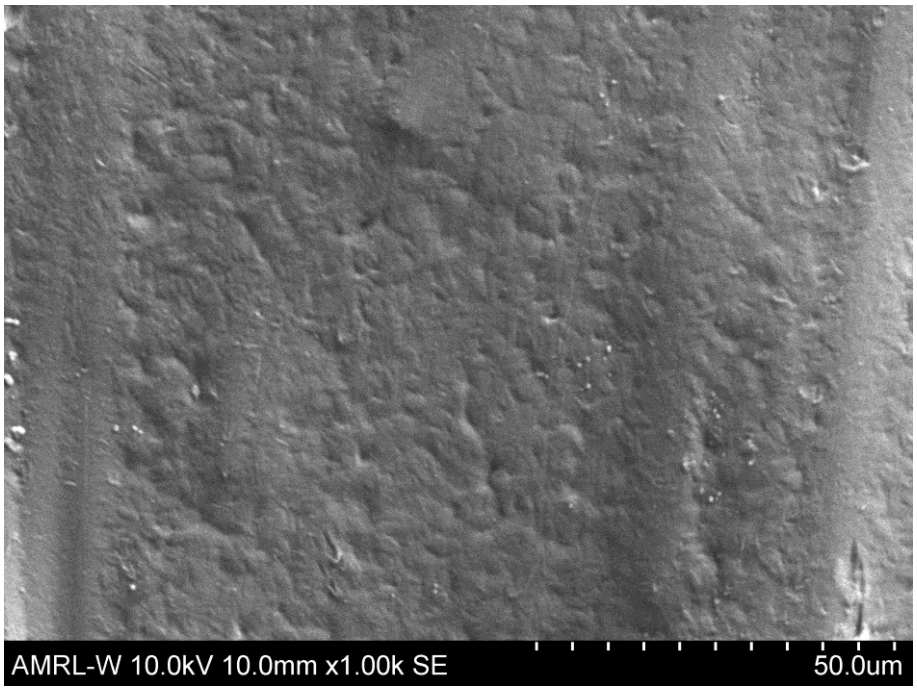

Figure 148. As deposited surface Nylon 12 CF, x1.00k magnification.

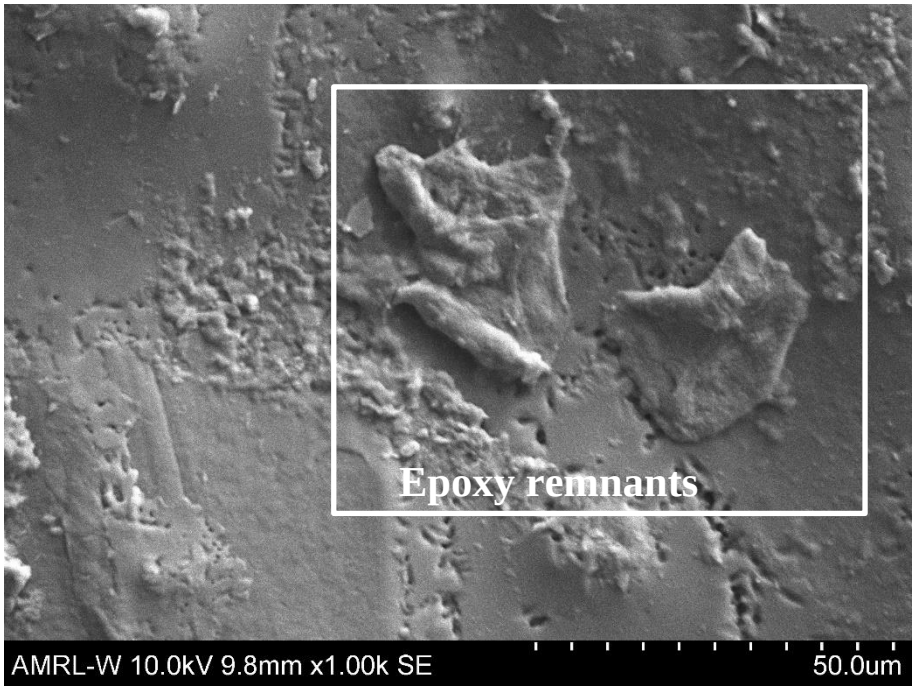

Figure 149. Nylon 12CF surface with epoxy seal, x1.00k magnification.

Figure 148 and Figure 149 compare the as deposited and epoxy sealed surface. The as deposited surface of N12CF is smooth with some surface texture. The following image shows an example of how the epoxy has bonded to the surface. This shows an increase in surface roughness and of epoxy on the N12CF in certain areas.

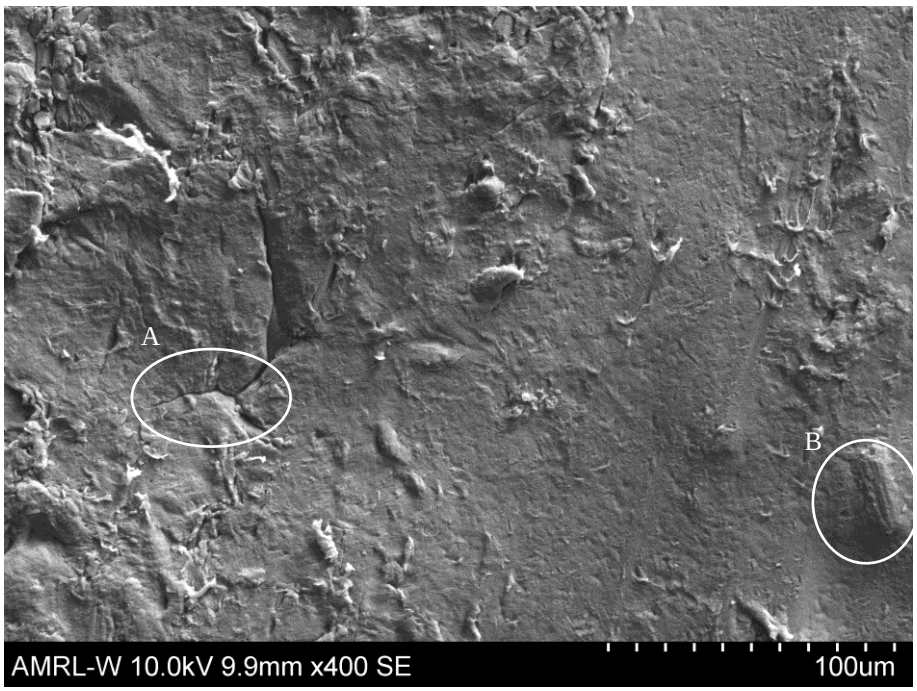

Figure 150. Edge of the wear scar Nylon 12CF 45,90 impingement angle. x400 magnification.

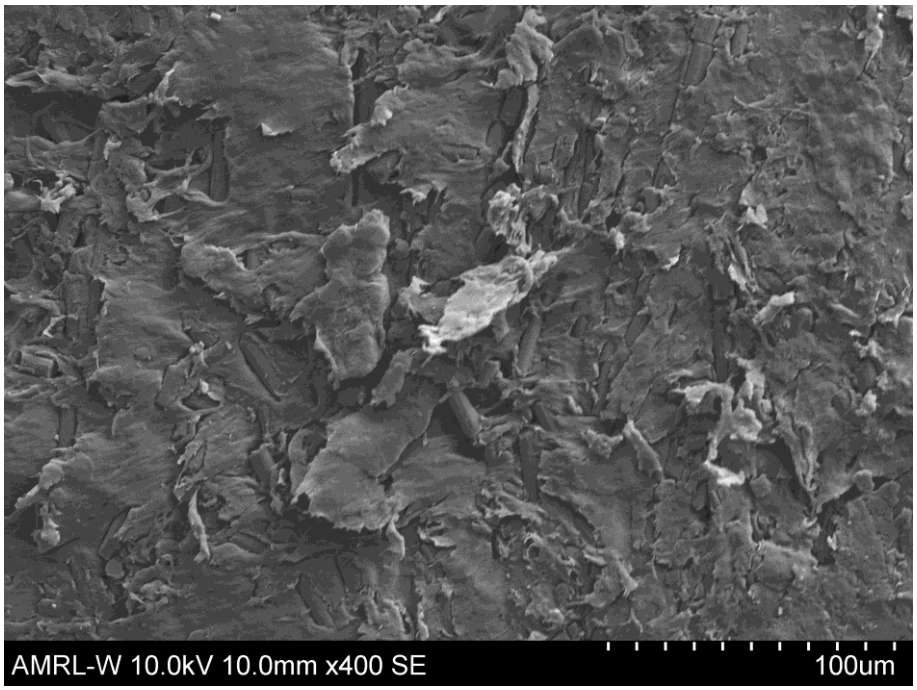

Figure 151. Edge of wear scar for Nylon 12CF 45,90 impingement angle with epoxy sealed surface. x400 magnification.

Figure 150 and Figure 151 show the edge of the wear scar for 45°,90° orientation as deposited and with epoxy sealing. As opposed to the Ultem 1010, for Nylon 12CF one of the identifiers of the presence of wear are exposed fibres. For the as deposited specimen, the formation of flakes due to micro-cutting and micro-ploughing is present over the surface at the edge of the wear scar as well as some cracking ('A') and some fibres nearer the surface ('B'). For 45°,90° a higher material loss was found for the epoxy sealed specimen than the as manufactured counterpart due to the raster acting as the 'fibre' with the epoxy acting as a 'matrix'.

The edge of the wear scar for this angle exhibits extensive material loss for the epoxy coated surface. When compared to the Ultem 1010, Nylon 12 has a greater ability to create chain entanglements with the epoxy as it is cured at elevated temperature [181]. As the sand impacts the surface, material will break away at the weakest point. Epoxy cures into a cross-linked network, while the Nylon 12 is comprised of semi-crystalline microstructure which demonstrates lower mechanical properties as this is due to

secondary bonding [182]. Therefore, as the epoxy creates interlinking cracks (brittle behaviour), and the surrounding Nylon 12 matrix is subjected to ductile failure the bonded material will be removed together. Additionally, the carbon fibres and rasters that are perpendicular to the flow will have lower resistance to bending induced by the particle impact leading to extensive damage. As seen in Figure 151, this created a surface with flake and debris covering nearly the entire surface that will be subjected to further wear. The effect of this was seen in the material loss where the Nylon 12CF specimens that have been sealed with epoxy exhibit greater values.

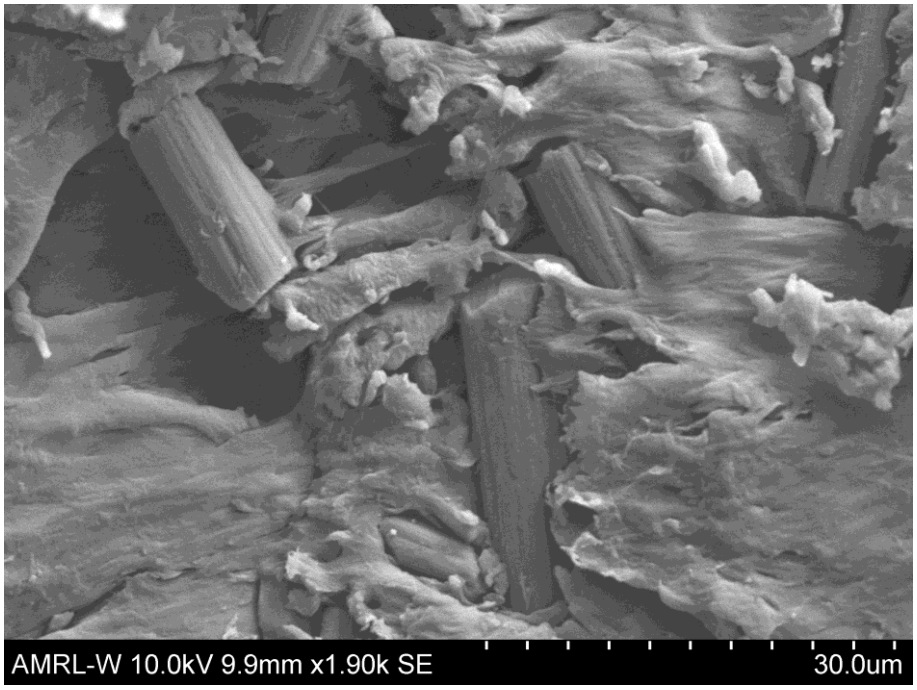

Figure 152. Exposed fibres at the edge of the wear scar for Nylon 12CF 45,90 impingement angle with epoxy sealed surface. X1.90k magnification.

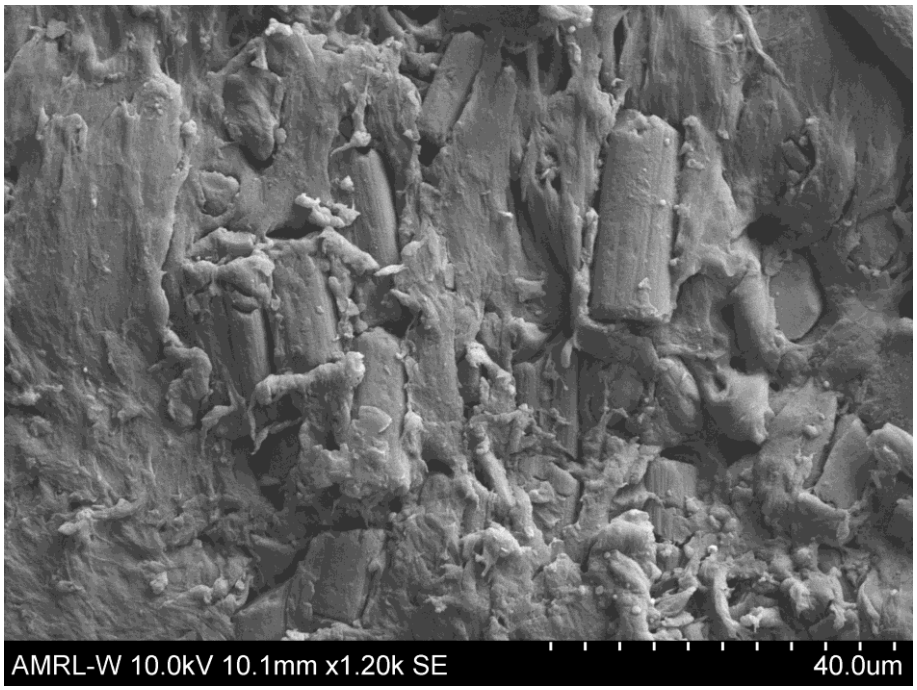

Figure 153. Exposed fibres at the edge of the wear scar Nylon 12CF 45,0 impingement angle. X1.20k magnification.

Figure 152 and Figure 153 show fibres at the onset of wear for the 45°,90° orientation with epoxy sealing and for 45°,0° as deposited. Fibres are shown to be exposed at the onset of wear no matter whether the epoxy is present or not. This was observed for both the 45°,0° and 45°,90° condition. The difference in size is most likely attributed to the chopping process of the fibres rather than erosion. The matrix material (Nylon 12) is more susceptible to damage from erosion as seen more clearly in Figure 152, where the matrix material is severely eroded, but the fibre remains present. From observation, it appears that the interface of the thermoplastic matrix with the carbon fibres is completely mechanical or frictional as gaps around the fibres can be seen as well as little to no remnants of matrix present the surface of the exposed fibres.

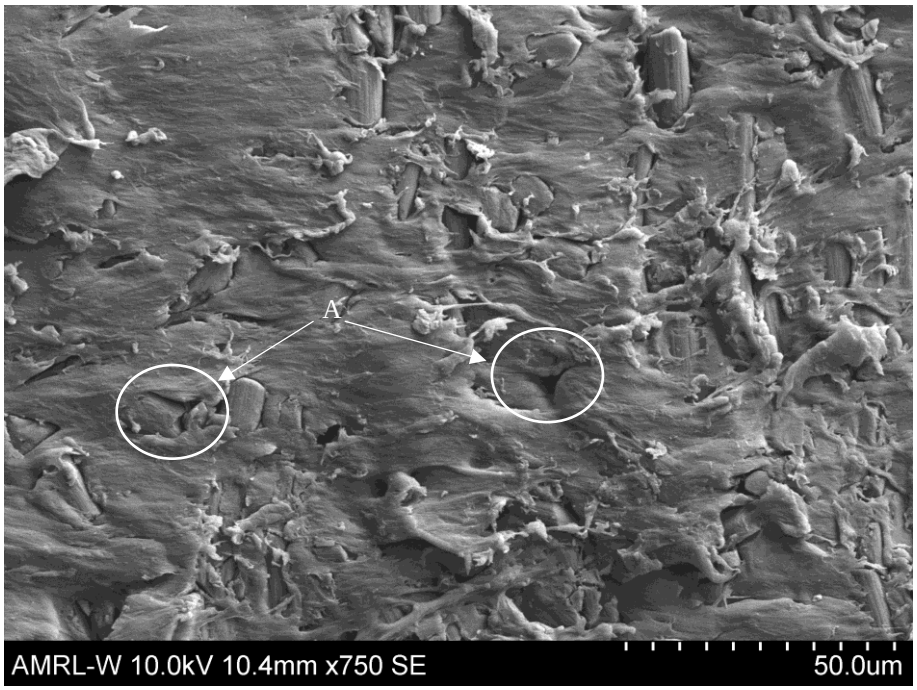

Figure 154. Details of wear scar Nylon 12CF 45,0 impingement angle with epoxy sealed surface, x750 magnification.

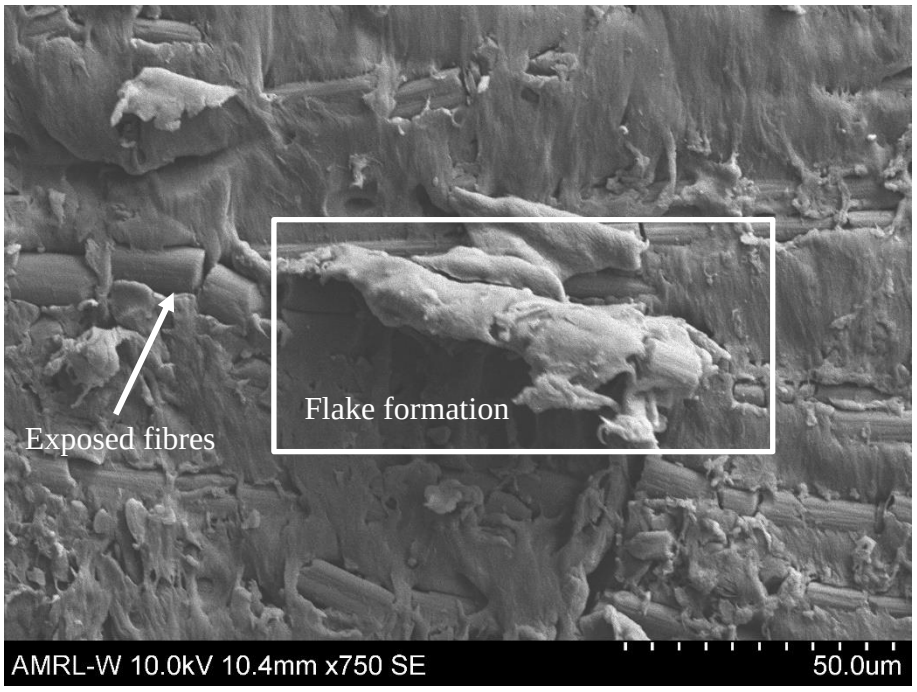

Figure 155. Details of wear scar Nylon 12CF 45,0 impingement angle, x750 magnification.

Figure 154 and Figure 155 show the difference within the wear scar for 45°,0° specimens sealed with epoxy and as deposited. The epoxy sealed specimen shows evidence of subsurface cracking (denoted as 'A') as well as micro-ploughing and micro-cutting. The as deposited specimen shows much larger flake formation plastic deformation exposing fibres below the surface. Within the wear scar the depth has exceeded the thickness of the printed layer, therefore the fibre direction will change. This will affect the progression of the wear as the fibre direction is known to have an effect on the erosion rate [125, 134, 183].

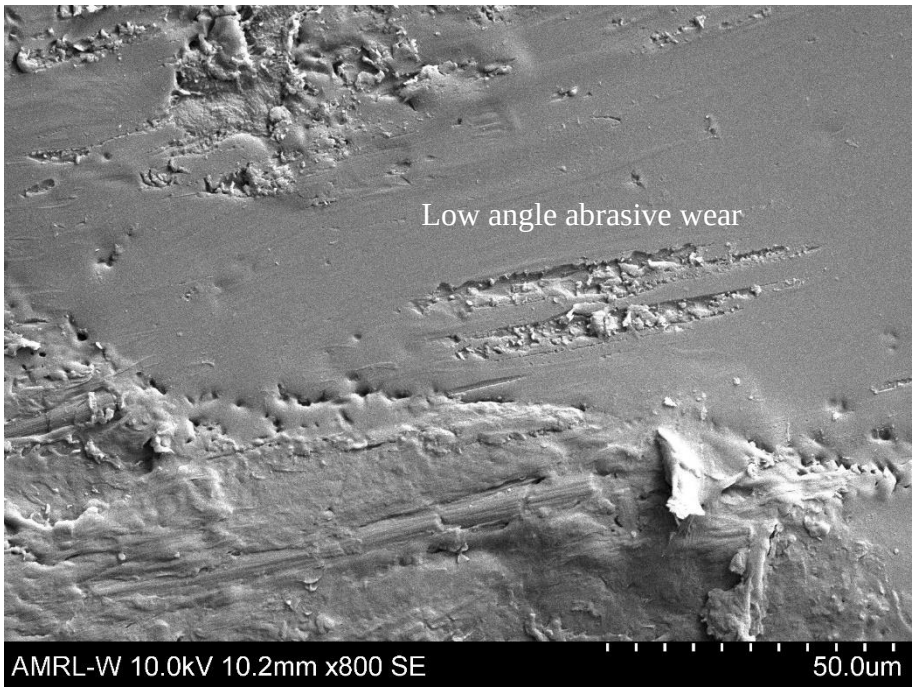

Figure 156. Details of secondary wear Nylon 12CF 45,0 impingement angle with epoxy sealed surface, x800 magnification.

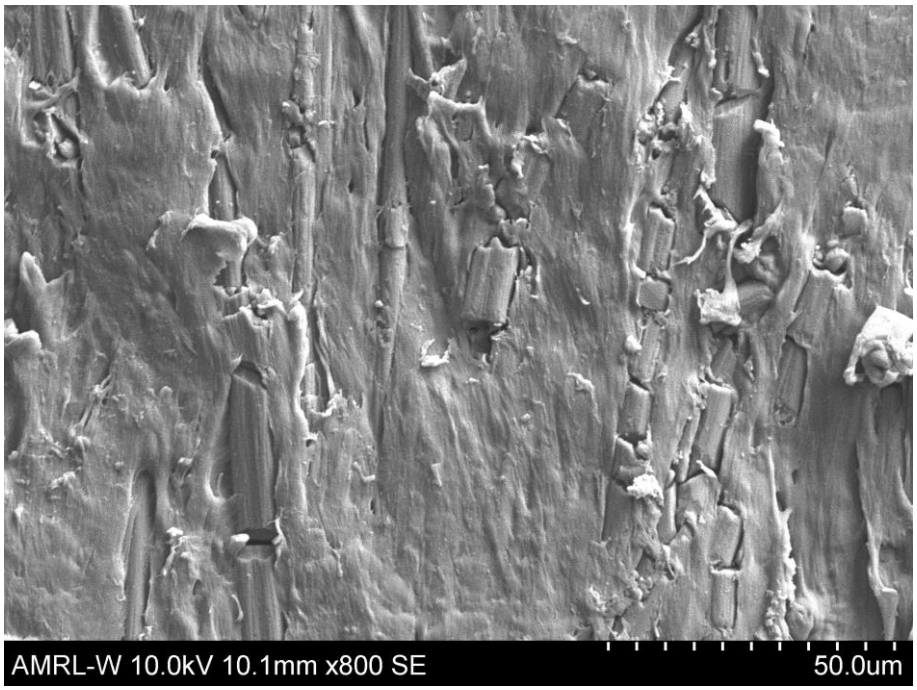

Figure 157. Details of secondary wear Nylon 12CF 45,0 impingement angle, x800 magnification.

Figure 156 and Figure 157 display secondary wear for 45°,0° with and without epoxy sealing. For the epoxy sealed specimen, linear abrasive wear and formations of cavities are very similar to behaviour exhibited for erosion of glass fibre reinforced epoxy from literature [143]. This signifies that for the secondary wear region, the epoxy will have a great influence on the wear. However, there is still some plastic deformation present in the bottom half of the image resulting from the ductile nature of the Nylon 12. For the as deposited specimen, plastic deformation is seen with the addition of broken fibres that are still embedded in the matrix but were not dislodged. In the secondary wear region only the top layer of material is worn. There is not exposure of sub-layers.

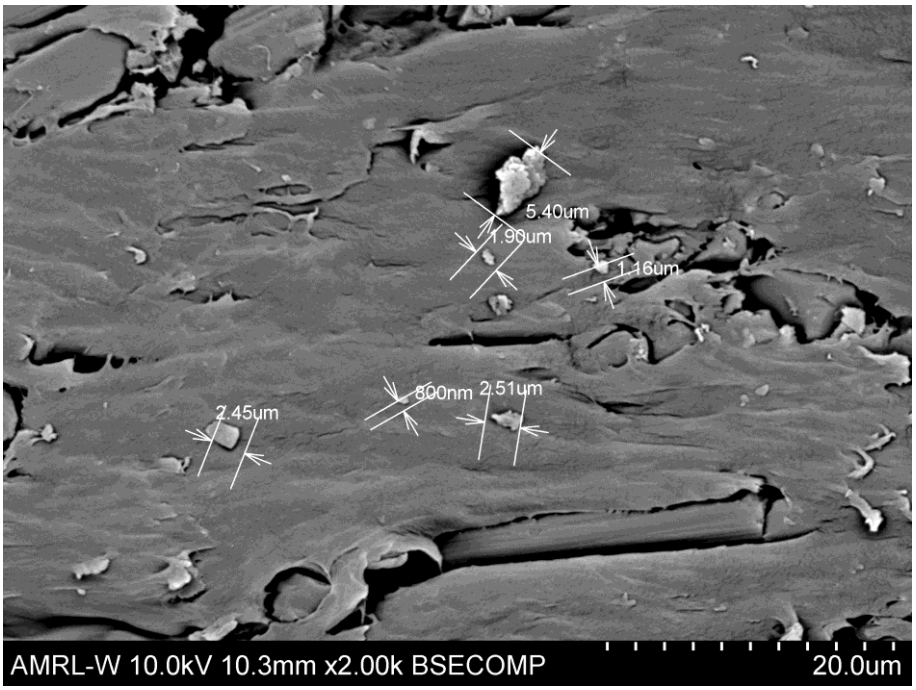

Figure 158. Sand found embedded in Nylon 12CF 45,0 impingement angle specimen with epoxy sealed surface, x2.00k magnification.

Figure 158 shows an image taken using back scattered electrons. The distinct elements present are distinguished by brightness. In this case anything made of silica (i.e., sand) will appear brighter than that made of a lower atomic number element such as carbon. In this image we can see fragments of sand that have embedded themselves in the surface of the Nylon 12CF specimen. This has already been shown via XCT analysis in Section 6.6.2 and has been further confirmed with SEM in Figure 158.

As with Ultem 1010, a cross section of the 45°,90° wear scar was analysed under an optical microscope (Figure 159). Exposed fibres and the difference in fibre orientation within each layer are observed. There was subsurface cracking and fragmentation as with Ultem 1010. The Ultem 1010 showed that the depth of the wear scar did extend beyond the 0.254mm layer, however for Nylon 12CF this is exceeded. The as deposited layer is slightly less thick than Ultem 1010, as seen in the XCT images (Figure 122and Figure 123), because the lower melt temperature and glass transition result in more flattening and neck growth between the deposited filaments. Image a)

in Figure 159 shows that within the direct impingement zone the cross section of the diameter of the fibre through the thickness meaning that the top layer is completely removed.

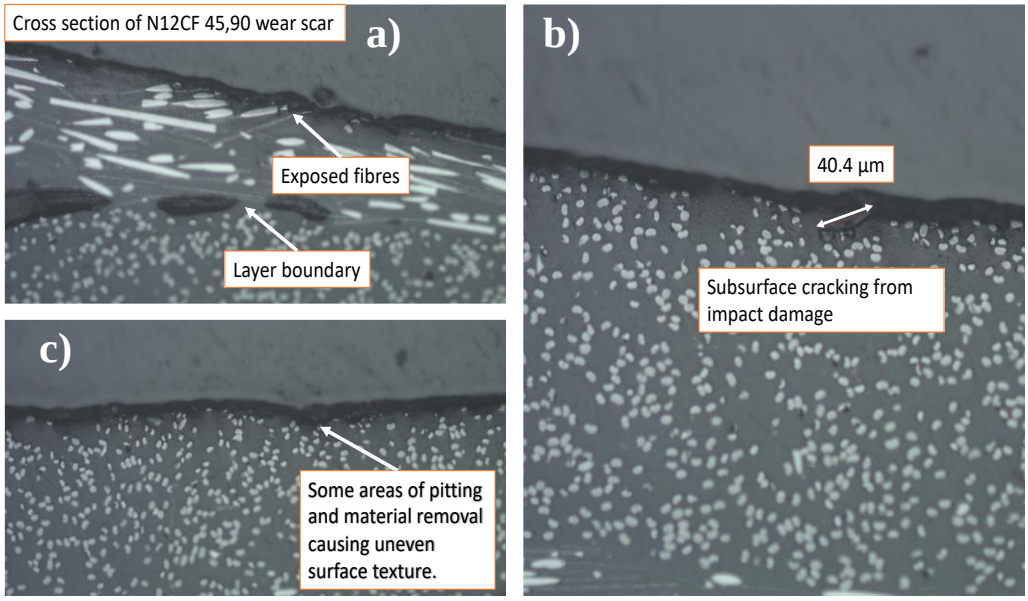

Figure 159. Cross section of Nylon 12CF wear scar showing exposed fibres and subsurface cracking.

At 90° the epoxy sealing provides the greatest advantage for erosion resistance out of all materials over the unsealed counterpart. Knowing that Nylon 12 is a softer material and epoxy is very strong and hard due to the cross-linking that occurs during curing for this thermoset polymer the addition of epoxy helps with the 90 degree performance overall. This is counter intuitive as the epoxy will have a more brittle nature than the Nylon 12 and signifies that the effect of the carbon fibres in the as deposited specimen drive the erosion response at 90°.

For the unsealed Nylon 12CF at 45° impingement angle, it is observed that the behaviour is in line with the behaviour of the Ultem 1010. This further corroborates that the sand particles are removing material within the air gaps between rasters in the 0° orientation, while they are losing energy when impacting the 90° orientation to

rasters. As with Ultem 1010, for the epoxy sealed specimens the air gaps are filled with a stronger material resulted in better wear resistance for the 0° to raster orientation. At 90° to the raster, the rate of removal of material is higher than 0° but also higher than the unsealed specimen for the same impingement angle. This requires further study; however, it could be due to fragments of epoxy that have been created due to brittle failure being bonded to the softer Nylon substrate and therefore carried away when plastic deformation occurs in the Nylon.

For the 20° impingement angle, the as deposited surfaces show better erosion resistance at 0° to flow than 90°. For the sealed specimens the results are nearly identical for mass loss between 0° and 90° orientation, where it would be expected that 90° would be higher as with sealed Ultem 1010 at 45°,90° and 20°,90° and as deposited Nylon 12CF at 45°,90°. The 20° impingement angle results in more abrasive wear regions than higher angles. As the sand particles are sliding over the surface it will take longer to bore through the upper layer.

6.6.4 Comparison of physical and mechanical properties

As discussed in the preceding sections, the surface of the additively manufactured specimens, the presence of fibres, and the impingement angle will have a great effect on the erosion mechanism and material loss. In an effort to understand if there are inherent characteristics of the material that drive erosion resistance the erosion rate was compared to the material properties relevant to this study (Table 22). With the exception of Ra and the hardness, all values were provided by the manufacturer of the materials.

Table 22. Material properties of specimens tested for slurry erosion.

Material	Ultimate Tensile Strength (MPa)	Modulus (GPa)	Tg (°C)	Ra (μm)	Hardness (Shore D)
Nylon 12CF	76	7.5	41	6.7	82.2
Ultem1010	81	2.7	215	21.4	87.1
Ultem 1000	85	3.2	217	0.164	88.9

In Figure 160, there is a clear trend of erosion rates decreasing with increasing tensile strength. This implies that stronger materials are more resistant to the solid particles and thus less failure occurs. However, reduction in erosion rates could also be due to a material's ability for stress hardening [184].

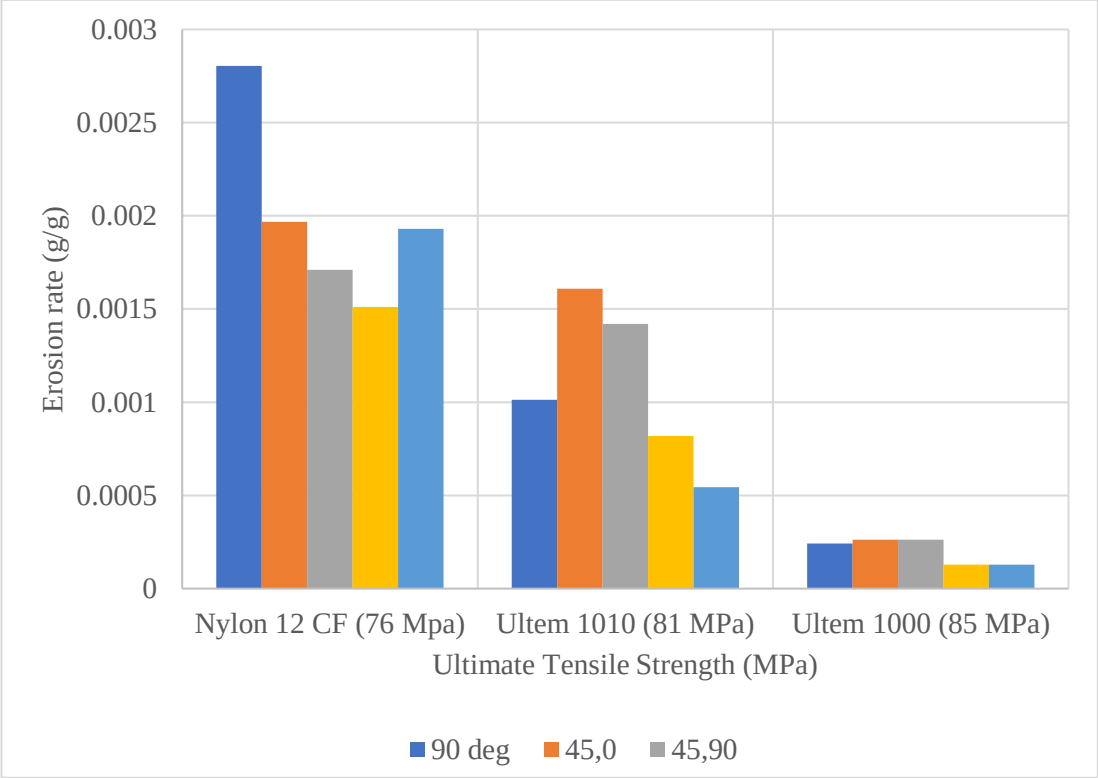

Figure 160. Erosion rates for each impingement angle with respect to tensile strength of target material.

Figure 161 compares the erosion rate to the tensile modulus. Looking at the two PEI materials, the 2.7 GPa modulus of Ultem 1010 results in higher erosion rates than the 3.2 GPa modulus Ultem 1000. However, in the case of the Nylon 12CF the tensile modulus is a product of the carbon fibre reinforcement. The stiffness of the carbon fibres and their orientation parallel to the tensile testing direction provide a large increase in modulus compared to the unreinforced PEI. This however does not translate to the wear resistance indicating that the process at a micro scale is not comparable to larger scaled tensile testing.

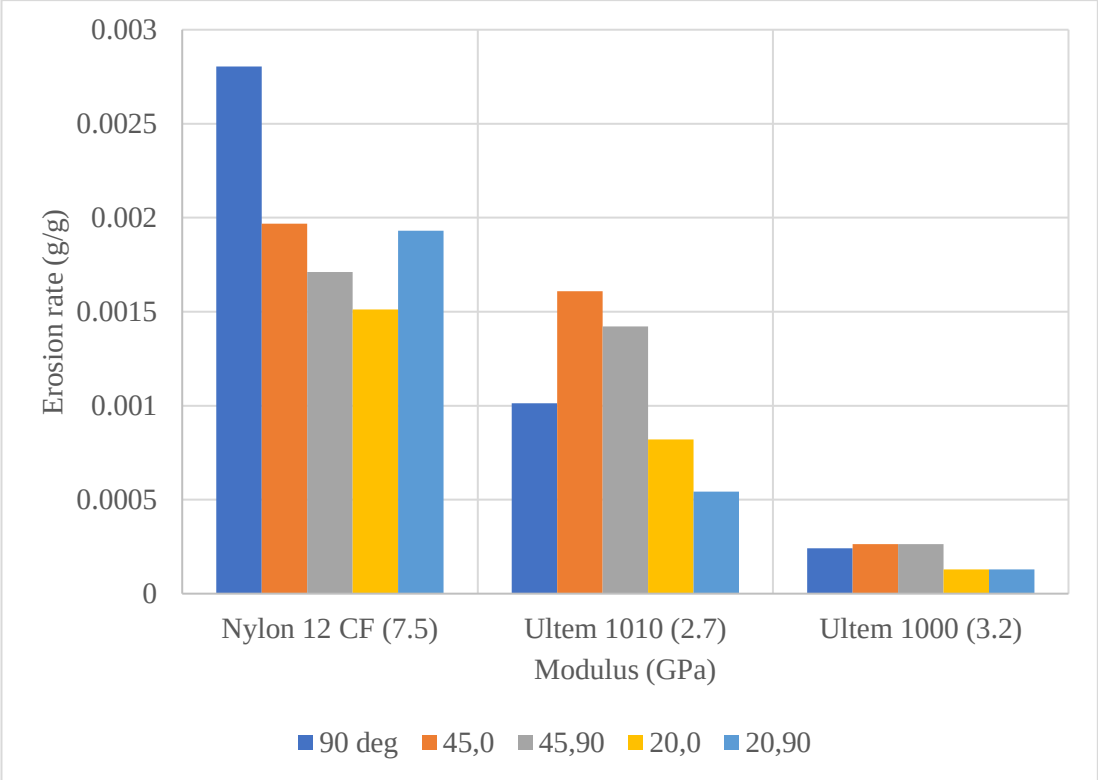

Figure 161. Erosion rates for each impingement angle with respect to tensile modulus of target material.

In Figure 162, the glass transition temperature is compared to the erosion rates for all impingement angles. Again, it is observed that there is a reduction in erosion with increasing Tg. The data points on the right represent the two PEI materials. It is known

that for erosion, lower Tg results in sand particles embedding in the material at early stages of erosion (known as incubation) which is not observed in higher Tg materials such as PEI [126]. However, the same authors have also found that erosion increases with increasing Tg which is not found in this study.

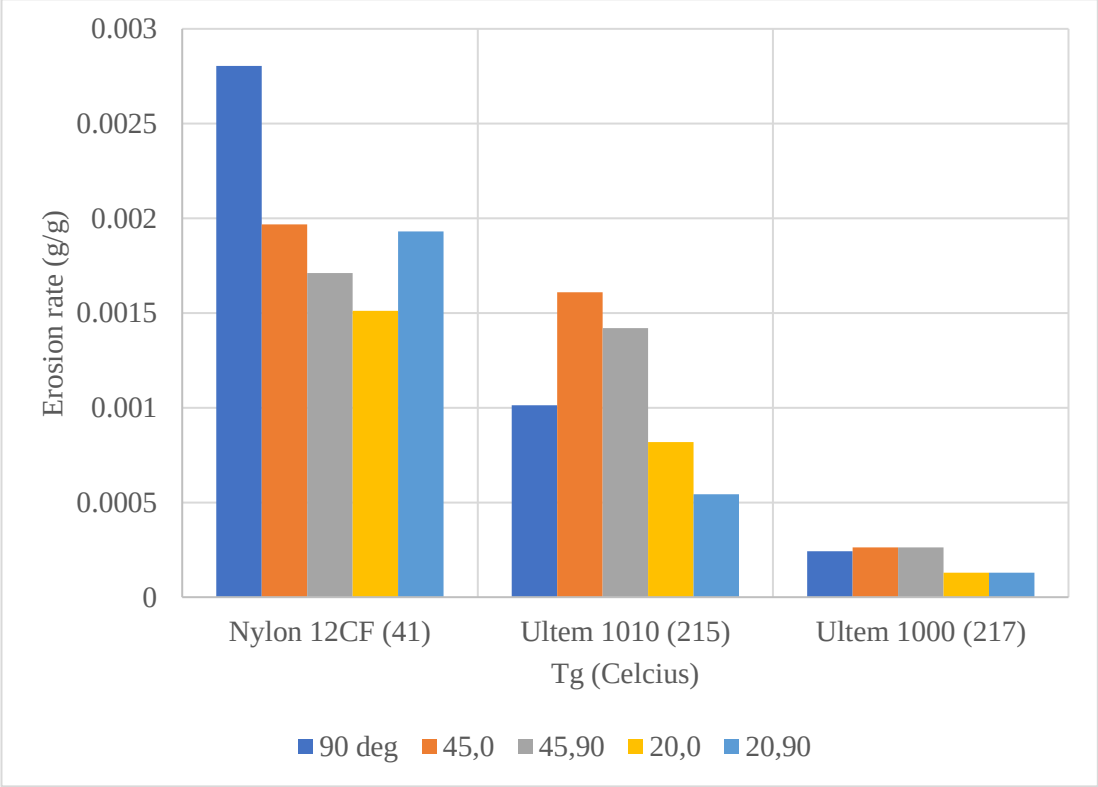

Figure 162. Erosion rates for each impingement angle with respect to glass transition temperature of target material.

Figure 163 compares the erosion rate to the surface roughness which plays an important role in erosion with respect to the impingement angle and the speed of the erodent [183]. Here there is not an apparent trend with relation to surface roughness. While the roughness of the Nylon 12CF specimens was lower than the 3D printed Ultem 1010, it exhibited greater wear. Ultimately, a combination of testing parameters, printing parameters, material properties and specimen preparation will have an effect on the erosion.

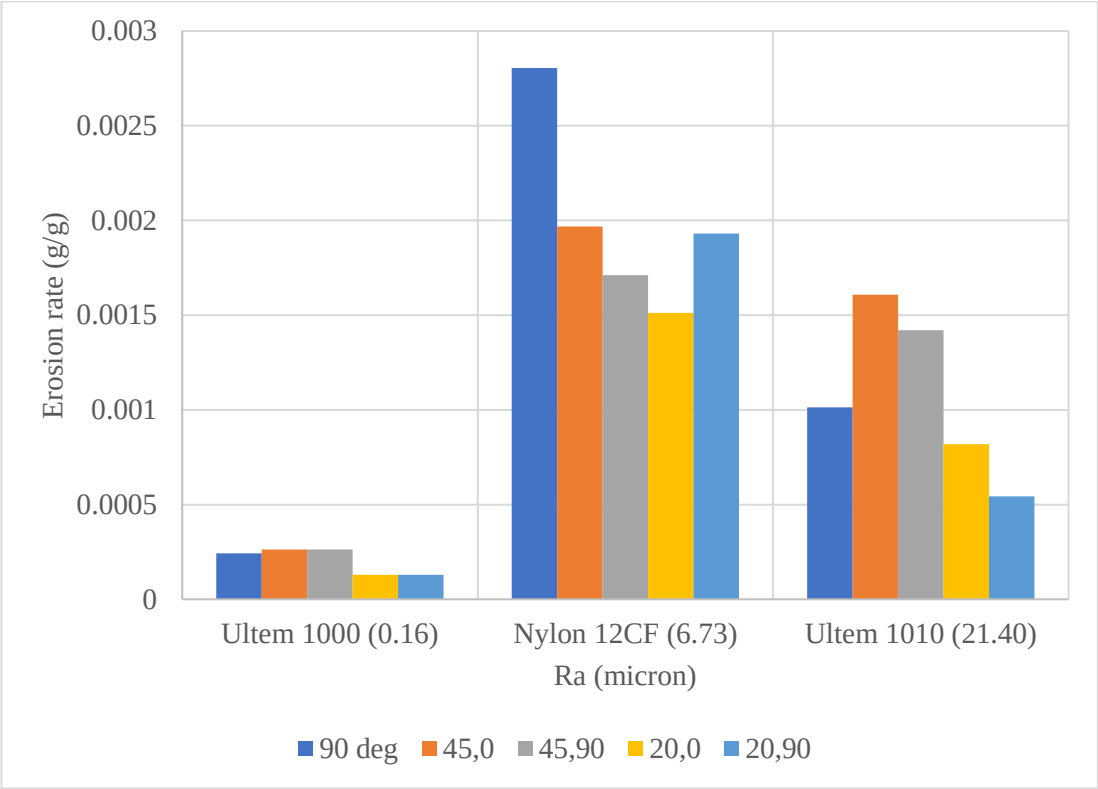

Figure 163. Erosion rates for each impingement angle with respect to surface roughness of target material.

Similarly, to tensile strength, an increase in the hardness of the target material does result in an increase in erosion resistance as seen in Figure 164. Simple models to describe sliding wear, such as the Archard equation, show that the total volume of debris created is inversely proportional to the hardness of the material [185]. Hardness is measured by impacting the material and measuring the indentation left, with greater depths corresponding to lower hardness. Thus, when examining an impact process such as erosion it is intuitive to correlate greater hardness with greater resistance.

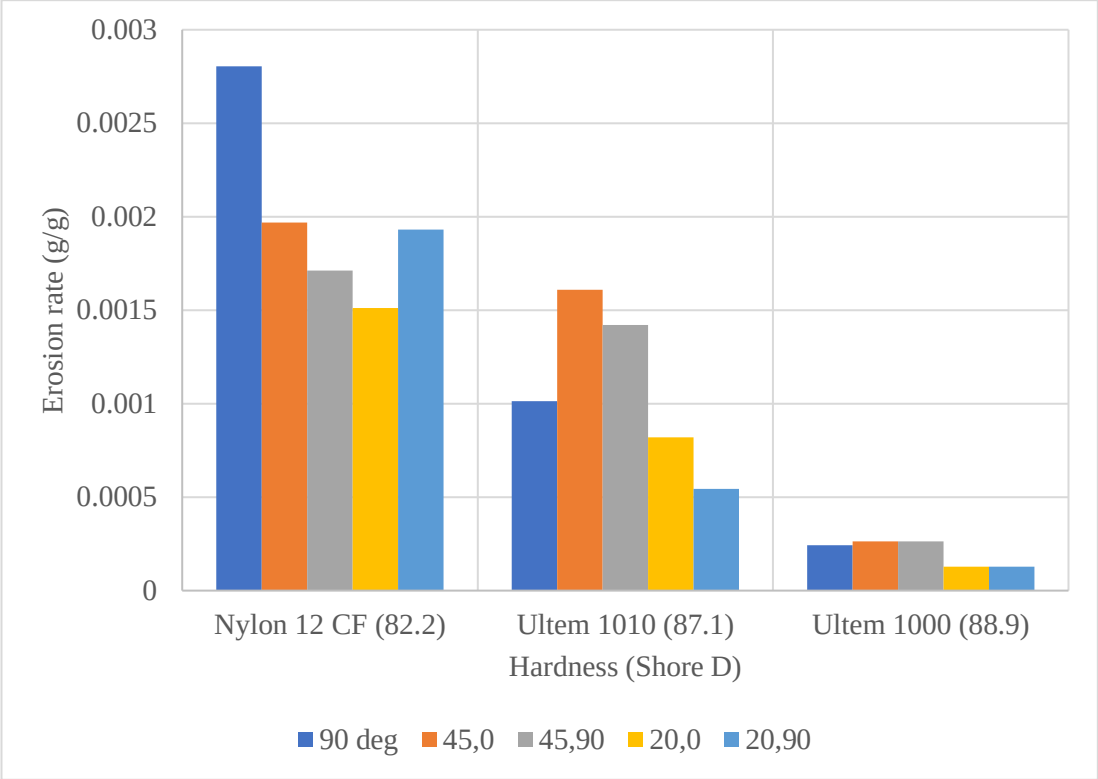

Figure 164. Erosion rates for each impingement angle with respect to hardness of target material.

6.6.5 Summary of discussion

Nylon 12CF experiences the most material loss at 90° impingement angle which implies that overall, the behaviour of the composite may align with brittle materials, however this is inconclusive due to the lack of data for angles 30° and 60° which are known to be particularly important for determining ductile and semi-ductile behaviour. For 45°, the 0° orientation to the layer resulted in greater wear than 90° due to the ability for the sand to erode between rasters. The erosion rate lowers for 45°,90° and 20°,0° with a jump up at 20°,90°. Here the ductile nature of the matrix is dominant rather than the brittle behaviour of the fibre. The induced roughness from the raster becomes a significant factor in wear at this low angle. For the fibres brittle cracking and pull out was observed with SEM, while the matrix exhibited ductile behaviour of

micro-cutting, micro-ploughing, and formation of flakes with the addition of interlinking cracks.

The epoxy sealed Nylon 12CF exhibited different behaviour than the as deposited Nylon 12CF. The peak of material loss is at 45° with 90° orientation to the raster (as sealed Ultem 1010 showed as well). The epoxy provided protection at the 90° impact angle with a significant reduction in material loss. 45°,90° and 20°,0° had worse wear than the unsealed specimens for the same angle and orientation. This is thought to be due to the entanglements of the DGEBA epoxy with the Nylon 12, possible during the time of curing of the epoxy sealant. The oven temperature was 70°C with local temperatures possibly exceeding this due to the exothermic reaction. This allowed for mobility in the Nylon 12 molecular chains. As the epoxy is worn it will remove the entangled Nylon with it. Additionally, previous studies showed an increase in mechanical properties and erosion resistance for Nylon 12 after exposure to water. The epoxy seal may be prohibiting the Nylon 12 from absorbing as much water during the 1-hour test, thus changing the performance. Further investigation would be needed on this. The wear mechanisms present from SEM are brittle cracking from the fibres and epoxy and micro-ploughing, micro-cutting, and plastic deformation from the matrix. Interlinking cracks are also present.

6.7 Conclusions

A fundamental investigation of the behaviour of additively manufacturer polymers and polymer composites was performed. After a review of the literature, it was found that this a very novel area of research and therefore much of the findings from this study do not have direct comparisons to existing results. In addition to this, the behaviour exhibited by a material is highly dependent on the parameter of the erosion experiment. By utilising the existing body of knowledge for erosion of traditionally manufactured polymers and polymer composites, the significant findings of this study are as follows:

1. The experimental methodology was developed and validated to evaluate the erosion and corrosion resistance of metallic and metal matrix composite

materials. Through the testing of Ultem 1000, the experiment was validated using Stokes number and erosion efficiency for use with polymeric materials as the results fell in line with the literature and expectations.

2. At the macro level, the shape of the wear scar for all materials were in line with expectations from literature and previous studies.

3. XCT analysis provided information regarding the internal structure of the printed materials as well as the calculation of sand embedded within the material. After visualising the sand and calculating the mass, it was found that any silica present was considered to be negligible. The internal structure of Ultem 1010 contains larger voids than the Nylon 12CF. This is due to the processing parameters and the higher Tg and melt temperature of the Ultem 1010.

4. Overall, Ultem 1000 performed better than any additively manufactured material. The sealed and unsealed Ultem 1010 specimens performed second best, with Nylon 12CF (sealed and unsealed) having the worst erosion performance.

5. Ultem 1010 exhibits semi-ductile behaviour with the peak of erosion observed at the 45° impingement angle. Material loss is observed to be higher when the flow is 0° to the raster, which is in line with the most recent literature. This is due to sand eroding within the air gap. The wear mechanisms present are micro-cutting, micro-ploughing, and interlinking cracking. The plastic deformation leads to the formation of flakes which are then subjected to further erosion and removal.

6. Ultem 1010 sealed with epoxy results in peak erosion at the 90° orientation to raster at the 45° and 20° impingement angles. This is due to a combination of

air gaps being filled with epoxy resulting in sand maintaining energy as it travels along the surface and further resistance provided by the filled air gaps for the 0° orientation. Using the conceptual model of a composite laminate, the rasters acting as fibres are more susceptible to erosion at 90° orientation due to less resistance to bending caused by particle impact. Overall, sealing the specimen provided protection at all angles except 20° impingement. At 90° impingement, the material loss is higher than 45°,0° signifying the impact of the brittle behaviour of the epoxy. The wear mechanisms observed are cracking, micro-cutting, micro-ploughing, and plastic deformation.

7. Nylon 12CF experiences the most material loss at 90° impingement angle which implies that overall, the behaviour of the composite may align with brittle materials, however this is inconclusive due to the lack of data for angles 30° and 60° which are known to be particularly important for determining ductile and semi-ductile behaviour. For 45°, the 0° orientation to the layer resulted in greater wear than 90° due to the ability for the sand to erode between rasters. The erosion rate lowers for 45°,90° and 20°,0° with a jump up at 20°,90°.

8. The epoxy sealed Nylon 12CF exhibited different behaviour than the as-deposited Nylon 12CF. The peak of material loss is at 45° with 90° orientation to the raster (as sealed Ultem 1010 showed as well). The epoxy provided protection at the 90° impact angle with a significant reduction in material loss. 45°,90° and 20°,0° had worse wear than the unsealed specimens for the same angle and orientation.

9. Comparison of the ranking of material loss from calculated volume loss and measured wear scar depth proved that abrasive wear outside the wear scar

cannot be considered negligible in a number of cases. Further studies would be recommended to quantify and analyse this phenomenon.

10. Overall, it does not appear that the surface texture of the additively manufactured samples provides a benefit for erosion resistance when compared to traditionally manufactured polymers. Sealing the material does result in a change in wear behaviour, but this differs depending on the target material and the testing parameters.

11. The error bars are markedly higher for the additively manufactured specimens versus the injection moulding Ultem 1000. This signifies that the printed materials are more sensitive to the exact experimental parameters. There is high variability in the findings depending on a number of factors: impingement angle, angle of rasters with respect to flow, sealing of porosity and addition of fibres. The main finding of this study is that these materials are highly adaptable and with further research could provide an advantage for erosion resistance.

12. The material properties do not show a clear correlation with the erosion rate. Erosion is dependent on a number of factors and thus cannot be predicted by a singular property or parameter.

7. Thesis conclusions and future work

7.1 Conclusions

Two work packages were undertaken for this investigation: a hydrocyclone case study and a fundamental wear investigation. Both studies produced data that supports a move to polymers and polymer composites made via additive manufacturing for suitable Weir applications.

The combination of the results of this research with the ongoing work in the field of additive manufacturing at the Weir Group creates the timely opportunity to further pursue this manufacturing method and explore the ability to bring these materials from the research realm into operating 150 CVD hydrocyclones. The fundamental study of erosion of additively manufactured polymers and polymer composites is an extremely novel topic with only two papers having been published. The findings presented in this thesis provides further contribution to this expanding field.

The significant findings are:

1. For hydraulic loading, the structural requirements of the 150 CVD casing are very low. For 3 bar pressurisation there are some locations of stress concentrations, however the majority of the structure exhibits lower stress.

2. Areas of stress concentrations that could be optimised for a design that was tailored to additive manufacturing and design work in order to eliminate stress concentrations and create more robust thicknesses where needed is required.

3. ABS is a suitable material for the structural requirements of the 150 CVD hydrocyclone. After 3 bar pressurisation and pressurisation to failure it exhibited adequate strength and did not fail until 11 bar (almost 4 times the requirement of the 150 CVD). Catastrophic failure can be anticipated to occur at locations where deposited material rasters meet, as shown in

Section 3.4 where the crack propagated along the length at the intersection of each circumferentially deposited raster.

4. ABS exhibits creep behaviour. The response of the material is dependent not only on the conditions of the loading, but also time. In a closed system, this will create feedback between the expansion of the vessel and the pressure within. The data shows that the system will attempt to achieve equilibrium, however it is anticipated that eventually the material will fail. After 6 days with only hydrostatic force applied, there were further creep events however the material did not fail or show significant signs of elongation or dilation.

5. Overall, Ultem 1000 performed better than any additively manufactured material. The sealed and unsealed Ultem 1010 specimens performed second best, with Nylon 12CF (sealed and unsealed) having the worst erosion performance.

6. Ultem 1010 exhibits semi-ductile behaviour with the peak of erosion observed at the 45° impingement angle with highest material loss is observed to be higher when the flow is 0° to the raster. The wear mechanisms present are micro-cutting, micro-ploughing, and interlinking cracking. The plastic deformation leads to the formation of flakes which are then subjected to further erosion and removal. Ultem 1010 sealed with epoxy results in peak erosion at the 90° orientation to raster at the 45° and 20° impingement angles. Overall, sealing the specimen provided protection at all angles except 20° impingement. At 90° impingement, the material loss is higher than 45°,0° signifying the impact of the brittle behaviour of the epoxy. The wear mechanisms observed are cracking, micro-cutting, micro-ploughing, and plastic deformation.

7. Nylon 12CF experiences the most material loss at 90° impingement angle which implies that overall, the behaviour of the composite may align with brittle materials, however this is inconclusive due to the lack of data for angles 30° and 60° which are known to be particularly important for determining ductile and semi-ductile behaviour. The erosion rate lowers for 45°,90° and 20°,0° with a jump up at 20°,90°. The epoxy sealed Nylon 12CF exhibited different behaviour than the as deposited Nylon 12CF. The peak of material loss is at 45° with 90° orientation to the raster (as sealed Ultem 1010 showed as well). The epoxy provided protection at the 90° impact angle with a significant reduction in material loss. 45°,90° and 20°,0° had worse wear than the unsealed specimens for the same angle and orientation.

8. Abrasive wear outside the wear scar cannot be considered negligible in a number of cases.

9. Surface texture of the additively manufactured samples does not provide a clear benefit for erosion resistance when compared to traditionally manufactured polymers. Sealing the material does result in a change in wear behaviour, but this differs depending on the target material and the testing parameters.

10. Overall, the 150 CVD is considered to be a good candidate for additive manufacturing via FDM. The structural requirements of the casing are such that ABS is satisfactory. The results of the erosion investigation provided a valuable contribution to the research field, however further work is necessary to meet the requirements of the 150 CVD.

7.2 Future Work

7.2.1 Case Study

The recommendations for future work are as follows:

1. In order to reduce the possibility of catastrophic failure, avoiding printing patterns where layers start and end on the same axis is recommended. This will prevent failure as seen in the ABS cylinder. If failure can be localised via design and printing parameters, then there is a possibility for repairs rather than replacement in the future.
2. A continuation of pressure testing for various geometry and materials is recommended in order to gain further knowledge on the behaviour of additively manufactured materials in this field.
3. A design that eliminates very sharp transitions and corners is recommended in order to better take advantage of the freedom that comes with using additive manufacturing and reduce possible stress concentrations and points of failure. Additionally, the creation of a more uniform body for the hydrocyclone that eliminates flanges could be possible.
4. Material modelling to understand the effects of the printing parameters is highly recommended. This could be done by creating a 3D model from XCT of a specimen.
5. A more sophisticated and repeatable methodology, for example using vacuum assisted resin transfer, is recommended.
6. Full scale printing and testing of an ABS 150 CVD with liner is recommended.
7. A fundamental investigation of the long term creep and fatigue behaviour of ABS for a pressure vessel would provide information on the longevity of the design and continue to add to the existing body of work in this area.

7.2.2 Wear

The recommendations for future work are as follows:

1. Continue to test additively manufactured materials to understand the effect of the following parameters: change in slurry concentration, change in speed of flow, addition of further impingement angles, addition of further angles of top layer with respect to flow, varying test lengths. For the Nylon 12CF, a comparison to Nylon 12 without reinforcement could provide further information on the benefit of the added carbon fibres.
2. A comparison of Nylon 12CF to a traditionally manufactured specimens would provide a baseline for comparison.
3. Further study to understand the significance of abrasive wear outside of the main wear scar.
4. Testing the bonding of the epoxy to the substrate materials would provide further information as to how this interacts with the wear resistance.
5. Wear testing was performed on the existing rigs at the Weir Advanced Research Centre; however, this is a very aggressive environment. Testing these materials in conditions more similar to that of the 150 CVD would provide information that is more directly relatable to the application. As this was an initial and fundamental study conditions were kept consistent to enable comparison to existing Weir data for further use in the future.

8. References

[1] Levesque M, Millar D, Paraszczak J. Energy and mining – the home truths. Journal of Cleaner Production. 2014;84:233-55.

[2] Walker CI, Robbie P. Comparison of some laboratory wear tests and field wear in slurry pumps. Wear. 2013;302(1-2):1026-34.

[3] Giourntas L. Investigation of erosion-corrosion behaviour of pump materials [Ph.D. thesis]: University of Strathclyde; 2016.

[4] Morrell S. Increasing profitability through integration of blasting and comminution effort. IIR CONF1998.

[5] Bruckard WJ, Sparrow GJ, Woodcock JT. A review of the effects of the grinding environment on the flotation of copper sulphides. International Journal of Mineral Processing. 2011;100(1):1-13.

[6] Topal M, Arslan Topal EIı, Öbek E. Remediation of pollutants with economical importance from mining waters: Usage of Cladophora fracta. Environmental Technology & Innovation. 2020;19:100876.

[7] Victor A. Goldade LSP, Anna V. Makarevich, Vladimir N. Kestelman. Plastics for Corrosion Inhibition. Germany: Springer-Verlag Berlin Heidelberg; 2005.

[8] Tetzlaff EJ, Goggins KA, Pegoraro AL, Dorman SC, Pakalnis V, Eger TR. Safety culture: a retrospective analysis of occupational health and safety mining reports. Safety and health at work. 2021;12(2):201-8.

[9] Kabir SMF, Mathur K, Seyam A-FM. A critical review on 3D printed continuous fiber-reinforced composites: History, mechanism, materials and properties. Composite Structures. 2020;232:111476.

[10] Ali MH, Batai S, Sarbassov D. 3D printing: a critical review of current development and future prospects. Rapid Prototyping Journal. 2019;25(6):1108-26.

[11] Chen W, Zhang Q, Cao H, Yuan Y. Process evaluation, tensile properties and fatigue resistance of chopped and continuous fiber reinforced thermoplastic composites by 3D printing. J RENEW MATER. 2022;10(2):329-58.

[12] Yang IH, Shin CB, Kim TH, Kim S. A three-dimensional simulation of a hydrocyclone for the sludge separation in water purifying plants and comparison with experimental data. Minerals Engineering. 2004;17(5):637-41.

[13] Abdollahzadeh L, Seyfi Mazraeno M, Hosseini SN, Fazlali A, Khatami M. Application of a 3D printed miniaturized hydrocyclone in biopharmaceutical industry-numerical and experimental studies of yeast separation from fermentation culture media. Prep Biochem Biotechnol. 2022;ahead-of-print(ahead-of-print):1-9.

[14] Ji L, Paul P, Shanbhag BK, Dixon I, Kuang S, He L. Emerging application of hydrocyclone in biotechnology and food processing. Separation and purification technology. 2022:122992.

[15] Aldrich C. Chapter One - Hydrocyclones. In: Tarleton S, editor. Progress in Filtration and Separation. Oxford: Academic Press; 2015. p. 1-24.

[16] Murray HH. Major kaolin processing developments. International Journal of Mineral Processing. 1980;7(3):263-74.

[17] Yalamanchili MR, Miller JD. Removal of insoluble slimes from potash ore by air-sparged hydrocyclone flotation. Minerals Engineering. 1995;8(1):169-77.

[18] Casali A, Gonzalez G, Torres F, Vallebuona G, Castelli L, Gimenez P. Particle size distribution soft-sensor for a grinding circuit. Powder Technology. 1998;99(1):15-21.

[19] Puprasert C, Hebrard G, Lopez L, Aurelle Y. Potential of using Hydrocyclone and Hydrocyclone equipped with Grit pot as a pre-treatment in run-off water treatment. Chemical Engineering and Processing: Process Intensification. 2004;43(1):67-83.

[20] Woodfield D, Bickert G. Separation of flocs in hydrocyclones—significance of floc breakage and floc hydrodynamics. International Journal of Mineral Processing. 2004;73(2):239-49.

[21] Concha F. Fluid mechanics fundamentals of hydrocyclones and its applications in the mining industry / [internet resource]. Cham, Switzerland: Cham, Switzerland : Springer; 2021.

[22] Vega-Garcia D, Brito-Parada PR, Cilliers JJ. Optimising small hydrocyclone design using 3D printing and CFD simulations. Chemical Engineering Journal. 2018;350:653-9.

[23] Shishkin RA, Yuferov YV. Technology for Producing Ceramic Materials for Hydrocyclone Linings. Glass Ceram. 2020;77(1-2):57-61.

[24] Levchenko GV, Svistelnik OY, Plyuta VL, Sychkov AB, Nesterenko AM. Manufacturing technology for cast inserts of new wear-resistant alloys for combined mill linings. Metallurgist. 2013;56(9-10):748-52.

[25] Shakeel Syed M, Rafeie M, Henderson R, Vandamme D, Asadnia M, Ebrahimi Warkiani M. A 3D-printed mini-hydrocyclone for high throughput particle separation: application to primary harvesting of microalgae. Lab on a Chip. 2017;17(14):2459-69.

[26] ASTM. Additive manufacturing — General principles — Fundamentals and vocabulary. 2021.

[27] Hull, Charles W. Apparatus for production of three-dimensional objects by stereolithography. 4 ed1986.

[28] Ngo TD, Kashani A, Imbalzano G, Nguyen KTQ, Hui D. Additive manufacturing (3D printing): A review of materials, methods, applications and challenges. Composites Part B: Engineering. 2018;143:172-96.

[29] Wang X, Jiang M, Zhou Z, Gou J, Hui D. 3D printing of polymer matrix composites: A review and prospective. Composites Part B: Engineering. 2017;110:442-58.

[30] Jancsurak J. Prototyping options. Appliance design. 1994;42(2):30.

[31] Kai CC, Jacob GGK, Mei T. Interface between CAD and Rapid Prototyping systems. Part 1: A study of existing interfaces. International journal of advanced manufacturing technology. 1997;13(8):566-70.

[32] Chua CK, Chou SM, Wong TS. A study of the state-of-the-art rapid prototyping technologies. The International Journal of Advanced Manufacturing Technology. 1998;14(2):146-52.

[33] Crockett R. Building the Future, One Layer at a Time.(rapid prototyping). The World & I. 1999;14(7):170.

[34] McKenna JF. RP made easy. Tooling and production. 2000;66(9):36-.

[35] Bernard A, Fischer A. New Trends in Rapid Product Development. CIRP Annals. 2002;51(2):635-52.

[36] Przekop RE, Kujawa M, Pawlak W, Dobrosielska M, Sztorch B, Wieleba W. Graphite Modified Polylactide (PLA) for 3D Printed (FDM/FFF) Sliding Elements. Polymers. 2020;12(6).

[37] Mohamed OA, Masood SH, Bhowmik JL. Optimization of fused deposition modeling process parameters: a review of current research and future prospects. Advances in Manufacturing. 2015;3(1):42-53.

[38] Masood SH. Intelligent rapid prototyping with fused deposition modelling. RAPID PROTOTYPING J. 1996;2(1):24-33.

[39] Srivatsan TS. Materials Processing Handbook, Joanna R. Groza, James F. Shackelford, Enrique J. Lavernia, and Michael T. Powers, Editors: CRC Press, Boca Raton, FL, 2007, 670 pages, ISBN: 978-0-8493-3216-6. Taylor & Francis Group; 2012. p. 1146-7.

[40] Anitha R, Arunachalam S, Radhakrishnan P. Critical parameters influencing the quality of prototypes in fused deposition modelling. Journal of Materials Processing Technology. 2001;118(1):385-8.

[41] Burke C, Dalal A, Abukhalaf A, Noorani R. Effects of process parameter variation on the surface roughness of polylactic acid (PLA) materials using design of experiments (DOE). IOP Conf Ser: Mater Sci Eng. 2020;897(1):12003.

[42] Singh R, Trivedi A. Experimental Investigations for Surface Roughness and Dimensional Accuracy of FDM Components with Barrel Finishing. Proc Natl Acad Sci, India, Sect A Phys Sci. 2017;87(3):455-63.

[43] Thrimurthulu K, Pandey PM, Venkata Reddy N. Optimum part deposition orientation in fused deposition modeling. INT J MACH TOOL MANU. 2004;44(6):585-94.

[44] Oropallo W, Piegl LA. Ten challenges in 3D printing. Engineering with Computers. 2016;32(1):135-48.

[45] Chohan JS, Singh R, Boparai KS, Penna R, Fraternali F. Dimensional accuracy analysis of coupled fused deposition modeling and vapour smoothing operations for biomedical applications. Composites Part B: Engineering. 2017;117:138-49.

[46] Bashford D. Thermoplastics : directory and databook. 1st . ed. London

New York: London

New York : Chapman & Hall; 1997.

[47] Melchels FPW, Feijen J, Grijpma DW. A review on stereolithography and its applications in biomedical engineering. Biomaterials. 2010;31(24):6121-30.

[48] Cho YH, Lee IH, Cho DW. Laser scanning path generation considering photopolymer solidification in micro-stereolithography. Microsystem Technologies. 2005;11(2):158-67.

[49] Haggerty JS, Sachs EM, Cima MJ, Williams PA. THREE-DIMENSIONAL PRINTING TECHNIQUES. 5 ed1991.

[50] Utela B, Storti D, Anderson R, Ganter M. A review of process development steps for new material systems in three dimensional printing (3DP). Journal of Manufacturing Processes. 2008;10(2):96-104.

[51] Gibson I, Shi D. Material properties and fabrication parameters in selective laser sintering process. Rapid Prototyping Journal. 1997;3(4):129-36.

[52] Goodridge RD, Shofner ML, Hague RJM, McClelland M, Schlea MR, Johnson RB, Tuck CJ. Processing of a Polyamide-12/carbon nanofibre composite by laser sintering. Polymer Testing. 2011;30(1):94-100.

[53] Goh KL. Reinforcing by Fibres. In: Goh KL, editor. Discontinuous-Fibre Reinforced Composites: Fundamentals of Stress Transfer and Fracture Mechanics. London: Springer London; 2017. p. 1-19.

[54] Sanei SHR, Popescu D. 3d-printed carbon fiber reinforced polymer composites: A systematic review. J COMPOS SCI. 2020;4(3):98.

[55] Stratasys launches carbon fiber-filled nylon for 3D printing. Reinforced plastics (London). 2017;61(4):218-.

[56] Ning F, Cong W, Qiu J, Wei J, Wang S. Additive manufacturing of carbon fiber reinforced thermoplastic composites using fused deposition modeling. Composites Part B: Engineering. 2015;80:369-78.

[57] Ahn S-H, Montero M, Odell D, Roundy S, Wright PK. Anisotropic material properties of fused deposition modeling ABS. RAPID PROTOTYPING J. 2002;8(4):248-57.

[58] Standard Test Method for Tensile Properties of Plastics.

[59] Standard Test Method for Tensile Properties of Polymer Matrix Composite Materials.

[60] Sun Q, Rizvi GM, Bellehumeur CT, Gu P. Effect of processing conditions on the bonding quality of FDM polymer filaments. RAPID PROTOTYPING J. 2008;14(2):72-80.

[61] Sood AK, Ohdar RK, Mahapatra SS. Parametric appraisal of mechanical property of fused deposition modelling processed parts. Materials & Design. 2010;31(1):287-95.

[62] Standards IOf. ISO/R 527:1966 Plastics — Determination of tensile properties. 1966.

[63] Standards IOo. ISO 178:1975 Plastics — Determination of flexural properties of rigid plastics. 1975.

[64] Standards IOo. ISO 179:1982 Plastics — Determination of Charpy impact strength of rigid materials. 1982.

[65] Torrado Perez AR, Roberson DA, Wicker RB. Fracture surface analysis of 3D-printed tensile specimens of novel ABS-based materials. Journal of failure analysis and prevention. 2014;14(3):343-53.

[66] Cole DP, Riddick JC, Iftekhar Jaim HM, Strawhecker KE, Zander NE. Interfacial mechanical behavior of 3D printed ABS. Journal of Applied Polymer Science. 2016;133(30).

[67] Goh GD, Yap YL, Tan HKJ, Sing SL, Goh GL, Yeong WY. Process–Structure–Properties in Polymer Additive Manufacturing via Material Extrusion: A Review. Critical Reviews in Solid State and Materials Sciences. 2019:1-21.

[68] Torrado AR, Roberson DA. Failure Analysis and Anisotropy Evaluation of 3D-Printed Tensile Test Specimens of Different Geometries and Print Raster Patterns. Journal of Failure Analysis and Prevention. 2016;16(1):154-64.

[69] Roberson DA, Torrado Perez AR, Shemelya CM, Rivera A, MacDonald E, Wicker RB. Comparison of stress concentrator fabrication for 3D printed polymeric izod impact test specimens. Additive Manufacturing. 2015;7:1-11.

[70] Uddin MS, Sidek MFR, Faizal MA, Ghomashchi R, Pramanik A. Evaluating Mechanical Properties and Failure Mechanisms of Fused Deposition Modeling Acrylonitrile Butadiene Styrene Parts. Journal of Manufacturing Science and Engineering. 2017;139(8).

[71] Al-Khalil MFS, Soden PD, Kitching R, Hinton MJ. The effects of radial stresses on the strength of thin-walled filament wound GRP composite pressure cylinders. International Journal of Mechanical Sciences. 1995;38(1):97-120.

[72] Arhant M, Briançon C, Burtin C, Davies P. Carbon/polyamide 6 thermoplastic composite cylinders for deep sea applications. Composite Structures. 2019;212:535-46.

[73] Velosa JC, Nunes JP, Antunes PJ, Silva JF, Marques AT. Development of a new generation of filament wound composite pressure cylinders. Composites Science and Technology. 2009;69(9):1348-53.

[74] Azeem M, Ya HH, Alam MA, Kumar M, Stabla P, Smolnicki M, et al. Application of Filament Winding Technology in Composite Pressure Vessels and Challenges: A Review. Journal of energy storage. 2022;49:103468.

[75] Guo K, Chen S, Wen L, Xiao J. Prediction of dome thickness for composite pressure vessels from filament winding considering the effect of winding pattern. Composite structures. 2022:116580.

[76] PD5500 AMD1 (09/18): Specification for unfired fusion welded pressure vessels. British Standards Institute; 2018.

[77] Ibrahim A, Ryu Y, Saidpour M. Stress Analysis of Thin-Walled Pressure Vessels. Modern Mechanical Engineering. 2015;Vol.05No.01:9.

[78] Ackermann M, Šafka J, Lachman M, Veselka F. Rapid Prototyping Technology for Special Pressure Vessels. Materials science forum. 2018;919:222-9.

[79] Abdalla HMA, Casagrande D, De Bona F, De Monte T, Sortino M, Totis G. An optimized pressure vessel obtained by metal additive manufacturing: Preliminary results. International Journal of Pressure Vessels and Piping. 2021;192:104434.

[80] Yelamanchi B, Mummareddy B, Santiago CC, Ojoawo B, Metsger K, Helfferich B, et al. Mechanical and fatigue performance of pressurized vessels fabricated with Multi Jet Fusion™ for automotive applications. Additive Manufacturing. 2021;44:102048.

[81] Gordeev EG, Galushko AS, Ananikov VP. Improvement of quality of 3D printed objects by elimination of microscopic structural defects in fused deposition modeling. PLOS ONE. 2018;13(6):e0198370.

[82] Lay M, Thajudin NLN, Hamid ZAA, Rusli A, Abdullah MK, Shuib RK. Comparison of physical and mechanical properties of PLA, ABS and nylon 6

fabricated using fused deposition modeling and injection molding. Composites Part B: Engineering. 2019;176:107341.

[83] Al-Hasni S, Santori G. 3D printing of vacuum and pressure tight polymer vessels for thermally driven chillers and heat pumps. Vacuum. 2020;171:109017.

[84] Belter JT, Dollar AM. Strengthening of 3D printed fused deposition manufactured parts using the fill compositing technique. PLoS One. 2015;10(4):e0122915.

[85] Hassani V. An investigation of additive manufacturing technologies for development of end-use components: A case study. International Journal of Pressure Vessels and Piping. 2020;187:104171.

[86] Australia SAo. AS 3678-1990 Structural steel - Hot-rolled plates, floorplates and slabs. 1990.

[87] Saravanan P, Selyanchyn R, Watanabe M, Fujikawa S, Tanaka H, Lyth SM, Sugimura J. Ultra-low friction of polyethylenimine / molybdenum disulfide (PEI/MoS2)15 thin films in dry nitrogen atmosphere and the effect of heat treatment. Tribology International. 2018;127:255-63.

[88] Bouaziz R, Truffault L, Borisov R, Ovalle C, Laiarinandrasana L, Miquelard-Garnier G, Fayolle B. Elastic Properties of Polychloroprene Rubbers in Tension and Compression during Ageing. Polymers (Basel). 2020;12(10).

[89] ASTM. Standard Test Method for Resistance to Short-Time Hydraulic Pressure of Plastic Pipe, Tubing, and Fittings. ASTM; 2018.

[90] Sergeichev I, Fedulov B, Fedorenko A, Zershchikov K, Lomakin E, Akhatov I. Constitutive material model for the design and virtual testing of pressure vessel service equipment manufactured from thermoplastic fiber-reinforced polymer composites. International Journal of Pressure Vessels and Piping. 2021;193:104475.

[91] Yu M-h. Advances in strength theories for materials under complex stress state in the 20th Century. Applied Mechanics Reviews. 2002;55(3):169-218.

[92] Kluczyński J, Szachogłuchowicz I, Torzewski J, Śnieżek L, Grzelak K, Budzik G, et al. Fatigue and fracture of additively manufactured polyethylene terephthalate glycol and acrylonitrile butadiene styrene polymers. International Journal of Fatigue. 2022;165:107212.

[93] Mu Q. Experimental data for creep and dynamic mechanical properties of polycarbonate and polycarbonate / acrylonitrile-butadiene-styrene. Data in Brief. 2022;42:108264.

[94] Sudduth RD. Comparison of the viscous and elastic components of two ABS materials with creep, stress relaxation and constant strain rate measurements using the universal viscoelastic model. Journal of applied polymer science. 2003;90(5):1298-318.

[95] Zhang H. Characterization of tensile, creep, and fatigue properties of 3D printed Acrylonitrile Butadiene Styrene: ProQuest Dissertations Publishing; 2016.

[96] Lim S, Rhee J, Nah C, Lee SH, Lyu M. Predicting the Long-term Creep Behavior of Plastics Using the Short-term Creep Test. International Polymer Processing. 2004;19:313-9.

[97] Mohamed OA, Masood SH, Bhowmik JL. Experimental investigation of time-dependent mechanical properties of PC-ABS prototypes processed by FDM additive manufacturing process. Materials Letters. 2017;193:58-62.

[98] Zhang H, Cai L, Golub M, Zhang Y, Yang X, Schlarman K, Zhang J. Tensile, Creep, and Fatigue Behaviors of 3D-Printed Acrylonitrile Butadiene Styrene. Journal of Materials Engineering and Performance. 2018;27(1):57-62.

[99] International A. ASTM D2990-17: Standard Test Methods for Tensile, Compressive, and Flexural Creep and Creep-Rupture of Plastics. 2017.

[100] Baker I. ABS Plastics. Switzerland: Switzerland: Springer International Publishing AG; 2018. p. 1-3.

[101] Hertzberg RW, Skibo MD, Manson JA. Fatigue Fracture Micromechanisms in Engineering Plastics. 100 Barr Harbor Drive, PO Box C700, West Conshohocken, PA 19428-2959: 100 Barr Harbor Drive, PO Box C700, West Conshohocken, PA 19428-2959: ASTM International; 1979. p. 471-500.

[102] Marissen R, Schudy D, Kemp AVJM, Coolen SMH, Duijzings WG, Van Der Pol A, Van Gulick AJ. The effect of material defects on the fatigue behaviour and the fracture strain of ABS. J MATER SCI. 2001;36(17):4167-80.

[103] Svarovsky L. 2 - Characterization of particles suspended in liquids. In: Svarovsky L, editor. Solid-Liquid Separation (Fourth Edition). Oxford: Butterworth-Heinemann; 2001. p. 30-65.

[104] Frosell T, Fripp M, Gutmark E. Investigation of slurry concentration effects on solid particle erosion rate for an impinging jet. Wear. 2015;342-343:33-43.

[105] Abdelbary A. 6 - Wear of polymer composites. Wear of Polymers and Composites. Oxford: Woodhead Publishing; 2014. p. 133-58.

[106] Aquaro D, Fontani E. Erosion of Ductile and Brittle Materials. Meccanica. 2001;36(6):651-61.

[107] Zahavi J, Schmitt GF. Solid particle erosion of reinforced composite materials. Wear. 1981;71(2):179-90.

[108] Koskela K, Lindgren M, Serna-Guerrero R. Slurry erosion resistance of polyethylene under conditions relevant for mineral processing. Wear. 2017;392-393:1-7.

[109] Larsen-Basse J, Tadjvar A. Slurry abrasion of polymers under simulated submarine conditions. Wear. 1988;122(2):135-49.

[110] Finnie I. Erosion of surfaces by solid particles. Wear. 1960;3(2):87-103.

[111] Zu JB, Hutchings IM, Burstein GT. Design of a slurry erosion test rig. Wear. 1990;140(2):331-44.

[112] Sparks AJ, Hutchings IM. Effects of erodent recycling in solid particle erosion testing. Wear. 1993;162-164:139-47.

[113] Stack MM, Pungwiwat N. Slurry erosion of metallics, polymers, and ceramics: particle size effects. Materials Science and Technology. 1999;15(3):337-44.

[114] Wensink H, Elwenspoek MC. A closer look at the ductile–brittle transition in solid particle erosion. Wear. 2002;253(9):1035-43.

[115] Friedrich K. Erosive wear of polymer surfaces by steel ball blasting. Journal of Materials Science. 1986;21(9):3317-32.

[116] Neilson JH, Gilchrist A. Erosion by a stream of solid particles. Wear. 1968;11(2):111-22.

[117] Tilly GP, Sage W. The interaction of particle and material behaviour in erosion processes. Wear. 1970;16(6):447-65.

[118] Hojo H, Tsuda K, Yabu T. Erosion damage of polymeric material by slurry. Wear. 1986;112(1):17-28.

[119] International A. ASTM G75-82 Standard Test Method for Determination of Slurry Abrasivity (Miller Number) and Slurry Abrasion Response of Materials (SAR Number).

[120] Barkoula NM, Gremmels J, Karger-Kocsis J. Dependence of solid particle erosion on the cross-link density in an epoxy resin modified by hygrothermally decomposed polyurethane. Wear. 2001;247(1):100-8.

[121] Arjula S, Harsha AP. Study of erosion efficiency of polymers and polymer composites. Polymer Testing. 2006;25(2):188-96.

[122] Rajesh JJ, Bijwe J, Venkataraman B, Tewari US. Effect of water absorption on erosive wear behaviour of polyamides. Journal of materials science. 2002;37(23):5107-13.

[123] Sundararajan G, Roy M, Venkataraman B. Erosion efficiency-a new parameter to characterize the dominant erosion micromechanism. Wear. 1990;140(2):369-81.

[124] Harsha AP, Thakre AA. Investigation on solid particle erosion behaviour of polyetherimide and its composites. Wear. 2007;262(7):807-18.

[125] Arjula S, Harsha AP, Ghosh MK. Erosive wear of unidirectional carbon fibre reinforced polyetherimide composite. Materials Letters. 2008;62(17):3246-9.

[126] Arjula S, Harsha AP, Ghosh MK. Solid-particle erosion behavior of high-performance thermoplastic polymers. Journal of Materials Science. 2008;43(6):1757-68.

[127] Giourntas L, Hodgkiess T, Galloway AM. Comparative study of erosion–corrosion performance on a range of stainless steels. Wear. 2015;332-333:1051-8.

[128] Lima CRC, Mojena MAR, Rovere CAD, de Souza NFC, Fals HDC. Slurry Erosion and Corrosion Behavior of Some Engineering Polymers Applied by Low-Pressure Flame Spray. Journal of Materials Engineering and Performance. 2016;25(11):4911-8.

[129] Debnath UK, Chowdhury MA, Nuruzzaman DM. The Experimental Characteristics and Evaluation of Nylon-12 in Erosion Process. Journal of testing and evaluation. 2017;45(3):773-87.

[130] Patnaik A, Satapathy A, Chand N, Barkoula NM, Biswas S. Solid particle erosion wear characteristics of fiber and particulate filled polymer composites: A review. Wear. 2010;268(1-2):249-63.

[131] Walley SM, Field JE. The Erosion and Deformation of Polyethylene by Solid-Particle Impact. Phil Trans R Soc Lond A. 1987;321(1558):277-303.

[132] Barkoula N-M, Karger-Kocsis J. Review Processes and influencing parameters of the solid particle erosion of polymers and their composites. Journal of Materials Science. 2002;37(18):3807-20.

[133] Hutchings IM. Ductile-brittle transitions and wear maps for the erosion and abrasion of brittle materials. Journal of physics D, Applied physics. 1992;25(1):A212-A21.

[134] Tewari US, Harsha AP, Häger AM, Friedrich K. Solid particle erosion of unidirectional carbon fibre reinforced polyetheretherketone composites. Wear. 2002;252(11):992-1000.

[135] Lhymn C, Wapner P. Slurry erosion of polyphenylene sulfide-glass fiber composites. Wear. 1987;119(1):1-11.

[136] Ruff AW, Wiederhorn S. Erosion by solid particle impact: US Department of Commerce, National Bureau of Standards; 1979.

[137] Bahadur S, Zheng Y. Mechanical and tribological behavior of polyester reinforced with short glass fibers. Wear. 1990;137(2):251-66.

[138] Bijwe J, Indumathi J, John Rajesh J, Fahim M. Friction and wear behavior of polyetherimide composites in various wear modes. Wear. 2001;249(8):715-26.

[139] Kim A, Kim I. Solid particle erosion of CFRP composite with different laminate orientations. Wear. 2009;267(11):1922-6.

[140] Tsuda K, Kubouchi M, Sakai T, Saputra AH, Mitomo N. General method for predicting the sand erosion rate of GFRP. Wear. 2006;260(9):1045-52.

[141] Akinci A, Ercenk E, Yilmaz S, Sen U. Slurry erosion behaviors of basalt filled low density polyethylene composites. Materials & Design. 2011;32(5):3106-11.

[142] Yabuki A, Sugita K, Matsumura M, Hirashima M, Tsunaga M. The anti-slurry erosion properties of polyethylene for sewerage pipe use. Wear. 2000;240(1):52-8.

[143] Ahamed RAR, Johnstone CM, Stack MM. Impact Angle Effects on Erosion Maps of GFRP: Applications to Tidal Turbines. Journal of Bio- and Tribo-Corrosion. 2016;2(2):14.

[144] Pettersson U, Jacobson S. Influence of surface texture on boundary lubricated sliding contacts. Tribology International. 2003;36(11):857-64.

[145] Coblas DG, Fatu A, Maoui A, Hajjam M. Manufacturing textured surfaces: State of art and recent developments. Proceedings of the Institution of Mechanical Engineers, Part J: Journal of Engineering Tribology. 2015;229(1):3-29.

[146] Han Z, Zhang J, Ge C, Lü Y, Jiang J, Liu Q, Ren L. Anti-Erosion Function in Animals and its Biomimetic Application. Journal of Bionic Engineering. 2010;7(4):S50-S8.

[147] Han Z, Zhu B, Yang M, Niu S, Song H, Zhang J. The effect of the micro-structures on the scorpion surface for improving the anti-erosion performance. Surface and Coatings Technology. 2017;313:143-50.

[148] Friedrich K. Polymer composites for tribological applications. Advanced Industrial and Engineering Polymer Research. 2018;1(1):3-39.

[149] Sedlaček M, Podgornik B, Ramalho A, Česnik D. Influence of geometry and the sequence of surface texturing process on tribological properties. Tribology International. 2017;115:268-73.

[150] Costa H, Hutchings I. Some innovative surface texturing techniques for tribological purposes. Proceedings of the Institution of Mechanical Engineers, Part J: Journal of Engineering Tribology. 2015;229(4):429-48.

[151] Goh GD, Yap YL, Tan HKJ, Sing SL, Goh GL, Yeong WY. Process–Structure–Properties in Polymer Additive Manufacturing via Material Extrusion: A Review. Critical Reviews in Solid State and Materials Sciences. 2020;45(2):113-33.

[152] Sood AK, Equbal A, Toppo V, Ohdar RK, Mahapatra SS. An investigation on sliding wear of FDM built parts. CIRP Journal of Manufacturing Science and Technology. 2012;5(1):48-54.

[153] Sun Q, Rizvi GM, Bellehumeur CT, Gu P. Effect of processing conditions on the bonding quality of FDM polymer filaments. Rapid Prototyping Journal. 2008;14(2):72-80.

[154] Mohamed OA, Masood SH, Bhowmik JL. A parametric investigation of the friction performance of PC-ABS parts processed by FDM additive manufacturing process. Polymers for Advanced Technologies. 2017;28(12):1911-8.

[155] Standard Test Method for Wear Testing with a Pin-on-Disk Apparatus.

[156] Hong Y, Zhang P, Lee K-H, Lee C-H. Friction and wear of textured surfaces produced by 3D printing. Science China Technological Sciences. 2017;60(9):1400-6.

[157] Lee Y-J, Lee K-H, Lee C-H. Self-Lubricating and Friction Performance of a Three-Dimensional-Printed Journal Bearing. Journal of Tribology. 2018;140(5).

[158] Hanon M, Kovács M, Zsidai L. Tribology behaviour investigation of 3D printed polymers. 2019;10:173–81.

[159] Abdollah MFB, Norani MNM, Abdullah MIHC, Amiruddin H, Ramli FR, Tamaldin N. Synergistic effect of loads and speeds on the dry sliding behaviour of fused filament fabrication 3D-printed acrylonitrile butadiene styrene pins with different internal geometries. The International Journal of Advanced Manufacturing Technology. 2020;108(7):2525-39.

[160] Aziz R, Ul Haq MI, Raina A. Effect of surface texturing on friction behaviour of 3D printed polylactic acid (PLA). Polymer Testing. 2020;85:106434.

[161] Boparai K, Singh R, Singh H. Comparison of tribological behaviour for Nylon6-Al-Al2O3 and ABS parts fabricated by fused deposition modelling: This paper reports a low cost composite material that is more wear-resistant than conventional ABS. Virtual and Physical Prototyping. 2015;10(2):59-66.

[162] Singh R, Singh S, Fraternali F. Development of in-house composite wire based feed stock filaments of fused deposition modelling for wear-resistant materials and structures. Composites Part B: Engineering. 2016;98:244-9.

[163] Bustillos J, Montero D, Nautiyal P, Loganathan A, Boesl B, Agarwal A. Integration of graphene in poly(lactic) acid by 3D printing to develop creep and wear-resistant hierarchical nanocomposites. Polymer Composites. 2018;39(11):3877-88.

[164] Ertane EG, Dorner-Reisel A, Baran O, Welzel T, Matner V, Svoboda S. Processing and Wear Behaviour of 3D Printed PLA Reinforced with Biogenic Carbon. Advances in tribology. 2018;2018:1-11.

[165] Lin L, Ecke N, Huang M, Pei X-Q, Schlarb AK. Impact of nanosilica on the friction and wear of a PEEK/CF composite coating manufactured by fused deposition modeling (FDM). Composites Part B: Engineering. 2019;177:107428.

[166] Prusinowski A, Kaczyński R. Tribological Behaviour of Additively Manufactured Fiber-Reinforced Thermoplastic Composites in Various Environments. Polymers. 2020;12(7).

[167] Abdelaal O, Heshmat M, Abdelrhman Y. Experimental investigation on the effect of water-silica slurry impacts on 3D-Printed polylactic acid. Tribology International. 2020;151:106410.

[168] Sınmazçelik T, Fidan S, Ürgün S. Effects of 3D printed surface texture on erosive wear. Tribology International. 2020;144:106110.

[169] Zhou L-y, Zhang H, Pei X-q, Friedrich K, Eger C, Zhang Z. Erosive wear of transparent nanocomposite coatings. Tribology International. 2013;61:62-9.

[170] Chen J, Guo Q, Zhang S, Wang X, Shao X. Research on Friction and Wear Behaviors of PEEK/PEI/PES Plastics Alloys under Sliding Contact Condition. Procedia Engineering. 2012;36:285-91.

[171] Chen H, Zhao H, Qu J, Shao H, Zhao S. Erosion–corrosion of thermal-sprayed nylon coatings. Wear. 1999;233-235:431-5.

[172] Brownlie FC. The role of materials engineering to mitigate corrosive wear in oil field pumping applications [Ph.D. Thesis]: University of Strathclyde; 2017.

[173] BS EN ISO 4288:1998: Geometric product specification (GPS). Surface texture. Profile method: Rules and procedures for the assessment of surface texture. British Standards Institute; 1997.

[174] Sinha SL, Dewangan SK, Sharma A. A review on particulate slurry erosive wear of industrial materials: In context with pipeline transportation of mineral−slurry. Particulate Science and Technology. 2017;35(1):103-18.

[175] Hutchings I, Shipway P. 6 - Wear by hard particles. In: Hutchings I, Shipway P, editors. Tribology (Second Edition): Butterworth-Heinemann; 2017. p. 165-236.

[176] Grewal HS, Singh H, Yoon E-S. Interplay between erodent concentration and impingement angle for erosion in dilute water–sand flows. Wear. 2015;332-333:1111-9.

[177] Tropea C, Yarin AL, Foss JF. Springer Handbook of Experimental Fluid Mechanics. Berlin, Heidelberg: Berlin, Heidelberg: Springer Berlin / Heidelberg; 2007.

[178] López A, Stickland MT, Dempster WM. CFD study of fluid flow changes with erosion. Computer Physics Communications. 2018;227:27-41.

[179] Giemza B, Domański M, Deliś M, Kapica D. Tribological properties of 3D printed components. Journal of KONBiN. 2018;48(1):447-63.

[180] Hanon MM, Marczis R, Zsidai L. Impact of 3D-printing structure on the tribological properties of polymers. Industrial lubrication and tribology. 2020;72(6):811-8.

[181] Deng S, Djukic L, Paton R, Ye L. Thermoplastic–epoxy interactions and their potential applications in joining composite structures – A review. Composites Part A: Applied Science and Manufacturing. 2015;68:121-32.

[182] Wang Y-Y, Chen S-A. Polymer compatibility: Nylon-epoxy resin blends. Polymer Engineering & Science. 1980;20(12):823-9.

[183] Sarı N, Sınmazçelik T. Erosive wear behaviour of carbon fibre/polyetherimide composites under low particle speed. Materials & Design. 2007;28(1):351-5.

[184] Oka YI, Yoshida T. Practical estimation of erosion damage caused by solid particle impact: Part 2: Mechanical properties of materials directly associated with erosion damage. Wear. 2005;259(1-6):102-9.

[185] Abdelbary A. 8 - Prediction of wear in polymers and their composites. Wear of Polymers and Composites. Oxford: Woodhead Publishing; 2014. p. 185-217.

[186] Chand N, Naik A, Neogi S. Three-body abrasive wear of short glass fibre polyester composite. Wear. 2000;242(1):38-46.

Appendix A.

A.1 Erosion characterisation of DMC

An initial study was conducted to understand the behaviour of polyester DMC under slurry conditions. There is little literature on the wear response for polymers filled with both particulates and fibres [130], although it has been more recently found that the addition of fibres and fillers will almost always result in an increase of tribological properties [148]. This would be a baseline for comparison of wear rate as this material meets the structural requirements of the 150 CVX hydrocyclone and has existing tooling and expertise within the sponsor company.

Table 23. Material breakdown of DMC used for erosion testing

Material Breakdown	Wt%
Polyester Resin	25%
Marble bi-product filler	56.25%
Chopped Strand Glass (6mm)	14%
Catalyst	4.75%

DMC, in line with nomenclature, has a dough like consistency. When uncured it requires little pressure to create pieces that will hold a general shape.

Table 24. Curing parameters of DMC for erosion testing.

Curing Parameter	Value
Temperature	160°C
Pressure	35 bar
Time	3 min.

This resulted in a specimen that was 38 mm in diameter and 3 mm in thickness.

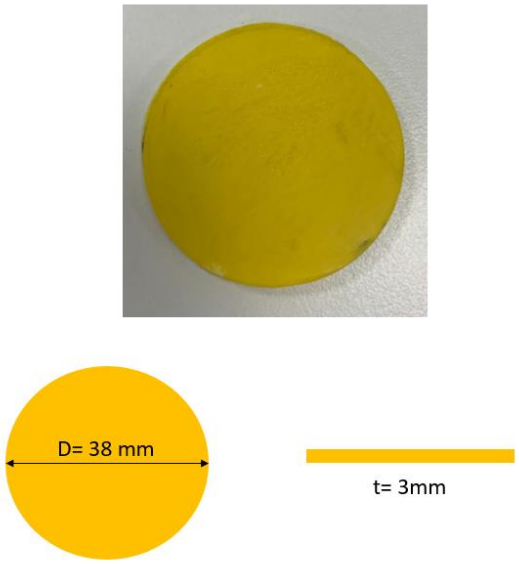

Figure 165. Dimensions of DMC sample for erosion testing

A.1.1 DMC mass loss

As the DMC was only tested for comparison purposes (the additively manufactured specimens are the focus of this research) and the tests could only be run for 30 minutes the results are separate.

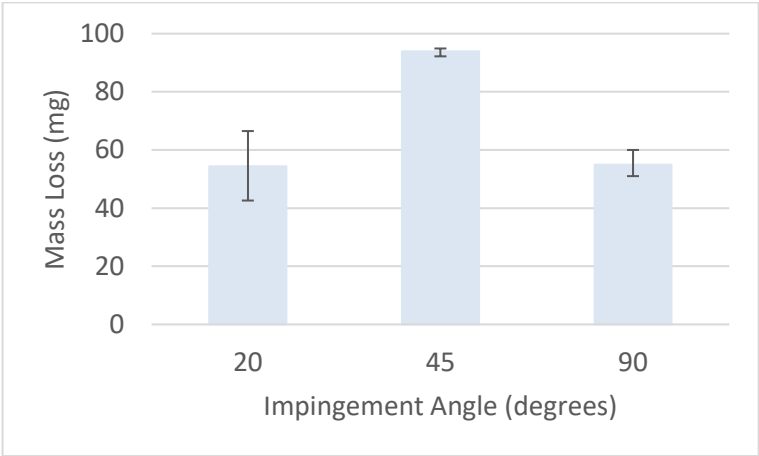

Figure 166. Comparison of mass loss (mg) for DMC samples at impingement angles of 20, 45 and 90 degrees.

A.1.1.1 DMC volume loss via XCT

After testing the samples were scanned in the XCT scanner in the Advanced Materials Research Laboratory at the University of Strathclyde. This produces a 3D stack of images that can be segmented an analysed. Image processing was completed using Dragonfly software and segmentation and measurement were done in ImageJ. An example of a classified image is shown in Figure 167. Everything that is white is recognised by the program, while the black part of the image is void.

Figure 167. Example of a classified slice image of a wear scar

The segmentation was completed by training the algorithm to recognise air vs. material. The volume loss for each sample was found by measure the 'white space' in 3D. The results are shown below. Error was calculated by dilating and eroding the 'white space' by 3 voxels.

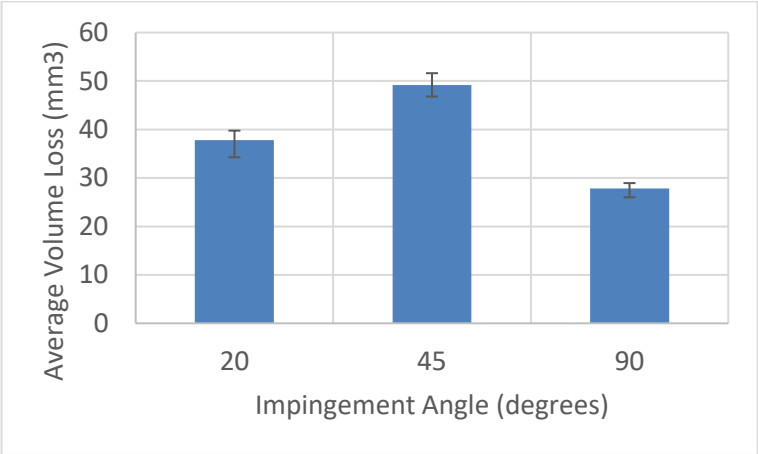

Figure 168. Comparison of volume loss (mm^3) for DMC samples at impingement angles of 20, 45 and 90 degrees.

The calculated volume loss from XCT segmented images was compared back to the mass loss via the density of the material.

Table 25. Comparison of calculated and measured volume loss data

Angle	Average Volume Loss (mm^3)	Calculated Mass Loss (mg)	Measured Average Mass Loss (mg)	Percent Error
20	37.8	68.0	54.4	25%
45	49.2	88.5	93.9	6%
90	27.8	50.1	54.9	9%

A.1.2 Microscopy

Normal impingement of the samples results in a circular wear scar with a concentric ring of abrasive wear around it. The abrasive wear is created by sand particles losing energy while boring into the material and being pushed out by incoming flow. Examples of the types of wear found at this angle are shown below.

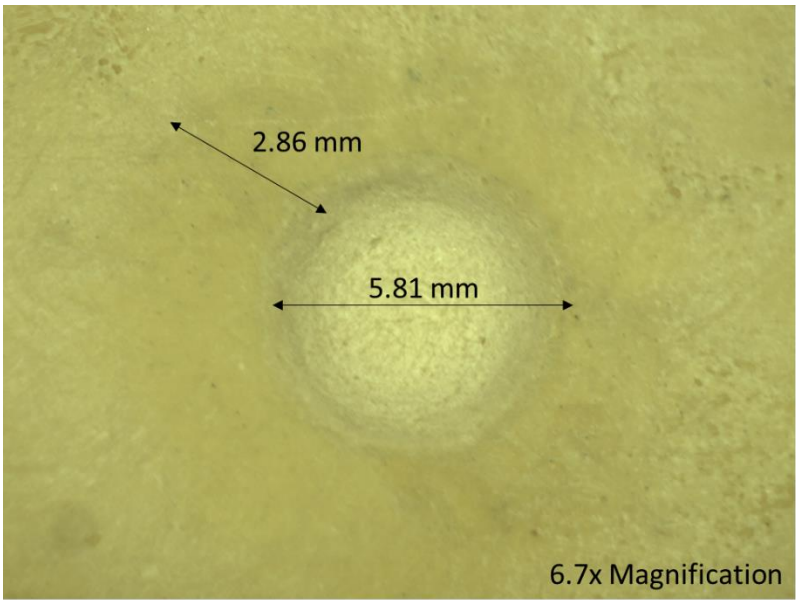

Figure 169. Wear scar at 90-degree impingement angle

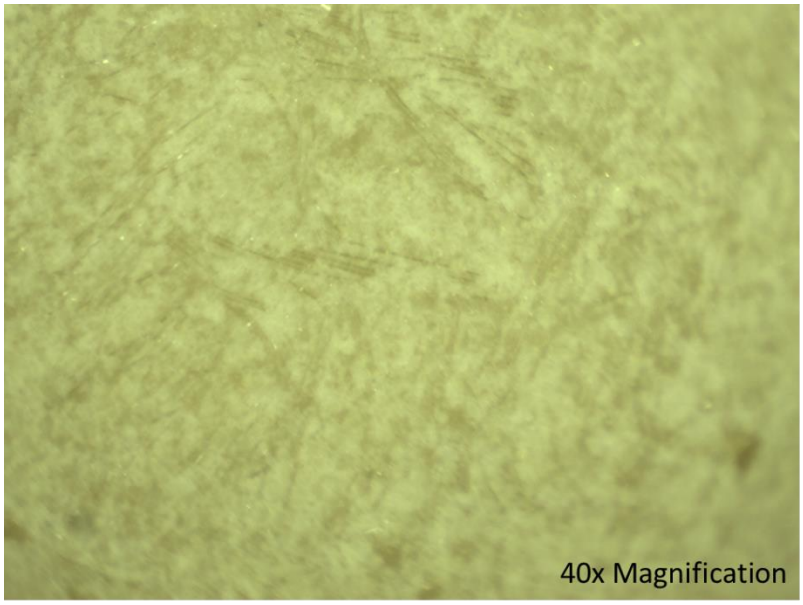

Figure 170. Damage inside 90-degree wear scar

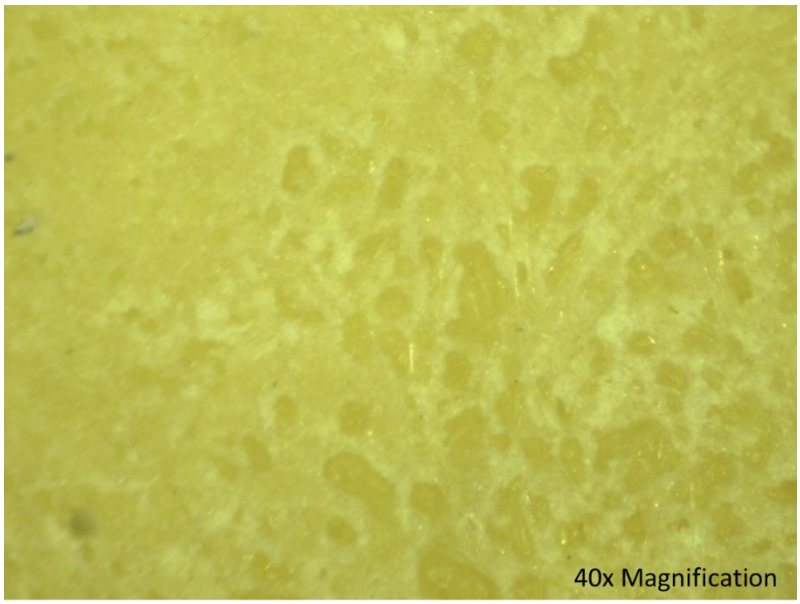

Figure 171. Damage at secondary wear scar at 90-degree impingement angle

Different to the normal impingement, 45-degree impingement creates a more oblique wear scar that starts shallow but rapidly becomes deeper. Once the particles lose energy from boring into the material, they are pushed out by incoming flow and create

a region of secondary wear similar to the 90-degree samples. The difference is that the abrasive wear region will only occur on one side of the scar (the left hand side of Figure 172).

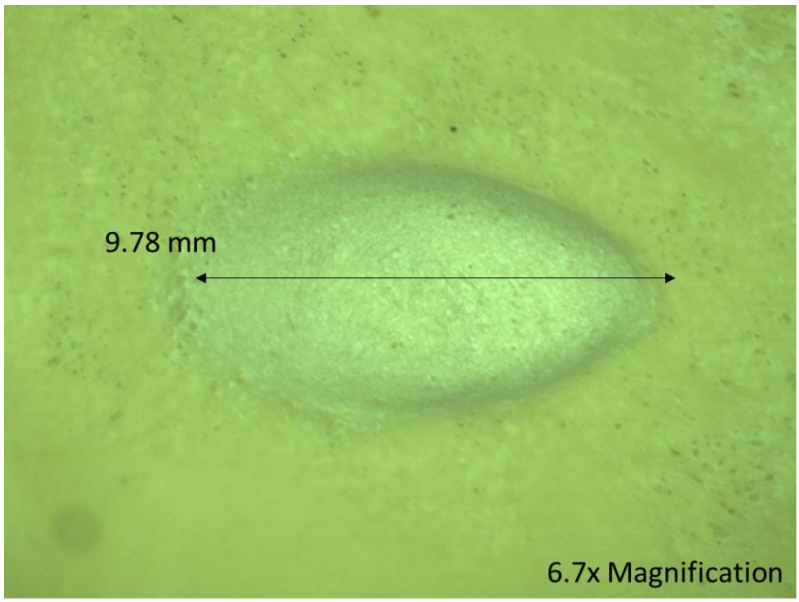

Figure 172. Wear scar at 45-degree impingement angle

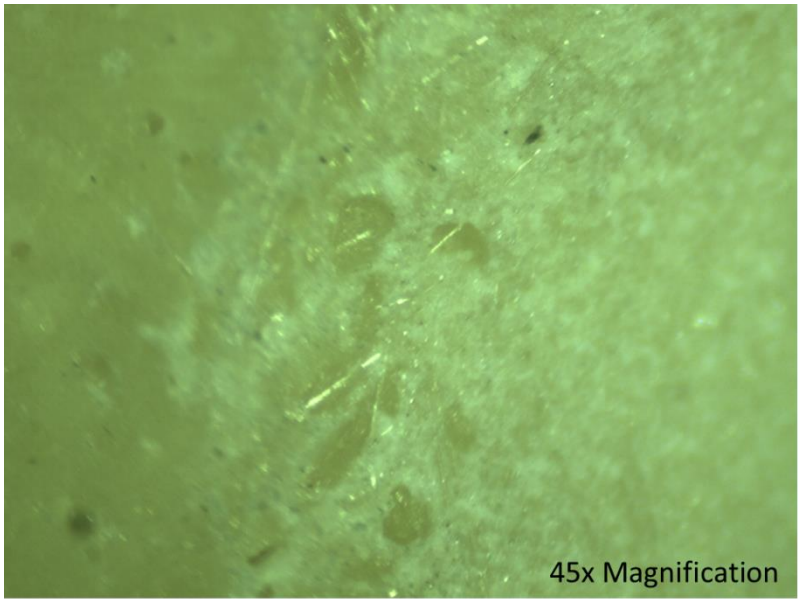

Figure 173. Damage at onset of wear at 45-degree impingement angle

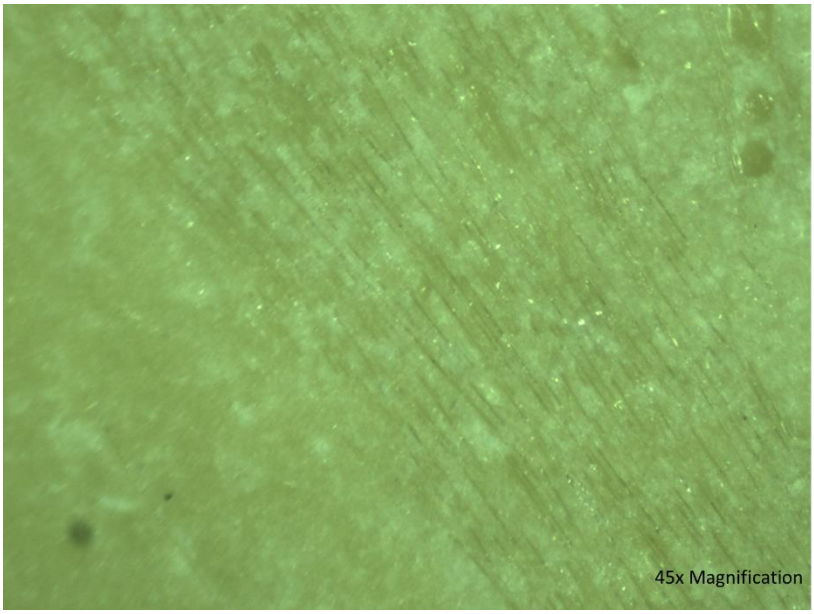

Figure 174. Damage at secondary wear normal to fibres at 45-degree impingement angle

The 20-degree impingement angle results in the longest and shallowest of the angles. While there is still a cavity formed in the primary wear it is spread out over much more area. Some secondary wear is seen but is not as apparent as at the 90 and 45-degree impingement angles.

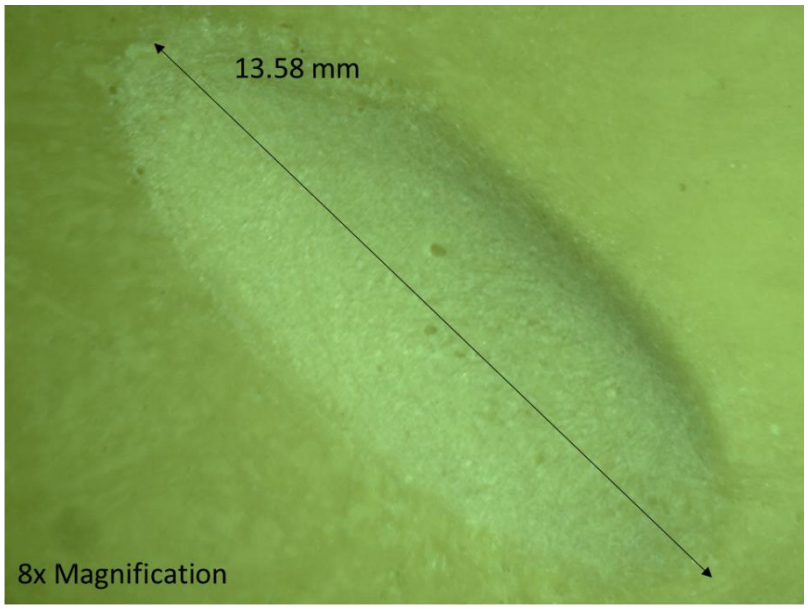

Figure 175. Wear scar at 20-degree impingement angle

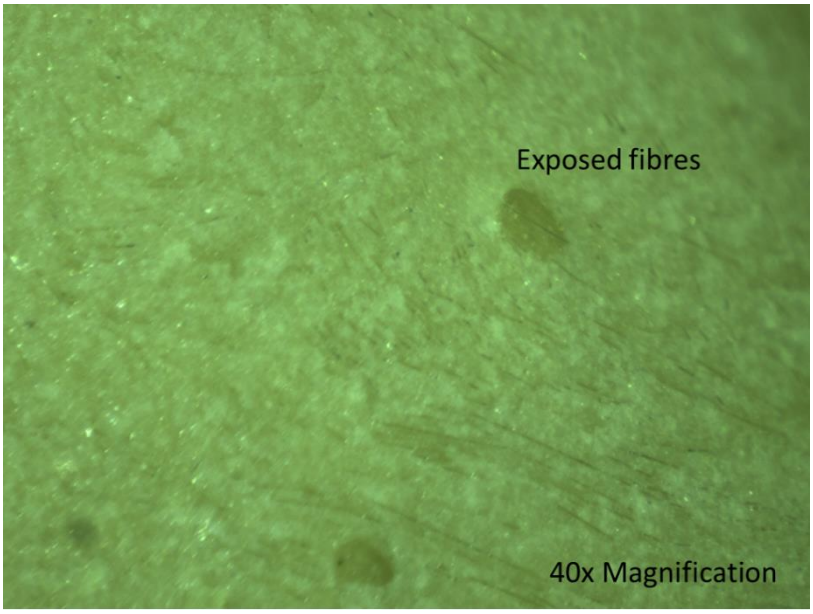

Figure 176. Damage inside wear scar at 20-degree impingement angle

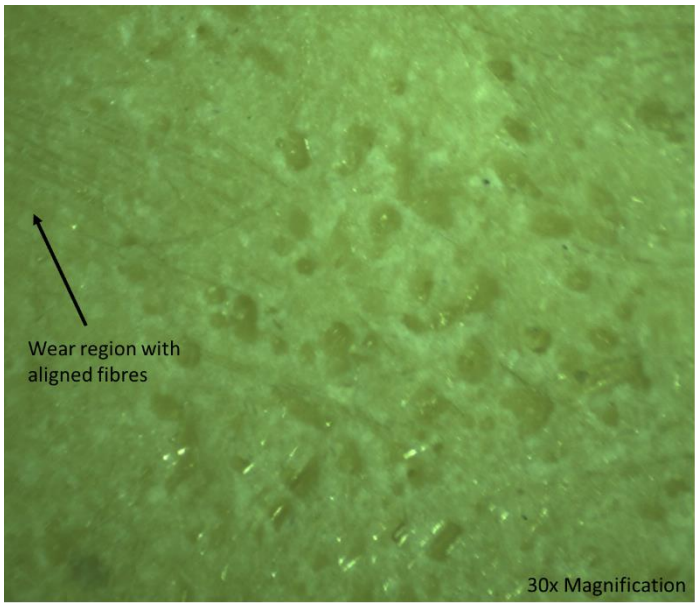

Figure 177. Damage at secondary wear scar at 20-degree impingement angle

The greatest mass loss is seen in the samples that were at 45-degrees from the flow with an average of 93.9 mg material eroded. The 90-degree and 20-degree samples were very close with 54.9 mg and 54.4 mg respectively. The volume loss calculations

showed that the 45-degree samples had the greatest loss again with 49.2 mm^3. This has an error of 6% compared to the measured mass loss after testing. The 90-degree samples showed the smallest amount of volume lost with 27.8 mm^3 with a difference of 9% from the measured mass loss. Both the 45-degree and 90-degree samples showed that the mass loss calculated from the XCT scans were less than that measures from direct weighing of the samples. The 20-degree samples however had a volume loss of 37.8 mm^3 and correlating 68 mg calculated mass loss which was 25% higher than the 54.4 mg mass loss from weighing the sample. This shows that the sand could be embedding itself in the material as the cavity created by the wear should have resulted in a larger measured mass loss. There is a possibility this is happening at other angles as well and it was not picked up in the image processing.

At 20-degrees there is still brittle fatigue occurring in the main area of the wear scar, however some pitting can be seen at the secondary wear area outside of the main cavity. In this area some regions where the fibres were aligned and near the surface appear to have resisted the erosion better than directly adjacent areas in which the fibres were more randomly oriented and further from the surface. Similar phenomena were observed at the 45-degree angle. This lends to suggest that closely packed fibres will provide resistance to slurry erosion in composites which is also found to be true in literature for abrasive wear of short glass fibre polyester composites [186].

Overall, the 45-degree samples experienced the most aggressive wear. In previous studies, it was found that for a testing conditions for tidal applications 45, 60 and 75 degree impingement angle resulted in the highest amount of wear [143] and observed for mineral processing applications [108]. From the observations, this is assumed to be caused by the synergistic effect of the sliding abrasion at the onset of the main wear scar and the removal of material by brittle fatigue over a large area than that of the 90-degree samples and a depth greater than that of the 20-degree samples.